

**NASA SPACE ENGINEERING RESEARCH CENTER
FOR UTILIZATION OF LOCAL PLANETARY RESOURCES**

**ANNUAL
PROGRESS REPORT
1992**

APR-92

**ORIGINAL CONTAINS
COLOR ILLUSTRATIONS**

**Director: T. Triffet
Co-Director, Science: J. Lewis Co-Director, Engineering: K. Ramohalli**

**THE UNIVERSITY OF ARIZONA
4717 E. Ft. Lowell Rd./AML
Tucson, AZ 85712**

Telephone: (602) 322-2304 FAX: (602) 326-0938

TABLE OF CONTENTS

Executive Summary

i

I. PROCESSING OF PROPELLANTS, VOLATILES, AND METALS

A. Reduction of Lunar Regolith

Propellant Production and Useful Materials:

Hardware Data from Components and the Systems

IA-1 -1

K. Ramohalli

Reduction of Iron Bearing Lunar Minerals
for the Production of Oxygen

IA-20 -2

C. Massieon, A. Cutler, and F. Shadman

Innovative Techniques for the Production of Energetic
Radicals for Lunar Processing, Including Cold Plasma

Processing of Local Planetary Ores

IA-63 -3

D. Bullard and D.C. Lynch

Oxygen and Iron Production by Electrolytic Smelting of Lunar Soil

IA-71 -4

R.O. Colson and L.A. Haskin

Experimental Study of the Electrolysis of Silicate Melts

IA-93 -5

R. Keller

Lunar Mining of Oxygen Using Fluorine

IA-103 -6

D.M. Burt, J.A. Tyburczy, J. Roberts, and R. Balasubramanian

Beneficiation of Ilmenite from Lunar Analog

IA-112 -7

G. Ramadorai and R. Dean

B. Reduction of the Martian Atmosphere

Extraction of Volatiles and Metals

From Extraterrestrial Materials

IB-1 -8

J.S. Lewis

Oxygen Production on Mars and the Moon

IB-10 -9

K.R. Sridhar, B. Vaniman, and S. Miller

C. Reduction of Carbonaceous Materials

Dehydration Kinetics and Thermochemistry of Selected Hydrous Phases,
and Simulated Gas Release Pattern in Carbonaceous Chondrites

IC-1 -10

K. Bose and J. Ganguly

II. PRODUCTION OF STRUCTURAL AND REFRACTORY MATERIALS

Melt-Processing of Lunar Ceramics

II-1 -11

B.D. Fabes, W.H. Poisl, D. Allen, M. Minitti, S. Hawley, and T. Beck

Recovery and Separation of Precious Metals From Space

II-13 -12

H. Freiser and S. Muralidharan

Development and Mechanical Properties of Construction Materials

II-16 -13

C.S. Desai

Large Area Solar Cells from Lunar Materials

II-28 -14

R. Bryant, P. Calvert, and J. Corley

III. RESOURCE DISCOVERY AND CHARACTERIZATION

Determination of Lunar Ilmenite Abundance from Remotely Sensed Data <i>S.M. Larson, D.E. Melendrez, J.R. Johnson, and R.B. Singer</i>	III-1 ~15
Composition of Near-Earth Asteroids <i>L.A. Lebofsky</i>	III-6 ~16
Spacewatch Discovery of Near-Earth Asteroids <i>T. Gehrels</i>	III-12 ~17
Abundance of ^3He and Other Solar-Wind-Derived Volatiles in Lunar Soil <i>T.D. Swindle</i>	III-19 ~18

IV. SYSTEM AUTOMATION AND OPTIMIZATION

Modeling, Simulation, and High-Autonomy Control of a Martian Oxygen Production Plant <i>L.C. Schooley, F.E. Cellier, F.-Y. Wang, and B.P. Ziegler</i>	IV-1 ~19
Development of a Material Processing Plant for Lunar Soil <i>U. Goettsch and K. Ousterhout</i>	IV-21 ~20
In-Situ Materials Processing Systems and Bioregenerative Life Support Systems Interrelationships <i>R. Frye and G.V. Mignon</i>	IV-30 ~21
Full System Engineering Design and Operation of an Oxygen Plant <i>J. Colvin, P. Schallhorn, and K. Ramohalli</i>	IV-33 ~22

V. DATABASE DEVELOPMENT

An Integrated Database with System Optimization and Design Features <i>A. Arabyan, P.E. Nikraves, and T.L. Vincent</i>	V-1 ~23
The Steward Observatory Asteroid Relational Database <i>M.V. Sykes and E.M. Alvarez del Castillo</i>	V-9 ~24
Near-Earth Asteroids: Observer Alert Network and Physical Observations <i>D.R. Davis and C.R. Chapman</i>	V-14 ~25

SERC PUBLICATIONS

Except for the *Resources of Near-Earth Space* reference volume, which must be ordered from the University of Arizona Press, the following publications of the Center are available without charge to qualified organizations and may be obtained by written request to the Director. **Requests must bear the letterhead of your organization.**

Those publications marked with an asterisk are finished products featuring overviews for corporate, government and university management, while those preceded by a dash are designed for the primary purpose of attracting potential students. The remainder contain detailed technical information on research and development projects, and are published in simplified form, with standardized binding and slightly non-uniform format, to permit rapid dissemination of results.

***PB-89 Program Brochure 1988-89**

***AER-90 Annual Executive Report 1989-90**

***AER-91 Annual Executive Report 1991-92**

***Newsletter:**

Vol. 1, Nos. 1-4, 1989-90

Vol. 2, Nos. 1-4, 1990-91

Vol. 3, No. 1, 1992

-AF-88 Advanced Flyer 1987-88

-CP-88 Center Poster 1987-88

Annual Progress Report:

APR-89 (1989)

APR-91/S (1990-91)

APR-91/F (1991)

APR-92 (1992)

First Annual Symposium on Space Mining and Manufacturing 1989

AIS-89/A Abstracts

AIS-89 Proceedings

Second Annual Symposium on Resources of Near Earth Space 1990

AIS-90/A Abstracts

AIS-90 Proceedings, incorporated in *Resources of Near-Earth Space*, J.S. Lewis and M.S. Matthews, eds. University of Arizona Press, Space Sciences Series, to be published March 1993.

Third Annual Symposium on Lunar Materials Technology 1992

AIS-92/A Abstracts

AIS-92 Proceedings

WR-89/1 Automation of Extraterrestrial Sources of Oxygen Production Workshop (AESOP) Report (1989)

WR-91/1 Magmaelectrolysis of Indigenous Space Materials (MISM) Report (1991)

TM-90/1 Mining Lunar Soils for He-3 1990

EXECUTIVE SUMMARY**1991-92**

The following reports, which cover the period from November 1, 1991 to October 31, 1992, document progress made in a number of areas during a highly successful year for UA/NASA SERC. Perhaps the most noteworthy achievement during the past year was NASA's award of a continuation grant to the Center. The \$1.5 million or more per year that the Center will receive for the next three years is a clear acknowledgement of the outstanding performance of faculty, staff, and students. The NASA-appointed Peer Review Team noted the Center's "first-rate performance and impressive accomplishments," its "extremely effective and well-matched management team, and its "impressive cadre of graduate and undergraduate students."

With funding assured, opportunity now exists for further development and refinement of the Center's research and education programs. Specific progress and accomplishments are briefly discussed in the following pages. Led by Professor Kumar Ramohalli, Co-Director for Engineering, and Professor John Lewis, Co-Director for Science, several of these projects have resulted in practical technologies for producing useful products from the materials and sources of energy that occur naturally in near-Earth space. The basic objective continues to be the introduction of significant cost savings in space missions through the utilization of locally available resources.

Beyond this, however, the activities of the Center constitute a unique educational program featuring the integration of engineering and science and a stimulating atmosphere for hands-on student involvement in research. Each of the professors whose work is described employs one or more graduate students as assistants, and often additional undergraduates. During this reporting period, the Center supported 26 graduate students and 11 undergraduates in research projects, all of whom were encouraged to cross-register in complementary science and engineering courses. Additionally, the Center continued its seminar series, where students learn to make technical presentations, and published an issue of *The SERC Newsletter* devoted entirely to student technical papers.

NASA's recognition and support insures the continuation of our dual commitment to the development of real technologies and hardware in the field of In Situ Resource Utilization (ISRU) and to educating the next generation of space professionals. The Center has achieved long-term stability even through times of intense competition for institutional funding and an extremely unpredictable economy. It is largely due to the work described below that we are able to report this success.

During the past year, **Professor Ramohalli**, Co-Director for Engineering, reports several major breakthroughs that involve technological, programmatic, and institutional issues. All of these were presented in his invited plenary paper at the 43rd Congress of the International Astronautical Federation, Washington, D.C., August-September 1992.

In the *technical category*, production of oxygen from carbon dioxide through disks, instead of tubes, resulted in two orders-of-magnitude increase in the yield rates per unit area in unit time compared with the earlier tube geometry. In addition, continuous operation over 800 hours showed a constant production rate. Scientific choice of the temperature-time history, along with a monolayer of carbon on the raw material, resulted in an important generalization of oxygen production from *any iron-bearing silicate* in lunar ISRU, thus removing the earlier restriction to ilmenite, which could require costly beneficiation. Additionally, a half-scale robotic soil processor was constructed for lunar applications, melt-spun glass fibers were produced in a solar furnace from simulated lunar soils, and siloxane polymers were produced from simulated lunar soils. The full-system testbed was also completed for the integrated production of a variety of useful products that include oxygen and hydrocarbons.

In the *programmatic category*, a four-cell solid electrolyte oxygen plant was designed, fabricated, tested, and shipped to NASA Lewis Research Center for demonstration purposes. Second-generation units of this design are now showing a fifty percent reduction in mass and a twofold increase in yield rates. Also, the cost-benefit of compressors for use in thin atmospheres (that of Mars, for example) was analyzed. In the *institutional category*, a new course, "Our Future in Space and Space in Our Future," was started as a Freshman Colloquium and proved to be highly successful. Graduate students from the Center were placed as summer interns at JPL (3), JSC (1), and LeRC (3). Education and outreach continued through presentations at local elementary, middle, and high schools, and through high school interns at the Center. The progress of individual engineering projects is briefly summarized under the appropriate headings in the order indicated in the Table of Contents.

Professors Shadman and Cutler investigated the kinetics and mechanism of the reduction of simulants of the iron-bearing lunar minerals olivine ($(\text{Fe,Mg})_2\text{SiO}_4$), pyroxene ($(\text{Fe,Mg,Ca})\text{SiO}_3$), and ilmenite (FeTiO_3), extending previous work with ilmenite. Fayalite is reduced by H_2 at 1070 K to 1480 K. A layer of mixed silica glass and iron forms around an unreacted core. Reaction kinetics are influenced by permeation of hydrogen through this layer and a reaction step involving dissociated hydrogen. Reaction mechanisms are independent of Mg content. Augite, hypersthene and hedenbergite are reduced in H_2 at the same temperatures. The products are iron metal and lower iron silicates mixed throughout the mineral. Activation energy rises with calcium content. Ilmenite and fayalite are reduced with carbon deposited on partially reduced minerals *via* the CO disproportionation reaction. Reduction with carbon is rapid, showing the carbothermal reduction of lunar minerals is possible.

Professor Lynch demonstrated that effective utilization of hydrogen in the reduction of ilmenite can be significantly enhanced in the presence of a non-equilibrium hydrogen plasma. Ilmenite at solid specimen temperatures of 600 °C to 970 °C were reacted in a hydrogen plasma. Those experiments revealed that hydrogen utilization can be significantly enhanced. At a specimen temperature of 850 °C the fraction of H_2 reacted was 24% compared to the 7% theoretical limit calculated with thermodynamic theory for the same temperature.

The work by **Professor Haskin and Dr. Colson** of Washington University the past year has featured two aspects: 1) electrolysis experiments on a larger scale and 2) collaboration with Carbotek Inc.

on the design of a lunar magma electrolysis cell. They had demonstrated previously that oxygen can be produced by direct electrolysis of silicate melts. Previous experiments using 50-100mg of melt have succeeded in measuring melt resistivities and oxygen production efficiencies, and have identified the character of metal products. They have now completed a series of experiments using 1-8 grams of silicate melt in alumina and spinel containers large enough to minimize surface tension effects between the melt and the wall and in the region of the electrodes. The purpose of these experiments was to demonstrate the durability of the electrode and container materials, demonstrate the energy efficiency of the electrolysis process, further characterize the nature of the expected metal and spinel products, measure the efficiency of oxygen production compared with that predicted on the basis of the smaller-scale experiments, and identify any unexpected benefits or problems of the process.

Dr. Keller of EMEC Consultants continued his research to demonstrate that melting and electrolyzing lunar silicates yields oxygen gas and potentially can be practiced in situ to produce oxygen. With the present experiments conducted with simulant oxides at 1425-1480 °C, it was ascertained that oxygen can be obtained anodically at feasible rates and current efficiencies. An electrolysis cell was operated with platinum anodes in a sealed vessel, and the production of gas was monitored. In these electrolysis experiments, stability of the anodes remained a problem, and iron and silicon did not reduce readily into the liquid silver cathode.

Experiments under the direction of **Professor Burt** of Arizona State University were directed toward generating elemental fluorine via the electrolysis of anhydrous molten fluorides. Na_2SiF_6 was dissolved in either molten NaBF_4 or a eutectic (minimum-melting) mixture of KF-LiF-NaF and electrolyzed between 450° and 600° C to Si metal at the cathode and F_2 gas at the anode. Ar gas was continuously passed through the system and F_2 was trapped in a KBr furnace. Various anode and cathode materials were investigated. Despite many experimental difficulties, the capability of the process to produce elemental fluorine was demonstrated. Professor Burt and his investigators have finished setting up the electrolysis line and have carried out 16 experiments, the first 15 of which are summarized in this report. They have successfully prepared fluorine by electrolysis, beginning with their third try on July 23.

Professor Ramadorai reported results obtained through optical microscopy studies on a meteoric eucrite sample called "Millbillillie Sample #173. Dry Magnetic separation was completed on campus in the Chemical Engineering Department, using the Frantz Isodynamic Separator at a series of current, forward, and side slope settings. Ferromagnetic particles were removed by a head magnet before the separation. The data from these tests indicated that (1 dry magnetic separation is effective only at sizes finer than 100 mesh (150 μm). In each case, dedusting of the sample to remove -400 mesh (37 μm) fines is essential. (2 The sample has to be ground to -200 (74 μm) mesh for magnetic separation to be effective. (3 The highest grade concentrate assaying 3.45 percent Ti was produced by magnetic separation of the -200 +400 mesh screen fraction at a current setting of 0.35 AMP. This concentrate contained 21.2 percent of the titanium values in the screen fraction and accounted for 2.72 weight percent of the sample used in the test. By changing vibrator feed rate, side slope, and forward slope settings, the Ti recovery can be increased to 52.4 percent, but the grade decreases to 0.98 percent Ti. The concentrate weight percent was 22.6 of the sample used in the testing.

Professor Lewis, Co-Director for Science, reports that recent progress in defining the physical, orbital, and chemical properties of the Earth-crossing asteroid and comet population has been integrated into an elaborate Monte Carlo model of the fluxes of bodies in the inner Solar System. This model is of use in projecting flight opportunities to as yet undiscovered near-Earth objects and

in assessing the impact hazard to life on Earth and the evolutionary consequences of impacts on the other terrestrial planets.

Further progress has also been made in defining desirable transportation system architectures for the use of non-terrestrial volatiles and metals, including the delivery of propellants to near-Earth space for fuelling of SEI-type expeditions, the construction and resupply of Solar Power Satellite constellations in various Earth orbits (including GEO and Highly Eccentric Earth Orbit (HEEO)), and retrieval of ^3He for use as a clean fusion fuel on Earth. These studies suggest a greater future role for SERC in the exploration of space energy sources to meet Earth's 21st-century energy requirements.

Laboratory studies of volatilization and deposition of ferrous metal alloys have demonstrated deposition of strong iron films from carbonyl chemical vapor deposition (CVD), showing the crucial role of additive gases in governing the CVD process, and pointing the way to specific experiments on extraction and deposition of ferrous metals from nonterrestrial materials.

Significant progress has been made by **Professor Sridhar** in the area of in-situ oxygen production. In order to reduce sealing problems due to thermal expansion mismatch in the disk configuration several all-Zirconia cells have been constructed and are being tested. Two of these cells have been run successfully for extended periods of time. One was run for over 200 hours and the other for over 800 hours. These extended runs, along with gas sample analysis, have shown that the oxygen being produced is definitely from CO_2 and not from air leaks or from the disk material. A new tube system is being constructed that is more rugged, portable, durable and energy efficient. The important operating parameters of this system will be better controlled compared to previous systems. An electrochemical compressor will also be constructed with a similar configuration. The electrochemical compressor will use less energy since the feedstock is already heated in the separation unit. In addition, it does not have moving parts.

As part of the continued program of study on the volatile bearing phases and volatile resource potential of carbonaceous chondrite, **Professor Ganguly** reported results of experimental studies on the dehydration kinetics of talc as a function of temperature and grain size (50 to 0.5 μm), on the equilibrium dehydration boundary of talc to 40 kbars, on a calorimetric study of enthalpy of formation of both natural and synthetic talc as a function of grain size, and preliminary results on the dehydration kinetics of epsomite. In addition, Dr. Ganguly and his team has carried out theoretical calculations on the gas release pattern of a C2(CM) carbonaceous chondrite, the Murchison meteorite.

During the past year **Dr. Fabes** continued to examine the kinetics of crystallization in simulated lunar regolith in an effort to optimize the microstructure and, hence, the mechanical properties of glass-ceramics. Dr. Fabes' group also examined the use of solar energy for melt-processing of regolith, and successfully produced strong ($> 630 \text{ MPa}$) glass fibers by melt-spinning in a solar furnace. A study of the mechanical properties of simulated lunar glasses was completed during the past year. As on Earth, the presence of moisture was found to weaken simulated lunar glasses, although the effects of surface flaws was shown to outweigh the effect of atmospheric moisture on the strength of lunar glasses. The effect of atmospheric moisture on the toughness was also studied. As expected, toughness was found to increase only marginally in an anhydrous atmosphere.

Professor Freiser and his team have developed a viable procedure centered around centrifugal partition chromatography (CPC), a multistage liquid-liquid partitioning technique for the separation of precious metals (Pt, Pd, Rh, Ir, Os, Ru). They have identified stable and inexpensive ligands that

can be readily recycled to achieve the separations of the precious metals. The separation methods developed so far yield three separate fractions: Pt, Pd, and Rh-Ir, and the Rh-Ir pair can be separated in a subsequent run. The total amount of precious metals separated in a single experiment varied from 1 to 50 mg. The factors affecting the efficiencies of these separations have also been studied. The kinetics of the decomposition of the complex and the ion pair have a major bearing on these efficiencies, with slow kinetics resulting in poor efficiencies. Methods for the improvement of the efficiencies have also been studied.

Professor Desai investigated a number of special issues related to the development of Intermediate Ceramic Composites (ICC). The Arizona Lunar Simulant used in these experiments was exhausted and a new batch prepared from crushed and ground basalt (Pomona Flow, Hanford, WA), in order to better fit the grain size distribution (GSD) with the Apollo sample. It was found that the liquefaction temperature of the modified simulant was about the same as that for the previous batch, and the chemical composition of both batches remained essentially the same. For the purpose of tensile testing a new and special grip system was designed and fabricated for flat specimens using the available MTS Test Frame. Ultrasonic characteristics (velocity, attenuation, and energy dissipation) will be monitored in order to identify the development of microcracking and fracture within the specimen in addition to its tensile characteristics.

The first goal of **Professor Calvert's** project is to produce polymers from materials available on the Moon. Since carbon would not be available from lunar materials, polydimethylsiloxane ($-\text{Si}(\text{CH}_3)_2-\text{O}-$)_n was manufactured first by controlled hydrolysis of $\text{SiCl}_2(\text{CH}_3)_2$. The next step was an attempt to make polydichlorosiloxane by controlled hydrolysis of SiCl_4 . At the end of the first year his group has recorded infra-red spectra indicating that this product has indeed been obtained.

The efforts of **Professor Singer's** project over the past year have been aimed at defining the peak abundance levels of high TiO_2 deposits on the highest spatial scales achievable from the ground (~ 500 m), and investigating possible phase function effects on the image ratios used to generate maps. Photometrically calibrated multispectral imaging data were obtained over four months at the Tumamoc Hill Observatory to achieve a full lunation of phase angles of five areas containing high and low abundance TiO_2 regions, representative highland material, pyroclastic deposits and the standard reference MS-2. A spin-off of this major observing effort was the acquisition of several excellent image sets with essentially pixel-limited (440m) resolution. New data provides important new confirmation of the complex small scale morphology of the high TiO_2 bearing deposits in the lunar regolith, and more precise abundance maps because of improved photometric controls.

Professor Lebofsky reported progress in his study to determine whether any of the near-Earth asteroids or the satellites of Mars contain hydrated phyllosilicate (clay) minerals. If these minerals are present, they would provide a ready source of water for propellant generation and use in life support systems. Professor Lebofsky's team finished a review paper on asteroid composition for the *Resources of Near-Earth Space* book which updates the existing review papers on asteroid compositions, and provides comprehensive spectral figures of all the asteroid and meteorite types in one place for the first time. The relationship between comets and asteroids is also being studied, and involves the observations of the mainbelt and near-Earth asteroids and in the development of the new taxonomic system using neural networks. The project has had outstanding success with low-albedo asteroids, to date having observed and studied about 75 low-albedo asteroids and small satellites out to at least 3μ .

Professor Gehrels continued to direct the Spacewatch program toward the overall scientific goal of surveying the solar system to find the various asteroid populations and study their statistics,

interrelations, and origins. The practical benefit to SERC is that the program will establish the locations of Earth-approaching asteroids that are accessible for utilization of their resources. The system can detect Earth-approachers in the 1-km size range even when they are far away, and can detect smaller objects when they are moving rapidly past Earth. Until Spacewatch, the size range of 6 - 300 meters in diameter for the near-Earth asteroids was unexplored. This important region represents the transition between the meteorites and the larger observed near-Earth asteroids. One of the Spacewatch discoveries, 1991 VG, may be representative of a new orbital class of object. If it is really a natural object, and not man-made, its orbital parameters are closer to those of the Earth than we have seen before. Its delta V is the lowest of all objects known thus far.

Professor Swindle continued studies defining the magnitude of systematic variations in solar wind fluence with lunar location. Volatiles implanted into the lunar regolith by the solar wind are potentially important lunar resources, and some have proposed that lunar ^3He could be used as a fuel for terrestrial nuclear fusion reactors. Since the terrestrial inventory of ^3He is so small, the lunar regolith, with concentrations of the order of parts per billion (by mass), might prove to be an economical source of ^3He . Solar-wind implantation is also the primary source of H, C and N in lunar soil. These elements could also be important, particularly for life support and for propellant production. Previously, calculations were made of the expected size of variations in the solar wind fluence. Currently, Professor Swindle's team has combined these calculations with estimates of lunar chemistry based on both telescopic and Apollo observations to identify sites that are promising either as resource areas, or as areas to test for the effects of saturation. To date they have acquired crucial lunar samples and performed some of the analyses to test for saturation.

Professors Schooley and Cellier are developing a high-autonomy intelligent command and control architecture for process plants used to produce oxygen from local planetary resources. A distributed command and control architecture is being designed and implemented so that an oxygen production plant, or other equipment, can be reliably commanded and controlled over an extended time period in a high-autonomy mode with high-level task-oriented teleoperation, from one or several remote locations. Progress has been made at all levels of the architecture.

Dr. Ousterhout is engaged in the design and construction of a one-half scale autonomous oxygen production facility for use in early missions to the Moon. The aim of this project is to develop a totally self-contained unit, able to operate autonomously, that is cost effective, lightweight, and fault tolerant. The scale model will be capable of scooping up (or digging) lunar soil, transferring the soil to a solar furnace, heating the soil in the furnace to liberate the gasses, and transferring the spent soil to a "tile" processing center. The model will be used in formulating assessments of the impact of different technologies on the overall systems design and integration.

Professors Nikravesh, Arabyan and Vincent have developed a customized, mission-specific relational database package that allows researchers working on the extraterrestrial oxygen manufacturing plant to enter physical description, engineering, and connectivity data through a uniform, graphical interface, and to store the data in formats compatible with other software also developed as part of this project.

Under the direction of **Dr. Sykes**, the Steward Observatory Asteroid Relational Database (SOARD) continues to provide data to fulfill requests by members of the space sciences community and will continue to grow as data is added to the database and new features are added to the program. SOARD has been created as a flexible tool for undertaking studies of asteroid populations and sub-populations, to probe the biases intrinsic to asteroid databases, to ascertain the completeness of data pertaining to specific problems, to aid in the development of observational programs, and

to develop pedagogical materials. To date SOARD has compiled an extensive list of data available on asteroids and made it accessible through a single menu-driven database program, which offers online help. User and programmer manuals are also available.

Drs. Davis and Chapman of the Planetary Science Institute continued the project to obtain physical observations on newly discovered Near-Earth Objects (NEOs) in order to provide fundamental data needed to assess the resources available in the population. With the goal of acquiring data on all objects brighter than magnitude $V = 17.0$, they have established an electronic mail alert and observer information service that informs observers around the world about the status of physical observations on currently observable NEOs.

omit

I. PROCESSING OF PROPELLANTS, VOLATILES, AND METALS

omit

A. REDUCTION OF LUNAR REGOLITH

497583
N93-26875

**Propellant Production and Useful Materials:
Hardware Data from Components and the Systems**

158348
p 19

**Kumar Ramohalli
University of Arizona/NASA Space Engineering Research Center**

Abstract

During the past year significant progress included a major breakthrough in oxygen production through discs (instead of tubes) that resulted in two orders-of-magnitude increase in the yield rates, proving that oxygen production from any iron-bearing silicate (avoiding costly beneficiation) in lunar ISRU; construction of a half-scale robotic soil processor; production of melt-spun fibers in a solar furnace; and the culmination of first-stage research in the construction (and delivery to NASA LeRC) of a self-contained portable oxygen plant that incorporates the first generation ISRU technologies developed at UA SERC. In addition, further reductions in mass and power needs were achieved in two smaller oxygen plants, which, however, have production rates far greater production rates.

SERC continued to attract bright students both at the undergraduate and graduate levels, and several area high school students through the Professional Internship Program (PIP) administered by the local school district. Invited lectures at elementary schools continue to draw enthusiastic response. Another important first was the creation of the Freshman Colloquium, "Space in Our Future, and Our Future in Space," geared toward women and minority students. This course proved to be a success, with more than one-half of the enrollment composed of women. In recognition of these important contributions, the author was appointed to the NRC Committee on Space Science Technologies.

Introduction

The fundamental aim continues to be the education of students in the areas of high-tech innovative space technologies and the actual hardware realization of the more promising concepts. It would be helpful to recognize that unless ISRU is advanced beyond paper studies and isolated laboratory investigations, its extraordinary potentials may never be realized. In fact, it has long been recognized that ISRU is perhaps the only means of achieving significant long-term cost savings in space missions. Unfortunately, much of the work has been at levels that may be described as TRL1 through TRL2, in the usual NASA ITP terminology, so that serious consideration by mission planners could not be assured. At the UA/NASA SERC, we have been fortunate to have support for advancement of technologies through TRL5.

The principal components of this year's work have been the oxygen production plant and its miniaturization; the robotic processing of lunar soils; production of polymers, ceramics, and glasses; development of a valid quantitative Figure-of-Merit to evaluate the overall impact of these on space missions; and the associated controls, simulations, and computations.

The virtues of in-situ resource utilization (ISRU) in introducing significant cost savings in space missions have received extensive attention in recent years.⁽¹⁻¹⁰⁾ Following this general acknowledgment of the potential for cost effectiveness, several studies have examined a theoretical "mission architecture" that could incorporate the ISRU components.⁽¹¹⁻¹⁵⁾ An interesting, and important, development has been the serious attention paid by industry to these resource utilization missions.⁽¹⁶⁻¹⁹⁾ This interest by industry signifies the recognition of long-term benefits of a tangible nature.

The initial activities and a general summary of the Center's activities have been reported earlier.^(20,21) The present chapter is a logical next step in the sequence of technical reports from the Center.⁽²²⁻²⁴⁾

The overall "game plan" at the Center is shown in Table 1. At regularly scheduled weekly meetings, innovative ideas are discussed in an open forum consisting of scientists, engineers, undergraduate and graduate students, faculty, and administrators. This free exchange of ideas results in a list of possible candidates for further pursuit. The promising ones are subjected to several reviews: internal reviews by the three Directors, semi-annual reviews by the Center Advisory Committee, and annual reviews by the NASA Technical Representative Committee. In addition, our concepts and results are

always subjected to peer review in journals, symposia, and external meetings. Those concepts that survive these reviews are selected for small-scale feasibility demonstrations; this is the first place where hardware experiments are committed. After extensive tests involving several operation scenarios that go beyond the expected boundaries of operation in applications, the more promising ones are selected for table-top units that now produce reasonably realistic quantities of end products. Understandably, only two or three concepts reach this stage because of resource requirements at these larger-scale production stages. Those that continue to prove promising at this stage are selected for breadboard development and testing at the highest level of technology demonstration, or TRL 5 in NASA terminology.

Another important aspect of our activities is our willingness and ability to apply basic knowledge and expertise to important specific national needs. Two such examples are discussed here: one is our design and demonstration of a common lunar lander (Artemis) concept that involves robotic processing of unbeneficiated lunar soils for oxygen (and construction materials) production, and the other is a portable oxygen plant that uses carbon dioxide as its feedstock (with obvious applications to Mars). The latter has already been delivered to NASA Lewis Research Center for demonstration purposes.

The activities at the Center are all aimed at ISRU for introducing significant cost savings and mission simplicity; the specific projects are logically divided into four major categories, or disciplines: (1) lunar, (2) Martian, (3) support, and (4) common technologies. In the lunar category, we are pursuing soil reduction through hydrogen and carbothermal processes, innovative non-equilibrium plasma processing for compact energy efficient reactors, solar processing through direct photon absorption, and some other specific studies that involve soil processing into dishes. In the Martian category, we are processing carbon dioxide to produce oxygen, using the spent (hot) stream to produce hydrocarbons (the hydrogen comes from a water electrolysis unit), and have an overall system design using modern software. A recent study has been started to explore the permafrost and its safe bearing capacity (in support of platforms and structures).

In the support technologies category, we are exploring mechanical properties, general-purpose software development for mission optimization, in-situ mechanical property measurements, and quantitative visualization through CAD.

In the common technologies category, we are developing intelligent semi-autonomous controls with

smart sensors, self-contained modular designs, quantitative bill of materials, compatibility testing, and an overall cost-benefit analysis that includes an examination of historical mission data.

This chapter concludes with a brief description of two applications: the common lunar lander and the portable oxygen plant that uses carbon dioxide.

The Component Activities

Lunar Resources

Lunar resources include various soils and ores. Initial studies were confined to the (much-studied) ilmenite processes.²³ A major breakthrough in 1992 extended the work to any iron-bearing silicate. The vapor deposition of a monolayer of (imported) carbon enabled the reduction of iron-bearing silicates. One representative result is shown in *Figure 1*. This forms the basis for our Artemis design. In our quest for high-tech efficient reactions, we are exploring cold plasma reactions of lunar ores and direct photon enhancement of chemical reactions. The non-equilibrium plasma enables high electron temperatures to be achieved while maintaining very low translational, rotational, and vibrational (sensible) temperatures; this fact results in good thermal efficiency in reactor design. Besides, the photon-electron interactions have a greater cross section than photon-molecule cross sections; this enables the direct deposition of solar energy into the reaction stream. The results are shown in *Figure 2*. The cold plasma in operation is shown in *Figure 3*. The general nature of the experimental setup for the microbalance investigation of lunar soils is shown in *Figure 4*. Details on the plasma reactor are given in reference 25.

Some of the beams and struts made from (authentically) simulated lunar soils are shown in *Figure 5*. The mechanical properties and their modifications through the use of small (<2% by total mass) quantities of fibers (in this scheme, to be imported from Earth, but in a subsequent scheme to be manufactured on the Moon from glassy silicates) were reported earlier.²³ More recent results have included the production of silicon-based polymers that could be used as the substrates for amorphous photovoltaic cells.

Martian Resources

Our basic work continues to develop newer technologies for oxygen production from carbon dioxide. The 16-cell unit that utilizes yttria-stabilized zirconia is shown in *Figure 6*. The screening matrix and the mass and energy needs are shown in Tables 2 and 3, respectively. A major

breakthrough occurred in the alternative disc technology. Compared to the earlier tube geometry, the discs have a far greater effective area. The results are shown in *Figure 7*; a dramatic comparison is shown in *Figure 8*. The effective area in the tube is clearly revealed in the IR thermogram of the tube in *Figure 9*.

A highly sensitive area of importance is the seal between the ceramic (ZrO_2) and the metal (Inconel) that houses the overall system. Major advances were made in recent months using shape-memory alloys that improve the seal at higher temperatures. Results are shown in *Figure 10*. Several in-house technologies of solid electrolytes, catalysts, and electrodes were all proven to be superior to what is commercially available. Generous support from JPL, where three of our students were hosted this summer, is acknowledged. This process of Martian CO_2 reduction is also studied in reference 26. Our early work was reported in reference 27.

The spent stream is rich in carbon dioxide and carbon monoxide. If separated, the carbon monoxide can be a valuable fuel on Mars. The separation process has been refined in the last few months. The basic scientific principle involves pressure cycling or temperature cycling. The adsorption/desorption is on a copper-based substrate. The results are shown in *Figure 11*.

Another use of the spent stream could be for the manufacture of hydrocarbons, if hydrogen can be made available. We have a water electrolysis system (WES), loaned to us by United Technologies, Hamilton Standard of Windsor Locks, Connecticut. The WES is shown in *Figure 12*. The principle of the WES is applicable to Martian plants, which could use water from the soil, polar caps, or even from the atmosphere. The hydrogen, so produced, is used in a Sabatier reactor (*Figure 13*). The overall scheme is shown in *Figure 14*, and the principal results are shown in *Figure 15*. Martin-Marietta is expected to fund a small grant at SERC for the study of "higher" chemistry from the hydrocarbons that can be produced starting from methane and hydrogen; it should be acknowledged that the initial construction of the Sabatier reactor was through an earlier MM grant to SERC.

Support Technologies

These include the intelligent controls and smart sensors. The overall view is shown in *Figure 16*. The controls have proven their applicability in several hundred-hour runs that were conducted during severe thunderstorms in Tucson, which resulted in natural (mains) power outages. The full-system operation was reported in reference 23.

Common Technologies

These include ceramics from local soils, mechanical properties of beams and struts made from soils, and quantitative CAD and visualization. The principal results arising from the ceramics research using lunar soil are shown in *Figure 17*.

Specific Applications

The general knowledge base and hardware experience present at The University of Arizona's Space Engineering Research Center have been applied to several national needs, of which two are described here.

Artemis (Lunar Lander)

This project involves the demonstration of a completely self-contained lander that weighs under 65 kg. The basic process is a reduction of any iron-bearing silicate. The reactor, made of a light ceramic, is capable of carbothermal or hydrogen reduction. The overall plant is shown as a scale model in *Figure 18*. A half-scale robotic unit has been built and demonstrated, using solar thermal energy. The full-scale unit's mass and energy balance are shown in Table 4. The sequence of operations is shown in Table 5. The unit is currently undergoing thorough testing and will be developed through TRL 5 in the coming year (*Figure 19*).

Portable Oxygen Plant

A small-scale (1 lb/day class) oxygen plant was designed and constructed using indigenous electrodes, catalysts, and electrodes. The completed unit is shown in *Figures 20* and *21*. The performance characteristics are shown in *Figures 22* and *23*; the unit has been shipped to NASA Lewis Research Center and is expected to be used in demonstrations in conjunction with a rocket motor that will burn the CO and O₂ so produced.

Since this unit is meant for thorough characterization at Lewis Research Center, only the proof-of-working data were obtained at the temperature of 800°.

These medium-temperature data must be interpreted with caution. The high temperatures (1000°C) will yield much higher O₂ production rates.

Summary and Conclusions

At The University of Arizona's Space Engineering Research Center, various activities are carrying novel ISRU concepts through idea generation, scientific screening, feasibility demonstrations, and full-system hardware. Several plants have been built and operated under realistic conditions for extended durations. It is expected that these hardware realizations of scientifically sound ISRU concepts will inspire confidence in mission planners, who could gain substantial cost benefits and acceptability by the general (tax-paying) public, who would then recognize that space ventures need not be costly if we use the local resources "out there."

Acknowledgments

The author thanks Drs. Robert Hayduk and Murray Hirschbein (Code RS, NASA HQ) for their support and the entire team at SERC for the data.

References

- ¹*Pioneering the Space Frontier*. Report by the (Presidential) National Commission on Space, New York: Bantam Books, 1986.
- ²Ash, R. L., Dowler, W. L., and Varsi, G. "Feasibility of Rocket Propellant Production on Mars." *Acta Astronautica* (5) 1978: 705-34.
- ³French, J. R., Norton, H. N., and Klein, G. A. "Mars Sample Return Options." *Aerospace America* (23) 1985: 50-53.
- ⁴Ash, R. L., Richter, R., Dowler, W. L., Hanson, J. A., and Uphoff, C.W. "Autonomous Oxygen Production for a Mars Return Vehicle." IAF-82-210, 1982.
- ⁵Carroll, W. F. (Ed.), *Research on the Use of Space Resources*. JPL Publication 83-86: 1983.
- ⁶Ash, R. L. and Cuda, V., Jr. "Technology Status Report for In Situ Propellant Production." Report to Jet Propulsion Lab. (1984).
- ⁷Frisbee, R. H. and Jones, R. M., "An Analysis of Alternate Hydrogen Sources for Lunar Materials to Earth Orbit." AIAA Paper 83-1344 (1983).
- ⁸Ramohalli, K. N., Dowler, W., French, J., and Ash, R. "Novel Extraterrestrial Processing for Space Propulsion." *Acta Astronautica* (15) 1987: 259-73.
- ⁹Ramohalli, K. N., Dowler, W., French, J. and Ash, R. "Some Aspects of Space Propulsion With Extraterrestrial Processing." *Journal of Spacecraft and Rockets* (24) 1987: 236-44.
- ¹⁰Ramohalli, K. N., Lawton, E., and Ash, R. "Recent Concepts in Missions to Mars -- Extraterrestrial Processing." *Journal of Propulsion and Power* (5) 1989: 181-87.
- ¹¹Stancati, M. L., Jacobs, M. K., Cole, K. J., and Collins, J. T. "In Situ Propellant Production:

Alternatives for Mars Exploration." Rept. SAIC-91/1052. Schaumburg, IL: Science Applications International Corp., 1991.

¹²Friedlander, A. and Cole, K. "Power Requirements for Lunar and Mars Exploration Scenarios." Rept. SAIC-89/1000. Schaumburg, IL: Science Applications International Corp., 1989.

¹³Sullivan T. A. and McKay, D. S. "Using Space Resources." Houston, TX: NASA Johnson Space Center, 1991.

¹⁴Duke, M. B. and Keaton, P. W. (Editors). "Manned Mars Missions," A Working Group Report. NASA M001. Los Alamos National Laboratories, 1986.

¹⁵Bon, Ranko (Instructor). "Settling the Asteroids." MIT4.58, Space Habitat Design Workshop. Massachusetts Institute of Technology, Cambridge, MA, 1989.

¹⁶Fluor Daniel. "Effective Lunar Facility Construction Concepts." Presentation to NASA Office of Exploration. Fluor Daniel, Irvine, CA., 1988.

¹⁷Altenberg, B. "Processing Lunar In-Situ Resources." Final Rept. Job No. 90634-002. Bechtel Group, Inc. San Francisco, CA, 1990.

¹⁸Alred, J. W., Kline, J. M., and Snauffer, M. J. "Indigenous Space Materials Utilization Experiment Design for the Common Lunar Lander." IAA-92-0160, 43rd Congress of the International Astronautical Federation, Washington, DC, 1992.

¹⁹Rosenberg, S. D. and Redd, L. R. "Lunar Propellant Manufacture and Its Economic Benefits for Space Transportation." IAA-91-637, 42nd Congress of the International Astronautical Federation, Montreal, Canada, 1991.

²⁰Office of the Vice President for Research. "Refineries in Space." *Report on Research* (4) No. 2: 19. Tucson: The University of Arizona, 1987.

²¹Ramohalli, K. "Mining the Air; Resources of Other Worlds May Reduce Mission Costs." *The Planetary Report* (11) 1991: 8-9, 11.

²²Lewis, J. S., Ramohalli, K., and Triffet, T. "Extraterrestrial Resource Utilization for Economy in Space Missions." Paper IAA-90-604, 41st Congress of the International Astronautical Federation, Dresden, West Germany, 1990.

²³Ramohalli, K. N. R. "Technologies of ISRU/ISMU." IAA-91-659, 42nd Congress of the International Astronautical Federation, Montreal, Canada, 1991 (to appear in *Acta Astronautica*).

²⁴Ramohalli, K. and Sridhar, K. R. "Extraterrestrial Materials Processing and Related Transport Phenomena." *J. Propulsion and Power* (8) 1992: 687-96.

²⁵Bullard, D. E., Lynch, D. C., and Davenport, W. G. "Non-Equilibrium Plasma Processing of Ores." *Thermal Plasma Applications in Materials and Metallurgical Processing* (N. El-Kaddah, ed.) Warrendale, PA: The Minerals, Metals & Materials Society, 1992: 175-91.

²⁶Bowles, J. V. and Tauber, M. E. "Propellant Production from the Martian Atmosphere." *Journal of Propulsion and Power* (8) 1992: 907-09.

²⁷Colvin, J., Schallhorn, and Ramohalli, K. "Propellant Production on Mars: Single Cell Oxygen Production Test Bed." AIAA 91-2444. AIAA/ASME/SAE/ASEE 27th Joint Propulsion Conference, Sacramento, CA, 1991. Accepted for publication in *AIAA J. Propulsion and Power*.

FIGURE 1

PROVEN OXYGEN PRODUCTION
solid carbon mixed with (simulated) lunar soil

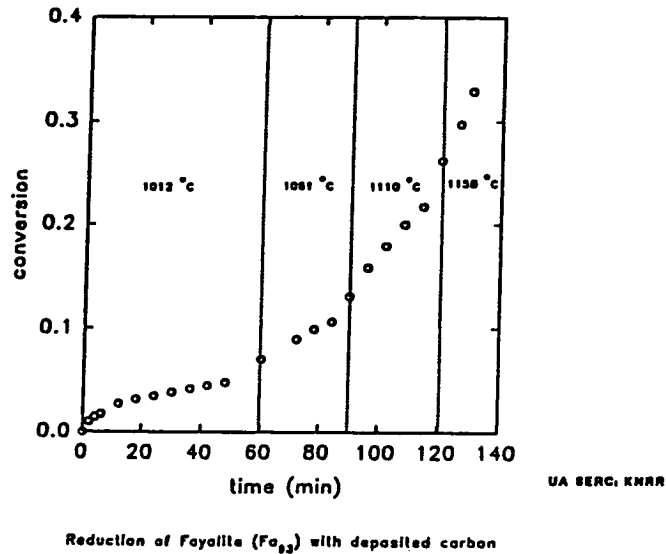


FIGURE 2

Graduate Students: Dan Bullard & Gary Thomas

Intent

Recovery Of Oxygen From Lunar Resources Using A Hydrogen Plasma

Major Achievements

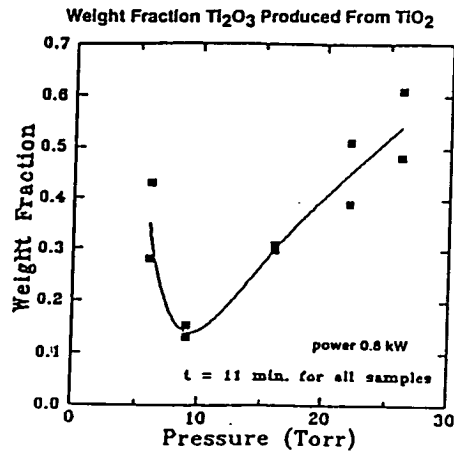
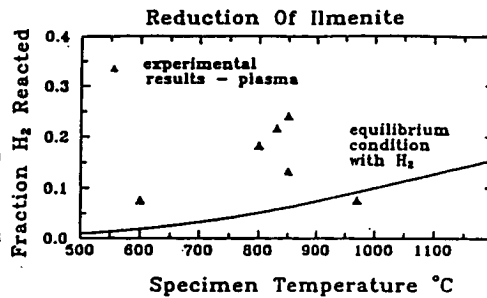
- Improved Efficiency In Hydrogen Utilization Over Conventional Heating
- Recovery of 1.5 atoms Of Oxygen Per Molecule Of $FeTiO_3$ Possible
- Evaluation Of Plasma Variables On extent Of Reaction

Comments

- Energy Efficiency For Production Of Plasma Can Approach 85 To 90%
- Particles 10 μm In Diameter & Smaller Can Be Reacted - Also Possibly Larger Particles
- Plasma - Solid Reaction Complete Within 2 Minutes At 700 °C And Below

Future Work / Work In Progress

- Design Of Fluidized Bed Plasma Reactor (50 To 100 g) To Improve Plasma - Solid Contact And Achieve Greater Efficiency In Hydrogen Utilization
- Evaluation Of Fundamental Kinetic Parameters
- Scale up



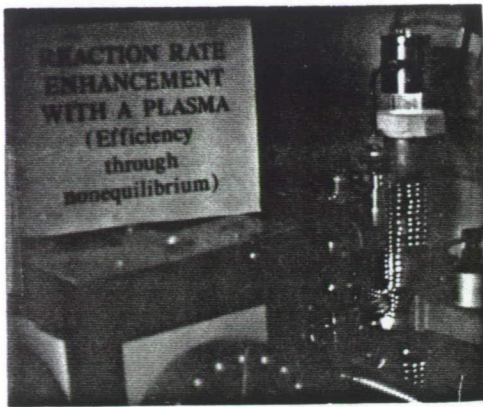


FIGURE 3. COLD PLASMA OPERATION.

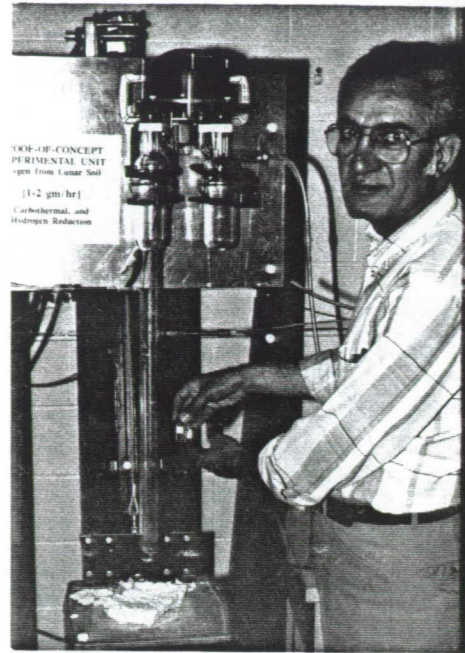


FIGURE 4. SETUP USED FOR MICROBALANCE INVESTIGATION.

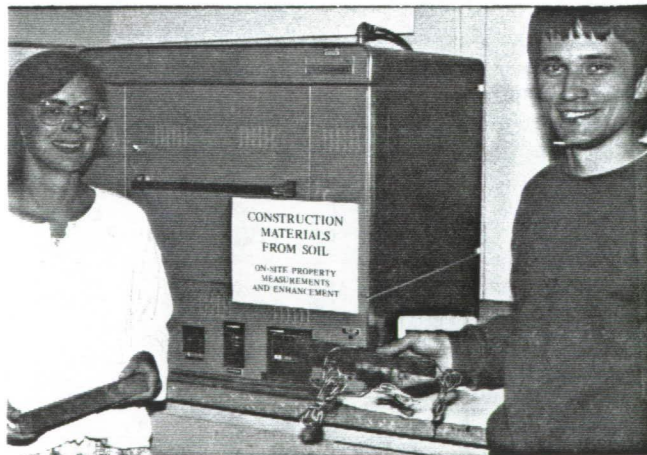


FIGURE 5. BEAMS AND STRUTS MADE FROM SIMULATED LUNAR SOILS.



FIGURE 6. SIXTEEN-CELL UNIT USED TO PRODUCE OXYGEN FROM YTTRIA-STABILIZED ZIRCONIA.

IN-HOUSE DISK RESULTS

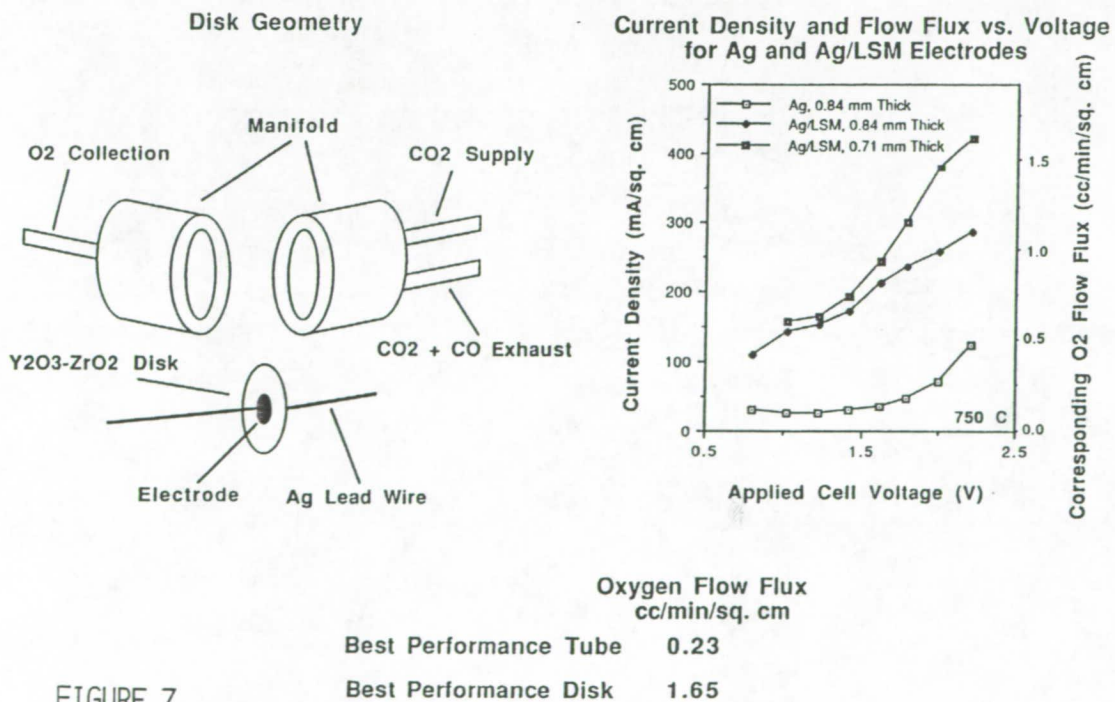


FIGURE 7

FIGURE 8

Measured Oxygen Flow vs Time

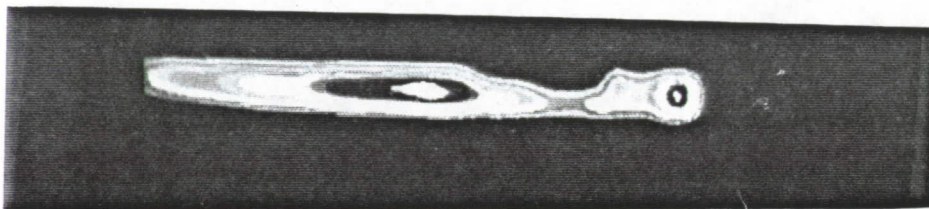
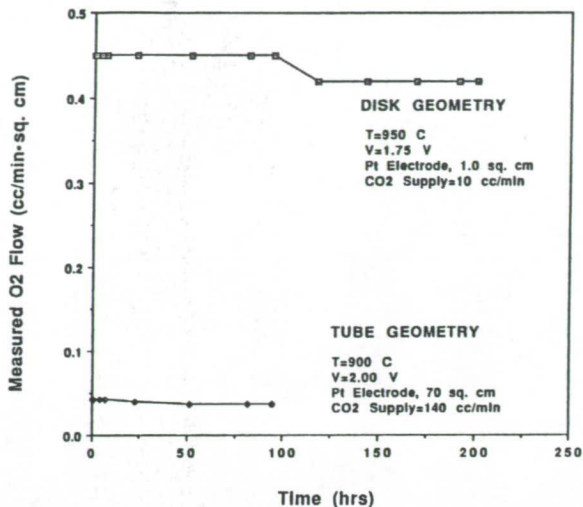
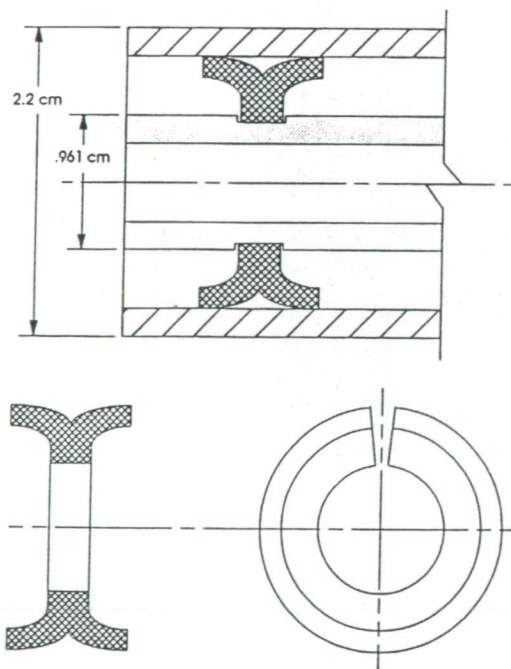


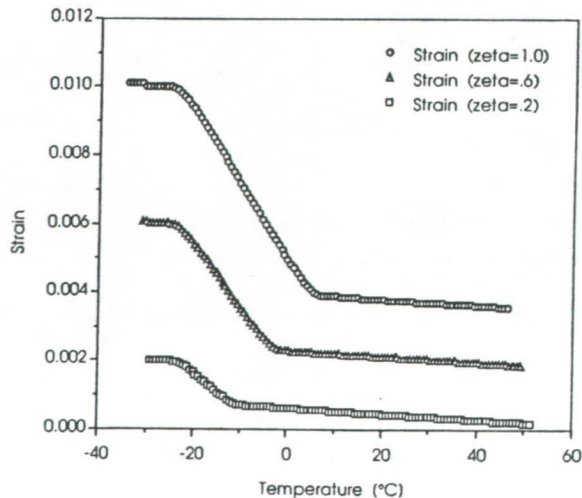
FIGURE 9. INFRARED THERMOGRAM SHOWING EFFECTIVE AREA OF THE TUBE ELECTROLYTE (ZrO_2).

FIGURE 10

High Temperature Seal using a Shape Memory Alloy



Strain Response of Controlled Recovery Heating



IA-13

The shape memory alloy that will be used is Ni-Ti.

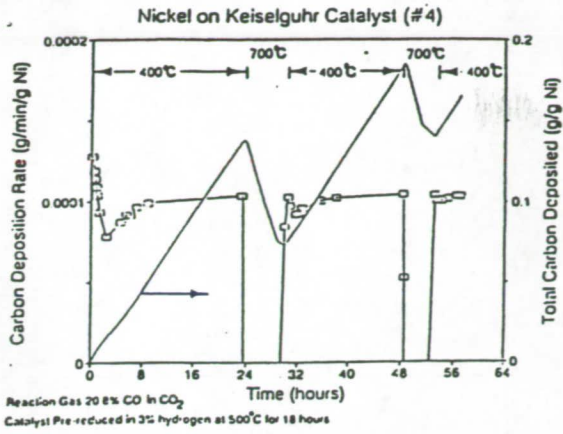


FIGURE 13. SABATIER REACTOR SETUP.

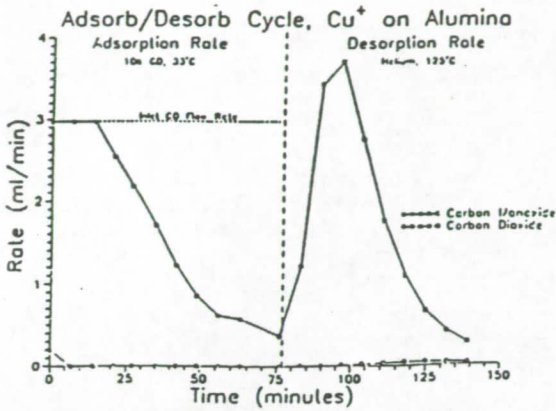


Fig. 11. Carbon monoxide removal from electrochemical cell discharge gas.

FIGURE 14
Sabatier "Test Tube" Reactor

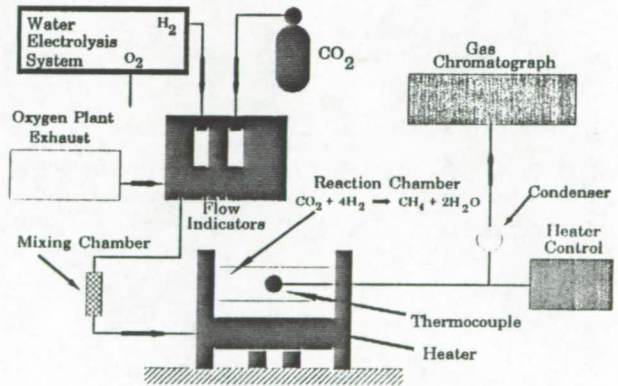


FIGURE 15

METHANE PRODUCED
O/F = 0.25, P = 1 atm

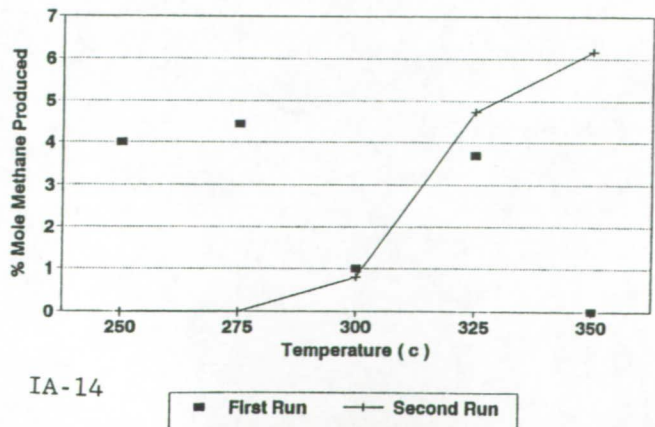
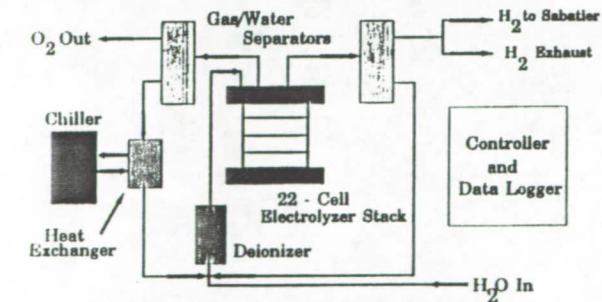


FIGURE 12
WATER ELECTROLYSIS SYSTEM



Experimental Mass and Flow Rates as a function of Electrolysis Current

Stack Amps	Oxygen Out		Hydrogen Out	
	kg/day	cc/min	kg/day	cc/min
8	0.72	375	0.09	750
15	1.85	970	0.24	1940
30	4.34	2275	0.55	4550



FIGURE 16. SUPPORT TECHNOLOGY SETUP, WITH SMART SENSORS AND DEDICATED ADAPTIVE CONTROLS.

Processing of Ceramics from Lunar Resources

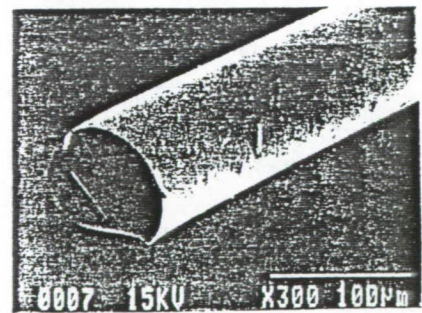
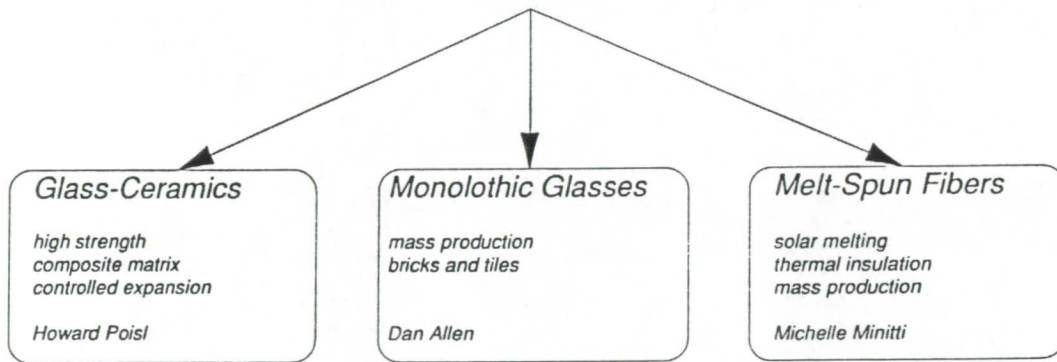


FIGURE 17

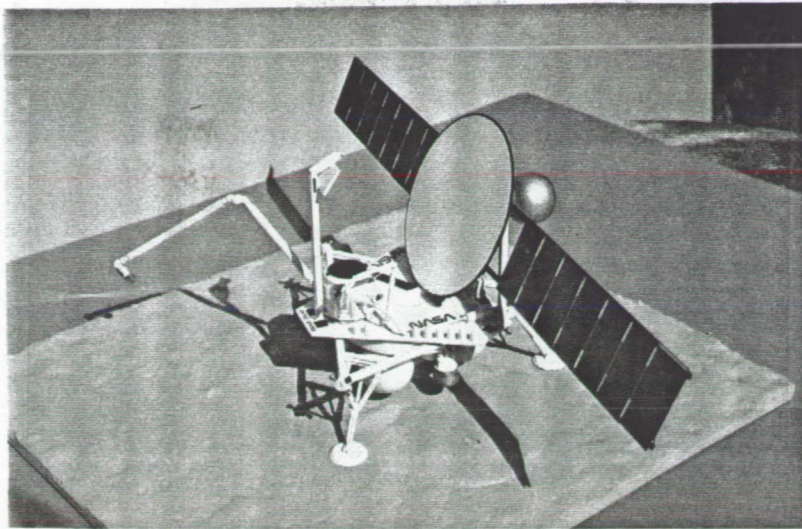


FIGURE 18

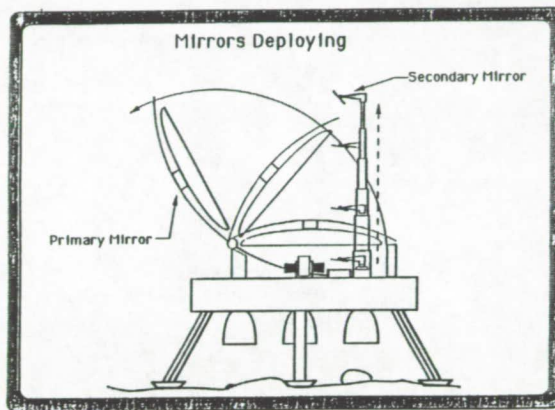
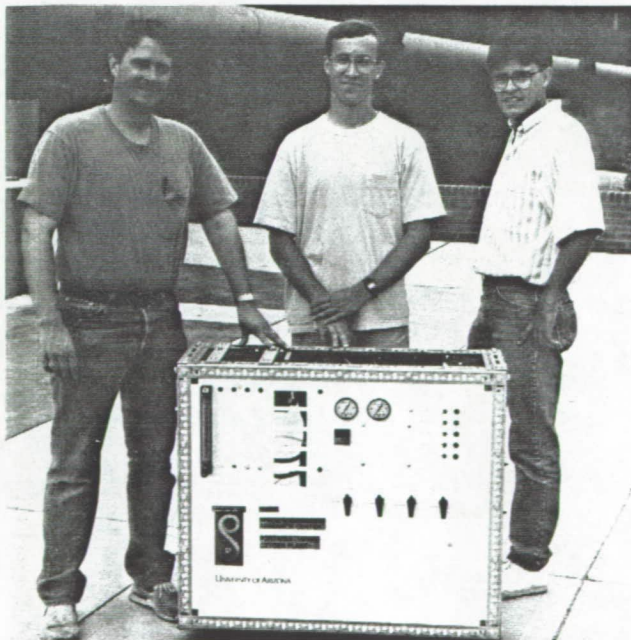


FIGURE 19



ORIGINAL PAGE
BLACK AND WHITE PHOTOGRAPH

FIGURE 20. PORTABLE OXYGEN PLANT ($\text{CO}_2 \rightarrow \text{O}_2$).

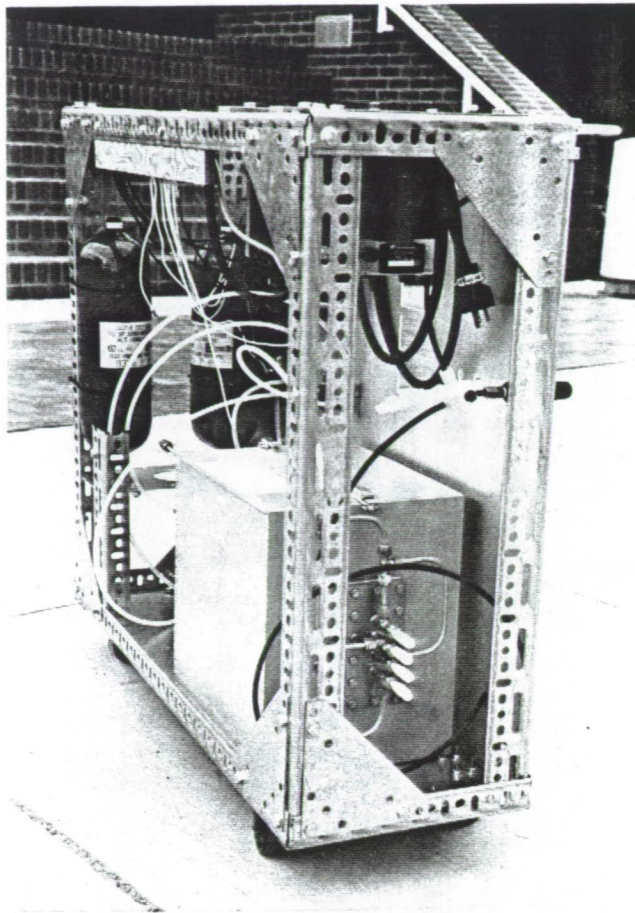


Fig. 21. Portable oxygen plant (cover removed).

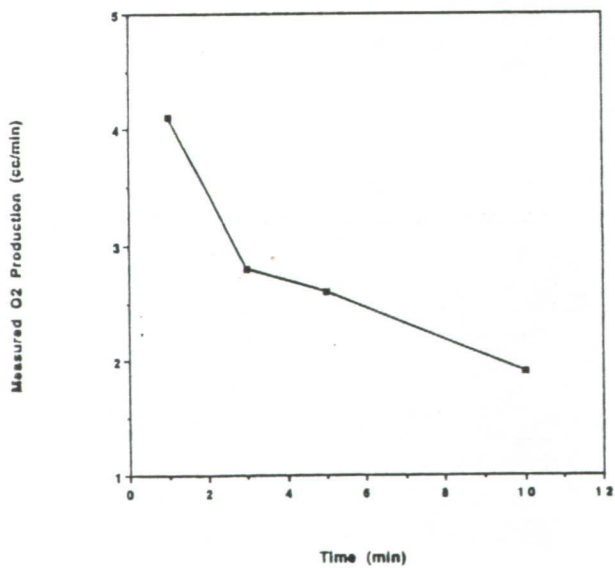


Fig. 22. Oxygen production versus time ($T = 800^{\circ}\text{C}$, $V = 2.00\text{ V}$, LSM/Pt electrode).

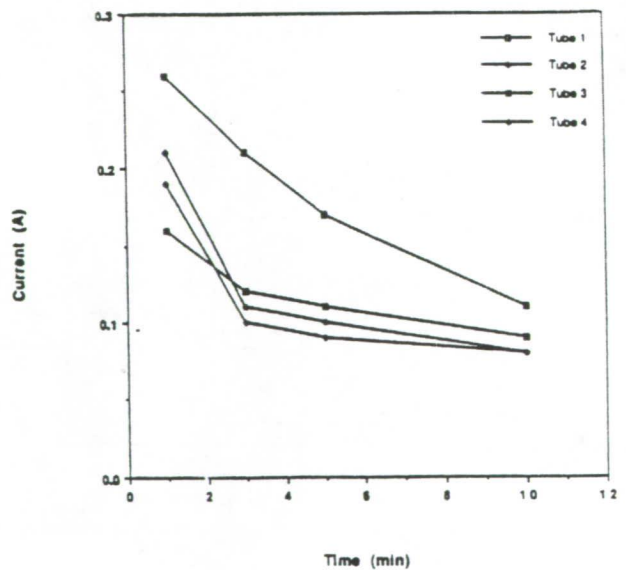


Fig. 23. Current versus time for Lewis unit tubes ($T = 800^{\circ}\text{C}$, $V = 2.00\text{ V}$, LSM/Pt electrode).

Table 1. The basic game plan for in-situ resource utilization.

NOVEL CONCEPTS IN HIGH TECHNOLOGY: "Anything Goes"
FEASIBILITY STUDIES: "Back-of-the-Envelope Calculations and "Test-Tube" Evaluations
SMALL-SCALE PROOF-OF-CONCEPT: Mathematical Models, Computer Simulations, First Hardware
BREADBOARD ENGINEERING DEMONSTRATIONS: Realistic Full-Size System at Realistic Production Rates
HIGHEST TECHNOLOGY READINESS LEVEL: Plans and Software Delivered to NASA and Industry

Table 2. Screening matrix for yttria-stabilized zirconia.

Tube	Electrode	Temperature (°C)	Applied Voltage	Oxygen Yield (cc/min)
C-4	Proprietary	825	2.40	11.75
C-6	Proprietary	825	2.98	12.90
C-7	Proprietary	825	2.37	7.0
SERC1	Ag/LSM	800	2.62	5.0
SERC2	Pt/LSM	1000	2.00	3.8
SERC3	Pd/LSM	850	2.00	2.9
SPECIAL	Undisclosed	900	2.00	22.4

Table 3. Mass and energy needs for oxygen production utilizing yttria-stabilized zirconia.^a

	Single-Cell Unit	4-Cell Unit 0.1 kg/day	16-Cell Unit 0.4 kg/day	Full-Scale Prototype 1-2 kg/day
Mass (kg)	4.08	13.15	52.16	113.0
Dimensions ^b (cm)	20×20×28	30×30×46	120×120×46	30×46×36
Power Needs: Thermal (kw)	0.37	0.50	2.00	4.80
Electrical (w)	3.0	12.5	50.0	150.0

^aImmediate Applications: portable 0.1 kg/day demo unit for LeRC; prove ability to engineer; package and operate at sites other than SERC.

^bZrO₂ subsystem only.

Table 4. Summary of mass and power needed for integrated oxygen production.

	Mass (kg)	Power (w)
Communications	3.5	10/120
Computer	4.25	16
Sensors/Acutators		
Servo motors (8)	6.4	480.0
Flow meters (2)	0.8	7.5
Pressure sensors (2)	0.1	0.2
Force/torque sensors (2)	1.0	*
Proximity sensors; strain gauge	*	*
Flow control valves (2)	1.2	2.4
Thermocouples (2)	*	*
CCD camera (1)	0.2	3.0
Mass spectrometer (1)	0.5	2.0
	10.2	495.1

*Negligible.

Table 5. Integrated oxygen production:
task decomposition.

Soil Sample Acquisition

- Move arm and gather soil
- Deposit in crucible through sieve

Reactor Operation

- Mix solid carbon powder with soil
- Insert crucible at the focus
- Control heating (mirror adjustment)
- Measure/identify gases
- Remove and store residue (tiles from slag)

Data Management

- Obtain measurements and store data

Telemetry and Upload

- Adjust antenna/transmit data
- Upload code and data

497584
N 9 3 5 2 6 6 7 6
158349
P-43

**Reduction of Iron-Bearing Lunar Minerals
for the Production of Oxygen**

Charles Massieon¹, Andrew Cutler² and Farhang Shadman³
Department of Chemical Engineering
University of Arizona

Abstract

The kinetics and mechanism of the reduction of simulants of the iron-bearing lunar minerals olivine ((Fe,Mg)₂SiO₄), pyroxene ((Fe,Mg,Ca)SiO₃), and ilmenite (FeTiO₃) are investigated, extending previous work with ilmenite.

Fayalite is reduced by H₂ at 1070 K to 1480 K. A layer of mixed silica glass and iron forms around an unreacted core. Reaction kinetics are influenced by permeation of hydrogen through this layer and a reaction step involving dissociated hydrogen. Reaction mechanisms are independent of Mg content. Augite, hypersthene and hedenbergite are reduced in H₂ at the same temperatures. The products are iron metal and lower iron silicates mixed throughout the mineral. Activation energy rises with calcium content. Ilmenite and fayalite are reduced with carbon deposited on partially reduced minerals *via* the CO disproportionation reaction. Reduction with carbon is rapid, showing the carbothermal reduction of lunar minerals is possible.

¹Graduate Student, Department of Chemical Engineering

²Research Assistant Professor, SERC

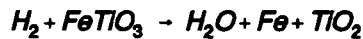
³Professor, Department of Chemical Engineering

Introduction

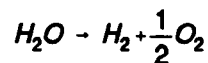
Although there is no atmosphere on the Moon, oxygen is available there, since the minerals that make up the Moon's surface are almost entirely oxides (Heiken *et al.*). One of the first activities of a manned lunar base will probably be the production of oxygen for export to Earth orbit, where it will be used as rocket propellant.

The oxygen will be produced by the chemical reduction of oxide minerals. Because the oxygen is tightly bound in the minerals, a fairly strong reducing agent must be used for the reaction to take place, and the selective reduction of the most easily reduced metal ions is likely to be the most economical process. Since strong reducing agents are very rare on the Moon, they will have to be imported from the Earth, and hence very expensive. Thus, any oxygen production process must recycle all but a very small fraction of the reducing agent.

The reducing agents that have received the most attention to date are hydrogen and carbon monoxide, and the mineral which has been most studied is ilmenite (FeTiO_3). Typical reactions using these for oxygen production are the reduction of FeTiO_3 with hydrogen



and the electrolysis of water



The hydrogen produced by electrolysis is then recycled to reduce more ilmenite. If carbon monoxide is used instead of hydrogen, carbon dioxide is produced in the reduction step, and it is electrolyzed to form oxygen and carbon monoxide.

Some studies have been done on the design and energy demands of such a project (Cutler, 1986; Cutler and Waldron, 1992; Waldron and Cutler, 1992), but the kinetics of the reduction of lunar minerals must be determined in order to design reactors and make reasonable estimates of design parameters such as energy demands. Because ferrous ions are the most easily reducible of the common metal ions on the Moon, the reduction of iron bearing minerals is of particular interest because it is expected to have the lowest energy cost for the oxygen produced.

Objectives

There are several reasons to consider minerals other than ilmenite and reagents other than H_2 and CO for the production of oxygen on the Moon. One problem with ilmenite is its abundance and distribution on the Moon. Ilmenite is not found in usable concentrations throughout the lunar surface. High ilmenite samples brought back from the Moon have only 10% ilmenite by volume, and many are much lower in the mineral (Heiken *et al.*, 1991). Since using lunar soil or rock as feedstock will require heating large amounts of inert solids, beneficiation will probably be necessary and recovering small amounts of ilmenite from the feed will be an expensive process. Further, an early lunar base will not be chosen solely for production of oxygen and may be in an ilmenite poor area, so the ability to handle other minerals may be necessary for the successful operation of an oxygen plant. The iron bearing silicates olivine and pyroxene are more widespread and make up a larger fraction of the rock and soil than ilmenite.

Another reason to study silicates is the mass fraction of oxygen in the mineral available for extraction. The oxygen available in $FeTiO_3$ makes up only 10% of its mass. Available oxygen is 12% of the mass of the pyroxene ferrosilite ($FeSiO_3$), and 16% of the mass of the olivine fayalite (Fe_2SiO_4).

Finally, the equilibrium conversion of the reducing gas is poor. At 1200 K, the equilibrium conversion of H_2 to H_2O by ilmenite is 7.6%, and the equilibrium conversion of CO to CO_2 is 5.9% (Shomate *et al.*, 1946). The equilibrium conversion of H_2 by Fe_2SiO_4 is somewhat better (Berliner and Shapovalona, 1966), although for $FeSiO_3$ it is worse (Chase *et al.*, 1985)(Figure 1.1). Because thermodynamic equilibrium is the upper limit on reactor performance, a large fraction of the reducing gas will not be converted in the reduction reactor, so gas reduction processes will be inefficient. Large gas flow rates will be necessary to carry the oxygen from the reactor, which causes problems in gas handling and higher energy demand to heat and cool the gas streams. Fe_2SiO_4 would give some improvement over $FeTiO_3$. Cutler and Waldron (1992) have proposed a countercurrent reactor system, in which pyroxenes are reduced by fresh H_2 coming from the electrolyser, ilmenite is reduced next, and olivines last in order to utilize all three minerals and have conversion as high as possible in the gas stream leaving the reduction reactor. Equilibrium conversion of D_2 is approximately 20% greater than that of H_2 (Cutler, 1991, personal communication), so that its use may improve reactor performance. Reduction with carbon rather than a gas allows complete utilization of the reducing agent and thus lower reactant flow rates. Carbon can be deposited on the iron bearing minerals in a separate deposition reactor. Although

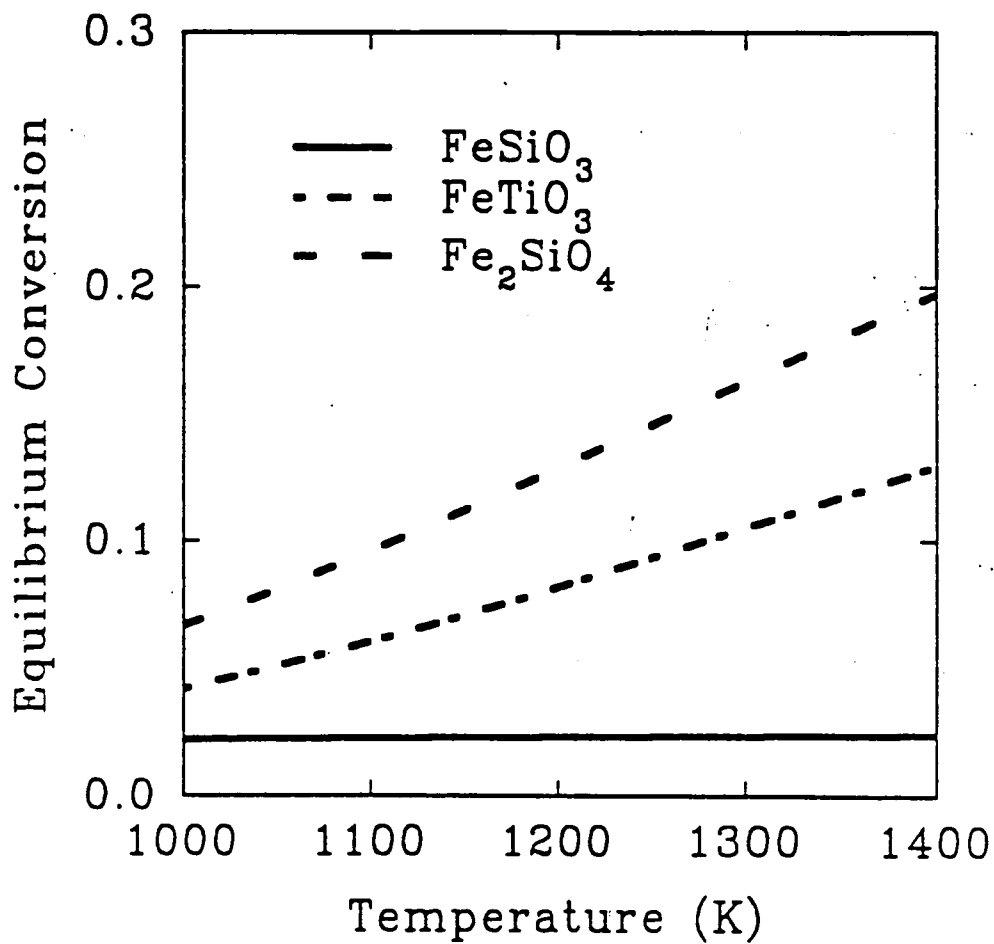


Figure 1.1 Equilibrium Conversion of H₂ by Ilmenite, Fayalite, and Ferrosilite.

this makes the process more complicated, the savings in gas flows may make it worthwhile.

The purpose of this study is to extend the work done on ilmenite to the iron bearing silicates olivine and pyroxene, and to make preliminary investigations on the feasibility of a carbon deposition and reduction process for ilmenite, olivine, and pyroxene. Kinetic parameters such as reaction order, apparent activation energy for these reactions, and the effect of impurities such as magnesium and calcium in the silicates are presented. These parameters should allow future workers in the field of space resources to design and compare oxygen production plants for the Moon.

Ilmenite

The reduction of ilmenite (FeTiO_3) with hydrogen and/or carbon monoxide has received the most study to date (Briggs and Sacco, 1990; Zhao, 1991; Zhao and Shadman, 1990 and 1991). The reduction reaction of ilmenite with the reducing agent R can be written as



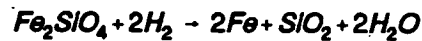
During reduction, a product layer of polycrystalline rutile (TiO_2) and iron metal forms. The iron is solid but mobile at reaction temperatures (ca. 1200 K) and migrates to the outside of the reduced grains, leaving the product of iron and rutile separated. Zhao found that the migration of iron plays an important role in the reduction of ilmenite. During the initial period of reduction, the iron has not yet formed nuclei on the outside of the grains, and it accumulates in the pores between rutile crystals, obstructing the diffusion of gases and slowing the reaction. The reaction is first order in both hydrogen and carbon monoxide, and the apparent activation energy is moderate (93 kJ/mol and 75 kJ/mol, respectively).

Olivine

Olivine is a fairly common mineral in the basalts which form the lunar maria, constituting up to 17% of these rocks (Heiken *et al.*). Olivine has the general formula $\text{M}^{+2}_2\text{SiO}_4$, where M^{+2} is any divalent ion close to the size of Fe^{+2} . It forms orthorhombic crystals. The metal ions in naturally occurring olivines are primarily ferrous and magnesium, although manganous ions can be an important impurity. The crystal structure of olivine strongly rejects trivalent ions such as Al^{+3} or Fe^{+3} , so terrestrial olivines make good lunar simulants, unlike terrestrial ilmenite, which contains significant amounts of ferric ion. This work studied the reduction of olivines in the Fe_2SiO_4 - Mg_2SiO_4 (fayalite-forsterite) series. A mineral in this series can be regarded as a nearly ideal solid solution of Mg_2SiO_4 and Fe_2SiO_4 (Deer *et al.*). Olivine which is more than 90 mol% Fe_2SiO_4 is called fayalite,

and olivine more than 90 mol% Mg_2SiO_4 is called forsterite. The solution $xFe_2SiO_4 \cdot (1-x)Mg_2SiO_4$ is referred to as Fa_{100x} (or $Fo_{100(1-x)}$ if x is close to zero). The composition of most lunar olivine is about Fa_{20} , but some is close to the end member, Fa_{100} . Since lunar olivines contain some Mg^{+2} , the effect of magnesium on reduction kinetics will be very important to lunar oxygen production.

Gaballah *et al.* (1975) studied the kinetics of the reaction



They found the rate is 1/2 order in H_2 between 1000 K and 1300 K, for p_{H_2} between 0.4 atm and 1.0 atm. They found the apparent activation energy to have different values in three temperature ranges: 230 kJ/mol from 1073 K to 1143 K, 263 kJ/mol from 1143 K to 1183 K, and 276 kJ/mol from 1183 K to 1303 K. They attributed these different regions to the phase transitions of quartz to tridymite at 1140 K, and α -Fe to γ -Fe at 1183 K. However, they did not report finding any tridymite in their products, only vitreous silica, quartz and cristobalite. Gaballah *et al.* did not report the amount of crystalline silica found in the products or show powder pattern X-ray diffraction (XRD) plots, and other workers found only traces of quartz or cristobalite (Minowa *et al.* 1968, Watanabe *et al.* 1968, Yanagihara and Kobayashi, 1969). From the activation energy graph published by Gaballah *et al.*, only random scatter about a line corresponding to $E = 263$ kJ/mol can be seen, rather than three different energies. Thus, there is little evidence in their paper to support the claim that the phase transitions of iron and silica are important in the reduction of fayalite. They also found that CO did not react with fayalite to any appreciable extent, which they attributed to the formation of Fe_3C , which increased the volume of solid products and sealed the reaction front from further reaction with CO.

Minowa *et al.* (1968) reduced Fe_2SiO_4 in 1 atm of H_2 . Using x-ray diffraction, they found that Fe_2SiO_4 first formed Fe and $Fe_{2-x}SiO_{4-y}$ when reduced, and upon further reduction formed iron metal and amorphous silica. During the initial part of the reduction, the rate followed McKewan's equation, which is the solution of the differential equation

$$\frac{dX}{dt} = k(1-X)^{2/3}$$

with the initial conditions

$$X = 0 \text{ at } t = 0$$

This equation models a reaction which is controlled by the reactant surface area, which is decreasing as the reaction consumes the solid. The formation of a nonporous layer of products slowed the reduction in the latter part of the reduction, and the data no longer fit McKewan's equation. Minowa *et al.* determined the activation energy for fayalite reduction to be 188 kJ/mol, which was also the activation energy they found for the synthesis of fayalite from quartz and wüstite (FeO). Watanabe *et al.* (1968) reduced fayalite containing some Mg in constant heating rate experiments. They did not extract any kinetic parameters from their data, but observed that Mg greatly slowed the reaction.

The morphology of the solid products has a strong effect on the rate of the reaction. During the reduction of fayalite, the volume of the solids decreases by about 10%. Thus, the products should form a porous polycrystalline layer providing the silica is quartz, tridymite, or cristobalite, but vitreous silica may form a nonporous layer around the fayalite. If the products are porous, the reaction would follow a standard shrinking core model. A nonporous layer may slow the reaction by causing a considerable resistance to mass transfer to and from the reaction front. Since diffusion through a solid is an activated process, the formation of a nonporous layer would not lead to kinetics well represented by a standard shrinking core model. Gaballah *et al.* found quartz and vitreous silica in unspecified amounts in their products at all temperatures, and cristobalite above 1140 K. Their conclusions depend strongly on the formation crystalline silica. Yanagihara and Kobayashi (1968) found only vitreous silica, while Minowa *et al.* (1968) reported that the silica was primarily vitreous with traces of quartz.

Pyroxene

Pyroxene is an extremely abundant and widespread mineral on the moon. Nearly all lunar rocks contain approximately 40% pyroxene by volume (Heiken *et al.*). The chemistry and mineralogy of pyroxene is more complicated than olivine. The general chemical formula of pyroxene is $M^{+2}SiO_3$, where M^{+2} is primarily calcium, magnesium, or ferrous ions. The less rigid crystal structure of pyroxene compared to olivine is reflected in its ability to accommodate up to 1/2 of its metal ions as the relatively large Ca, and also in the ability to substitute trivalent ions for both the divalent metals and the silicon. Pyroxene can crystallize with 2 different crystal structures: orthorhombic for low calcium minerals, and monoclinic for high calcium minerals. The nomenclature of pyroxene is shown in Figure 1.2. In this work, we studied the reduction of three terrestrial pyroxenes with both crystal structures: augite and hedenbergite (both monoclinic) and hypersthene (orthorhombic).

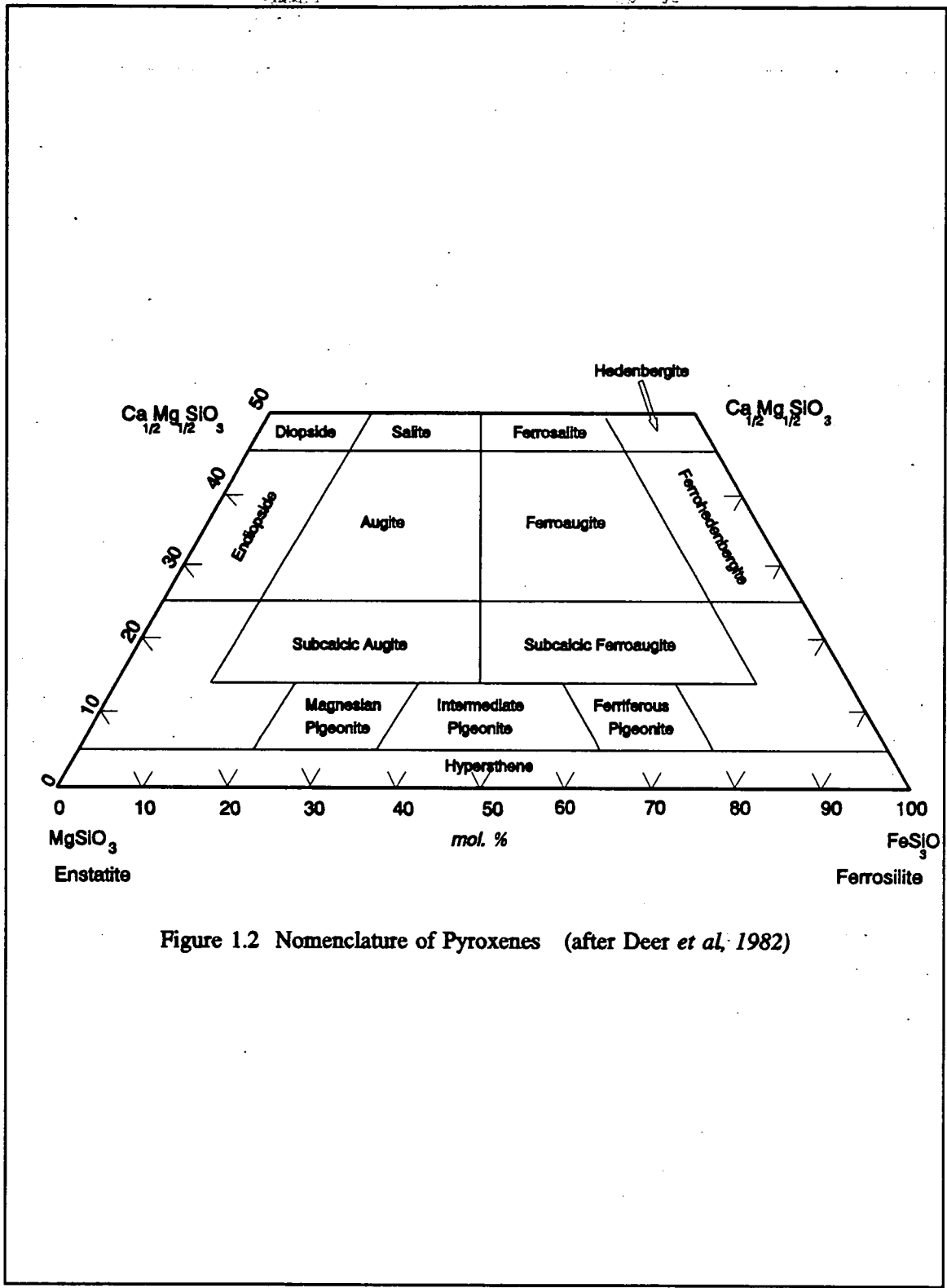


Figure 1.2 Nomenclature of Pyroxenes (after Deer *et al.*, 1982)

The reduction of pyroxene has generated less interest than the reduction of olivine or ilmenite. An extensive literature search, including Chemical Abstracts, Engineering Index, and Metallurgical Abstracts, uncovered no literature on the subject, and general texts on pyroxene such as Deer *et al.* do not mention it.

Carbothermal Reduction

Schematics of a carbothermal and CO reduction process for iron bearing minerals are shown in Figure 1.3. For comparison, flows and stream compositions assuming ilmenite feed and equilibrium in the reactors are shown. The gas leaving the carbothermal reduction reactor is assumed to be in equilibrium with carbon rather than ilmenite, since it is in closer contact with carbon just before it leaves the reactor. Although the reactors will not reach 100% efficiency as shown, the reduction of gas flow rates by an order of magnitude and the much higher quality of the gas going to the electrolyser indicate that carbothermal reduction of iron bearing minerals is an appealing alternative to reduction with CO or H₂. It is also possible that carbon may effectively reduce olivine and pyroxene, giving carbothermal processes more flexibility than CO processes.

Thermodynamic equilibrium of the reagents imposes an upper bound on the conversion of a reactor. Good reactor design can approach but never surpass this limit. The low equilibrium conversion of both H₂ and CO by ilmenite (Shomate *et al.*, 1946) causes some severe problems in the reduction process. Although the equilibrium conversion of H₂ by fayalite improves on ilmenite (Figure 1.1), it is still fairly low. As mentioned in the section on fayalite, CO does not react with fayalite to any appreciable extent (Gaballah *et al.*, 1971). Since carbon does not have the equilibrium limitations of the reducing gases, its use makes possible complete utilization of the reducing agent. However, it does introduce some problems of its own. Reduction and electrolysis products are CO and CO₂, and so carbon must be produced from these gases. In order to avoid difficult solid handling and mixing problems, it should be deposited directly on the feed to the reduction reactor. Also, since carbon is scarce on the Moon (Heiken *et al.*, 1991), the loss of any carbon in the spent feed must be avoided. If the gas in contact with Fe product is too high in CO, cementite (Fe₃C) may be produced. If the solids in the reduction reactor are mixed to any extent, some carbon will leave with the spent feed. Removing reducing agents from the solids will require another process step after reduction, and this step will be more difficult with solid carbon than either H₂ or CO.

The reaction this process uses to deposit carbon is the carbon monoxide disproportionation reaction,

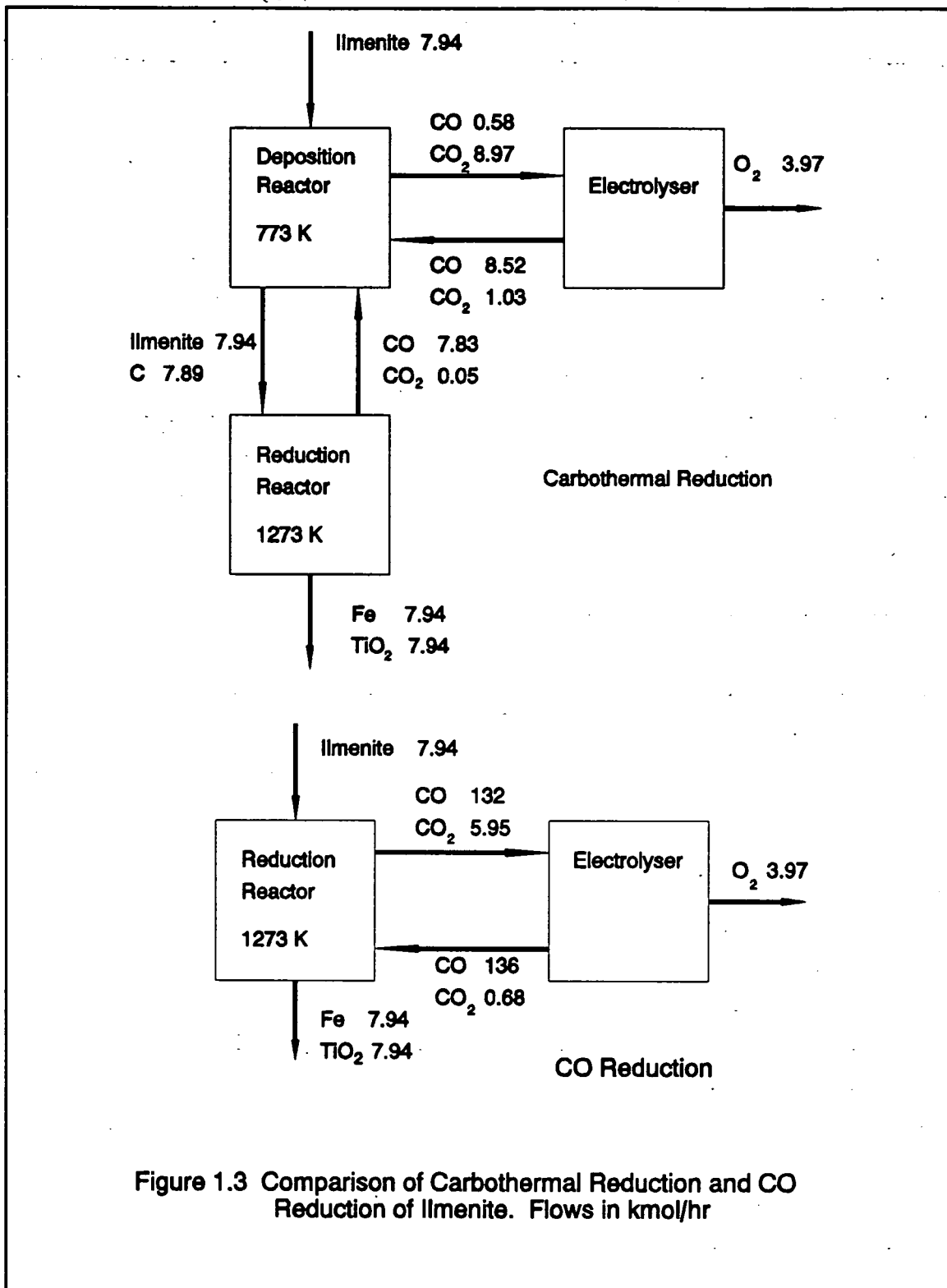


Figure 1.3 Comparison of Carbothermal Reduction and CO Reduction of Ilmenite. Flows in kmol/hr



This reaction is thermodynamically favored at 800 K (Wagman *et al.*), but it is slow unless a catalyst is present. Catalysts used for this process will be mixed into and lost with the minerals being reduced, and so must be available in sufficient quantities locally. Iron is a product of the reduction of ilmenite (Zhao, 1991; Zhao and Shadman, 1990 and 1991; Briggs and Sacco, 1991), and is known to be a catalyst for CO disproportionation (Audier *et al.*, 1983; Guinot *et al.*, 1981). Unfortunately, the range of gas compositions in which iron is active is small, and lies outside the range of interest for this process (Audier *et al.*, 1983). The gas compositions of the deposition reactor favor the formation of Fe₃C, which is not catalytically active. The presence of small amounts of H₂ in the gas accelerates CO disproportionation and inhibits the formation of Fe₃C, and H₂ can reactivate Fe₃C (Olsson and Turkdogan, 1974; Turkdogan and Vinters, 1974; Walker *et al.*, 1959). Walker *et al.* found that the amount of H₂ has little effect on the rate between 743 K and 801 K, but has a major effect above 850 K. Above 850 K, they found a gas composition with maximum rate of deposition. Olsson and Turkdogan attributed the effect of small amounts of H₂ to catalytic activity.

Reduced iron-bearing minerals contain iron metal, so some reduced materials could be mixed with fresh feed to supply catalyst for CO disproportionation. A small amount of H₂ could be added to the gas stream to aid carbon deposition. If carbonaceous waste is used to make up reactant losses, it will contain some H₂ from polymers and other sources. Since the equilibrium constant of the CO disproportionation reaction begins to drop rapidly above 800 K, deposition should take place below this temperature. The rate of deposition is sensitive to surface area, and increases as the reaction proceeds. This is due to the fragmentation of iron by growing carbon filaments (Guinot *et al.*, 1981). The iron produced by ilmenite reduction is already in small particles on the outside of the product grains (Zhao and Shadman, 1990; 1991), and is easily accessible as catalyst. The accessibility of the iron product of silicate reduction as a catalyst for carbon deposition needs to be investigated.

Reduction of Olivine With Hydrogen

Experiments

Three olivines of different magnesium content, two fayalites and one forsterite, in the forsterite-fayalite series were used in the reduction experiments. A naturally occurring fayalite with 93% of the metal as Fe and 7% as Mg (Fa₉₃) was purchased from Ward's Natural Science. It is found in rocks from the Forsythe Iron Mine, Hull Township, Quebec, containing Fa₉₃, magnetite, and traces of other minerals. The rocks were crushed to less than 80 μm to give grains of the individual

minerals. Inspection with a microscope confirmed that grains of this size were largely a single mineral. This fayalite is a transparent yellow, and the magnetite and other minerals are very dark or black, which allows easy identification of the fayalite. The magnetite was removed with a small permanent magnet. A Frantz L-1 Isodynamic separator was then used to remove the last traces of the magnetite and also other minerals included in the fayalite matrix. Although experiments were not done to determine specific magnetic susceptibility precisely, the separations performed gave a specific susceptibility between $76 \times 10^{-6} \text{ cm}^3/\text{g}$ and $100 \times 10^{-6} \text{ cm}^3/\text{g}$, which is in the range of values reported for this mineral (Bleil and Petersen, 1982).

The other fayalite, with all metal as Fe (Fa_{100}) was synthesized in our laboratory. A 2:1 molar ratio of wüstite (FeO , 99.9% pure, from CERAC Advanced Specialty Inorganics) and vitreous silica (SiO_2) were mixed. This mixture was then melted in a 1018 steel cup with an oxy-acetylene torch. The oxygen/acetylene ratio of the torch was adjusted to give a slightly reducing flame. The iron of the steel cup ensured that there was no Fe^{+3} in the silicate melt. The melt was then cooled as slowly as possible, so that large crystals of the minerals would form. The product was a mixture of fayalite and either vitreous silica or wüstite, depending on how successfully oxygen had been excluded from the cup during melting. This was then crushed to give grains of the individual minerals, and the fayalite recovered by magnetic separation.

The forsterite was San Carlos peridot purchased from Ward's Natural Science. The Arizona Sonora Desert Museum also donated some sand and rough 1 cm stones of this mineral. The forsterite from Ward's Natural Science is clear light green 1/2 cm tumbled stones. The composition of the mineral from the two sources was the same, and varied from stone to stone between Fa_{14} to Fa_6 . Several large stones which showed few inclusions and had a composition of Fa_6 were used for reduction experiments. No mineral separations were necessary, since the stones used had no other minerals in them.

The separated olivines were then analyzed by powder pattern X-ray diffraction (XRD) (Figures 2.1 and 2.2) and scanning electron microscopy with energy dispersive X-ray spectroscopy (SEM/EDS) to identify the minerals and determine their composition. The bulk composition was also determined using atomic absorption spectroscopy.

The olivine was ground, washed in acetone to remove fines, and sieved, and the fraction between $38 \mu\text{m}$ and $45 \mu\text{m}$ was pressed into disks 8mm in diameter and 0.6 mm thick. These were cut into

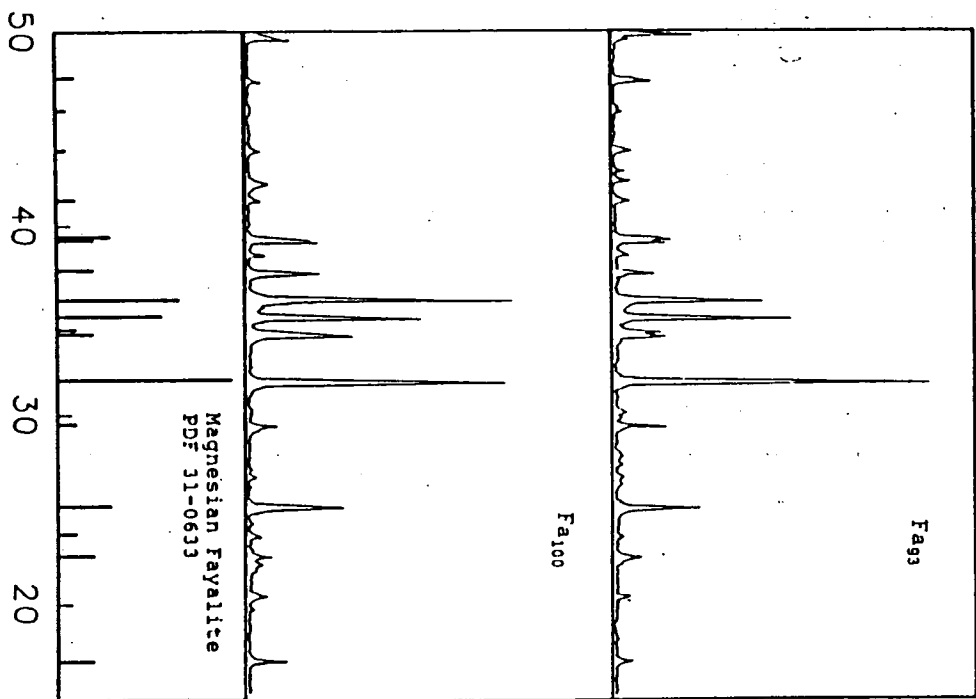


Figure 2.1
Powder Pattern X-ray
Diffraction of Fayalite

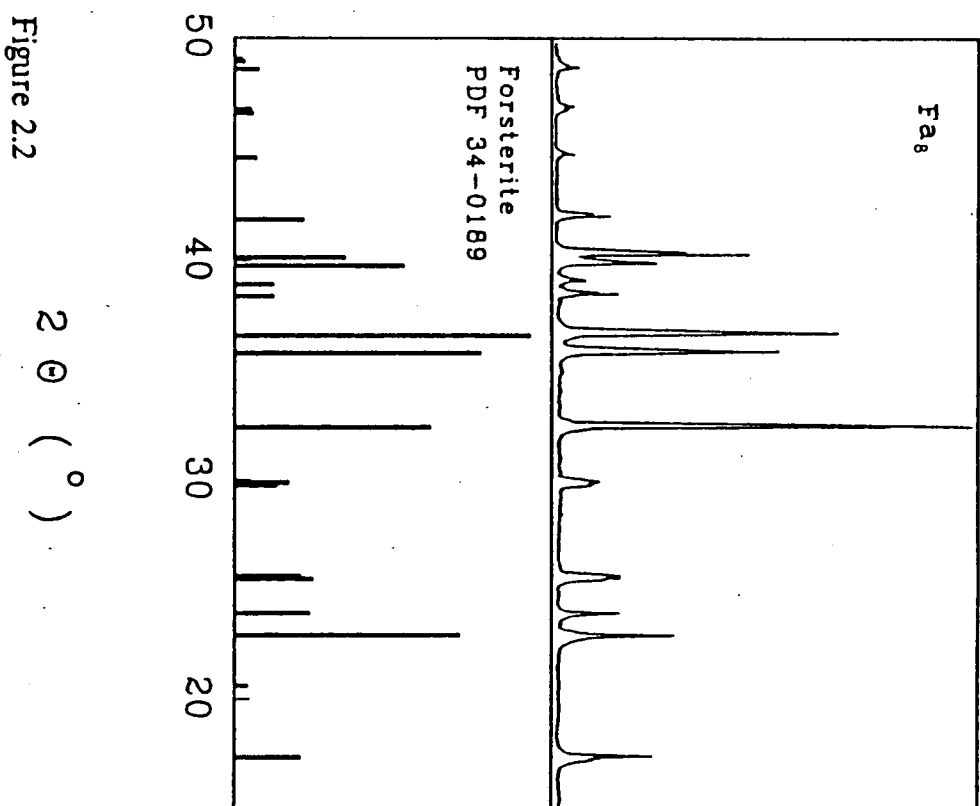


Figure 2.2
Powder Pattern X-ray Diffraction of Forsterite

rectangular flakes, approximately 5mm × 6mm. The dies used by Yi Zhao (Zhao, 1991) for the preparation of ilmenite pellets were made of 316 stainless steel, and were too soft for use with silicates. The pistons bent and galled in the die body, causing irreparable damage to the die. This problem was solved by making the die bodies of hardened 416 stainless steel, and the pistons of air hardened A2 tool steel. Zhao (1991) had shown that these pellets did not cause any significant mass transfer resistance for ilmenite experiments done in our lab, so they should not cause any for reactions with silicates, which are slower than those with ilmenite.

A schematic of the reactor system used in our experiments is shown in Figure 2.3. The system consisted of a gas mixing section, a Cahn 1000 electronic microbalance, a quartz glass reactor, a moveable furnace with controller, and a nondispersive infrared CO/CO₂ analyzer and gas chromatograph downstream of the reactor. All experiments were done at ambient pressure, 0.93 atm. Reaction progress was continuously monitored with the electronic balance and the output recorded with a strip chart recorder and a computer data acquisition system. The gas chromatograph was used to set up the gas before the reaction, but could not be used during an experiment because it caused flow and pressure variations in the reactor. The mineral sample was placed in a Pt wire basket suspended from the balance. The reactor system was then closed and purged with 99.999% pure N₂ for at least 3 hours to remove oxygen. Then the flow of reacting gas was started. The flow was 400 cm³/min at 0.93 atm and 295 K in all experiments. Zhao (1991) showed that this flow eliminated all interphase mass transfer resistance in the same reactor system with faster ilmenite reactions, so it could also do so in these experiments. When the system stabilized, the reaction was started by quickly raising the furnace. The temperature in the reactor, measured with a type K thermocouple, stabilized at its final value in 2 or 3 minutes. The furnace was lowered at the end of the experiment, which caused the reactor temperature to decrease very rapidly and quench the reaction. Gas flow past the sample caused the weight reading to increase due to drag. The drag was measured as the difference between the weight just before lowering the furnace and after all gas flow had stopped. The drag was subtracted from the weight readings taken during the experiment to give actual weights. Because the drag depends on reactor temperature, weight readings could not be used until the temperature stabilized at the start of an experiment. Experiments were performed to determine the amount of adsorbed volatiles. In these experiments, the reactor was brought to reaction temperature in N₂, and then the H₂ flow was started. There was some loss of volatiles, and this loss was estimated for each run and subtracted from the initial mass.

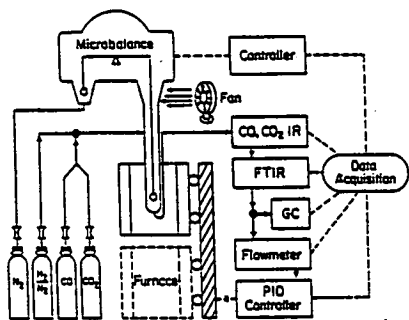


Figure 2.3 Schematic of the Reactor System
 IR: Non-dispersive infrared analyzer; GC: gas chromatograph

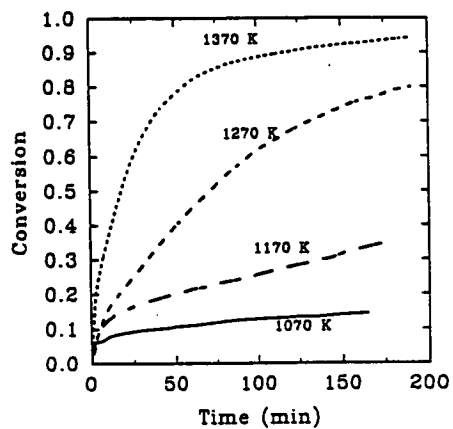


Figure 2.4 Reduction of Fe_{3O_4} in 0.14 atm H_2

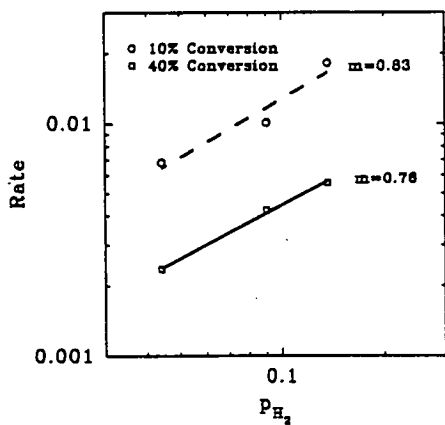


Figure 2.5 Effect of Hydrogen Partial Pressure on the Reduction of Fe_{3O_4}

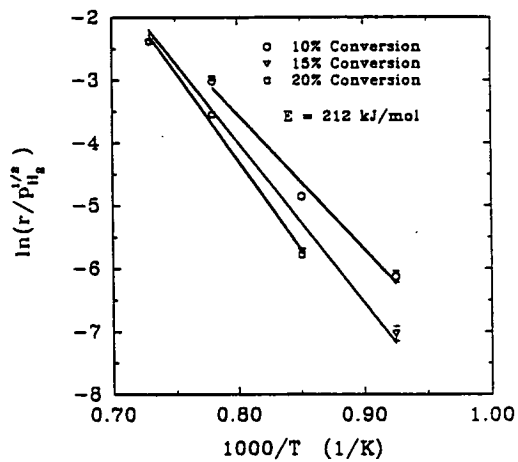


Figure 2.6 Apparent Activation Energy of the Reduction of Fayalite with H_2

Samples of the solid reaction products were mounted in epoxy and polished at Buehler Southwest Research Laboratory. This reveals the particle cross sections for SEM/EDS analysis. SEM micrographs were made with backscattered electrons. Backscattered electron signal strength is primarily a function of average atomic number, so regions with high average atomic number such as high iron phases are brighter than low average atomic number regions. Other samples were ground for XRD. Single crystal silicon slides were used for XRD in order to eliminate any interfering signal from the slide, and so that glass, which produces a low, broad, and noisy signal at low angles, could be positively identified as part of the sample. The combination of SEM/EDS analysis and powder X-ray pattern diffraction allowed conclusive identification of the products.

Results

The naturally occurring fayalite, Fa_{93} , was reduced with mixtures of 0.047 to 0.14 atm H_2 in N_2 at a total pressure of 0.93 atm and at temperatures from 1070 K to 1370 K. Figure 2.4 shows the temporal profile for these reactions in 0.14 atm H_2 at 1070, 1170, 1270, and 1370 K. Conversion in the plot is the fraction of the iron in the mineral that has been reduced to metallic iron. These curves show that the reduction proceeded rapidly until conversion was about 15%, and then slowed considerably. The effects of H_2 concentration are shown in Figure 2.5. The reduction of Fa_{93} is 0.8 order in H_2 . This is somewhat higher than the findings of Gaballah *et al* for Fa_{100} at $0.4 \text{ atm} \leq P_{\text{H}_2} \leq 1 \text{ atm}$. The activation energy didn't change in the course of the reaction. The apparent activation energy is $212 \pm 5 \text{ kJ/mol}$ (Figure 2.6), much lower than the values reported by Gaballah, but slightly higher than that of Minowa.

Figure 2.7 is an SEM micrograph of a typical grain of partially reduced Fa_{93} . The medium grey core of the grain is fayalite of the same composition as the starting material. The core is surrounded by a layer of very finely mixed iron and silica. The two small grey areas at the lower right of the product layer have a metal to silicon ratio close to 1, characteristic of pyroxene rather than olivine. Mg and Mn in these two areas are slightly enriched relative to Fe as compared to the starting material. The SEM micrograph of nearly fully converted Fa_{93} (Figure 2.8) shows almost all of the fayalite has been converted to a mixture of silica and iron. The two medium grey areas near the top of the grain are olivine, considerably enriched in Mg and Mn from the starting material. The lighter regions in the relatively dark silica phase seem to have some Mg, although they are too small for accurate EDS analysis.

Powder pattern XRD of partially and fully reduced Fa_{93} is shown in Figure 2.9. The only crystalline

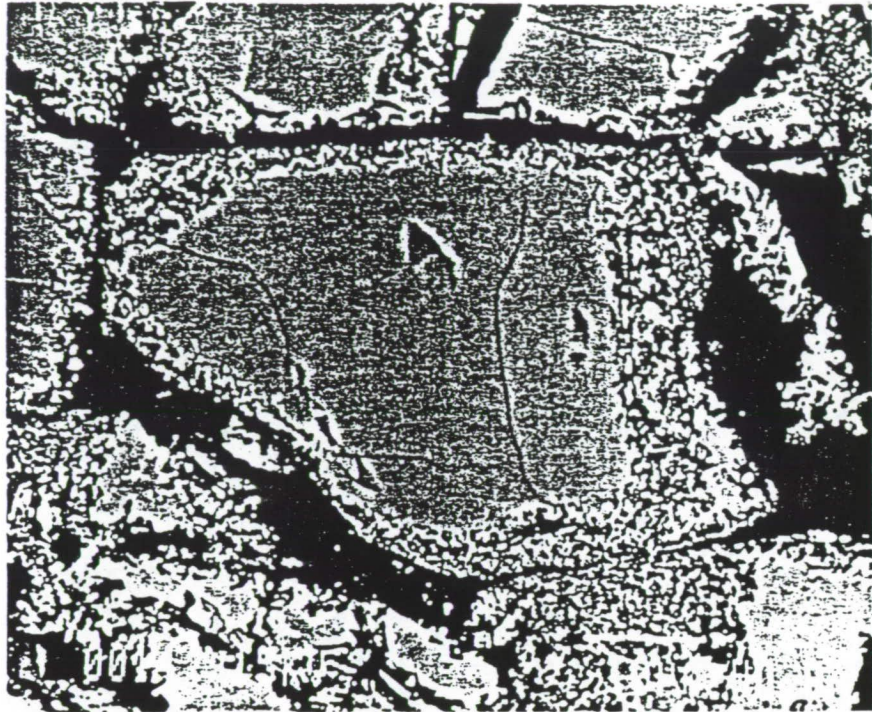


Figure 2.7 SEM Micrograph of a Cross Section of Partially Reduced $\text{Fe}_{3}\text{O}_{4}$

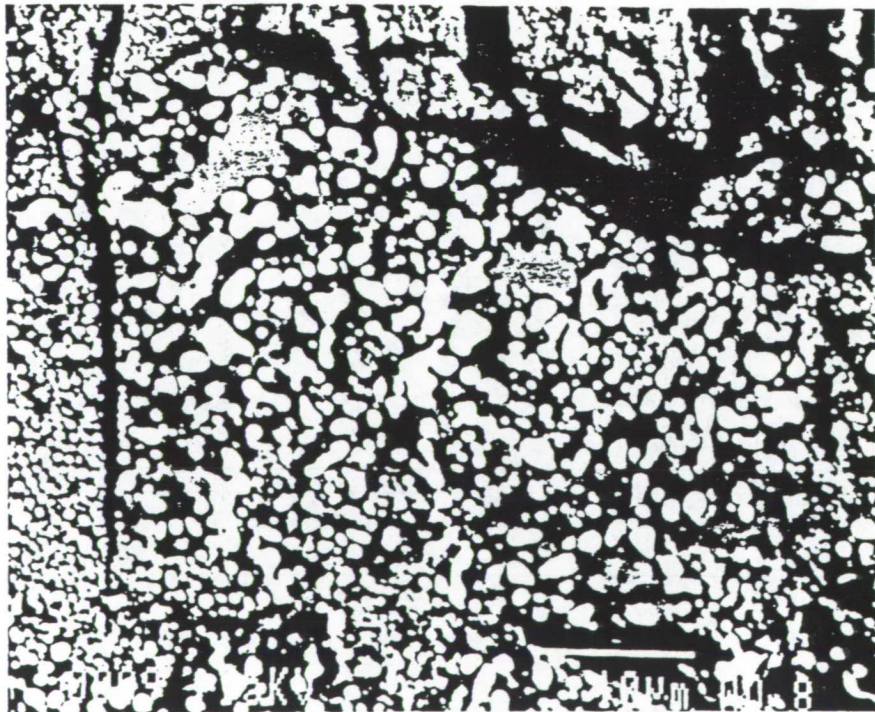


Figure 2.8 SEM Micrograph of a Cross Section of Completely Reduced $\text{Fe}_{3}\text{O}_{4}$

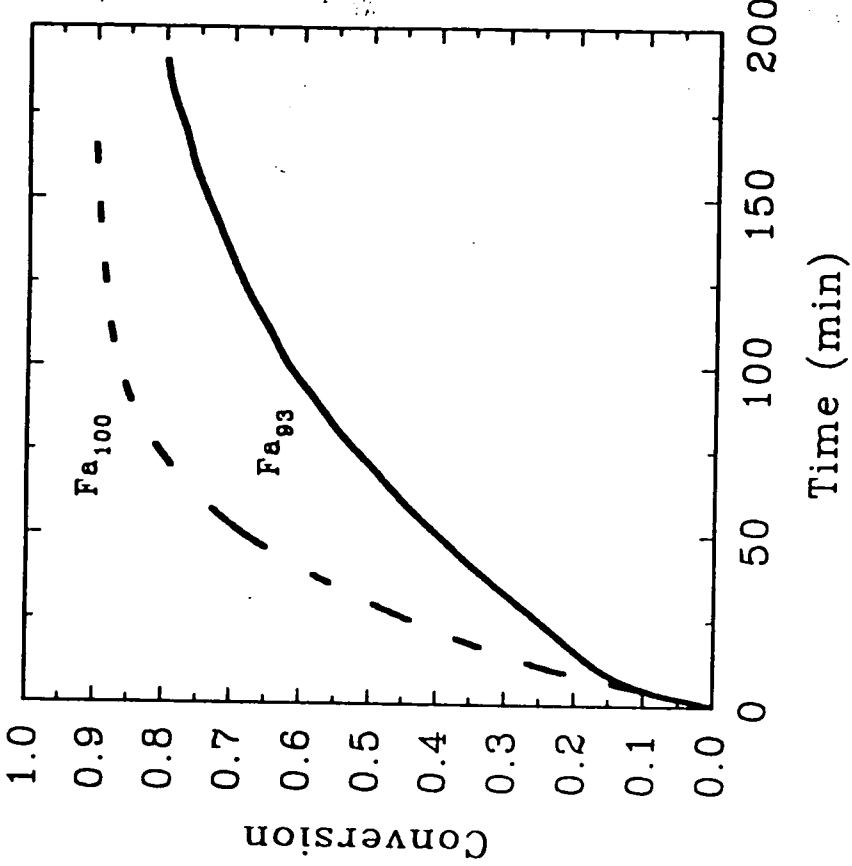


Figure 2.10 Effect of Magnesium on the Reduction of Fayalite with H₂

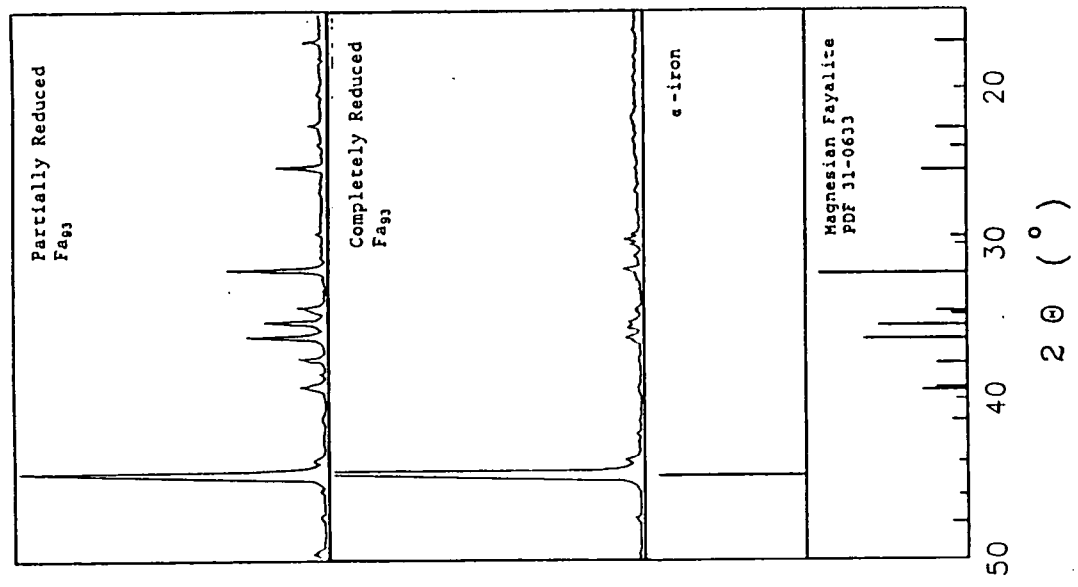


Figure 2.9 Powder Pattern X-ray Diffraction of Reduced Fa₉₃

phases appearing are fayalite and iron. The noise at low 2θ indicates a glassy phase. The XRD pattern of fully reduced Fa_{93} shows mostly iron with a small amount of olivine remaining. The olivine pattern is shifted slightly from Fa_{93} , indicative of a more Mn rich mineral. Only evidence of vitreous silica, and no quartz, tridymite, or cristobalite is seen in the XRD patterns of fully and partially reduced Fa_{93} .

To study the effects of Mg on the reduction of fayalite, Fa_{100} was prepared in our laboratory. The reduction of fayalite is slowed greatly by small amounts of magnesium (Figure 2.10), and the temperature at which reduction occurs at an appreciable rate is increased. The apparent activation energy for reduction of Fa_{100} is 200 ± 8 kJ/mol (Figure 2.11), again much closer to Minowa's value than Gaballah's. Figure 2.12 is a cross section near the end of a grain of partially reduced Fa_{100} . It has a layer of finely mixed iron and silica surrounding the core. Grains sectioned through the middle (for instance, the small grains on the far right of the micrograph) have a uniform core of fayalite, but the core of this grain has a mottled appearance, and EDS gives an iron to silica ratio close to 1, as for a pyroxene, but which varies with Fe slightly higher in the brighter areas. No pyroxene can be detected in the XRD pattern of this material (Figure 2.13), and none was present in the starting material. We believe that this is a section through the reaction front, and that this is evidence that the iron is reduced in the fayalite matrix, and then migrates out towards the layer of mixed Fe and silica, leaving a thin zone deficient in iron and oxygen compared to fayalite, but which has not yet formed silica and iron. Figure 2.14 shows a grain of nearly completely converted Fa_{100} . This is the more typical situation of a fayalite core surrounded by mixed iron and silica. As before, the only crystalline phases indicated by XRD are Fe and fayalite.

The reduction experiments with Fa_6 did not yield reproducible results. The combination of extremely small mass changes and long experiment times was partly the reason. Figure 2.15 shows the conversion in a typical run at 1387 K in 0.14 atm H_2 . The period of slow reduction at the start occurred in all runs, but was of highly variable length. Experiments done at lower temperatures did not produce any measurable reaction. Figure 2.16 is an SEM micrograph of a cross section of partially reduced Fa_6 . The bright spots are Fe, the light streaks are regions of high Fe, and the grey regions are Fa_6 . No silica phases could be found, and XRD revealed only olivine, since the amount of Fe produced was below detectability limits of the diffractometer.

Discussion

Although the presence of small amounts of magnesium greatly affects the reduction rates of fayalite,

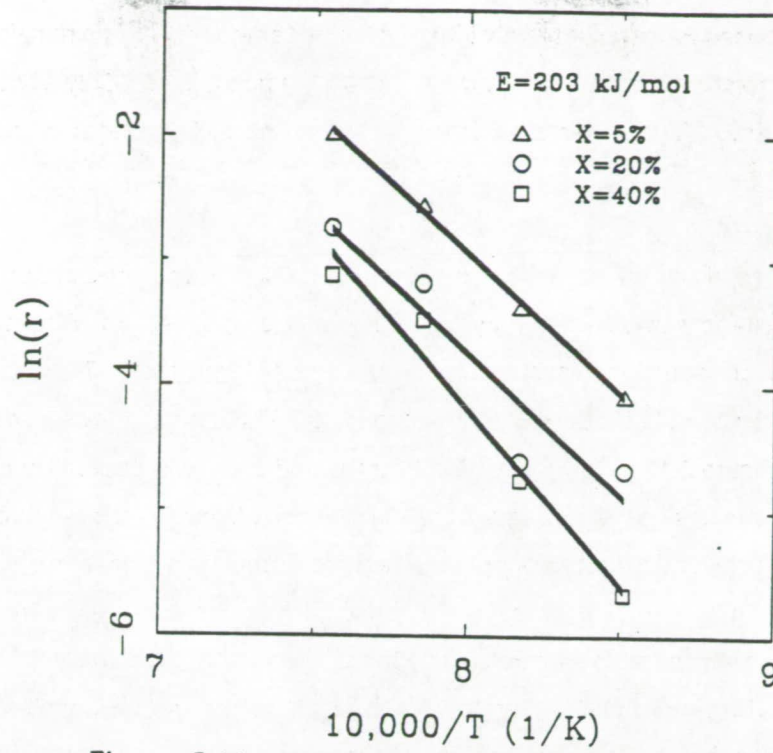


Figure 2.11 Apparent Activation Energy of the Reduction of Fa_{100} with H_2

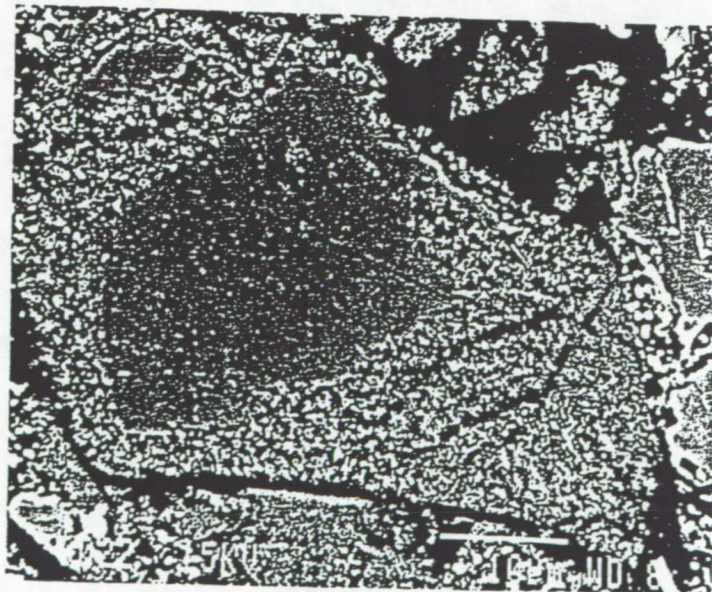


Figure 2.12 SEM Micrograph of a Cross Section of the Reaction Front in Partially Reduced Fa_{100}

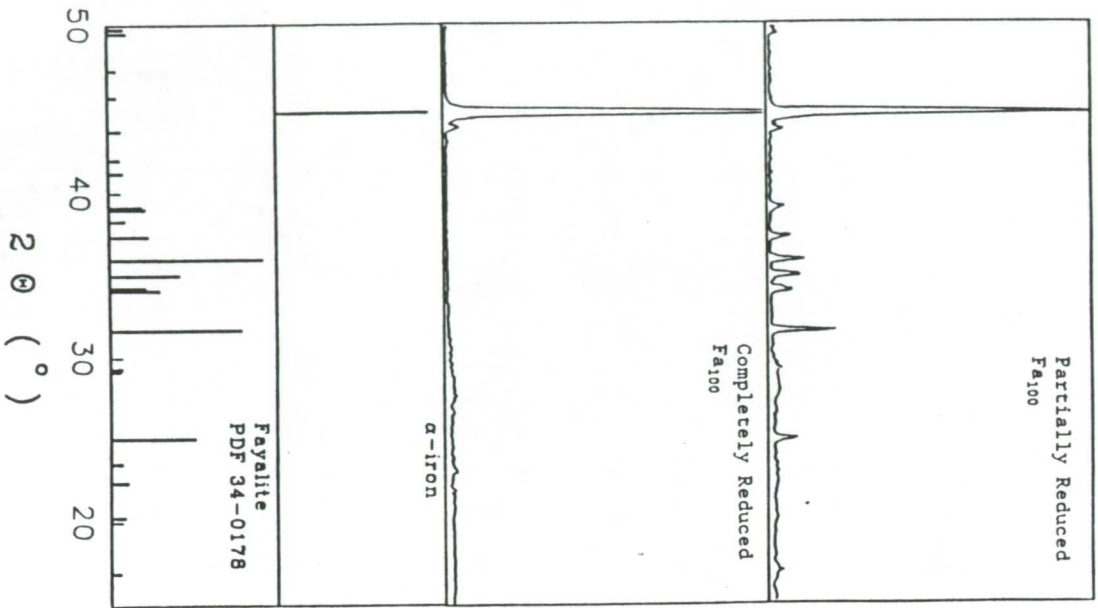


Figure 2.13 Powder Pattern X-ray Diffraction of Reduced Fe_{100}

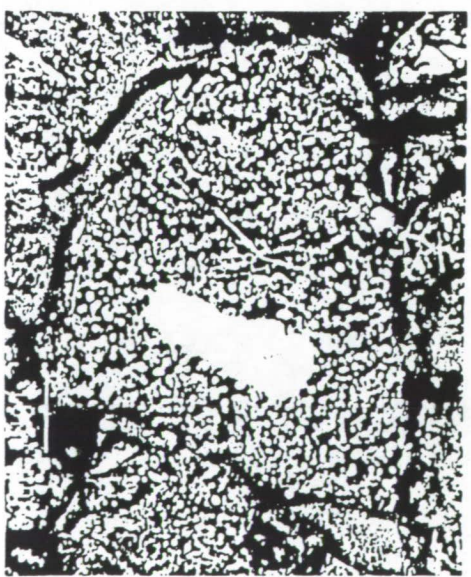


Figure 2.14 SEM Micrograph of a Cross Section of Completely Reduced Fe_{100}

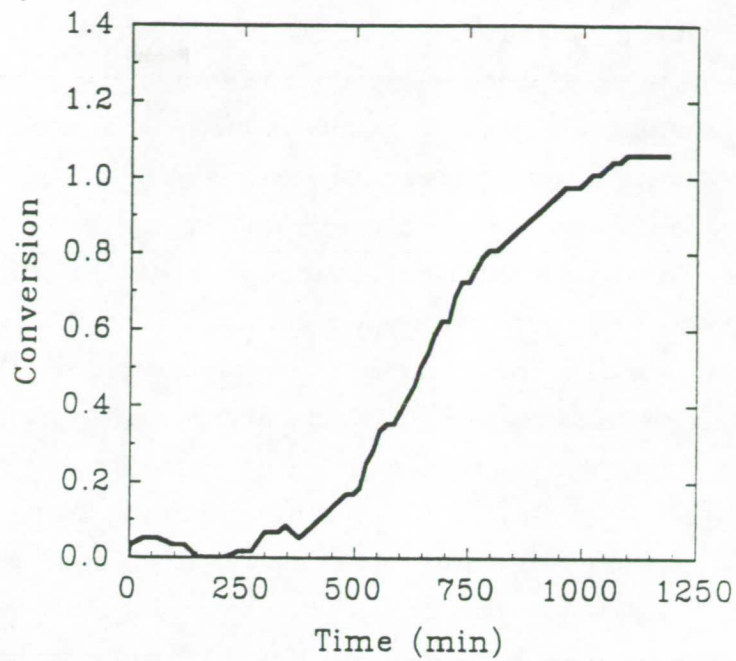


Figure 2.15 Reduction of Fe_3O_4 in 0.14 atm H_2 at 1387 K

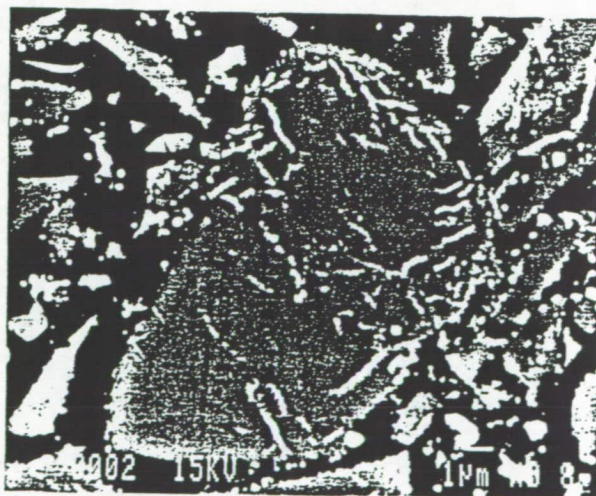


Figure 2.16 SEM Micrograph of a Cross Section of Partially Reduced Fe_3O_4

it does not seem to change the mechanism of the reaction. As shown in Figure 2.10, the effect of magnesium on reaction rates is too great to be acting simply as a diluent of the iron. The rate is 0.8 order in p_{H_2} between 0.047 and 0.14 atm, somewhat greater than the 1/2 power dependence determined by Gaballah *et al.* at hydrogen partial pressures between 0.4 atm and 1.0 atm for Fa_{100} . Magnesium does not have an effect on the apparent activation energy in this range of compositions, either. The activation energies we determined, 212 ± 5 kJ/mol for Fa_{93} and 203 ± 8 kJ/mol for Fa_{100} , are much closer to the value determined by Minowa *et al.* (188 kJ/mol) than those of Gaballah *et al.* (263 kJ/mol). The activation energy is close to that found by Minowa for the formation of Fe_2SiO_4 from quartz and FeO. In materials where diffusion through the pores dominates reaction kinetics, the apparent activation energy approaches 1/2 the intrinsic activation energy as the reaction approaches completion. In the reduction of fayalite, activation energy does not vary with conversion, so the diffusion of gases through pores in the product layer is not important. The distribution of iron throughout the product also suggests that the silica formed is not porous. Iron, although solid, is mobile at these temperatures and tends to agglomerate. In the case of ilmenite, where the solid product is polycrystalline rutile and iron, the iron diffuses along the surface of the pores in the rutile and forms large particles on the outside of the product layer (Zhao and Shadman, 1991). Formation of a nonporous silica layer would also explain the extremely slow rate of reduction of fayalite by CO observed by Gaballah *et al.*, since silica glass is virtually impermeable to CO and CO_2 .

SEM and XRD analysis shows that metallic iron mixed with amorphous silica forms a nonporous layer around a core of unreduced fayalite. Magnesium and manganese, less reducible than iron, migrate to stay in the fayalite. During the course of the reaction, the concentration of iron in the fayalite being reduced gradually decreases. No gradients of Mg were observed in the core with SEM/EDS, although the diffusivity of Mg in fayalite is of order of magnitude 10^{-12} cm^2/sec (Deer *et al.*), and the characteristic time for diffusion across a grain is 4000 hr. Pyroxenes, such as FeSiO_3 , do not form as an intermediate product, and the SiO_2 does not crystallize. Pyroxenes which could be produced in the compositions studied here are not thermodynamically stable (Bowen and Shairer, 1935). Phase transitions between SiO_2 polymorphs requiring rearrangement of the Si-O lattice are slow, and the formation of pyroxene or crystalline SiO_2 (quartz, tridymite, or cristobalite) would require extensive reordering of the Si-O lattice in fayalite (see, for example, Deer *et al.*, 1982). Since pyroxene is not thermodynamically stable, and rearrangement of oxygen-silicon lattices are slow, pyroxene is not formed as an intermediate, and the silica formed is amorphous. During reduction, the x-ray diffraction pattern of fayalite gradually disappears except for a peak

corresponding to 0.207 nm (at $2\theta = 43.8^\circ$) (Figures 2.9 and 2.13). Minowa *et al.* reported a similar peak at 0.222 nm. This distance is approximately the average distance between the M^{+2} and oxygen ion in fayalite (0.2072 nm to 0.2291 nm) (Birle *et al.*, 1968), and may indicate the preservation of some of the fayalite crystal structure in the silica. Evidence of the $Fe_{2-x}SiO_{4-y}$ intermediate proposed by Minowa is shown in Figure 2.12, an SEM micrograph cross section of the end of a grain of partially reduced Fa_{100} . The section goes through the reaction zone. In this area, the composition is variable, with an Fe/Si ratio of around 1. This ratio is characteristic of a pyroxene, but no pyroxene is detected in such samples by XRD. The brighter regions in the mottled area are higher in Fe, and appear to be regions where Fe is beginning to agglomerate. The brighter, uniform cores of the small grains on the right of the micrograph are fayalite. Since the iron does not form larger agglomerations near the outside of the grains where it has had longer to migrate than near the reaction zone, it appears that the formation of vitreous silica immobilizes it. Thus, during reduction the grains of fayalite are divided into three regions: an inner core of unreacted fayalite, a very thin layer of FeO deficient intermediate which retains some of the fayalite crystal structure, and an outer layer of mixed iron metal and amorphous silica. The iron is mobile in the intermediate product, and forms small agglomerations, but is immobilized when the fayalite structure is converted to amorphous silica. Hydrogen must cross the layer of silica glass to reach the reaction front, and the water produced must cross it to leave. The permeability of hydrogen in silica glass is first order in H_2 with an activation energy of 37.2 kJ/mol (Lee *et al.*, 1962). The permeability does not depend on the OH or metal impurity of the glass and is probably due to diffusion of H_2 molecules through interstitial sites in the silica (Lee, 1963). Since the reduction of fayalite is lower order in H_2 and the apparent activation energy is 212 kJ/mol, permeability of silica to H_2 does not completely control the reaction kinetics. A calculation based on the conditions shown in Figure 2.7 shows that hydrogen transport through the silica does influence the kinetics of fayalite reduction. The permeability of hydrogen in silica at 1270 K is 2.5×10^{-12} mol H_2 /cm-atm-s (Lee *et al.*, 1962). If one assumes that the grains are cubes 40 μm on a side with a 1.5 μm layer of silica, the reaction rate corresponding to maximum H_2 transport is 5.4×10^{-3} min⁻¹. The observed rate for this reaction is 4.2×10^{-3} min⁻¹. This indicates that permeation of H_2 through silica is important in the reaction kinetics, although H_2 order and activation energy indicates that it is not controlling. Chemical solubility of hydrogen as OH groups on the Si-O lattice predominates over physical solubility as H_2 molecules in vitreous silica at temperatures above 800 K (Shackleford and Masaryk, 1976), and the solubility is proportional to $p_{H_2}^{1/2}$ (Bell *et al.*, 1962). The hydroxyl radicals are much more reactive than H_2 molecules, and are possibly an intermediate species in the reaction. Lee (1963) found that the chemical solubility of hydrogen is dependent on the formation and thermal history of the silica,

so estimates of the OH content of the silica formed during the reaction cannot be made from available data. Shackleford and Masaryk determined the binding energy of dissociated H species in silica glass to be about 260 kJ/mol, somewhat higher than the apparent activation energy of reduction. Partial control of the rate by the less activated permeation of H₂ in silica would reduce the apparent activation energy from this value, and give a reaction order in H₂ between those of permeation and dissociation of hydrogen.

From this evidence, the reaction kinetics of fayalite with hydrogen are partly determined by the permeation of H₂ through vitreous silica which forms a layer around the partially reacted fayalite, and partly by a step involving chemical reaction of hydrogen with the fayalite. The chemical reaction may be the dissociation of H₂ into hydroxyl groups on the Si-O lattice. The substitution of magnesium for ferrous ions in fayalite slows reaction with H₂ more than expected if it simply acted as a diluent. Magnesium and manganous ions diffuse to stay primarily in the fayalite. Although we could not detect it, magnesium may be concentrated near the reaction zone since it diffuses through fayalite very slowly. This would amplify the effect of magnesium on reaction rates. Magnesium also stabilizes the fayalite structure, as shown by its effect on melting temperature (Bowen and Shairer, 1935), which could contribute to its slowing of the reaction. The stabilization of fayalite by magnesium would also explain the results of the experiments with Fa₈, which reacted extremely slowly, and did not form a silica phase.

Reduction of Pyroxene With Hydrogen

Experiments

Reduction experiments were performed on three different pyroxenes. Two of these, augite (a clinopyroxene) and hypersthene (an orthopyroxene) are common in samples returned from the Moon (Heiken *et al.* 1991). The third, hedenbergite (a clinopyroxene), is less common, but provides useful results on the effect of iron concentration on reaction kinetics and mechanism. All three minerals were purchased from Ward's Natural Science. The augite is in approximately 1/2 cm crystals from Chernosin in the former U.S.S.R. SEM and XRD analysis showed that the crystals have few inclusions, and were not compositionally zoned. The chemical composition of the augite is Fe_{0.13}Mg_{0.44}Ca_{0.43}SiO₃. The hypersthene is large rocks from St.-Ludger-de-Milot, Quebec. It, too, was reasonably uniform. Its chemical composition is Fe_{0.19}Mg_{0.79}Ca_{0.02}SiO₃. No separations were performed on these two minerals. The hedenbergite is a minor constituent of the fayalite/magnetite rocks from the Forsythe Iron Mine, Hull Township, Quebec. It was recovered during the magnetic

separations of this rock, and contains some ferrosilite. The mass susceptibilities of hedenbergite and ferrosilite are close, and these two minerals could not be separated. The chemical composition of the hedenbergite is $\text{Fe}_{0.43}\text{Mg}_{0.10}\text{Ca}_{0.47}\text{SiO}_3$ and the ferrosilite is $\text{Fe}_{0.93}\text{Mg}_{0.07}\text{SiO}_3$.

The experimental procedure for pyroxene is the same as that for olivine. Samples of the reaction products were prepared for SEM/EDS and XRD as before.

Results

The hypersthene was reduced in 0.14 atm H_2 at 1190 K, 1280 K, and 1390 K (Figure 3.1). Mass changes during these experiments were small, and took place over long time periods, but the results were repeatable, unlike those for Fa_8 . The majority of the mass loss took place in the first few minutes of the experiment, when the reactor system had not yet stabilized. After the initial mass loss, the rate of reduction was slow and close to constant. To obtain an estimate of the apparent activation energy, we fit a line to the constant rate portion of the reduction curve, and used the slope as the rate of reaction. The apparent activation energy is 72 kJ/mol (Figure 3.2). An SEM micrograph of partially reduced hypersthene is shown in Figure 3.3. The brightest areas are iron, the light grey is MgTiO_3 , and the dark grey is hypersthene. The band of iron and MgTiO_3 is probably a reduced ilmenite inclusion. A few small grains have small specks of iron in a matrix of hypersthene and a darker material. The dark regions are too small for EDS analysis, but may be silica or a low iron pyroxene.

The augite was reduced in 0.14 atm H_2 at 1090 K, 1180 K, 1280 K and 1380 K (Figure 3.4). The iron content of the augite is less than that of the hypersthene, and so mass loss during the experiments was smaller. The augite showed the same drop in mass during the first few minutes of an experiment as hypersthene. After that, the rate was fairly steady, although less so than for hypersthene. The apparent activation energy of the reduction of augite with H_2 was estimated in the same way as that of hypersthene. The estimated activation energy is 150 kJ/mol (Figure 3.5). Figure 3.6 is an SEM micrograph of a cross section of partially reduced augite. The only phase large enough for EDS analysis is augite. The extremely bright specks are probably iron. A small grain of augite with some bands of darker material containing iron specks can be seen in the lower center of the photo.

Hedenbergite was reduced in 0.14 atm H_2 at 1170 K, 1270 K, and 1370 K (Figure 3.7). It, like the other pyroxenes, showed a rapid rate in the initial period of the reaction, followed by a slower,

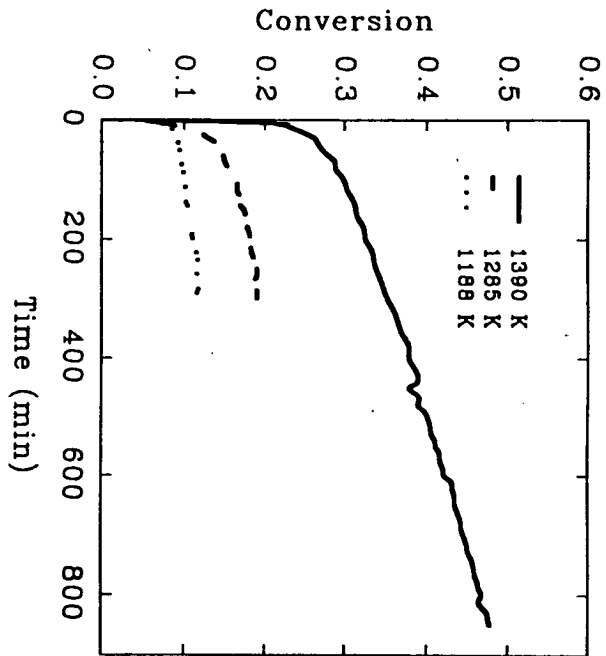


Figure 3.1 Reduction of Hypersthene in 0.14 atm H₂

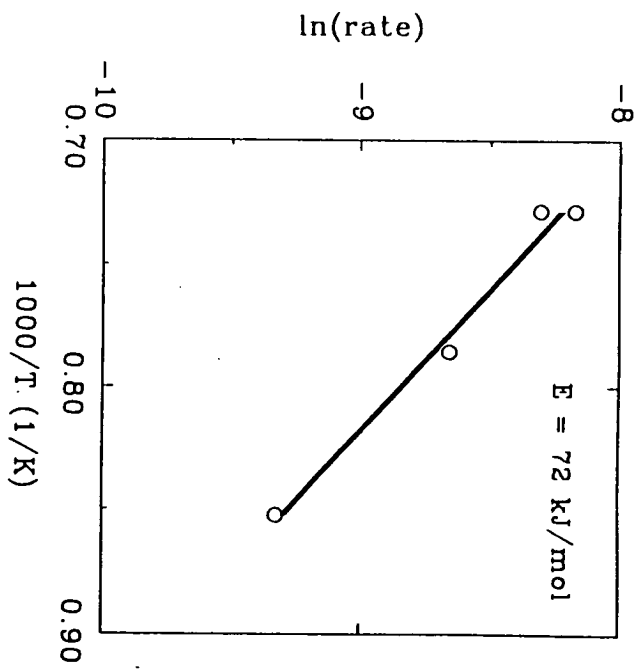


Figure 3.2 Apparent Activation of the Reduction of Hypersthene with H₂

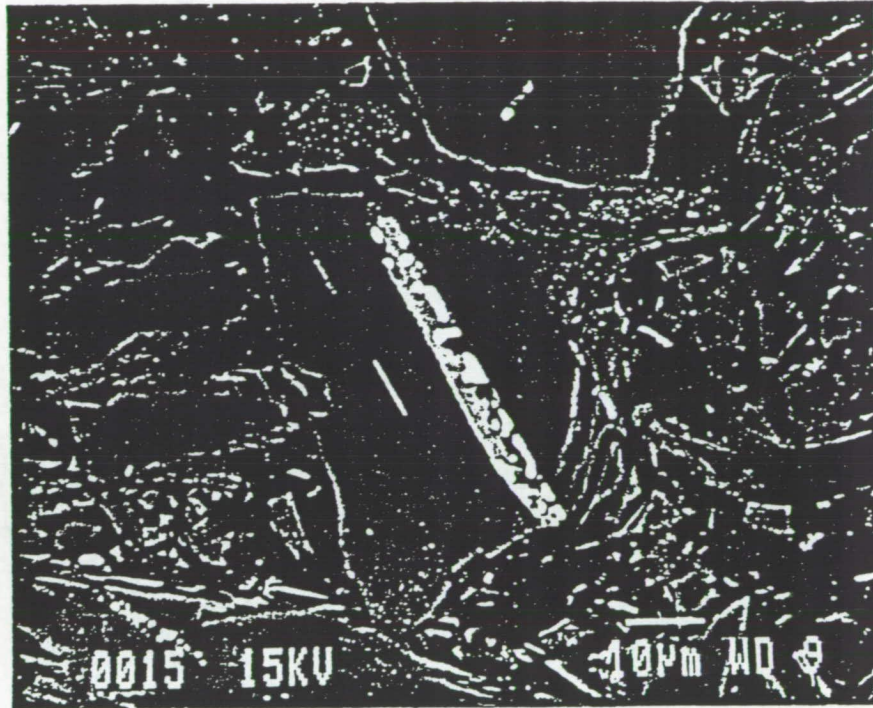


Figure 3.3 SEM Micrograph of a Cross Section of Partially Reduced Hypersthene

steady reaction rate. The reduction was much faster than either hypersthene or augite, with conversion approaching 90% after 3 hours. Additional experiments were made at 1270 K in 0.047 and 0.093 atm H₂ to determine the order of the reaction with respect to hydrogen. The order steadily increased from 0.57 at 20% conversion to 0.87 at 40% conversion (Figure 3.8). The apparent activation energy from the three experiments done at 0.14 atm H₂ is 204 kJ/mol (Figure 3.9). This did not change with conversion, and is the same as fayalite. Figures 3.10 and 3.11 are SEM micrographs of partially and completely reduced hedenbergite, respectively (Conversion calculated from mass loss data). In Figure 3.10, the dark grey phase is hedenbergite of the same composition as the starting material, light grey is Fa₉₃, and the white spots are iron. The Fa₉₃ appears to be partially reduced, but the hedenbergite does not. Although a survey of the pellet showed that most of the grains are hedenbergite, a significant fraction are Fa₉₃. In Figure 3.11 (completely reduced hedenbergite), the white spots are iron. In the upper left is a grain that appears to be reduced ferrosilite. Some ferrosilite remains (grey phase) and the iron forms very large agglomerations in a silica matrix (very dark phase) in this area. The center grain is reduced Fa₉₃, with iron in a silica matrix. The other grains, more typical of the whole sample, are partially reduced hedenbergite. These consist of hedenbergite (light grey) with regions of a low iron product containing iron agglomerates. The composition of the low iron product is Fe_{0.16}Mg_{0.06}Ca_{0.77}SiO₃. This has the metal to silicon ratio of a pyroxene, but has too much Ca to lie in the region of stability for this family of minerals. The chemical formula is that of a pyroxenoid, which has a triclinic crystal structure. The powder pattern XRD of these two products is shown in Figure 3.12. The pattern of partially reduced hedenbergite shows α-iron, clinopyroxene, and some lines that could not be identified. These lines are not those of pyroxene, wollastonite (a pyroxenoid, CaSiO₃), olivine, or a crystalline form of silica. The pattern from the fully reduced hedenbergite shows α-iron, clinopyroxene, and cristobalite. This is the only evidence of crystalline silica found in any of the reaction products.

Discussion

The pyroxenes we used, because of their slow reduction rates and small mass losses, are difficult to study. The reduction curves (Figures 3.1, 3.4, and 3.7) of all three are similar, with an initial jump followed by a period of steady rate of reaction. Since the total mass loss for these minerals is small, desorption of water or other volatiles or preferential reduction of more reactive impurities could cause this. The amount of volatiles was estimated and their effect corrected for in the same way as for fayalite. As the micrographs of hedenbergite indicate, the preferential reduction of impurities may be the cause of the initial jump. XRD did not show the presence of Fa₉₃, which indicates that it constitutes less than approximately 5 wt% of the sample, but some was found with SEM/EDS.

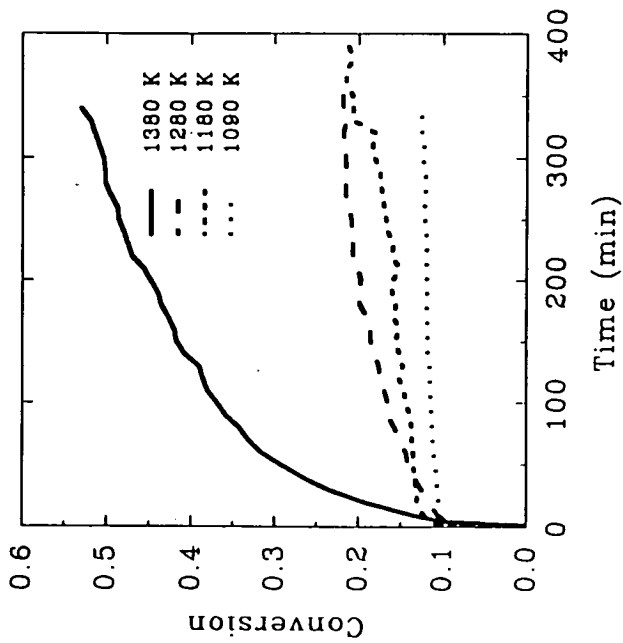


Figure 3.4 Reduction of Augite in 0.14 atm H₂

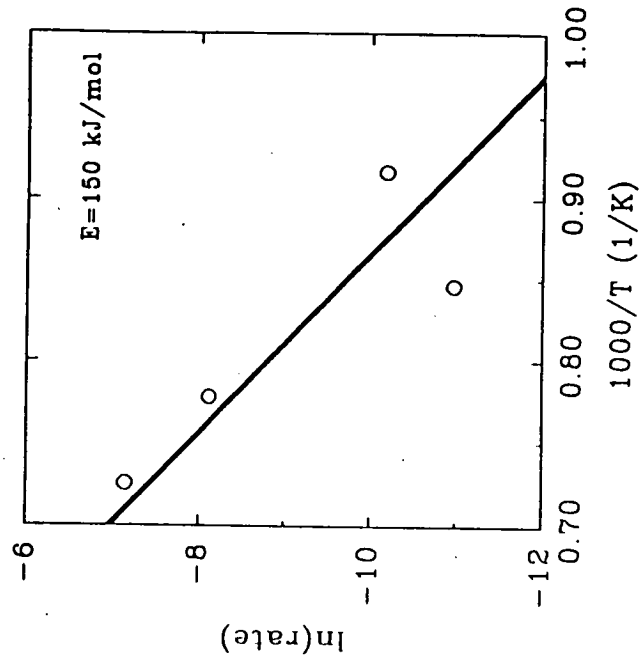


Figure 3.5 Apparent Activation Energy of the Reduction of Augite with H₂



Figure 3.6 SEM Micrograph of a Cross Section of Partially Reduced Augite

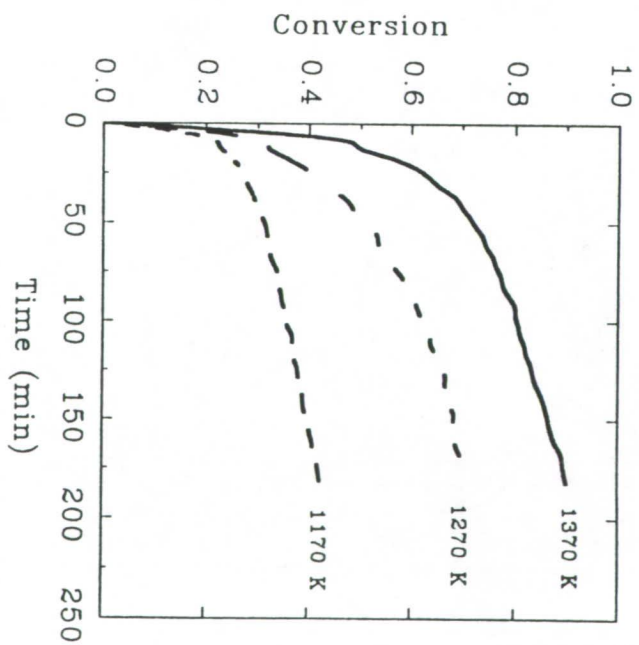


Figure 3.7 Reduction of Hedenbergite in 0.14 atm H₂

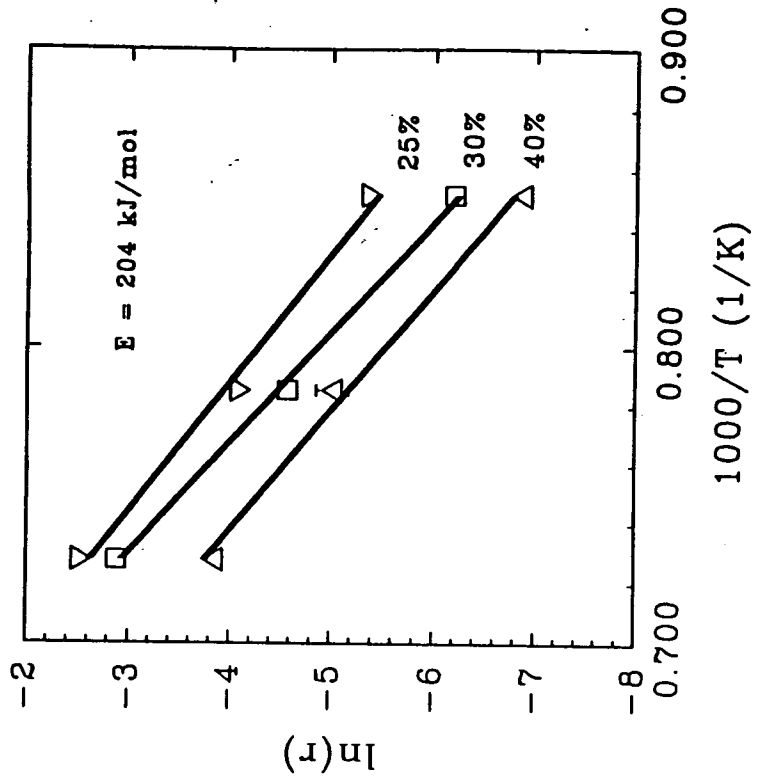


Figure 3.8 Effect of Hydrogen Partial Pressure on the Reduction of Hedenbergite

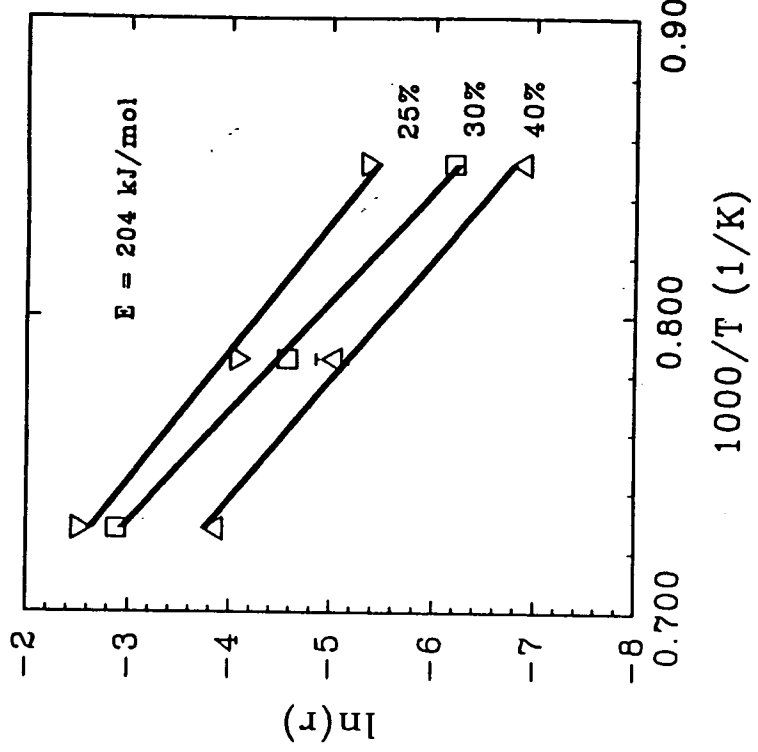


Figure 3.9 Apparent Activation Energy of the Reduction of Hedenbergite with H_2



Figure 3.11 SEM Micrograph of a Cross Section of Completely Reduced Hedenbergite

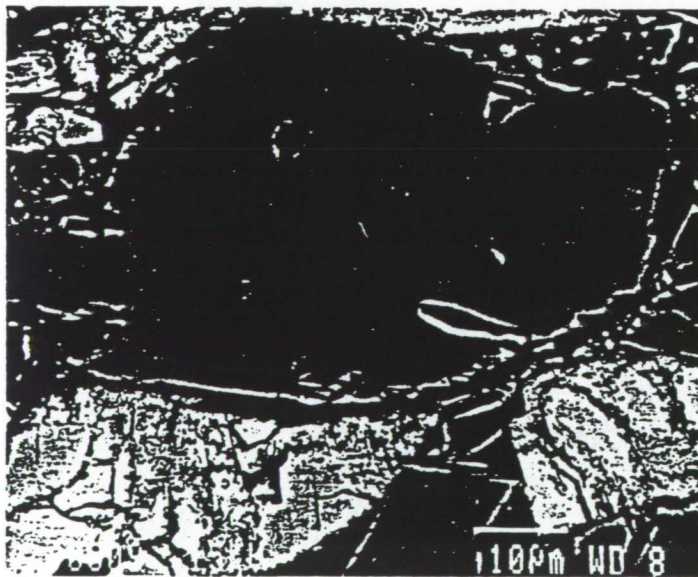


Figure 3.10 SEM Micrograph of a Cross Section of Partially Reduced Hedenbergite

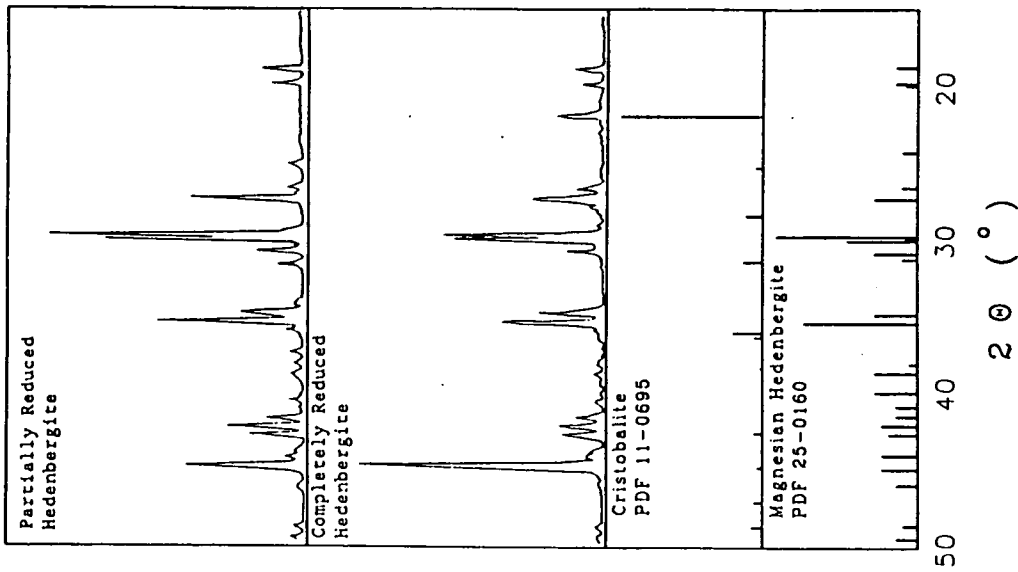


Figure 3.12 Powder Pattern X-ray Diffraction of Reduced Hedenbergite

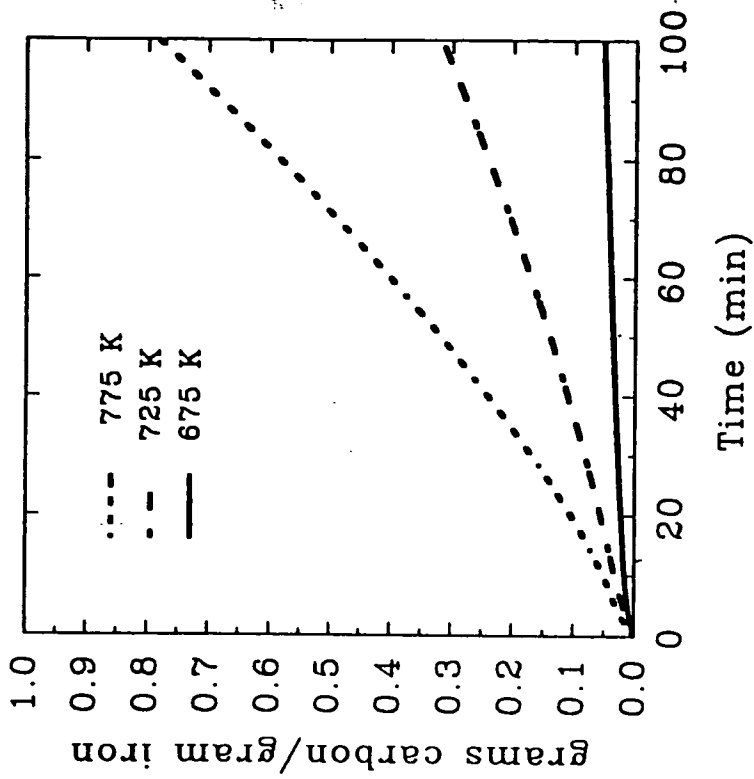


Figure 4.1 Deposition of Carbon on Iron in 0.08 atm H_2 and 0.26 atm CO

Ilmenite inclusions in the hypersthene (Figure 3.3) also reduce faster than the pyroxene. However, none of the starting materials had impurities of more than 5 wt%, as shown by XRD. Also, the reduction of fayalite and ilmenite would not be completed in the first few minutes of reaction. That all three, from different sources, had the same shaped reduction curve indicates that this may be a phenomenon intrinsic to the reaction of iron-bearing pyroxene with H₂.

The apparent activation energy varied considerably for the three minerals, generally increasing with Ca content, from 72 kJ/mol for hypersthene, to 150 kJ/mol for augite, and 204 kJ/mol for hedenbergite. The activation energy of hedenbergite did not change with conversion. The agreement between apparent activation energy of hedenbergite and Fa₉₃, the major impurity, seems suspicious. Further experiments with this mineral should be performed to determine if this is a reflection of the reduction of fayalite or a coincidence. The order of hydrogen pressure dependence in the reduction of hedenbergite increased steadily with conversion, from 0.57 at 20% conversion to 0.87 at 40% conversion. This suggests that the intrinsic order is 1/2, and the apparent order rises as diffusion through the growing product layer becomes more important in determining the rate. However, the micrographs of reduced hedenbergite show a product phase forming throughout the grain and not on the outside, so that the distance that H₂ must diffuse through the products is not increasing. This implies that diffusion through a layer of products is not important.

The product morphology in pyroxene reduction differs greatly from fayalite. For all three pyroxenes, the reduction appears to occur throughout the grain, and not along a reaction front separating products and an unreacted core. Hedenbergite was the only pyroxene with a silica product. Augite and hypersthene had very small specks of iron form, mainly but not exclusively on the outside of grains. Hedenbergite formed a product with a chemical formula similar to wollastonite, a pyroxenoid, but no pattern similar to wollastonite's appeared in XRD. It could be that the change in the Si-O lattice from clinopyroxene to wollastonite is too great to allow fast recrystallization, similar to the situation with fayalite. Cristobalite, the high temperature polymorph of SiO₂, was also formed. It formed at 1370 K, below the temperature of thermodynamic stability (1740 K). However, this mineral is known to form outside of its phase field if conditions are favorable, especially if crystallization is rapid (Berry and Mason, 1959). The iron in reduced ferrosilite forms large agglomerations, suggesting that it remains mobile. The iron formed in the reduction of hedenbergite also seems to be able to form large agglomerations.

The reduction of pyroxene is a complicated subject, and the study presented here gives only

preliminary findings. With only three different pyroxenes, the dependence of kinetic parameters on the chemical composition cannot be determined. The results do show some important difference from fayalite. The activation energy depends on the composition of pyroxene. The solid products do not form a layer around a shrinking core, but form throughout the grain. The order of hydrogen increases from 0.57 to 0.87 with conversion, suggesting a change of mechanism from one of 1/2 order to one of first order as the reaction proceeds. Further experiments are necessary to reach firm conclusions.

Carbothermal Reduction of Iron Bearing Minerals

Experiments

The general procedure used for carbon deposition and reduction experiments was the same as that for olivine. However, because the large changes in volume during the experiment would probably cause a pressed pellet to disintegrate, powdered samples were used instead. The powder was placed in a small quartz bucket (1 cm i.d., 1.5 cm deep) suspended on the microbalance. Iron titanate (CERAC, 99.9% pure) and iron (Alfa Catalog Chemicals) were used in experiments to find a suitable catalyst and conditions for carbon deposition. Both powders are $-45 \mu\text{m}$. The gas mixture used for these experiments was 0.08 atm H_2 and 0.26 atm CO in N_2 . The outlet gas was monitored continuously with a nondispersive infrared analyzer for CO and CO_2 . The amount of carbon deposited was measured by mass gain during the experiment, CO_2 in the outlet gas, and by monitoring mass changes while burning off deposited carbon in air after the deposition experiment.

Deposition/reduction experiments were performed with iron titanate (CERAC) and Fe_{93} . The iron titanate was the same as was used for the deposition experiments, and also for the reduction experiments of Yi Zhao (Zhao, 1991). A gas mixture of 0.23 atm CO and 0.02 atm H_2 was used for both prerduction and deposition. The ilmenite was reduced in this gas at 1270 K to 25% conversion, and the furnace was lowered to stop the reaction. After the furnace had cooled to the deposition temperature, it was raised and the deposition begun. When the desired amount of carbon had been deposited, the furnace was again lowered to stop the reaction. The CO and H_2 were turned off, and the system purged with N_2 for at least 2 hours. The furnace, heated to the reduction temperature, was raised to start the reduction reaction. The Fe_{93} used for deposition/reduction experiments was the same as that used for the H_2 reduction experiments. The only change in the experimental procedure for ilmenite was during prerduction. Since Gaballah *et al.* reported that CO did not reduce fayalite to any extent, 0.14 atm H_2 was used instead of the CO/ H_2 mixture.

Results

The results to find a catalyst for carbon deposition are summarized in Table 4.1.

Table 4.1 Catalysts of CO Disproportionation

Catalyst	Conditions	Analysis	Result
FeTiO ₃	643 K to 833 K up to 30% CO in N ₂	TGA, Nondispersive Infrared analysis, Burn off C	Did not catalyze carbon deposition
Fe	643 K to 833 K up to 30% CO in N ₂	TGA, Nondispersive Infrared analysis, Burn off C	Did not catalyze carbon deposition
Fe	673 K to 773 K 20% to 30% CO 2% to 9% H ₂ in N ₂	TGA, Nondispersive Infrared analysis	Catalyses carbon deposition

Ilmenite did not catalyze the CO disproportionation reaction. No weight gain or CO₂ in the outlet gas were observed. In some experiments with iron without H₂ in the gas stream, a small amount of CO₂ was observed in the outlet gas at the start of the experiment before the temperature stabilized and reliable weight measurements were possible, but it lasted only a few minutes and no weight gain was seen after the system temperature stabilized. The results of deposition experiments using iron and a gas mixture of 0.08 atm H₂ and 0.26 atm CO are shown in Figure 4.1. The deposition was slow and the rate steady at 680 K. At 730 K and 780 K, the rate was much higher and increased throughout the experiment.

Since iron in the presence of H₂ can catalyze carbon deposition, partially reduced ilmenite or fayalite should also do so, since there is some iron in the reduction products of these minerals. The gas mixture used for deposition of carbon on these minerals was 0.23 atm CO and 0.02 atm H₂. Figure 4.2 shows the deposition of carbon on 27% reduced FeTiO₃ and 27% reduced Fa₉₃ at 750 K in this gas mixture. The deposition (per gram iron) was slower for both partially reduced minerals than for iron only, and the deposition on Fa₉₃ was slower than FeTiO₃. However, both showed the steadily increasing rate observed with iron in this temperature range.

Reduction of ilmenite and Fa₉₃ with deposited carbon at 1270 K is shown in Figures 4.3 and 4.4, respectively. Two experiments were performed with ilmenite, one with excess ilmenite and one with excess carbon. Reduction in both cases was very rapid until one of the reagents was consumed,

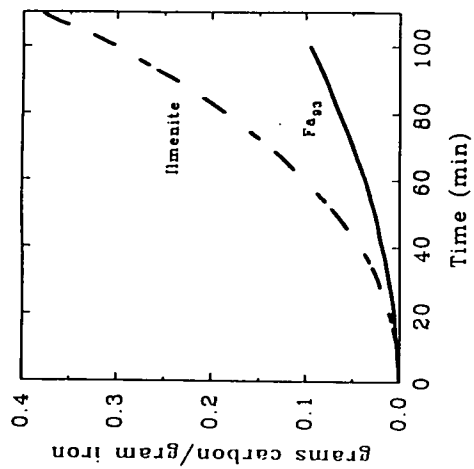


Figure 4.2 Deposition of Carbon on 27% Reduced Ilmenite and 27% Reduced Fe₃O₄

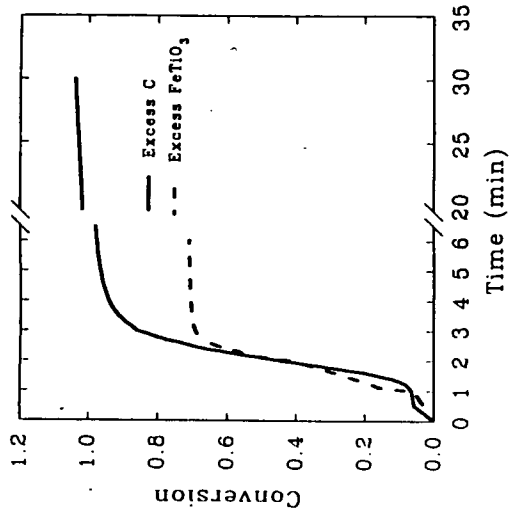


Figure 4.3 Reduction of Ilmenite with Deposited Carbon

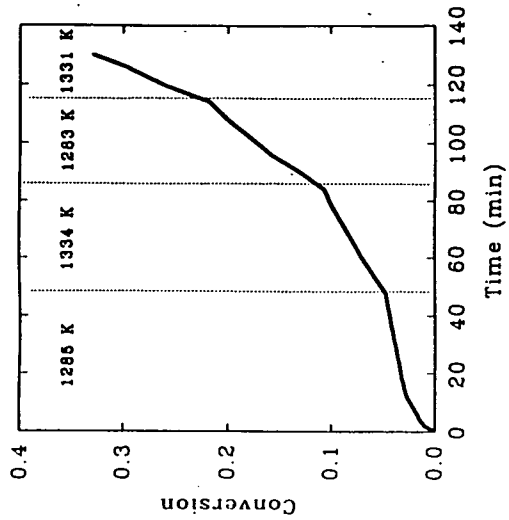


Figure 4.4 Reduction of Fe₃O₄ with Deposited Carbon

the reaction lasting only two or three minutes. When excess carbon was used, the weight loss continued, albeit much more slowly, until the experiment was stopped after 30 minutes. The conversion in this experiment reached values above 1, indicating that some TiO_2 may have reacted with the carbon. Reduction of Fa_{93} with deposited carbon was much slower. The temperature was raised in steps of about 50 K from 1280 K to 1430 K to observe its effect on reaction rate. Even at the higher temperature, reduction was not complete when the experiment was ended after 135 minutes. In all the carbothermal reduction experiments, only CO and no CO_2 was observed in the product gas.

Discussion

As one would expect from the literature, iron catalyzes CO disproportionation in the conditions of interest for the deposition reactor only when H_2 is present. Ilmenite did not catalyze the reaction under any conditions, and judging from the lack of extensive carbon deposits on the quartz glass reactor, silicates do not catalyze the reaction either. This is an advantage for the process, since it allows deposition of carbon only on the minerals and not on the reactor walls.

Deposition was slower on partially reduced ilmenite or partially reduced Fa_{93} than on iron powder. This is because the iron on partially reduced minerals is less accessible to the gas than iron powder, and so has less active surface area at the start of deposition. Deposition on Fa_{93} is slower than on ilmenite because the iron produced by reducing fayalite is mixed in a silica glass matrix and is sealed off from the CO. In both cases, the deposition rate steadily increases as carbon growth fragments the iron and surrounding materials, increasing the active surface area.

Deposited carbon rapidly reduces ilmenite, and achieved conversions above 1 after relatively short times. Final conversion above 1 indicates that TiO_2 formed in the initial reduction of ilmenite is reacting with carbon. The product of this reaction may be a substoichiometric titanium oxide (such as $\text{TiO}_{1.9}$) or titanium carbide (TiC). Although the higher O_2 production caused by this further reaction is beneficial for the production of lunar O_2 , formation of TiC would present a problem. Since carbon is scarce on the Moon, nearly all the carbon used for reduction must be recovered and recycled. Recovering it from TiC may present difficult problems. A related problem is the possibility of forming Fe_3C , since iron may be in close contact with carbon during reduction. The nature of carbothermal reduction products is an area which needs further study. The reduction of fayalite with deposited carbon was much slower than ilmenite, but still took place at an appreciable rate. This is in contrast with the reduction of fayalite with CO, which Gaballah *et al.* report did not occur to

any extent. Gaballah *et al.* attribute the slow reaction between fayalite and CO to the formation of Fe_3C , which increased the volume of the reduction products and sealed the reaction front from further reaction. This should also occur during reduction with carbon, but apparently did not. If the reaction products are a mixture of iron in silica glass, as they are for reduction with H_2 , it is not clear how the reducing agents can cross the product layer. Further study is needed to find the reaction mechanism.

The experiments done here indicate that a carbothermal reduction process for oxygen production on the Moon may be feasible. Because the use of a deep bucket to hold the minerals causes diffusion resistance, no kinetic parameters were derived. Much work remains to be done on this process. A reactor system that does not have diffusion resistance must be designed to derive the kinetics of the reactions. Carbon in the products (dissolved in iron, or as Fe_3C or TiC) is a real concern and must be investigated. However, the carbothermal reduction process works for ilmenite and fayalite, and is a promising alternative to gas reduction processes.

Conclusions and Recommendations

This study has determined the kinetic parameters and important steps of the reaction mechanism for the reduction of fayalite with hydrogen at partial pressures between 0.046 atm and 0.14 atm. The apparent activation energy is 212 ± 5 kJ/mol and did not change much with magnesium content. The reaction is 0.8 order in hydrogen. The solid reaction products are silica glass and iron, with the iron intimately mixed in a silica matrix. Reaction kinetics are influenced by the permeation of H_2 through the silica and chemical reaction of dissociated H_2 with fayalite. An intermediate depleted in FeO is formed and iron is mobile in it, but on further reduction it forms glass, and the iron is immobilized.

The kinetics of reduction of pyroxene by H_2 is more complicated than fayalite due to the greater variations in chemistry of this mineral. The apparent activation energies for reduction in 0.14 atm H_2 are 72 kJ/mol for hypersthene, 150 kJ/mol for augite, and 204 kJ/mol for hedenbergite. Activation energy increased with calcium content. The hydrogen dependence of reduction of hedenbergite increases with conversion from 0.57 at 20% conversion to 0.87 at 40% conversion. Although this suggests that diffusion is increasingly important in the kinetics as the reaction proceeds, SEM micrographs show products mixed throughout the pyroxene and not forming a layer on the outside, which implies that the diffusion path length is not increasing. The iron appears to

remain mobile in the products, and cristobalite was formed in the reduction of hedenbergite at 1370 K.

The preliminary experiments reported here show that the carbothermal reduction of iron-bearing lunar minerals is possible. Carbon can be deposited from CO using the iron metal in partially reduced minerals as a catalyst if a small amount of H₂ is present. Reduction of ilmenite with deposited carbon is very rapid at 1270 K, and conversions above 1 are possible, indicating that the carbon is reacting with the TiO₂ formed in the reduction of ilmenite. Reduction of fayalite at 1270 K with carbon is much slower, but proceeds at a reasonable rate.

Recommendations

Much work remains to be done on the reduction of olivine with H₂. An oxygen production plant will use hydrogen pressures higher than those used here, so experiments should be done to see if the kinetic parameters derived at low pressures hold for higher pressure. Olivines higher in magnesium than the fayalites used here should be made and their reduction studied. Avoiding compositional zoning due to fractional crystallization will be very important in olivine synthesis. Other metal substituents may have a different effect than magnesium, so olivines containing them should be reduced. The Smithsonian Institute has donated some natural olivines to this project, some of which have significant amounts of manganese. Since Mn⁺² is the most common metal in lunar olivine after Mg⁺² and Fe⁺², these will provide good materials for reduction experiments. The loss of reactants is important in the design of a lunar oxygen plant, and significant amounts of H₂ and H₂O can be chemically bound in silica glass (Lee, 1962). The amount of hydrogen that remains in the silica should be determined.

Further work with pyroxene depends on successful synthesis of this mineral. A series of minerals with compositions varied so that a systematic study of the effects of composition on reduction kinetics should be made. Experiments to find the cause of the extremely rapid mass loss in the first few minutes of the experiments are needed. A thorough examination by SEM of the products of a reaction stopped just after this period is the first place to start. Synthesized minerals should also allow determination of whether impurities are responsible for the rapid mass loss during the first few minutes of the experiment. As with olivine, experiments should be performed to determine if the kinetic parameters derived here hold at higher hydrogen pressure.

The most important problem for carbothermal reduction of iron-bearing minerals is loss mechanisms

for carbon. The formation of carbides of iron, titanium, and silicon during reduction will make carbon recovery difficult. TiC and SiC should be easily identified with XRD, but the patterns for Fe₃C and Fe are very similar and other methods may be needed to differentiate between them. The kinetic parameters for deposition of carbon and reduction with carbon and their dependence on initial conversion, mineral composition, and other process variables should be determined. The carbothermal reduction of pyroxene can be investigated when a sufficient supply of pyroxene has been synthesized.

References

- Audier, M.; Coulon, M.; Bonnetain, L. Disproportionation of CO on Iron-Cobalt Alloys I. Thermodynamic Study. *Carbon*, 1983, 21(2), 93-97.
- Bell, T.; Hetherington, G.; Jack, K. H. *Phys. Chem. Glasses*, 1963, 3, 141.
- Berliner, L.D.; Shapovalona, R.D. Thermodynamics of the Equilibrium of Fayalite (Iron Orthosilicate) with Hydrogen. *Russian Journal of Physical Chemistry* 1966 40 (11), 1561-62.
- Berry, L. G.; Mason, B. *Mineralogy Concepts Descriptions Determinations*, W. H. Freeman and Company, San Francisco, Ca. 1959.
- Birle, J. D.; Gibbs, G. V.; Moore, P. B.; Smith, J. V. Crystal Structures of Natural Olivines. *Amer. Min.* 1968, 53, 75-80.
- Bliel, U.; Petersen, N. in *Landolt-Börnstein Numerical Data and Functional Relationships*. Springer-Verlag, New York 1982 N.S. V/1b, 317-20.
- Bowen, N. L.; Shairer, J. F. The System, MgO-FeO-SiO₂. *Am. J. Sci.*, 5th ser. 1935, 29, 174-80.
- Briggs, R. A.; Sacco, A. Hydrogen Reduction Mechanisms of Ilmenite Between 823 and 1353 K. *J. Mater. Res.* 1991, 6 (3), 574-84.
- Chase, M. W., Jr.; Davies, C. A.; Downey, J. R., Jr.; Frurip, D. J.; McDonald, R. A.; Syverud, A. N. JANAF Thermochemical Tables. *J. Phys. Chem. Ref. Data* 1985 Suppl.
- Cutler, A. Power Demands for Space Resource Utilization. *Space Nucl. Power Syst.*, 1986, 25-42.
- Cutler, A. H.; Waldron, R. D. Evaluation of Processing Options for Lunar Oxygen Production. Proceedings of Space '92, ASCE, Denver, CO, June 1-4, 1992.
- Deer, W. A.; Howie, R. A.; Zussman, J. *Rock Forming Minerals*, 2nd ed.; Halsted Press: N.Y., 1982.
- Gaballah, I.; Jeannot, F.; Gleitzer, C.; Dufour, L. C. Cinétique de Réduction de l'Orthosilicate de Fer Fe₂SiO₄ (Fayalite) par H₂, CO et les Mélanges CO+H₂. *Mém. Sci. Rev. Métallurg.* 1975.
- Guinot J.; Audier, M.; Coulon, M.; Bonnetain, L. Formation and Characterization of Catalytic Carbons Obtained from CO Disproportionation Over an Iron Nickel Catalyst. *Carbon* 1981 19 95-98.

Heiken, G. H.; Vaniman, D. T.; French, D. E., eds. *Lunar Sourcebook*: Cambridge Univ. Press, 1991.

Lee, R. W. Diffusion of Hydrogen in Fused Quartz. *J. Chem. Phys.* 1963, 38 (2), 448-55.

Lee, R. W.; Frank, R. C.; Swets, D. E. Diffusion of Hydrogen and Deuterium in Fused Quartz. *J. Chem. Phys.* 1962, 38 (4), 1062-71.

Minowa, S.; Yamada, M.; Torii, C. *Tetsu to Hagane* 1968 54 (12) 1203-16.

Olsson, R. G.; Turkdogan, E. T. Catalytic Effect of Iron on Decomposition of Carbon Monoxide:II. Effect of Additions of H₂, H₂O, CO₂, SO₂, and H₂S. *Met. Trans.*, 1974, 5, 21-26.

Shackelford, J. F.; Masaryk, J. S. The Thermodynamics of Water and Hydrogen Solubility in Fused Silica. *J. Non-Crystalline Solids*, 1975, 21, 55-64.

Shomate, C. H.; Naylor, B. F.; Boericke, F. S. Thermodynamic Properties of Ilmenite and Selective Reduction of Iron in Ilmenite. *U.S. Bureau of Mines Report of Investigations 3864*, 1946.

Turkdogan, E. T.; Vinters, J. V. Catalytic Effect of Iron on Decomposition of Carbon Monoxide: I. Carbon Deposition in H₂-CO Mixtures. *Met. Trans.*, 1974, 5, 11-19.

Wagman, D. D.; Kilpatrick, J. E.; Taylor, W. J.; Pitzer, K. S.; Rossini, F. D. Heats, Free Energies, and Equilibrium Constants of Some Reactions Involving O₂, H₂, H₂O, C, CO, CO₂, and CH₄. *J. Res. NBS*, 1945, 34 143-61.

Waldron, R. D.; Cutler, A. H. Evaluation of Processing Options for Lunar Oxygen Production. *Proceedings of Space '92, ASCE, Denver, CO, June 1-4, 1992.*

Walker, P. L.; Rakszawski, J. F.; Imperial, G. R. Carbon Formation From Carbon Monoxide Over Iron Catalysts. II. Rates of Carbon Formation. *J. Phys. Chem.*, 1959, 63, 140-49.

Watanabe, K.; Tanimura, T.; Yoshii, Y. Study of Reduction in Systems of Wüstite, Silica, and a Third Oxide. *Hokkaido Daigaku Kogakuku Kenkyu Hokoku* 1968 48 45-54.

Yanagihara, T.; Kobayashi, T. The Reduction of Fayalite with Hydrogen. *Nippon Kinzoku Gakkai shi* 1969, 33 (3), 313-17.

Zhao, Y. Doctoral Diss., Dept. of Chemical Engineering, University of Arizona, Tucson, AZ., 1991.

Zhao, Y.; Shadman, F. Reduction of Ilmenite with Hydrogen. *Ind. Eng. Chem. Res.* 1991, 30, 2080-2087.

Zhao, Y.; Shadman, F. Kinetics and Mechanism of Ilmenite Reduction with Carbon Monoxide. *AIChE J.*, 1990, 36(9), 1433-38.

497585
N93-26677

**Innovative Techniques for The Production of Energetic Radicals for Lunar Processing
Including Cold Plasma Processing of Local Planetary Ores**

D. Bullard and D. C. Lynch

Department Of Materials Science and Engineering

The University of Arizona

S3-25
158350
p. 8

Abstract

Hydrogen reduction of ilmenite has been studied by a number of investigators as a potential means for recovery of oxygen from lunar soil. Interest in this process has always rested with the simplicity of the flow diagram and the utilization of established technology. Effective utilization of hydrogen in the reduction process at temperatures of 1200 °C and below has always been disappointing and, as such, has led other investigators to focus attention on other systems.

Effective utilization of hydrogen in the reduction of ilmenite can be significantly enhanced in the presence of a non-equilibrium hydrogen plasma. Ilmenite at solid specimen temperatures of 600 °C to 970 °C were reacted in a hydrogen plasma. Those experiments revealed that hydrogen utilization can be significantly enhanced. At a specimen temperature of 850 °C the fraction of H₂ reacted was 24% compared to the 7% theoretical limit calculated with thermodynamic theory for the same temperature.

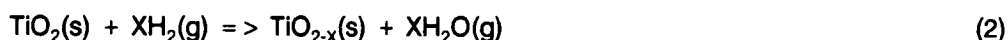
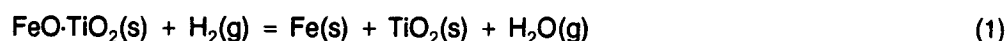
An added advantage for a hydrogen plasma involves further reduction of TiO₂. Reduction of the iron oxide in ilmenite yields TiO₂ and metallic iron as by products. Titanium forms a number of oxides including TiO, Ti₂O₃, Ti₃O₅ and the Magneli oxides (Ti₄O₇ to Ti₅₀O₉₉). In conventional processing of ilmenite with hydrogen it is possible to reduce TiO₂ to Ti₇O₁₃ within approximately an hour, but with poor utilization of hydrogen on the order of one mole of H₂ per thousand. In the cold or non-equilibrium plasma TiO₂ can be rapidly reduced to Ti₂O₃ with hydrogen utilization exceeding 10%. Based on design considerations of the plasma reactor greater utilization of the hydrogen in the reduction of TiO₂ is possible.

Introduction

The most attractive source of lunar oxygen from energy considerations is that associated with iron in the mineral ilmenite, FeO-TiO₂. Investigators in their efforts to recover that oxygen, have primarily focused their attention on H₂, CO, and C reduction of the mineral. Carbon is a highly effective reducing agent. However, processes based on solid carbon are more complex than those involving H₂ and CO. While processes based on H₂ and CO are simpler, the thermodynamic equilibrium limits effective use of those reducing agents.

That limit, however, can be surpassed with the aid of electromagnetic energy in the form of a non-equilibrium plasma. It is not that the restrictions of thermodynamics are violated, but that the system be viewed as consisting of separate parts whose thermodynamic parameters can be adjusted separately. In a plasma-solid reactor there are atoms bound in the solid reactant, gaseous molecules, and free electrons all of which can have different temperatures. Electrons accelerated by a high frequency electro-magnetic field have temperatures between 10,000 to 40,000 K. Charged molecules, because of their mass, cannot respond to the applied high frequency radiation. In addition, physical procedures for transferring energy between free electrons and molecules in a cold plasma are inefficient. As a result, the cold plasma consists of high temperature electrons and molecules (including positive ions) at temperatures only a few hundred degrees above ambient temperature.

Reaction Chemistry -- In conventional heating reduction of ilmenite involves the reactions,



condensation and then electrolysis of the H₂O for release of the oxygen and recycle of the hydrogen as shown in *Figure 1*. The thermodynamic equilibrium for reaction 1 is represented graphically in *Figure 2*, where it can be seen that at 500°C the fraction of hydrogen that can be reacted amounts less than 1%. That percentage grows to only 15% at 1200 °C. In conventional processing the practical value of X that can be achieved in reaction 2 is 0.15.

In a non-equilibrium plasma both diatomic and monatomic hydrogen are available for reaction. The latter is formed as a result of inelastic collisions between H₂ and energetic electrons and positive

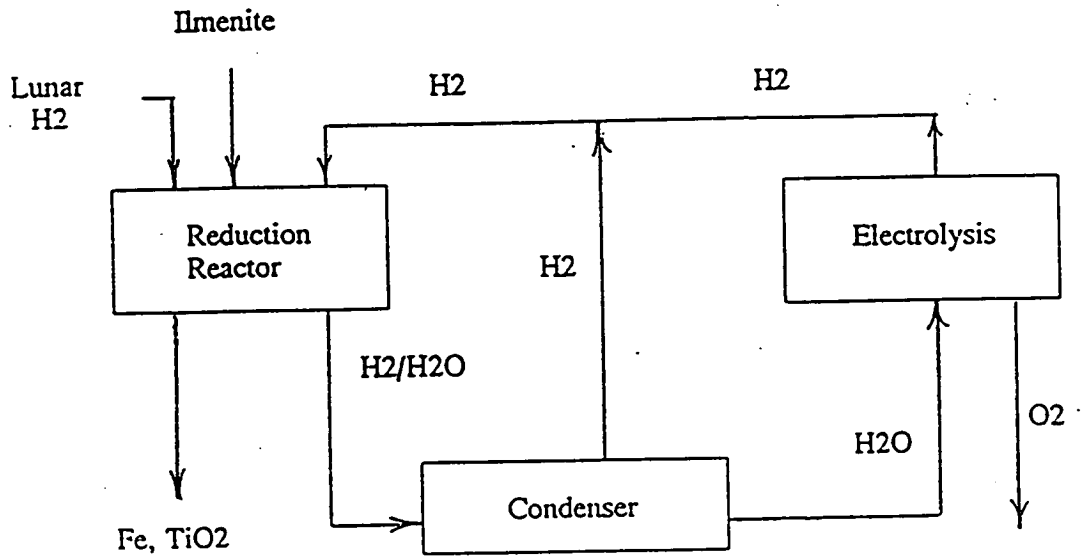


Figure 1. Schematic Design of System for Recovery of Oxygen From Lunar Regolith Using Hydrogen Reduction

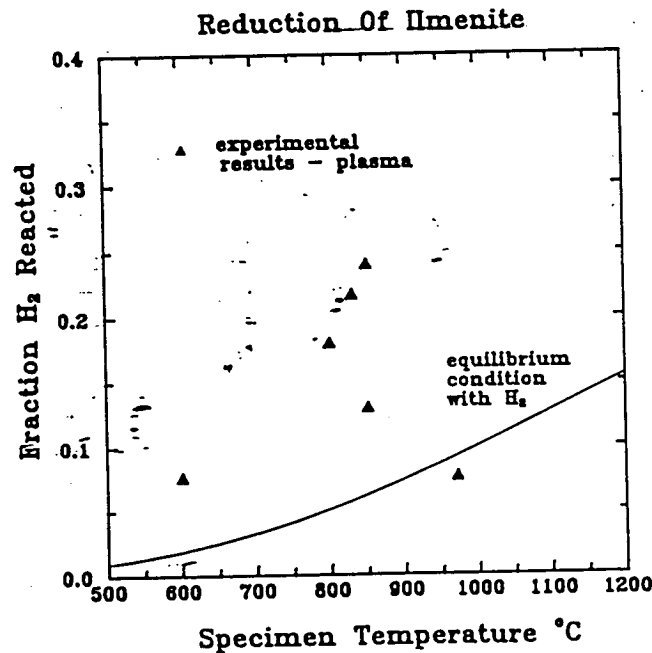
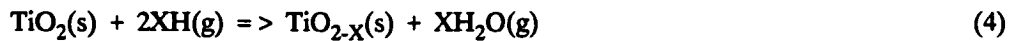
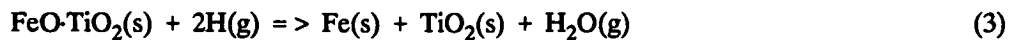
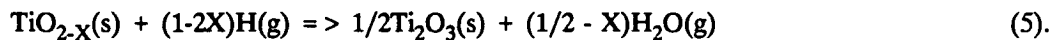


Figure 2. Representation of the thermodynamic equilibrium for both the thermal and plasma processing of ilmenite. Thermal processing makes use of only a fraction of the hydrogen present, while plasma processing theoretically allows nearly 100 percent of the hydrogen available for reaction. The actual experimental results achieved with the plasma are indicated.

ions. The latter are accelerated through the Debye sheath that surrounds the ilmenite particles. Reduction of ilmenite in a plasma follows the following sequence of reactions:



and



Reactions 1 and 2 also occur as a result of sample heating. An additional 30% of oxygen can be recovered with the plasma in comparison to that achieved with conventional heating. Moreover it can be recovered in a substantially shorter period.

Experimental

The effectiveness of a cold plasma for reducing ilmenite and TiO_2 has been tested in the apparatus shown in *Figure 3*. That apparatus consists of a microwave generator which emits microwaves at 2.45 GHz along a waveguide to the applicator where solid specimens are reacted in a hydrogen plasma. A specimen is rotated during an experiment to ensure even heating. A mass spectrometer has been used to follow the rate at which water vapor is evolved, and to quantify results. X-ray diffraction (XRD) analysis was used to both identify solid products and quantify the extent of their formation.

Ilmenite reacted in a hydrogen plasma yielded improved efficiency in hydrogen utilization. As noted earlier, the extent of reaction 1 is thermodynamically limited. That is not the situation with reaction 3. The high chemical potential of monatomic hydrogen pushes reaction 3 to the right, the theoretical limit being near complete consumption of the hydrogen, as shown in *Figure 2*. Ilmenite reacted at a specimen temperature of 850 °C yielded hydrogen consumption rates of 13 to 24%. That value is substantially better than the 6% predicted in *Figure 2* for conventional heating at 850 °C. The enhanced utilization has been achieved even though the reactor is not specifically designed for extensive interaction between the specimen and the plasma. Utilization of a fluidized bed reactor should improve plasma-solid contact.

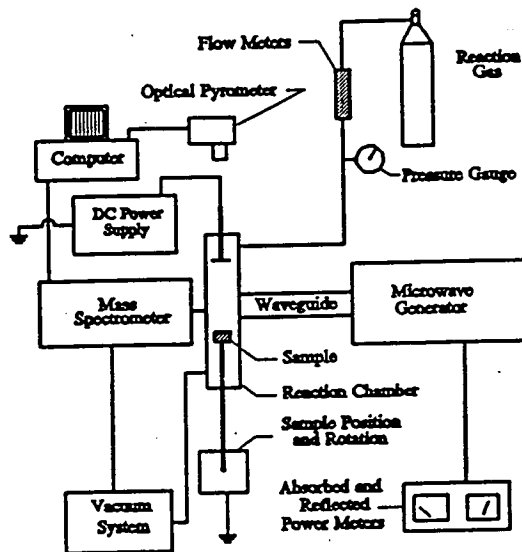


Figure 3. Schematic of the plasma processing system. The sample holder can be directly inserted into the XRD for analysis of the solid product layer.

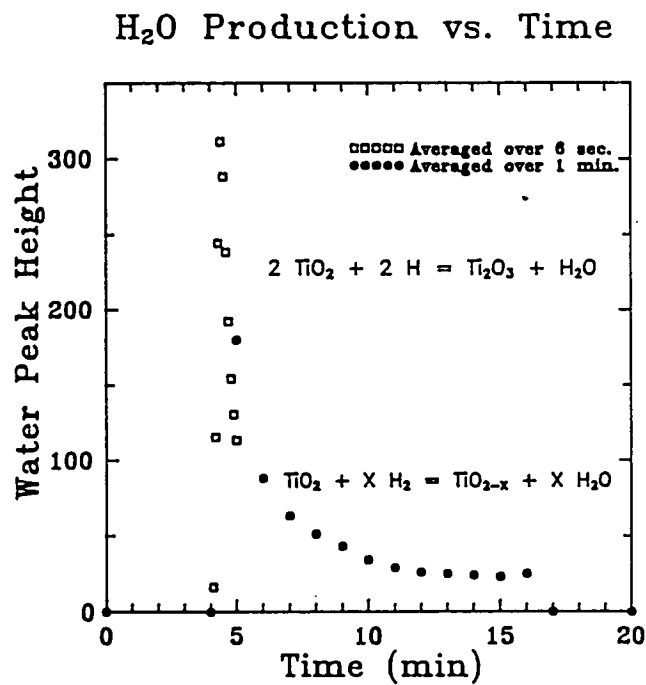


Figure 4. A plot of the H₂O signal from the mass spectrometer as a function of reaction time. This signal is characteristic of a surface reaction.

Plasma-solid contact has to do with the Debye sheath than actual physical contact between the ilmenite and the plasma. Non-conducting particles and insulated particles in a high frequency plasma become negatively charged due to the mobility of the electrons. The electrons responding to the field are accelerated quickly as a result of their small mass. Some of those electrons will impact solid particles and since they are more mobile than the positive ions a negative charge builds up on the surface of the particle. The resulting potential difference between the particle and the plasma is referred to as the Debye sheath. Positive ions that enter the sheath due to random thermal motion are accelerated toward the particle surface where they can break bonds and thereby enhance reaction rates.

Achieving the appropriate conditions across the Debye sheath is not always reproducible. The wide variation in the fraction of hydrogen reacted at 850 °C and the low value at 970 °C is attributed to this condition. The fraction of hydrogen reacted at 970 °C is slightly less than the equilibrium condition for that temperature. It is suspected at that temperature that the low fraction of hydrogen reacted is associated with improper conditions at the sheath and thus the impact of the plasma is not experienced.

Experimentally it has been determined that the presence of a ground in the system has a significant impact on the Debye sheath and the acceleration of ions across the sheath. The extent of the impact of the ground has been demonstrated with the reduction of TiO_2 . Selection of that compound is based on the fact that ilmenite can be reduced with both H_2 and H , whereas TiO_2 is only reduced in significant amounts with monatomic hydrogen. Use of TiO_2 allows us to evaluate the role plasma variables (pressure, power absorption, "etc.) have on the Debye sheath and the reduction process.

Figure 4 indicates that water vapor is evolved instantaneously with ignition of the plasma. Evolution of water peaks within the first minute of reaction, and then decreases to a steady state value after approximately 8 minutes. At the peak the mole fraction of water is on the order of 10 mole percent. At the same time the surface of the specimen changes from white (TiO_2) to black. The black product extends to a depth of 1 mm and is characteristic of both Ti_2O_3 and TiO_{2-x} .

XRD analysis of the solid product revealed it to be principally Ti_2O_3 with some residual TiO_2 . The spectra for both of these phases showed excellent agreement with the standard spectra. Quantitative XRD analysis revealed that up to 60% of the specimen surface, to a depth of 5 mm, was converted to Ti_2O_3 , as shown in *Figure 4*. Notice that in that figure the volume fraction of Ti_2O_3 remains constant with time. That information, coupled with the results in *Figure 4*, suggest that the

conversion of TiO_2 to Ti_2O_3 is complete after 8 minutes. According to reaction 2, the weight fraction of TiO_2 continues to decrease with time due to the continued production of TiO_{2-x} . The sum of the volume fractions in *Figure 5* do not add up to one at any specific time because experimental evidence indicates that TiO_{2-x} is amorphous.

A plasma and solid must have contact in order for a plasma-solid reaction to take place. Confinement of the black product layer to the surface in contact with the plasma strongly suggests that effective use of the plasma will require design of a reactor that has greater spacing between particles. A plasma cannot form or be maintained in the interstices of a powdered specimen if particles are too close because the sheaths overlap. A fluidized bed reactor is under construction to overcome this problem.

Energy Considerations

Energy, and in particular electrical energy, will be limited on the Moon and must be used effectively. A microwave-induced plasma is energy efficient. Energy in the form of electromagnetic radiation must be continuously applied to maintain the plasma. The efficiency of converting DC current to microwaves is reported as high as 90.4% at optimum conditions and 84% for extended periods. The plasma is highly efficient in the absorption of microwaves, with efficiencies approaching 100%. The extent to which the energy in the plasma can be utilized in chemical reaction is still under investigation.

Concluding Remarks

Processing of lunar regolith with a plasma offers more than just an increase in the amount of oxygen recovered per mass of soil. It offers a chemistry that can be used with both refractory and easily reduced oxides. In the case of the former the reduction process involves oxides that can be reduced to suboxides, such as TiO_2 , Al_2O_3 , and SiO_2 . As a result, it may be possible to use the regolith without beneficiation.

Another advantage of cold plasma processing is that the only consumable resource is the electricity used to maintain the plasma. As the reactant, hydrogen can be recovered by electrolysis and any losses can be made up with lunar hydrogen.

An additional advantage of cold plasma processing involves reactor life and safety issues. Enhanced

reaction rates at reduced temperatures reduces thermal degradation of the containment vessel. An applied magnetic field to contain the plasma can eliminate chemical attack of the vessel by ions and radicals. In an emergency, the reduction process can be brought to a halt with the extinguishing of the plasma by eliminating electrical power, or either reducing or increasing the pressure.

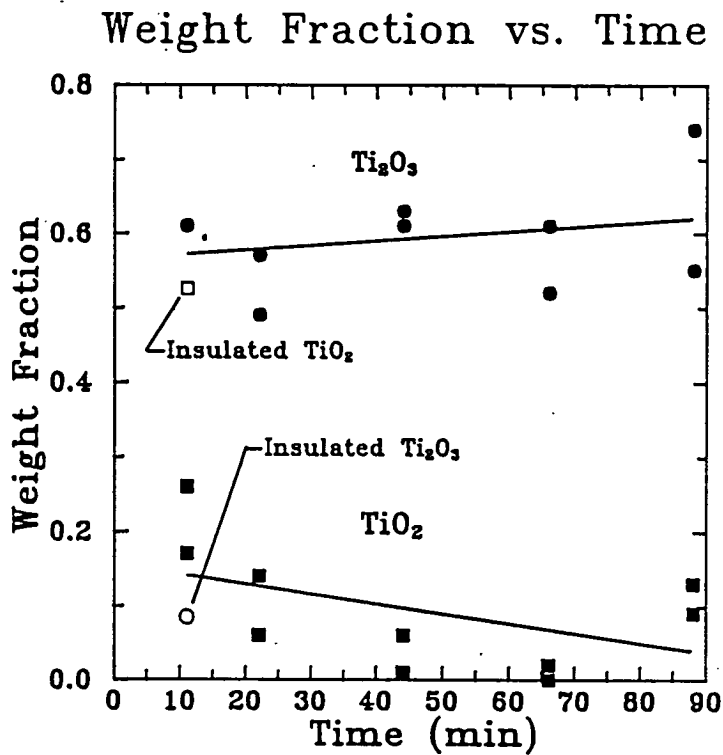


Figure 5. The production of Ti_2O_3 appears to be over after 8 minutes of reaction, while depletion of TiO_2 continues for longer periods. The data points labeled "Insulated" indicate the importance of a ground in the system in order the reaction to proceed.

497586

N 93 = 26678
34-25

Oxygen and Iron Production by Electrolytic Smelting of Lunar Soil

158351

R. O. Colson and L. A. Haskin

P- 22

Department of Earth and Planetary Science and McDonnell Center for the Space Sciences

Washington University

Abstract

Our work of the past year has involved two aspects: 1) electrolysis experiments on a larger scale than we had done before and 2) collaboration with Carbotek Inc. on design for a lunar magma electrolysis cell. These are discussed more in the paragraphs below.

We have demonstrated previously that oxygen can be produced by direct electrolysis of silicate melts (Lindstrom and Haskin, 1979; Haskin et al., 1986). Previous experiments using 50-100mg of melt have succeeded in measuring melt resistivities, oxygen production efficiencies, and have identified the character of metal products (Colson and Haskin, 1990; Colson, 1990; Haskin et al., 1992). We have now completed a series of experiments using 1-8 grams of silicate melt, done in alumina and spinel containers sufficiently large that surface tension effects between the melt and the wall are expected to have minor effect on the behavior of the melt in the region of the electrodes. The purpose of these experiments was to demonstrate the durability of the electrode and container materials, demonstrate the energy efficiency of the electrolysis process, further characterize the nature of the expected metal and spinel products, measure the efficiency of oxygen production and compare to that predicted on the basis of the smaller-scale experiments, and identify any unexpected benefits or problems of the process. Four experimental designs were employed, illustrated in *Figures 1, 2, and 3*, with a fourth design being analogous to *Figure 2* but using spinel rather than alumina tubes. Detailed results of these experiments are given in the appendix ("Summary of scaling-up experiments"); a general report of the results is given below in terms of implications of the experiments on container materials, cathode materials, anode materials, bubble formation and frothing of the melt, cell potential, anode-cathode distance, oxygen efficiency, and energy efficiency.

Our collaboration with Carbotek Inc. included providing advice and expertise on ceramic, metal, and silicate melt behavior during electrolysis as pertains to the SBIR Phase I design of a magma electrolysis cell. This collaboration was interactive, involving several extended discussions over the phone and in person in which we provided information about relevant properties of silicate melts and offered extensive suggestions about the design of the cell, both in terms of what can be expected to work based on our experimental experience and what monitoring capabilities should be built into the experiments to allow results to be adequately understood. We also contributed suggestions for experimental measurements, procedures, and post-experimental analyses for their proposed Phase II experimental work.

Container material:

We continue to use spinel containers successfully in experiments, with no indication of chemical corrosion of the containers. However, some spinel containers contain sufficient porosity (as much as 30%) and permeability that silicate melt substantially invades the spinel wall leading to a loss of silicate from our experiments and weakened container walls. The most porous spinels appear to have substantially poorer strength characteristics as well and tend to break under the weight of the assembly itself (e.g. experiments Elec2R, Elec2T). We note that containers made of denser spinel show no indication of invasion by the silicate melt or of breaking during experiments. Thus, high-density spinel must be used for the electrolysis cell.

We also did several experiments (Elec2L-Elec2O) in higher-density alumina containers. These containers showed better strength characteristics than the high-porosity spinel and were not invaded by melt. However, the reactions Al_2O_3 (container) \rightarrow Al_2O_3 (melt) and Al_2O_3 (container) + MgO (melt) \rightarrow MgAl_2O_4 (spinel) (coating the inner container wall), sharply increased viscosity of the melt and decreased conductivity. Loss of Al_2O_3 from the wall would eventually corrode the wall as well. Thus, if alumina is found to have better strength properties than even the low-porosity spinel, it can only be used as a container if it is coated with spinel on the face contacting the melt.

Cathode design:

An attempt was made in experiments Elec2E-Elec2K (see *Figure 1*) to effect a solid wire connection to the molten metal cathode (Fe-Si) through a small hole in the spinel container. This failed because the connecting wire quickly melted and the connection was lost (because surface tension effects prevented the molten metal from making a connection through the small hole in the ceramic). We achieved a workable connection to the cathode in experiments Elec2L-Elec2T (see

Figure 2) by extending the metal cathode (we used steel) to regions of the furnace sufficiently cool that the metal does not melt. Connection to a Pt lead wire was made in this cooler region. We believe that in a scaled-up cell the connection to the Fe-Si molten pool will have to be made by some Fe-Si alloy which is cooled to keep it solid. In the highest-T parts of this lead, the molten Fe-Si alloy making up the anode pool will contact a solid metal Fe-Si alloy consisting of about 50 mole% Si (e.g. Lyman, 1973). As the lead continues to cooler regions, an Iron lead may be desirable to improve conductivity (which is decreased sharply by Si); and ultimately to an even higher-conductivity material at the lowest temperatures where little diffusion occurs.

We found that the molten Fe-Si cathode pool beads strongly in spinel or alumina containers (e.g. see *Figure 4*). This beading is a serious problem in our small experiments where the tendency to bead is on a larger scale than our experiments. This beading is alleviated somewhat when the metal pool rests on a solid metal base, as in Elec2L-Elec2T (*Figure 2*), and may be less of a problem in larger-scale cells. Nevertheless, the constraint that cathode-anode distance be small (0.5-2cm, Colson and Haskin, 1990, Haskin et al., 1992) means that the effect of beading of the metal pool must be watched when demonstration-scale experiments are done.

Anode material:

We continue to use Pt anodes successfully. It might also be possible to use other conductors (e.g. Mo) plated with Pt to protect the metal from the corrosive melt. Although we have not tested these, such configurations have been suggested for use at oxygen-generating electrodes (Harris et al., 1985; McCullough and Mariz, 1990). We observe two events to cause the deterioration of the Pt anodes. The first is oxidation of the Pt when it remains in contact with an oxygen bubble rather than the silicate melt. This occurs when the oxygen produced at the anode fails to escape upward as fast as it is produced. Solutions to this problem are discussed below in the section labeled "Bubble formation and frothing in the melt". Because it is impossible to keep the Pt completely free of oxygen (since the oxygen is being produced there), some oxidation of the Pt is inevitable. We have reported previously (Colson and Haskin, 1992) that the Pt anode appears to be stabilized dynamically by being continuously oxidized and reduced. Whether this oxidation-reduction process destroys the anode over long periods of time remains to be seen. The second cause of Pt anode deterioration is mixing of cathodic metal to the anode, causing it to melt, lose its shape, and incorporate silicate melt (as seen in *Figure 5*). This latter cause of deterioration also greatly decreases the efficiency of oxygen production. Solutions to this problem are discussed below in the sections "Anode-cathode distance" and "Cell potential".

Bubble formation and frothing of the melt:

As we have reported previously (Colson and Haskin, 1992), frothing of the melt is one of the primary causes of energy inefficiency. We identify two causes of frothing: 1) failure of oxygen formed at the anode to escape and 2) formation of Mg gas at the cathode. The latter of these is discussed below in the section "Cell potential". The former depends on the composition of the silicate melt in the cell, the current density of the cell, and the design and orientation of the anode. We have reported previously that SiO₂ and Al₂O₃ concentrations in the melt must be kept low (Colson and Haskin, 1992). This observation is confirmed in these experiments in which high Al₂O₃ experiments (run in alumina containers) resulted in runaway frothing at current densities corresponding to $<0.05\text{A}/\text{cm}^2$ cross-sectional area of the container, whereas low Al₂O₃ experiments (run in spinel containers) did not have runaway frothing at least to $0.2\text{A}/\text{cm}^2$. In addition, cell resistance in the low Al₂O₃ experiments was comparable to that in the high Al₂O₃ experiments even though the current density in the low Al₂O₃ experiments was 4-times higher and the anode-cathode distance was 3 times greater (1.5cm in the low Al₂O₃ experiments, 0.5cm in the high Al₂O₃ experiments). These differences can be seen by comparing experiments Elec2L-O to Elec2R-T in the appendix.

Of equal importance, but somewhat harder to quantify, is the design of the anode. Depending on subtle differences in the shape and orientation of the anode, we have observed several different frothing behaviors: 1) low resistance (few bubbles adhering to the anode) at low current density, with cell resistance increasing to very high values once some threshold current density is reached. We believe this is caused by frothing, i.e. formation of bubbles that do not coalesce or escape from the melt. 2) A cyclic variation in resistance, with a gradual increase in resistance up to a threshold value at which a very rapid increase in resistance to very high values is followed by a rapid decrease to the low value of the cycle. We believe this is caused by the gradual growth of one bubble (or a few) caught underneath the anode which eventually escapes once it reaches sufficient size. 3) A relatively stable cell resistance which is much higher than melt conductivity would suggest it should be. We believe this is caused by a "steady state" number of bubbles clinging to the Pt anode or "perched" bubbles as was observed in Elec2M (shown schematically in *Figure 6*).

The relative severity of these problems depends on fairly subtle differences in the anode configuration. However, some consistent dependencies on the design can be extracted. *Figure 7* illustrates various anode designs and resultant cell resistances. A general observation is that fewer, larger gaps in the anode are better than more, smaller gaps. In fact, higher currents can often be

achieved by smaller anodes because of the resulting greater space for bubbles to escape. Thus, in this report we use current density relative to the cross-sectional area of the container rather than relative to the anode surface area itself.

Cell potential:

Constraints on cell potential include 1) current density constraints discussed above 2) lower-potential limit set by the need to reduce Si as well as Fe, and 3) upper-potential limit set by the need to avoid producing Mg gas.

Current density in general should be maximized, within the constraints of potential discussed below, by maintaining the melt composition at low SiO₂ + Al₂O₃ concentrations and optimizing the design of the anode so that bubble formation and frothing do not greatly increase cell resistance as current density increases. Because reaction kinetics are fairly fast (Haskin et al. 1992), current density is limited primarily by the rate at which reduction components are transported to the electrodes. Thus, keeping "fresh" silicate mixed to the electrodes is important. We observe strong compositional gradients in the silicate melts of our experiments, consistent with minor depletion of FeO and SiO₂ in the vicinity of the cathode. However, because SiO₂ and FeO are major constituents of the melt, sufficient FeO + SiO₂ always remains available for reduction. In the worst case of our experiments (Elec2N, in which the potential was sufficiently high to reduce nearly all constituents of the melt), FeO is completely depleted in the vicinity of the cathode, and SiO₂ concentration is decreased but still comprises nearly 37% of the total melt near the cathode. Although this decrease in concentration results in a slight increase in the potential required to reduce SiO₂, the effect of this depletion on energy efficiency is insignificant relative to other effects.

Si must be reduced as well as Fe, otherwise solid Fe dendrites form (at T below the Fe melting point only) that eventually short the cell. The potential needed to reduce Si in addition to Fe is about 1.4-1.5 volts in excess of the IR potential (in air). Iron dendrites formed in experiment Elec2O, run at about 1.33 volts in excess of IR potential, are shown in *Figure 8*. These dendrites form complex "bubble-like" patterns in the silicate melt, with the interiors of the bubbles reduced relative the exteriors. Some of these "Fe bubbles" are void after the experiment, suggesting they were filled by some gas during the electrolysis. We do not know the identity of this gas and offer no explanation for why the bubble interiors are reduced relative to the exteriors.

If the potential becomes sufficiently large (about 1.8 volts in excess of IR potential in air) Mg gas

is produced. This gas rises through the melt reacting to form MgO and Fe+Si. The Fe+Si so formed exists as very small beads (~1micrometer and less) that remain in suspension in the melt and mix to the anode, decreasing efficiency and destroying the anode if in sufficient quantity. In addition, although the gas reacts away before it has risen more than a few millimeters through the melt, it creates a bubble horizon between the anode and cathode that greatly increases cell resistance. For these reasons, potential should be maintained such that Mg gas is not produced in significant amounts. *Figure 5* illustrates the distribution of Mg bubbles in Elec2N, run at 1.8 volts in excess of IR potential.

Anode-cathode distance:

We have reported previously (Haskin and Colson, 1992) that anode-cathode distances on the order of 0.5-1 cm are desirable in order to minimize cell resistance and thus energy lost to resistive heating. However, such small distances may be physically difficult to achieve in a large cell. We have now identified additional reasons to maintain a larger anode-cathode distance. In our experiments, the interface between the metal and melt is sufficiently turbulent that Fe-Si metal beads, whose density differs very little from that of the melt, can become suspended in the melt (see *Figure 5*). These metal beads can get mixed to the anode, causing both deterioration of the anode and a large decrease in oxygen production efficiency when Fe and Si, rather than oxygen, are oxidized at the anode. We have not observed this to occur where the cathode-anode distance is > 1cm.

We have done electrolysis experiments with anode-cathode distances in the 1.5-2cm range. Cell resistance is still sufficiently low that high energy efficiency is attained, as discussed below in the section "Energy efficiency".

A second cause of mixing of metal to the anode is related to very small (~1micrometer) metal beads suspended in the melt. These have also only been observed <1cm from the cathode, but because of their small size could presumably be mixed throughout the melt. We believe these are formed by Mg gas (see "cell potential" above) and so can be largely avoided.

Oxygen efficiency:

We have predicted previously how oxygen production efficiency should vary as a function of concentration of divalent iron in the melt. For our experiments, these efficiencies should be between about 65 and 85 % (FeO is about 2-3% of silicate melt). For two experiments, observed efficiencies

(as estimated by metal produced) are much lower than predicted, being in the range of 11-16%. Metal produced was estimated by both petrographic/analytical estimates and by mass-balance calculations based on initial and final melt compositions. In the two experiments with lower-than-predicted efficiencies, metal was mixed to the anode either due to dendrite formation at too low potentials (Elec2O) or formation of small metal beads by Mg gas at too high potentials (Elec2N). We believe that the difference in predicted versus observed efficiencies in these experiments is due primarily to mixing of cathodic metal to the anode. This interpretation is supported by the results of Elec2P, in which oxygen production was measured continuously by a Y-stabilized zirconia electrolyte sensor during electrolysis too short to allow much mixing of cathodic metal to the anode. Measured efficiency for this experiment is 50-60% as shown in *Figure 9*. Expected efficiency is about 70%. In an experiment at intermediate potentials (Elec2M), oxygen production was estimated based on oxidation of a Ni wire above the cell and oxidation of divalent Fe in the melt above the anode. In this experiment, oxygen production + oxidized iron matched closely that expected, suggesting that metal mixing to the anode was an insignificant problem at the intermediate potentials.

We conclude that efficiencies will approach those we have predicted previously if mixing of cathodic metal to the anode is minimized by increasing anode-cathode distances and if cell potentials are maintained in the range where both Fe and Si are produced, but Mg gas is not produced.

Energy efficiency:

As shown in the appendix, energy efficiency for electrolysis is quite high for the cases in which mixing of cathodic metal to the anode is insignificant. For example, in Elec2T, with a spinel container and a low-SiO₂, Al₂O₃ melt, potential in the range where Fe and Si but not Mg gas are produced, cathode-anode distance of about 1.5cm, and current density of 0.22A/cm² (cross-sectional area of container), energy used is only about 3.4 times the theoretical energy to reduce SiO₂.

References

- Colson, R. O. (1990) Characterization of metal products of silicate melt electrolysis. Lunar and Planetary Science XXI, Lunar and Planetary Institute, Houston, p 214-215.
- Colson R. O. and Haskin L. A. (1990) Lunar oxygen and metal for use in near-earth space: Magma electrolysis. In Engineering, Construction, and Operations in Space II, ASCE, NY, p 187-196.
- Colson R. O. and Haskin L. A. (1992) Producing oxygen by silicate melt electrolysis, In Resources

of Near-Earth Space (Ed. J. Lewis) Univ Ariz Press (in press).

Harris, J. H., Grassali R. K., Tenhover A. M., and Ward M. D. (1985) Electrolytic processes employing platinum based amorphous metal alloy oxygen anodes, Eur. Pat. Appl. EP 164,200.

Haskin L. A., Lindstrom D. J., Semkow K. W., and Lewis R. H. (1986) Lunar soil and rock as a source for propellant and constructional materials in space. McDonnell Center for the Space Sciences Report TEL-107, 29p.

Haskin L. A., Colson R. O., Lindstrom D. J., Lewis R. H., and Semkow K. W. (1992) Electrolytic smelting of lunar rocks for oxygen and iron. In Lunar bases and space activities of the 21st century, Lunar Planetary Inst, Houston (in press).

Haskin L. A. and Colson R. O. (1992) Steady state composition with low Fe²⁺ concentrations for efficient O₂ production by "magma" electrolysis of lunar soils. In Engineering, Construction, and Operations in Space III, ASCE, NY p. 651-665.

Lindstrom D. J. and Haskin L. A. (1979) Electrochemical preparations of useful material from ordinary silicate rocks. Proc. Princeton Conf. Space Manufact., AIAA, 3, p129-134.

Lyman T. (ed) (1973) Metals handbook 8th edition Vol. 8 Metallography, structures, and phase diagrams, Am Soc. Metals, Metals Park, Ohio, 466p.

Figure 1. Design for Elecss2E-Elecss2K.

Figure 2. Design for Elecss2L-Elecss2O. Experiments Elecss2P-Elecss2Q are analogous except spinel rather than alumina is used to contain the silicate melt.

Figure 3. Design for Elecss2P-Elecss2Q.

Figure 4. Beading of Fe-Si molten alloy in silicate melt.

Figure 6. Schematic diagram of Elecss2M, showing gas bubble perched below anode.

Figure 7.

Figure 5. Elecss2N, schematic diagram and backscattered electron image.

Figure 8. Elecss2O, cathode at bottom, anode is at top.

Figure 9. Measured oxygen production rate versus current in Elecss2P.

APPENDIX

Summary of "Scaling-up" Experiments

First Set: Elecss1-Elecss2

Set-up: Pt crucible, Pt wire anode, Ir wire cathode (both inserted from the top as straight wires),
T=1480-1490 | C, CO₂ atm., 1.9g of SS + 5.6% A12.

Example experiment: Elecss2

Experiment duration= 4min 44sec
Cell potential= 2.4 to 9.8 volts
Ean-Eca= 1.4 volts
current= 0.18 amps
amp-sec= 49.3 coulombs
current density= 4 amps/cm² (anode surface area)
expected efficiency= >85%
expected oxygen produced= 0.0035 grams
energy/energy to split SiO₂
if 100% efficiency= 8.5

Observations: Violent frothing of melt results in dramatic increase in cell resistance; where cathode touched Pt crucible the Pt melted, indicating presence of Si.

Second Set: Elecss3-Elecss6

Set-up: Spinel crucible, Pt wire anode, Ir wire cathode (both inserted from the top as straight wires, distance between electrodes ~0.4cm), T=1480 | C, CO₂ atm., 0.64g of SS + 5.6% A12.

Example experiment: Elecss6

Experiment duration= 30min 33sec
Cell potential= 2.3 volts
Ean-Eca= 1.45 volts

current = 0.023 amps
amp-sec = 41.6 coulombs
current density = 0.15 amps/cm² (anode surface area)
expected efficiency = >85%
expected oxygen produced = 0.0035 grams
energy/energy to split SiO₂
if 100% efficiency = 2.16

Observations: Frothing ~ doubled cell resistance; Fe+Si observed at cathode; Spinel crucible survived >2hrs in contact with melt with no signs of corrosion; Spinel precipitated at the cathode; Ir cathode deteriorated leaving a black cloud of submicron sized Ir particles in vicinity of cathode.

Third Set: Elec7-Elec17

Purpose: Study effect of anode configuration (e.g. straight wire vs coils of varying "tightness", Pt screen, moving anode up and down, anode at different depths in melt, etc.) on resistance increase caused by frothing.

Set-up: Spinel crucible, Pt wire anode, Pt wire coil cathode entering through a hole in the bottom of the crucible, electrodes ~ 0.5cm apart, T=1490 | C, CO₂ atm., ~0.5g of SS + 5.6% Al₂O₃.

Example experiment: Elec14

Experiment duration = 5min 43sec
Cell potential = 1.2-3.4 volts
E_{an}-E_{ca} = 0.8 volts
current = 0.04 amps
amp-sec = 13.7 coulombs
current density = 0.3 amps/cm² (1/2 anode surface area)
current density = 0.08 amps/cm² (crucible x-sectional area)
expected efficiency = >85%
expected oxygen produced = 0.00097 grams
energy/energy to split SiO₂
if 100% efficiency = 1.88
energy/energy to split FeO
if 100% efficiency = 3.36

Observations: Main variable affecting frothing is current density relative to cross sectional area of crucible, other variable of minimal effect. Resistance increases progressively and ultimately sample is lost from crucible due to frothing for all configurations and current densities (<0.015 to >0.3A/cm²).

Fourth Set: Elec2A-Elec2D

Set-up: Spinel crucible, Pt wire coil anode (0.02" dia), Pt wire coil cathode (0.04" dia) entering through a hole in the bottom of the crucible, electrodes ~ 0.5cm apart, T=1490 | C, CO₂ atm., ~1.29g of SS₂ + 4.8% Al₂O₃ (SS₂ is lower in SiO₂ and Al₂O₃ than SS).

Example experiment: Elec2D

Experiment duration = 37min 21sec
Cell potential = 0.92 volts
E_{an}-E_{ca} = 0.8 volts
current = 0.025 amps
amp-sec = 58.5 coulombs
current density = 0.2 amps/cm² (1/2 anode surface area)
current density = 0.06 amps/cm² (crucible x-sectional area)

expected efficiency= >85%
expected oxygen produced= 0.0041 grams
energy/energy to split SiO₂
if 100% efficiency= 0.87
energy/energy to split FeO
if 100% efficiency= 1.55

Observations: Frothing in this composition does not get out of hand if current density is < ~0.2A/cm², otherwise resistance increases rapidly until sample froths out of container. Gas appears to be generated at the cathode. Pt is mobile in cathode vapor bubbles. Anode is reacting (oxidizing?) during electrolysis but appears to not migrate far before Pt-oxides are reduced by the melt. Spinel crucible failed near the cathode, perhaps due to reaction with cathodic vapor.

Fifth Set: Elec2E-Elec2K

Set-up: Spinel crucible held in a steel container, molten (Zn,Ni), (Ni), or solid Pt cathode connection through a hole in the bottom of the crucible to the steel container, Pt wire coil anode inserted from the top, electrodes ~ 0.5cm apart, T=1440-1450 | C, Argon atm., ~0.4 to 1g of SS2 + 5-13% A12. General observations: Combination of failure (melting) of steel when in contact with the cathode product, solubility of Argon in metal product, vapor formed by degassing of steel, tendency of molten metal to bead, and tendency of molten metal to not make an electrical connection through a small hole in the bottom of the crucible make this configuration unsuited for the long-term electrolysis experiments and simulation of a "real" working cell for which it was intended. Metal has high surface energy with both silicate melt and spinel crucible; 0.7cm "cliffs" are possible (FeSS₂) suggesting that on the scale of 0.5cm (necessary electrode separation) this may be a problem.

Example experiment: Elec2I

Experiment duration= 27min 38sec
Cell potential= 1.25 volts
E_{an}-E_{ca}= 0.9 volts
current= 0.023 amps
amp-sec= 43 coulombs
current density= 0.065 amps/cm² (crucible x-sectional area)
expected efficiency= 68%
expected oxygen produced= 0.0024 grams
energy/energy to split SiO₂
if 100% efficiency= 1.47
energy/energy to split FeO
if 100% efficiency= 2.63

Observations: Connection between molten pool and steel container was not achieved, so current flow is through the narrow silicate melt "neck" drilled in the bottom of the crucible; molten metal appeared to "float" up from bottom of crucible and to bead strongly.

Sixth Set: Elec2La,b-Elec2O

Set-up: Experiment contained in an alumina tube (inside dia ~ 0.8-0.9cm); cathode is steel rod inside tube stabilized by T gradient (extends to cool parts of furnace ~1100-1200 | C); anode is Pt coil inserted from top of tube, T=1440 | C; Argon atm.; In Elec2L,N,O the glass is exposed to air and the steel rod to Argon; In Elec2M the glass is sealed from air and a package of Ni metal is suspended over the melt to "capture" escaping oxygen. 4-5.3g of SS2 + 10-13%A12 in L and M; ~2g SS2+10% A12 plus ~0.2g A12 added in increments in N and O.

Example experiment: Elec2Lb

Experiment duration= 28min 31sec
Cell potential= 2.77 volts
Ean-Eca= 1.45 volts
current= 0.094 amps
amp-sec= 167.7 coulombs
current density= 0.15 amps/cm2 (crucible x-sectional area)
current density= 0.22 amps/cm2 (1/2 Pt anode area)
expected efficiency= 69%
expected oxygen produced= 0.01 grams
energy/energy to split SiO2
if 100% efficiency= 3.21

Observations: Amount of metal produced ~ that expected on basis of current if all product is Fe; Frothing extended glass ~7cm (factor of 3 to 4) up alumina tube beyond where it was expected to extend. Both Si and Fe produced.

Note: design permits new feedstock to be introduced periodically from top of alumina tube, permits anode to be raised or lowered during the experiment, and an oxygen getter can be attached to top of alumina tube to measure oxygen production.

Example experiment: Elec2M

Experiment duration= 1hr 29min 18sec
Cell potential= 2.14 volts
Ean-Eca= 1.34 volts
current= 0.05 amps
amp-sec= 267.9 coulombs
current density= 0.085 amps/cm2 (crucible x-sectional area)
current density= 0.139 amps/cm2 (1/2 Pt anode area)
expected efficiency= 74%
expected oxygen produced= 0.016 grams
observed oxygen production:
Oxygen trapped in Ni above cell 0.0034g
Oxygen in Fe2O3 in glass (assuming all Fe above anode is oxidized) 0.0112g
energy/energy to split SiO2
if 100% efficiency= 2.31

Observations: No indication that alumina tube is failing; periodic (4 to 8 min) increase then rapid decrease in resistance due to accumulation of bubbles under anode; presence of bubbles generated near the cathode; Fe above anode was oxidized by oxygen produced suggesting that good efficiency requires a low percentage of total melt be above the anode. Metal produced is mostly Fe forming partially oxidized dendrites and plating the steel cathode. The Pt anode is oxidized where it contacts gas (O2) bubble but is not oxidized where it is in contact with melt.

Note: experiment is closed, products can be quantitatively accounted for.

Example experiment: Elec2N

Experiment duration= 8hrs 15min (2hrs 24min)
Cell potential= 1.3 - 15 V (2.6 V)
Ean-Eca= 1.2 - 2.3 V (1.8 V)
current= 0.034 - 0.095 A (0.034 A)
amp-sec= 1227 C (294 C)
current density (crucible x-sectional area)= 0.05-0.16 A/cm² (0.06)
current density (1/2 Pt anode area)= 0.1-0.3 A/cm² (0.104)
expected efficiency= 75%
calculated efficiency (from metal produced)= 16%
metal produced= calculated O₂
Si: 0.0108g 0.0123g
Fe: 0.0096g 0.00274g
Ti: 0.00088g 0.00059g
Mn: 0.00014g 0.00004g
Cr: 0.00028g 0.00013g
calculated oxygen produced= 0.0158 grams
energy/energy to split SiO₂ 17 (12)
energy/energy to split SiO₂
if 100% efficiency= 2.6 (1.8)

(Values in parentheses are for the last 2.5 hrs of electrolysis where cell resistance was lowest because of anode design and current density.)

Observations: Substantial Al₂O₃ dissolves into the melt from the container, increasing viscosity and resistivity and causing spinel to precipitate on the cell wall. Efficiency << expected because of mixing of metal to the anode, observed in periodic decrease in Ean-Eca (as metal mixed to the anode is reoxidized), deterioration of the anode (causing it to melt and mix with silicate melt), observed suspended metal particles, and mass balance calculations indicating that SiO₂ and FeO are increased in concentration near the anode. Bubbles at bottom of cell may be Mg (g) (potential is sufficiently high). This Mg would quickly back-react with the melt reducing Fe etc. and, in fact, there is a distinct boundary at the line of bubbles (Fe-poor below line). These bubbles increase cell resistance and mix metal to the anode and may also cause the formation of submicron-sized metal particles (seen in sample in vicinity of bubble line) that remain in suspension and eventually mix to the anode. Thus, the upper potential limit may be where Mg (g) begins to form. Periodic addition of feedstock during the experiment results in periodic decrease in cell resistance, apparently due to "clearing" of bubbles from the anode; there is no concurrent decrease in the potential required to get a given current. "Stirring the melt by moving the anode up and down does not decrease resistance and in some cases increases it. In addition, stirring mixes more metal to the anode causing reduced efficiency (as evidenced by change in cell potential at constant current). The effect of anode design is discussed after expt Elec2O.

Note: Compositional maps of the quenched sample combined with periodic sampling of the melt during the experiment combine to permit mass-balance calculations to be made of products (spinel, melt, residual melt) and the amount of Al₂O₃ added from the cell wall. Metal composition was also determined by direct microprobe analyses and amount was estimated from diffusion profiles in the cathode and point-counting of metal suspended in melt.

Example experiment: Elec20

Experiment duration= 5hrs 50min
Cell potential= 1.5 - 3.1 V (2 V)
Ean-Eca= 1.28 - 1.48 V (1.33 V)
current= 0.034 A
amp-sec= 722 C
current density (crucible x-sectional area)= 0.057 A/cm²
current density (1/2 Pt anode area)= 0.104 A/cm²
expected efficiency= 80%
calculated efficiency (from Fe produced)= 11%
metal produced= calculated O₂
Fe: 0.0232g 0.00663g
calculated oxygen produced= 0.00663 grams
energy/energy to split FeO 12.3
energy/energy to split FeO
if 100% efficiency= 1.7

(Values in parentheses are mean values for experiment)

Observations: Substantial Al₂O₃ dissolves into the melt from the container, increasing viscosity and resistivity and causing spinel to precipitate on the cell wall. Efficiency << expected because of mixing of metal to the anode causing a decrease in Ean-Eca to ~0.1-0.4V lasting ~15 min in one case as the metal oxidizes. This amount of metal-cycling (that observed to occur in a few distinct events) cannot account for all the decrease in efficiency, and it is likely there is also a continuous feed of metal to the anode. Stirring by moving the anode up and down appears to exacerbate this problem. Adding new Al₂O₃ does not appear to clear bubbles from the anode as it did in Elec2N, although the bubble problem is less significant than in that experiment. Progressive increase in cell resistance is likely due Al₂O₃ dissolution into the melt. The cell shorted when Fe dendrites connected electrodes. Product metal was Fe (solid), as expected from Ean-Eca potential. These dendrites formed "bubbles" filled by either glass or gas of unknown origin. The glass on the interiors of the "bubbles" appears more reduced than on the exterior, as in A12-1cg.

Note: Fe metal produced was calculated by mass balance.

Anode design effects (from Elec2N unless noted, ~same anode surface area unless noted, first value is cell resistance in ohms 10 minutes after start of electrolysis at 0.049A, second value where given is a 'steady state' cell resistance at 0.049A, the third value where given is the 'steady state' cell resistance at 0.034A). Summary: fewer large spaces are better than more small spaces in anode.

92.4 >92.4 42

69.8 80 <70
(SA ~25% more than others)

60.2 68 >45

38 68 21

18 >18 22
from Elec20

Seventh Set: Elec2P-Elec2Q

Set-up: Experiment contained in an spinel tube (inside dia ~ 1.6cm) couched inside an alumina crucible; cathode is a steel rod inside the crucible and bottom part of the spinel; anode is Pt coil inserted from above, $T=1440\text{ }^{\circ}\text{C}$; Argon atm.; Oxygen produced is measured continuously by a yttria-stabilized zirconia electrolyte oxygen sensor inside the furnace a few inches below the experiment. 8.9 grams glass is 10% A12, 90% "steady state".

Example experiment: Elec2P

Experiment duration= 5 min
Cell potential= 4 volts
Ean-Eca= 1.46 volts
current= 0.25 amps
current density= 0.12 amps/cm² (crucible x-sectional area)
current density= 0.24 amps/cm² (1/2 Pt anode area)
expected efficiency= 67%
measured efficiency= 63%
energy/energy to split SiO₂
if 100% efficiency= 4.1

Observations: Oxygen produced varies with current as expected (see Fig.??). Short duration of experiment due to failure of the alumina crucible along fractures formed during a previous heating and quenching cycle.

Eighth Set: Elec2R-Elec2T

Set-up: analogous to Sixth Set except used spinel rather than alumina tubes and electrodes ~1.5cm apart rather than ~ 0.5cm apart. Cell is exposed to air. 4-8 grams glass added is 12% A12, 88% "steady state".

Example experiment: Elec2R

Experiment duration= 30min (ran longer)
Cell potential= 3.4 (1.5-5.5) volts
Ean-Eca= ~1.2 volts
current= 0.06 (0.056-0.072) amps
current density= 0.11 amps/cm² (crucible x-sectional area)
current density= 0.17 amps/cm² (1/2 Pt anode area)
expected efficiency= 75%
energy/energy to split SiO₂
if 100% efficiency= 3.0

Observations: Substantial melt (more than half) goes into porous spinel, porous spinel is structurally weak, need denser spinel. Periodic gradual increase in resistance up to 74 ohms or so followed by rapid decrease to 13 ohms or so (resistances are avgs over 27 seconds), presumably as a bubble grows between the anode and cathode, then escapes. (The anode ring was attached to the lead such that Pt wires partially blocked the space in the center of the ring, possibly explaining difficulty for bubbles to escape).

Example experiment: Elec2T

Experiment duration= 12 min (ran longer)
Cell potential= 3.8 volts
Ean-Eca= 1.42 volts
current= 0.116 amps

current density= 0.2 amps/cm² (crucible x-sectional area)
current density= 0.2 amps/cm² (1/2 Pt anode area)
expected efficiency= 75%
energy/energy to split SiO₂
if 100% efficiency=n 3.4

Observations: Porous spinel is structurally weak, need denser spinel. No indication of significant frothing up to maximum applied current density (0.2A/cm²).

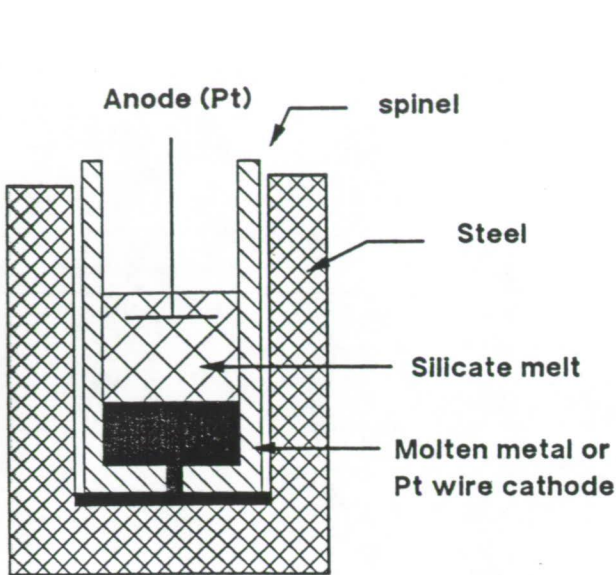


Fig. 1 Design for Elec2E-Elec2K.

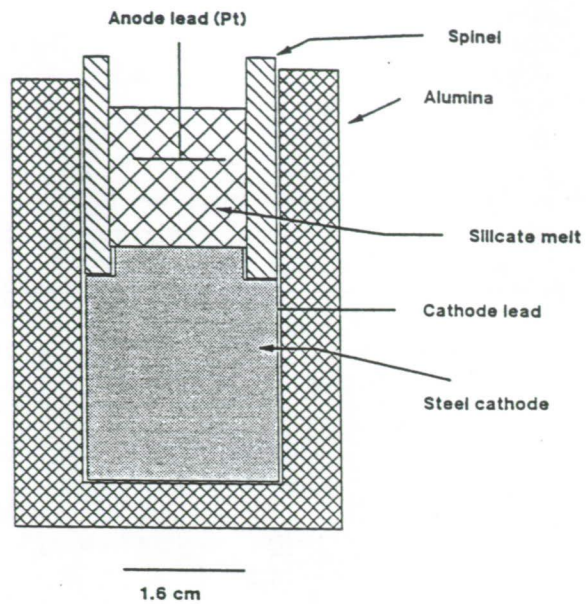


Fig. 3 Design for Elec2P-Elec2Q.

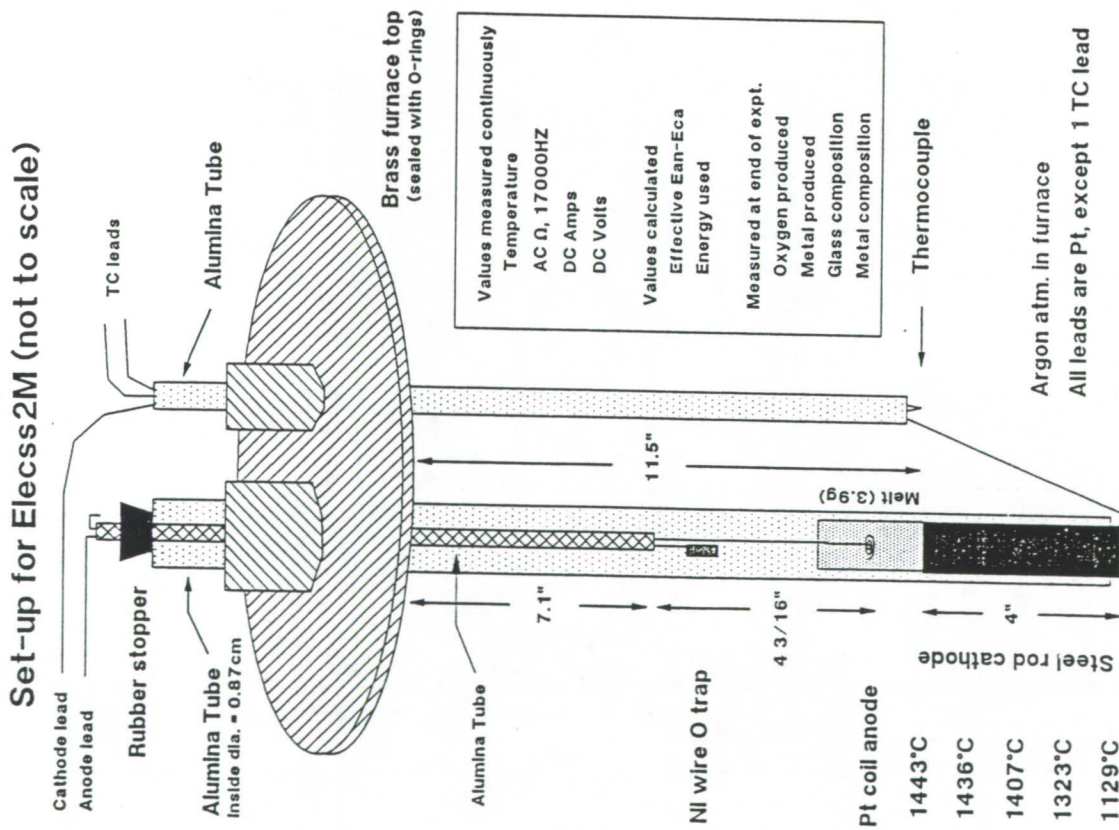
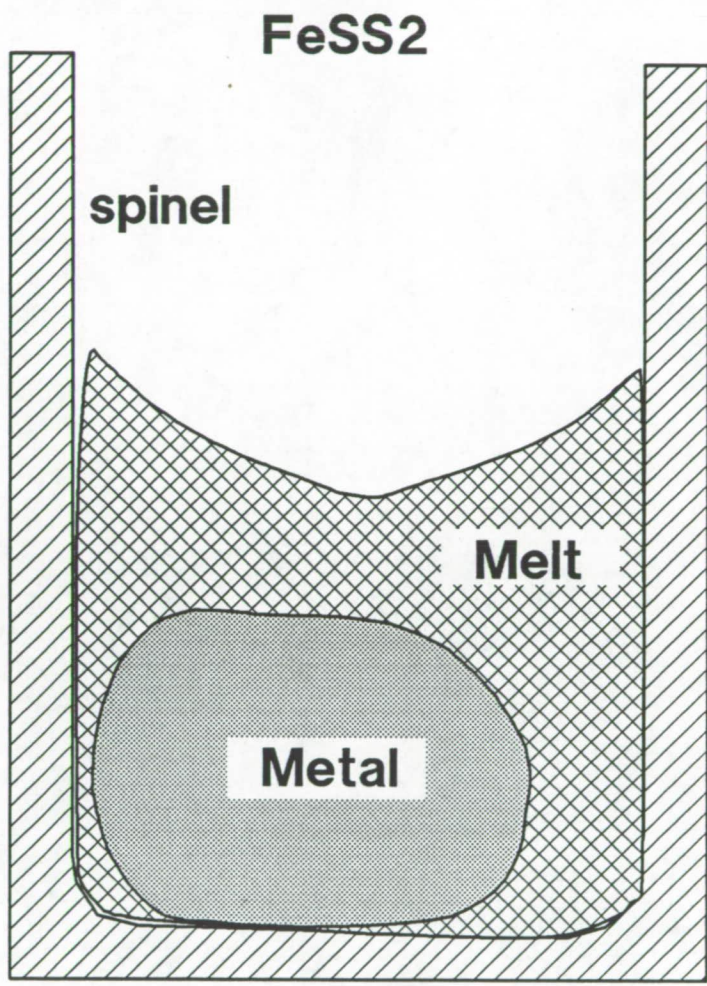
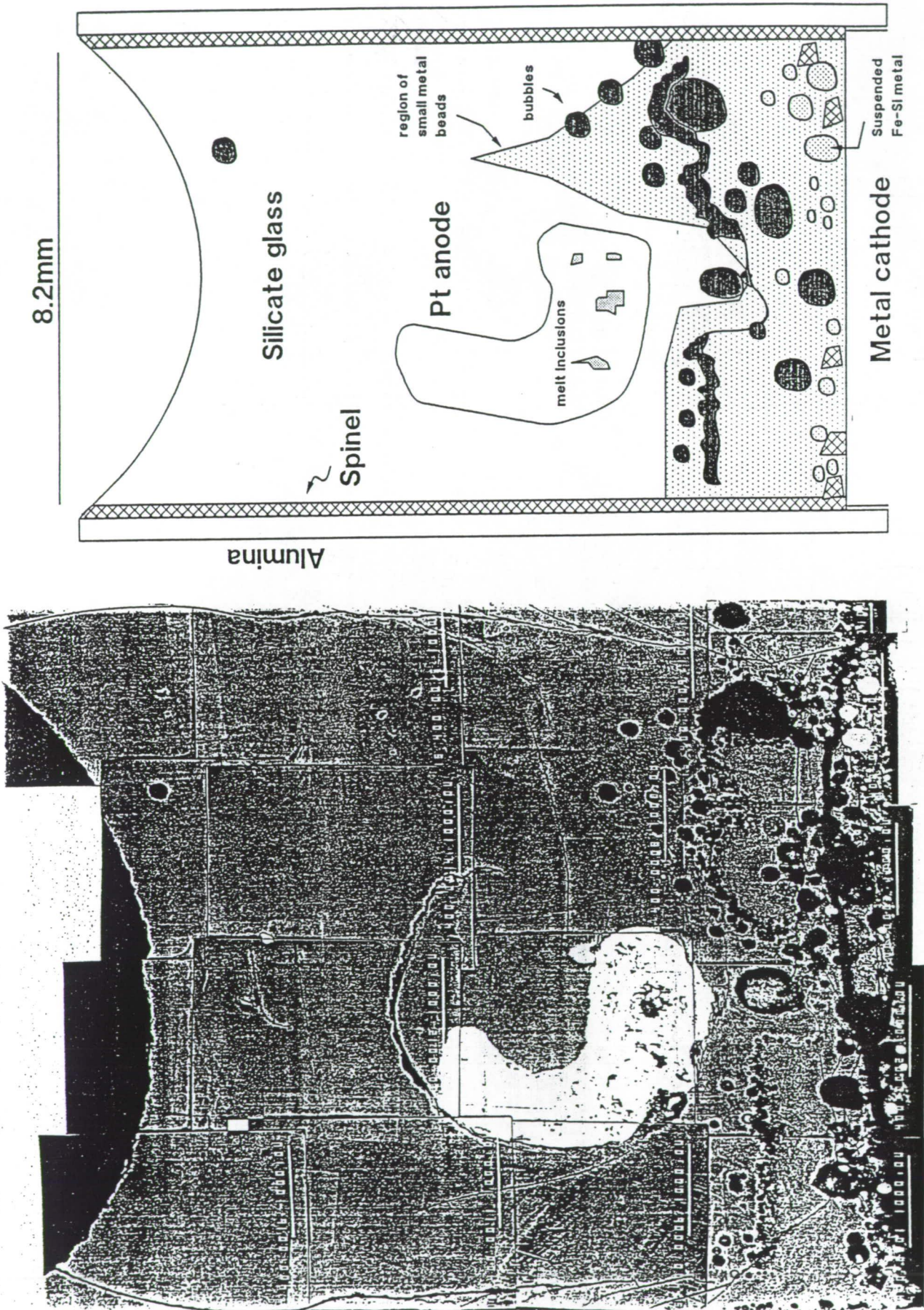


Fig. 2 Design for Elec2L-Elec2O. Experiments Elec2P-Elec2Q are analogous except spinel rather than alumina is used to contain the silicate melt.



**17.5 mm
to scale**

Fig. 5 Elecs2N, schematic diagram and backscattered electron image.



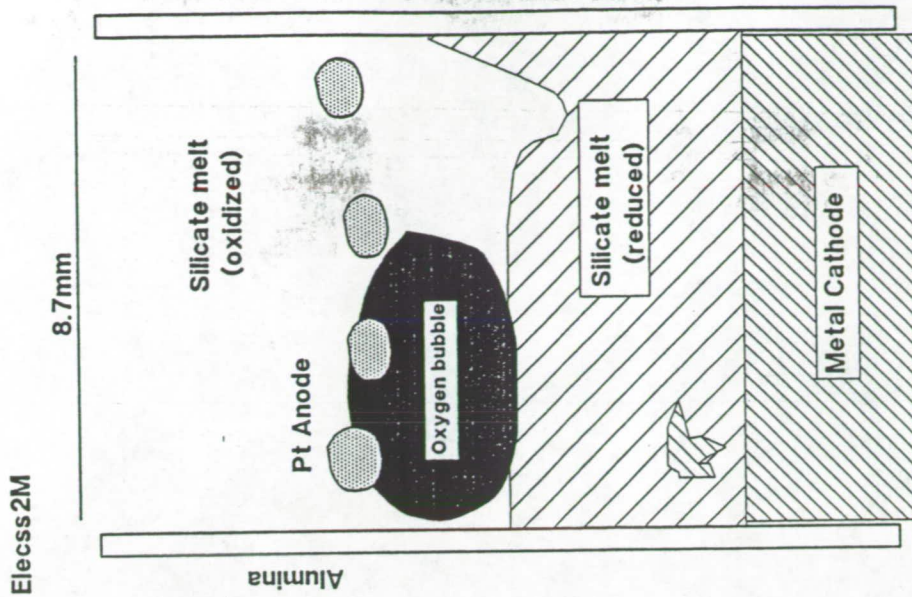


Fig. 6 Schematic diagram of Elec2M, showing gas bubble perched below anode.

Effect of Anode design on cell resistance increase due to frothing¹

Anode Design	Resistance after 10min at 0.049A	Resistance after >> 10min at 0.049A	Resistance after >> 10min at 0.034A	Cell Model
	92.4	>93	42	Elec2N
	69.8	80	<70	Elec2N ²
	60.2	68	>45	Elec2N
	38	68	21	Elec2N
	18	>18	22	Elec20

Summary: Fewer bigger holes are better than more littler holes.

¹ Cell parameters such as electrode separation, melt composition etc. are approximately the same.

² Anode surface area ~25% greater than for other anodes.

Fig. 7.

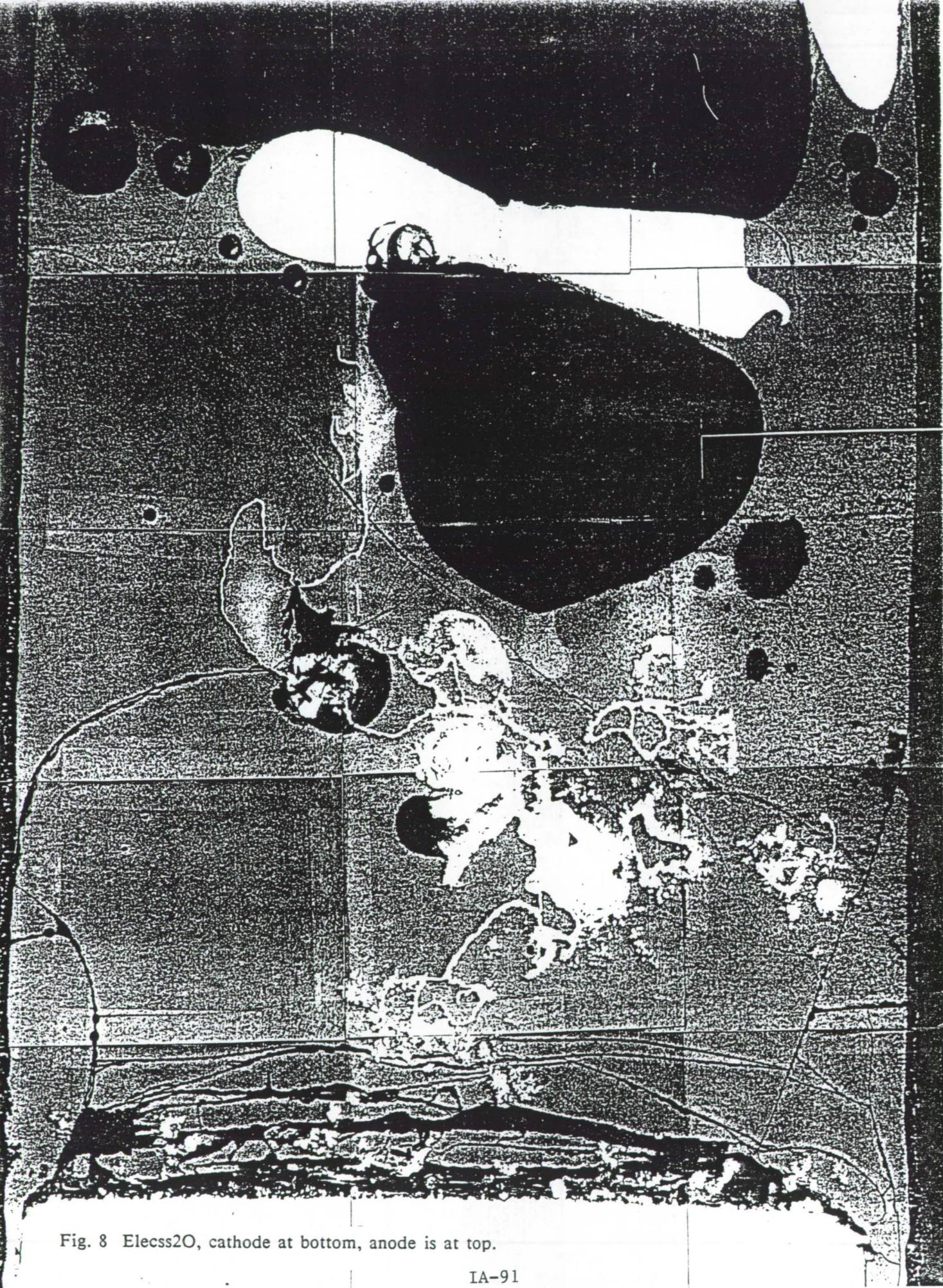


Fig. 8 Elecs2O, cathode at bottom, anode is at top.

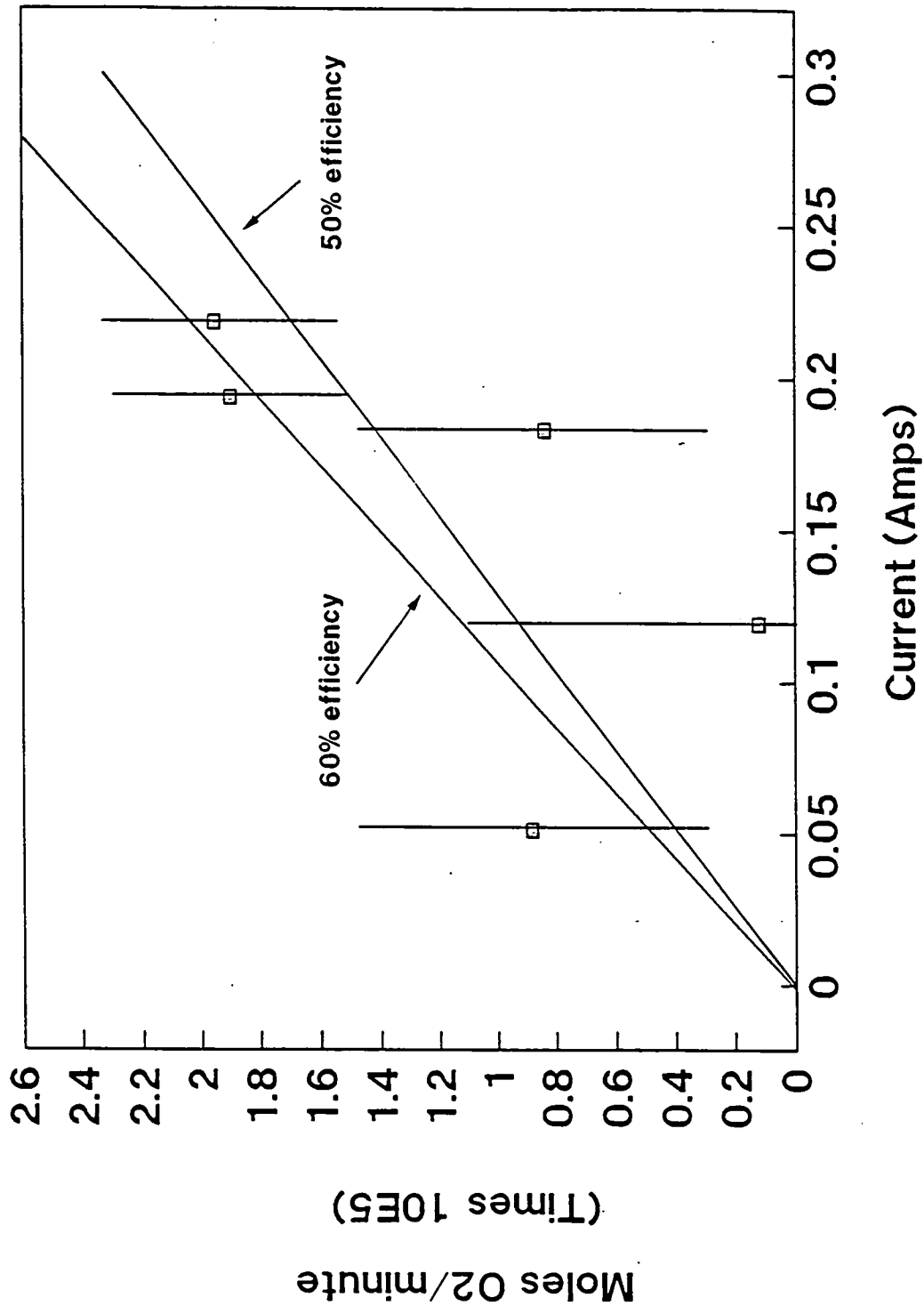


Fig. 9. Measured oxygen production rate versus current in Elecsc2P.

497587
N93-26679

55-25

158352

p. 10

Experimental Study of the Electrolysis of Silicate Melts

**Rudolf Keller
EMEC Consultants**

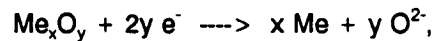
Abstract

Melting and electrolyzing lunar silicates yields oxygen gas and potentially can be practiced in situ to produce oxygen. With the present experiments conducted with simulant oxides at 1425-1480 °C, it was ascertained that oxygen can be obtained anodically at feasible rates and current efficiencies. An electrolysis cell was operated with platinum anodes in a sealed vessel, and the production of gas was monitored. In these electrolysis experiments, stability of anodes remained a problem, and iron and silicon did not reduce readily into the liquid silver cathode.

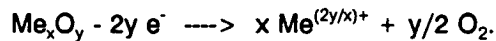
Principles of Magma Electrolysis

Raw materials readily available on the lunar surface are generally oxides. They contain copious amounts of oxygen for potential use as propellant or for life support. Elemental oxygen can be obtained by chemical oxidation or electrochemically. Melting available silicates and electrolyzing this melt appears particularly attractive because of its conceptual simplicity. This approach has been called "magma electrolysis". Its fundamentals have been studied in recent years at Washington University in St. Louis^(1,2,3).

Lunar raw materials for in-situ utilization include primarily silicates that contain various amounts of other oxides such as aluminum oxide, calcium oxide, magnesium oxide, iron (Fe²⁺) oxide, titanium oxide, etc. These silicates can be melted at temperatures of 1400 °C and higher, and electrolyzed to reduce metal components at the cathode,



and to oxidize oxides to oxygen at the anode,



When the electrolysis is conducted to produce oxygen as the product of primary interest, the melt can be partially electrolyzed and residual oxides discarded, possibly along with some metallic products. Reduction potentials and mass transport conditions determine which metals will be preferentially reduced.

The selection of conditions has been discussed previously^(4,5), also advantages and disadvantages of the process⁶.

The feasibility of "magma electrolysis" to produce lunar oxygen rests, we believe at this stage, upon the following key issues:

- (1) Electrolyte Conductivity. To obtain acceptable production rates at reasonable space-time yields and energy efficiency, the specific conductance of the molten material must be high and remain high during the electrolysis.
- (2) Current Efficiency. The process must have an acceptable faradaic yield. Low current efficiencies may result from reoxidation of cathode products; metals often are soluble in molten

electrolytes and solid metallic products may become dispersed in them, then react upon reaching anode products. Current efficiencies can also be affected by the oxidation of lower valent species to higher valent ones, as in the case of Fe^{II} to Fe^{III}. The presence of two- and three-valent iron may lead to electronic conductance of the electrolyte.

(3) Separation of Products. Products need to be removed from the system. This applies to the oxygen gas as well as to metals that form at the cathode.

(4) Stability of Electrode and Containment Materials. Because high temperatures and aggressive melts are involved, materials requirements are non-trivial.

Goal of the Present Experimentation

The experimentation focused primarily on the anodic current efficiency in the electrolysis of molten silicates: how much oxygen is actually produced? Oxygen evolved anodically was to be collected in a closed system and the production rate evaluated quantitatively. The size was to exceed that of previous small-scale approaches, in dimensions as well as production rates.

Experimental Equipment and Procedures

The main challenge consists in capturing the oxygen quantitatively, without any losses towards the outside and without any reaction with cell parts such as metals or carbon. By designing a system with minimal overpressure and relying on ceramic components for parts exposed to high temperatures wherever possible, we succeeded to conduct experiments producing the desired information. Nevertheless, the experimentation had its difficulties and not every run was productive.

An electrolysis cell was placed in a alumina tube, as represented in *Figure 1*. Two alumina crucibles contained the electrolyte and the liquid metal cathode. Amounts of about 270 g silver were used for the cathode, part of this metal placed as cathode connection in the space between inner and outer alumina crucible. Four small holes were drilled in the inner containment crucible to allow current to pass. Electrical connection to the cathode metal was made by means of a shielded graphite rod. The electrolyte was contained in the inner crucible above the metal pad. A platinum sheet anode was suspended into the electrolyte.

Silver was selected as the cathode metal because of its high density, its convenient melting point (a liquid cathode substrate is preferred), and its absence in the electrolyte. A ferrosilicon cathode may eventually be used in magma electrolysis, but the employment of such a composition would have distorted some of our results because of silicon reacting with electrolyte components, mainly

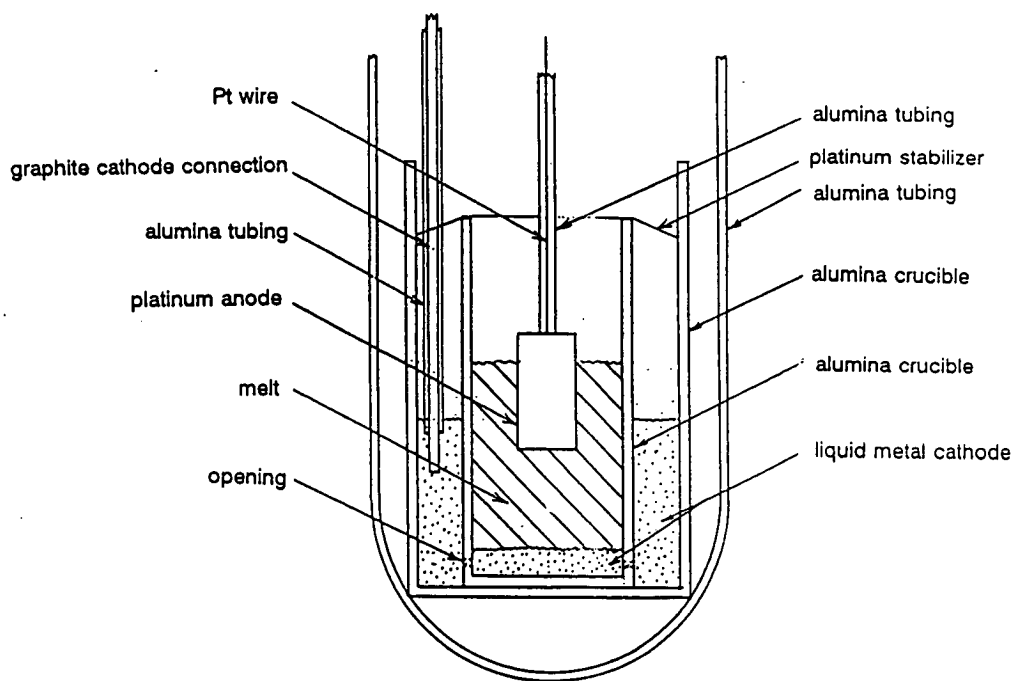


Figure 1 Experimental Arrangement to Determine Gas Anodically Produced in the Electrolysis of Molten Oxides ("Magma Electrolysis")

reducing iron oxide, and cathodic current efficiencies for iron and silicon could not have been examined.

As shown in *Figure 2*, the cell arrangement was placed in a sealed alumina tube which was connected to an apparatus measuring changes in the gas volume. The cell was kept in a DELTECH furnace at the desired temperature, typically at 1425-1460 °C. The tube protruded out of the high-temperature furnace and was sealed on top with a stainless steel lid. Provisions were made to fill the tube with inert gas (helium was preferred over argon or nitrogen because argon was the carrier gas in the gas chromatographic analysis and the presence of nitrogen was used to indicate leakage of air into the system).

The arrangement was assembled at room temperature. Before electrolysis was started, it was brought to the desired temperature. After melting of the metal and oxides, thermal equilibrium was established. Electrolysis was initiated and changes of the gas volume in the sealed system determined, using a burette and a leveling device. Gas samples could be taken for analysis.

Currents applied were normally about 2 A. With a platinum sheet anode of 1.5 cm x 1.0 cm, immersed 1.0 cm into the electrolyte, the nominal anodic current density was 1 A/cm². Larger anodes were used in a few late experiments, increasing currents to 5 A and reducing nominal current density to 0.5 A/cm². At the current of 2 A, 0.6 g oxygen would be produced per hour at 100 % faradaic current efficiency. This corresponds to a volume of 2600 ml at 1425 °C or 456 ml at 25 °C. The targeted duration of a single experiment was usually 6 hours.

While the measurement of gas volume changes was the main indication for oxygen production, additional information was obtained from an analysis of the gas. A sample was collected, at the end of the experiment, in a gas sampling device and submitted to the Pittsburgh Applied Research Corporation for analysis. Complete mixing of the gas contained inside and outside the high-temperature vessel and a value for the total gas volume were assumed to calculate the amount of oxygen produced. Corrections were made for the formation of CO₂ by reaction with the graphite of the cathode connection and for the penetration of air, as indicated by the presence of nitrogen. In some cases, escape of helium from the gas mouse after sampling was suspected, this problem being alleviated by switching from a plastic to a glass device.

Cathodic current efficiencies based on metallic products collected in the silver cathode were also

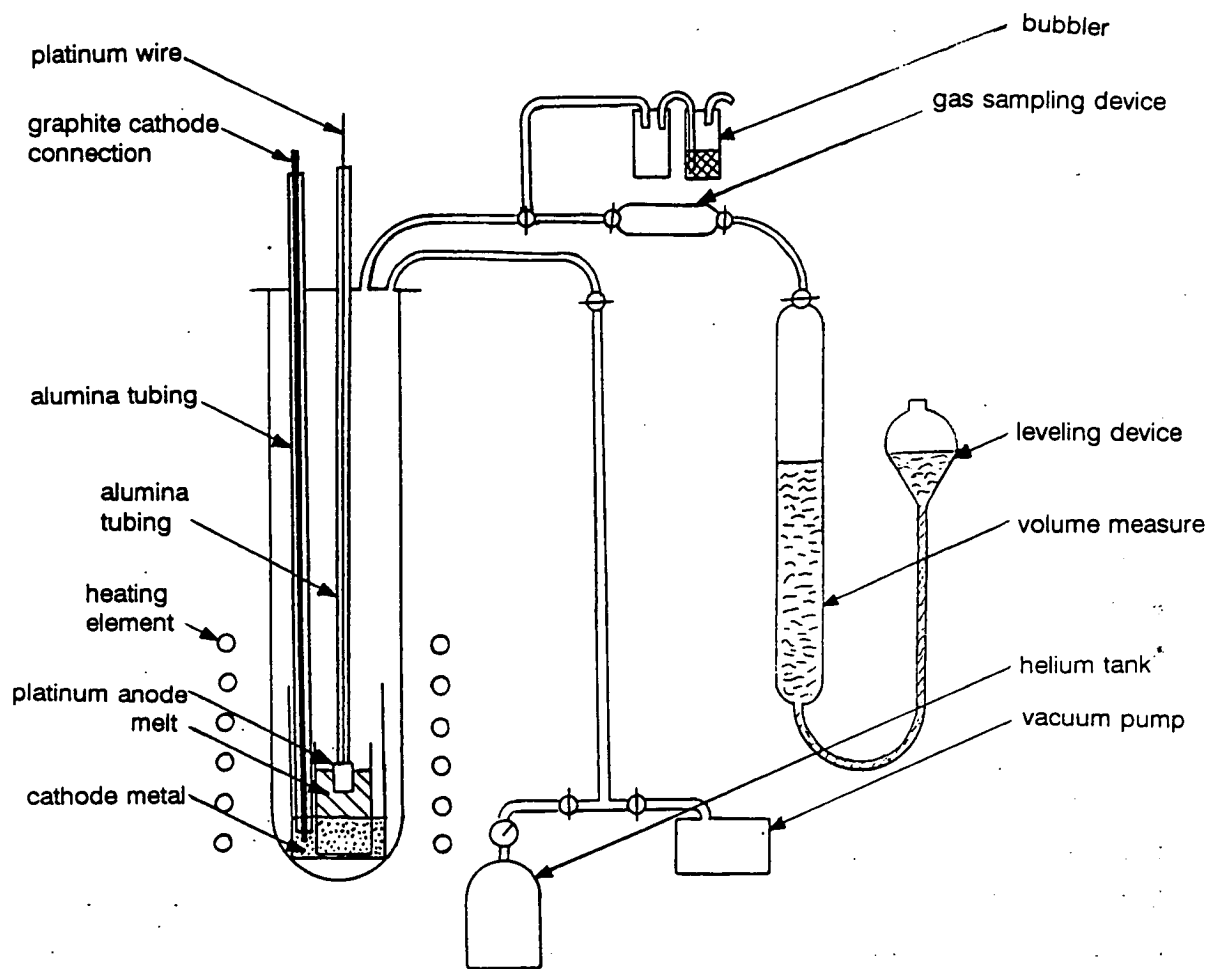


Figure 2 Experimental Arrangement to Determine Gas Anodically Produced in the Electrolysis of Molten Oxides ("Magma Electrolysis")

determined. Following solidification of the melt, the metal was physically separated from the alumina crucibles and remaining electrolyte. The metal then was remelted and sampled with a quartz tube. Samples were analyzed, again, by the Pittsburgh Applied Research Corporation.

Selection of Electrolytes

Experiments were performed with four electrolyte compositions:

- (1) Minnesota Lunar Simulant, MLS-1
- (2) Composition B, selected to represent a steady state electrolyte⁵; partially electrolyzed basaltic ore (composition proposed by Haskin and Colson⁷ as representative), with all the iron oxide and 50 percent of the silicon oxide reduced, then 10 percent of fresh ore added (Fe_3O_4 was substituted for FeO)
- (3) Composition C, free from iron oxide, representing an aluminosilicate slag composition remaining as electrolyte according to Haskin and Colson¹, minor constituents not considered
- (4) Cryolite, Na_3AlF_6 , with 10 % Al_2O_3 added; used for comparison purposes; electrolysis at 1000 °C

The compositions are given in Table 1. While MLS-1 was used as received from the University of Minnesota, the other combinations were synthesized from commercially available chemicals.

Table 1. Composition of Electrolytes

Component	MLS-1 (A)	B	C
SiO_2	43.86 wt%	41.25 wt%	37.08 wt%
Al_2O_3	13.68 wt%	21.36 wt%	18.64 wt%
FeO	13.40 wt%		
Fe_2O_3	2.60 wt%		
Fe_3O_4		1.58 wt%	
TiO_2	6.32 wt%	0.25 wt%	16.52 wt%
MgO	6.68 wt%	17.62 wt%	27.77 wt%
CaO	10.13 wt%	17.95 wt%	
Na_2O	2.12 wt%		
K_2O	0.28 wt%		
P_2O_5	0.20 wt%		

Experimental Results

The experimental results are summarized in Table 2.

Table 2. Summary of Experimental Results

Expt	Electrolyte	Duration	CE by Volume	CE by O ₂ %	CE by Metal	Anode Results
3-01	A	2hr 5min	3.2%	---	---	no change
3-02	C	6 hrs	30.9%	---	---	small chg
3-03	C	6hr 12min	42.2%	---	19.1%	1/3 gone
3-05	B	6 hrs	27.7%	---	---	destroyed
3-08	C	5hr 30min	20.1%	14.7%	63.7%	1/3 gone
3-09	cryolite	2hr 45min	64.3%	---	59.0%	no change
3-10	cryolite	3hr 40min	105.9%	---	112.0%	no change
3-11	A	6 hrs	0.0%	---	---	no change
3-12	B	2hr 10min	76.5%	78.6%	39.7%	destroyed
3-13	C	1hr 18min	0.0%	---	---	---
3-15	C	5hr 30min	49.0%	77.6%	56.3%	2/3 gone
3-16	B	2hr 29min	71.1%	112.8%	82.1%	destroyed
3-17	C	4hr 58min	21.9%	10.3%	42.6%	1/4 gone
3-18	B	2hr 12min	70.7%	105.3%	90.6%	destroyed
3-19	B	2hr 42min	75.2%	67.3%	57.3%	destroyed
3-20	B	1hr 40min	52.5%	37.4%	---	destroyed

Current efficiencies ranging from 52 to 76 percent were obtained with composition B, a composition representing projected electrolyte composition in a cell operating at steady state. These values are quite respectable for a molten salt electrolysis of this scale. Gas volume changes appeared to be the more reliable indicator, although some reasonable agreement was generally obtained in experiments in which a glass sampling vessel had been used (polymer vessels were used in Experiments # UoA-3-16 & 18, which probably led to excessively high oxygen concentrations due to escape of helium). Electrolysis of composition B normally could be maintained for less than 3 hours, however, as the platinum anode was destroyed.

Current efficiency based on metal products was equally high, reaching 90 percent in one case. It is remarkable, however, that neither iron nor silicon were found in the silver cathode metal after electrolysis; the aluminum content corresponded to 81.3 % current efficiency, the magnesium content to 9.3 %. Evidentially there was no problem with evaporation of magnesium, as is being reported by Haskin and Colson³.

With the iron-free electrolyte, composition C, anodic current efficiencies ranged from 20 to 49 percent. Appreciable silicon deposition, corresponding to 33 and 19 % Faradaic efficiency, was only observed in two cases. Anodes lasted better in this electrolyte, although the experiments usually also had to be terminated before reaching the full 6 hours.

Anode deterioration appeared to be minimal when electrolyzing MLS-1. In this case, oxygen evolution was practically zero, probably due to the high iron oxide content which led to a different anodic reaction.

In the runs with cryolite at 1000 °C, gas current efficiencies of 64 and 106 % were obtained, values consistent with expectations, considering chemistry and accuracy of the method. Platinum anodes remained intact during the electrolysis duration of 2.75 and 3.67 hours, respectively.

Synopsis

Anodic production of oxygen at adequate current efficiencies was demonstrated for conditions representative of envisioned processing. High iron oxide content in the electrolyte appeared to reduce current efficiency drastically.

Contrary to expectations, iron was never found in the cathode silver, silicon only in exceptional

cases. These metals probably were reduced but remained suspended in the electrolyte. At moderate concentrations, this did not seem to affect anodic current efficiencies.

Stability of the platinum anode was unsatisfactory in all cases yielding good anodic current efficiencies. Functioning of a cathode containing iron and silicon should be studied in future efforts. A major future thrust, furthermore, should address the stability of anodes.

Acknowledgements

Experiments were conducted by William H. Retsch, Jr. and Michael B. Fisher, with guidance by Kirk T. Larimer, Research Metallurgist, and Warren E. Haupin, Consultant. Discussions were held with Prof. Larry Haskin and Dr. Russ Colson of Washington University, St. Louis. These contributions to the effort are gratefully acknowledged.

References

¹Haskin, L.A. and R.O. Colson. MISM progress at Washington University. University of Arizona Workshop on Magmaelectrolysis of Indigenous Space Materials (August 1991).

²Colson, R.O. and L.A. Haskin. "Producing oxygen by silicate melt electrolysis. In *Resources of Near-Earth Space*, edited by J.S. Lewis and M.S. Matthews. Tucson: University of Arizona Press (in press).

³Colson, R.O. and L.A. Haskin. Oxygen and iron production by electrolytic smelting of lunar soil (this report).

⁴EMEC Consultants. Experimental study of the electrolysis of silicate melts. Final Report (Fiscal Year) submitted to the University of Arizona/NASA Space Engineering Research Center for the Utilization of Local Planetary Resources (December 1990).

⁵Keller, R., K.T. Larimer, and W.E. Haupin. MISM experiments at EMEC Consultants. Report for University of Arizona Workshop on Magmaelectrolysis of Indigenous Space Materials (August 1991): 24-36.

⁶Keller, R. Lunar production of oxygen by electrolysis. *Proceedings of the 10th Biennial SSI/Princeton Conference on Space Manufacturing* (1991).

⁷Haskin, L.A., R.O. Colson, D.J. Lindstrom, R.H. Lewis, and K.W. Smekow. Electrolytic smelting of lunar rock for oxygen, iron, and silicon. Manuscript dated December 1989; accepted for the *Proceedings of the 2nd Conference on Lunar Bases and Space Activities of the 21st Century*. Houston, April 1988.

⁸Haskin, L.A. and R.O. Colson. Steady state composition with low Fe²⁺ concentrations for efficient O₂ production by "magma electrolysis of lunar soils. *Space '92 - Proceedings of the Third International Conference on Engineering, Construction and Operations in Space*. Denver, June 1992.

497588
N93-26680

56-25

158353

p-9

Lunar Mining of Oxygen Using Fluorine

**Donald M. Burt, James A. Tyburczy, Jeffery J. Roberts,
and Rajan Balasubramanian**

**Arizona State University
Department of Geology**

Abstract

Experiments during the first year of the project were directed towards generating elemental fluorine via the electrolysis of anhydrous molten fluorides. Na_2SiF_6 was dissolved in either molten NaBF_4 or a eutectic (minimum-melting) mixture of KF-LiF-NaF and electrolyzed between 450° and 600° C to Si metal at the cathode and F_2 gas at the anode. Ar gas was continuously passed through the system and F_2 was trapped in a KBr furnace. Various anode and cathode materials were investigated. Despite many experimental difficulties, the capability of the process to produce elemental fluorine was demonstrated.

Introduction

We are engaged in experiments to produce fluorine by the electrolysis of anhydrous molten fluorides, with application to the mining of oxygen on the Moon. Fluorine, as the most reactive element, readily releases oxygen from all oxygen-bearing rocks and minerals. Stable isotope geochemists have carried out this reaction successfully for more than 30 years in Ni crucibles at a temperature of about 500° C.

Fluorine can only be produced by electrolysis. Conventionally, an HF-KF mixture is electrolyzed at moderate temperatures to yield H₂ at the cathode and F₂ at the carbon anode (e.g., Ellis and May, 1986). This route does not readily lend itself to recycling of the fluorine, all of which would have to be brought from Earth (as a stable inert salt, in the present process). The problem is that the hydrogen produced at the cathode is a relatively poor reducing agent.

An alternative fluorine-generating process, devised by D.M. Burt in 1989 (unpublished), produces by-product silicon (for solar cells) as well as oxygen, and results in all of the F₂ being recycled (in principle, at least). A lunar silicate rock is partially fluorinated by F₂ gas, yielding pure O₂ gas, then the residue is heated in the lunar vacuum to release gaseous SiF₄. The SiF₄ is trapped in NaF-bearing anhydrous molten salts as Na₂SiF₆, which is electrolyzed to Si metal at the cathode and F₂ gas at the anode, thus completing the cycle. Inasmuch as SiF₄ is the most volatile common fluoride, this process should work with any unbeneficiated lunar silicate rock.

Personnel

The apparatus was largely designed and set up this spring by Dr. Jeff Roberts, a former student of Prof. Jim Tyburczy. He left in June to accept a job at Lawrence Livermore Labs and was replaced by Mr. Rajan Balasubramanian, an ASU Chemical Engineering graduate student. Mr. Balasubramanian finished designing and assembling the apparatus in early July and has carried out the actual experiments since then. Prof. Tyburczy left for a sabbatical year at SUNY Stony Brook in August.

Progress

Since our progress report of May 28, 1992 we have finished setting up the electrolysis line and have carried out 16 experiments, the first 15 of which are summarized on the appended table. We have successfully prepared fluorine by electrolysis, beginning with our third try on July 23. Not

unexpectedly, we also have encountered many experimental difficulties.

We had, somewhat surprisingly, no problems with corrosion of the Inconel 601 electrolysis vessel, its water-cooled stainless steel top, or the inner alumina crucible in which we melted the electrolytes, at run temperatures up to 600 C (a technique used by Mamentov and Laher, 1989). The KBr furnace at about 200 C seemingly trapped nearly all of the F_2 formed as KF by releasing Br_2 ; we had no detectable releases of F_2 gas from the system.

Our initial few runs involved sheet graphite cathodes and anodes and low-melting $NaBF_4$ (M.P. 408° C) as the electrolyte (Mamentov and Laher, 1989). After run 4, we abandoned $NaBF_4$ in favor of a eutectic (minimum-melting) mixture of KF-LiF-NaF (M.P. 459° C: e.g., Minh and Redey, 1987) owing to the high volatility of the former. $NaBF_4$ releases gaseous BF_3 when heated, which gas was not trapped by our KBr furnace at 200° C, even with NaF placed at the downstream end. We detected this problem by the characteristic fuming of BF_3 when it contacted the water we had at the end of the line to measure gas flow via bubbling rate (Topchiev et al., 1959, p. 25). White borate deposits partly blocked the glass tube, which locally was etched by the HF formed by the reaction of BF_3 with the water.

We abandoned the graphite electrodes after 9 runs because of their relatively poor electrical conductivity (reducing the electrode spacing did not help much, revealing that salt conductivity was not the major problem). (We did produce some Si on the cathode by using long run times and small electrode spacing.) The metals that we tried later (inconel, copper, titanium, and nickel, to date) were much better conductors of electricity, although they suffered more severe anode corrosion.

Problems and Solutions

Our other experimental difficulties are summarized below, together with the measures we undertook to alleviate the problems. Many of these difficulties undoubtedly resulted from our inexperience in molten salt electrolysis.

1. The KF-LiF-NaF mixture (especially KF) is highly hygroscopic. To minimize this problem, samples were weighed out rapidly just before a run, then placed in a stream of dry argon, and left to dry out at $T > 300^\circ C$ for an hour before proceeding with the run. Cell resistivity was then monitored as the salt was heated to melting.

2. The maximum internal temperatures were much cooler (50-100° C) than those measured by the external thermocouple, as revealed by our initial failure to melt the charge. We placed an alumina-sheathed internal thermocouple in later runs.

3. The closely- and evenly-spaced furnace windings, short length, and water-cooled top of our electrolysis vessel resulted in a undesirably high vertical temperature gradient in the electrolysis cell (100° C over a few cm, as revealed by raising and lowering the internal thermocouple). The alumina-sheathed thermocouple and especially the two cold metal electrode leads immersed in the salt made the problem worse, as did the cold stream of argon being directed downwards through the top. The only remedy was to carry out the experiments at much higher temperatures (more than 100° C greater) than initially planned. After run 9, we reshaped the furnace (removed the top) so as to place the bottom of the reaction vessel at the hot spot of the furnace, rather than above it. This slightly alleviated, but did not cure, the problem.

4. The high vertical temperature gradient made the salts remain solid (crystalline) on top. They tended to form a impermeable crust on top of the molten electrolyte, clinging to and even climbing the metal electrode supports. In one run, #3, this crust trapped the first fluorine gas we produced as tiny fluid inclusions, which decrepitated "explosively" (in tiny gas puffs) after the run was opened and the adsorbed water began to dissolve the salts. The remedy was, again, to carry out the electrolysis at a high enough temperature (about 600° C) to make sure all of the salt was melted. The problem worsened when we began using metal electrodes; at this point we started preheating the furnace to over 700° C, then cooling it down for the actual electrolysis.

5. Even with these measures, KF-LiF-NaF melts that were relatively rich in Na_2SiF_6 (up to 4%) tended to climb up the walls of the container and also up the electrodes. Placing a small ceramic cap or "protector" over the place where the electrode joined the metal carrier, especially for the cathode, helped somewhat. In later runs we tried to retract the electrodes and thermocouple before cooling off the run, in order to facilitate their examination and cleaning (otherwise they were trapped in rock-hard frozen electrolyte and had to be laboriously chipped or dissolved free); vertical creep of the electrolyte made this impossible in some Si-rich runs (crystallized electrolyte crust "froze them in place" during the run).

6. In runs with less Si or those electrolyzed for longer periods or at higher currents, all of the Si dissolved in the electrolyte was apparently used up (by deposition at the cathode) and at that

point the metallic anode became highly corroded. Fluorine produced at the anode reacted with it and the resulting fluoride dissolved in the melt; the metal reprecipitated at the cathode dendritically (and the fibrous dendrites eventually shorted out the cell). At this point the cell was producing no F_2 gas but was merely electrorefining the metal of the anode. This was especially visible in the runs with Cu electrodes (#12 and #13), but it also happened to inconel (#14) and Ti (#15). TiF_4 is a gas at high temperatures, but much of it appears to have been reabsorbed by reaction with the melt.

7. Our major problem was the failure of the cold trap (a simple U-tube) to trap the Br_2 released into the Ar gas stream by reaction of F_2 with KBr in our horizontal tube fluorine-trapping furnace. We tried switching from an ice-water bath to a dry ice bath, but this didn't help. Using a liquid nitrogen bath resulted in condensation of liquid argon from the argon gas stream; this rapidly blocked the U-tube and was abandoned. Our resident fluorine expert, Prof. Paul Knauth, tells us that a simple U-tube works for trapping diffuse Br_2 in a vacuum; apparently the thermal vibrations of all of the accompanying Ar atoms in our experiments prevent the Br molecules from condensing (they are "hustled on through" the cold U-tube, instead of sticking to its walls). We could try using dry N_2 in place of Ar as the gas stream, with liquid nitrogen bathing the U-tube, or could try using a vacuum (our present set-up is not vacuum tight). In order to measure fluorine production quantitatively, we shall have to come up with a different method of measurement, such as an ion-sensitive electrode.

We can, nevertheless, demonstrate that we have been making considerable fluorine, if not exactly how much. Not only did tiny fluid inclusions of F_2 gas in salt crust react explosively with water after run #3, as mentioned above (the reaction $F_2 + H_2O = 2HF + O_2$), but also optical examination of the material filling the KBr furnace after 13 runs revealed that much of it had been converted to KF. This was accomplished by examining a crushed sample on a glass microscope slide under a cover slip using an oil of refractive index 1.555, which nearly matches that of KBr (1.559), making KBr grains appear nearly invisible. Any conversion to KF is detected by the much lower refractive index of the latter (1.363).

Results

1. Fluorine was produced.
2. KF-LiF-NaF eutectic better than $NaBf_4$ owing to volatility of latter.

3. Graphite anode seemingly nonreactive with F_2 , but such a poor conductor that only tiny currents could be maintained; some Si was produced.
4. Metal anodes (Cu, Ti, inconel, Ni) corroded rapidly and metal reprecipitated at the cathode (electrorefining) after Si in the melt was used up.

Major Discoveries

1. Fluorine can be produced by anhydrous molten salt electrolysis; this can be carried out in alumina crucibles inside an inconel or nickel reaction vessel at temperatures up to 600 C.
2. The eutectic (minimum melting) mixture of KF-LiF-NaF worked much better as the electrolyte than $NaBF_4$, owing to the high volatility of the latter.
3. Sheet graphite anodes were less subject to corrosion than the metals we tried (inconel, Ni, Cu, and Ti) and conveniently broke off when it was time to free them from the electrolyte, but were such poor conductors of electricity that only long run times and close electrode spacing allowed visible production of Si at the cathode.
4. The metal electrodes corroded rapidly at the anode and the metal reprecipitated dendritically at the cathode (electrorefining); this problem was probably caused by the low initial Si contents of the melts; all of the Si was precipitated at the cathode quite rapidly. Two differently-colored layers of precipitate were commonly observed on the cathode after these experiments, the inner one presumably being Si and the outer one the cathode metal.
5. Many experimental problems remain to be solved.

Future Research

Continued funding is requested to carry out the following experiments:

1. Continue electrolysis experiments with other metals and forms of carbon other than graphite as the anode material.
2. Determine the composition of the metals deposited at the cathode by using electron microprobe microanalysis.

3. Devise a different method of measuring fluorine production quantitatively, either by replacing Ar by N₂ in the gas stream, or by redesigning the apparatus to work in a vacuum, or by using an ion sensitive electrode to measure F in aqueous solution.
4. Redesign the furnace and reaction vessel to minimize temperature gradients, thereby minimizing several experimental problems involving electrolyte crusts and vertical creep, and also minimizing anode corrosion by allowing electrolysis at lower temperatures. Two modifications that could be tried with our present set-up involve air instead of water cooling of the top of the reaction vessel and pre-heating of the argon stream before it enters the reaction vessel.
5. Initiate experiments on partial fluorination of silicate rocks and on SiF₄ release by pyrolysis of partly fluorinated rocks.

References

- Ellis, J.F. and G.F. May. Modern fluorine generation. *J. Fluorine Chem.* 33 (1986): 133-47.
- Mamantov, G. and T.M. Laher. Production of fluorine by the electrolysis of calcium-fluoride-containing tetrafluoroborate melts, *J. Electrochem. Soc.* 136 (1989): 673-76.
- Minh, N.Q. and L. Redey. Reference electrodes for molten electrolytes, in *Molten Salt Techniques* (ed. D.G. Lovering and R.J. Gale) (New York: Plenum, 1987): 105-287.
- Topchiev, A.V., S.V. Zavgorodnii, and Y.M. Paushkin. *Boron Fluoride and its Compounds as Catalysts in Organic Chemistry* (transl. by J.T. Greaves). (New York: Pergamon Press, 1959).

Run No	Composition	Wt. of Electrolyte	Max. Outside Temp.	Max. Inside Temp.	Resistance (Minimum)	Voltage	Current	Electrode Material	Comments
						Volts	Amp.		
1	NaBF ₄ = 90% Na ₂ SiF ₆ = 10%	25.4 gms	490 C	-	28 k ohms	-	-	Graphite	Electrolyte not completely molten.
2	NaBF ₄ = 95% Na ₂ SiF ₆ = 5%	25.256 gms	560 C	-	10.81 k ohms	-	-	Graphite	Electrolyte molten. Gray crystalline material on top of electrolyte.
3	NaF = 10% KF = 44% LiF = 44% Na ₂ SiF ₆ = 2%	22.462 gms	650 C	-	35 ohms	2.9 - 3.4 4.6 - 5.6 4.8 - 7.0 5.4 - 8.2	.1 .2 .3 .4	Graphite	Black material deposited on the cathode. Sparks of smoke observed while dismantling. Grayish material observed on the anode.
4	NaBF ₄ = 95% Na ₂ SiF ₆ = 5%	22.39 gms	625 C	492.7 C	27.38 k ohms	15 - 25 V	.1	Graphite	KBr analysed microscopically. Abundant fluid inclusions present. No visual formation of KF.
5	NaF = 10% KF = 44% LiF = 44% Na ₂ SiF ₆ = 2%	21.232 gms.	656 C	552 C	0.43 k ohms	15 V 20 V 25 V	0.04 - 0 A 0.03 - 0 A 0.12-0.01 A	Graphite	1 M KI solution used as final trap in Run # 5.
6	NaF = 10% KF = 44% LiF = 44% Na ₂ SiF ₆ = 2%	24.82 gms.	640 C	516 C	128 k ohms	25 V	0.01 - 0.1 A	Graphite	Poor conductivity of electrodes.
7	NaF = 11% KF = 41% LiF = 44% Na ₂ SiF ₆ = 4%	27.895 gms.	600 - 675 C	446 - 476 C	34.68 k ohms	25 V	0 - 0.03 A	Graphite	No bubble on electrolyte surface. No visual depos. of Si on cathode. Electrolyte fully molten.
8	NaF = 11.5% KF = 42% LiF = 46.5%	24.497 gms.	650 C	575 - 581 C	0.78 k ohms.	25 V 15 V	0.03 - 0.05 A 0.03 - 0.04 A	Graphite	Observed a major temperature gradient inside the cell. (summarized at end of report.) Very little electrolysis occurred.
9	NaF = 10.5% KF = 42% LiF = 46.5% Na ₂ SiF ₆ = 1%	28.666 gms.	650 - 660 C	589 - 598 C	0.52 k ohms.	25 V	0.02 - 0.07 A	Graphite	Black Material (Si?) found around the cathode. Electrolyte surface was silvery (Na or K?). Many bubbles on electrolyte surface. Electrolyte contained dendrites. Electrolyte melt crust found half-way up the crucible.

10	NaF = 10.5 § KF = 42 § LiF = 46.5 § Na2SiF6 = 1 §	28.581 gms.	660 C	575 - 580 C	0.347 k ohms.	2.2 V 2.3 V 2.4 V 2.2/2.5 V	0.10 A 0.2 A 0.30 A 0.40 A	Inconel	Good conductivity from use of metal electrode. White crust on top. Grayish white crust below. Anode was quite corroded. Much metal deposited on cathode.
11	NaF = 10.5 § KF = 42 § LiF = 46.5 § Na2SiF6 = 1 §	27.997 gms.	680 - 700 C	573 - 590 C	10.68 k ohms.	15 V 1.9 V	0.04 A 0.10 A*	Anode-Graphite Cathode - Ni	Reduced electrode spacing from 20mm to 6mm. Electrolyte fully molten. Preheated melt to 650 prior to electrolysis at 580 C. This avoided the formation of crust. * Reading after switching electrodes.
12	NaF = 9.5 § KF = 42 § LiF = 46.5 § Na2SiF6 = 2 §	27.14 gms.	675 C	605 C	0.8097 k ohms.	1.6 V 1.8 V 2.0 V 2.1 V 2.5 V	0.10 A 0.20 A 0.30 A 0.40 A 0.50 A	Copper	Electrode Spacing - 8mm. Preheated melt to 725 C before electrolysis. No crust. Electrolyte surface orange in color. Electrodes shorted by metal deposition. Anode was corroded. Si deposited on the cathode.
13	NaF = 8.5 § KF = 42 § LiF = 46.5 § Na2SiF6 = 3 §	29.314 gms.	675 C	-	.2 k ohms.	1.6/1.7 V 1.8	0.10 A 0.20 A	Copper	Electrodes shorted by metal deposition. Anode was corroded. Electrode spacing - 19mm. Tried to use liquid N2 to trap Br2. But froze argon instead. Hence used dry ice in cold trap. No success. Analysed KBr trap microscopically. Observed KP.
14	NaF = 8.5 § KF = 42 § LiF = 46.5 § Na2SiF6 = 3 §	30.611 gms.	675 C	-	12.23 ohms.	1.3 V 1.6/1.7 V	0.10 A 0.20 A	Inconel	Electrolyzed for only one hour to avoid shorting of electrodes, at low current. Cathode had large Si deposit. Anode was corroded. Cathode deposit had 3 layers. Innermost layer was black. (Si?) Second layer was brownish. (Ni?) Outermost layer appeared to be molten salt. Electrodes pulled out of the melt before cooling down.
15	NaF = 8.5 § KF = 42 § LiF = 46.5 § Na2SiF6 = 3 §	31.6375 gms.	650 C	599 C	57 ohms.	0.8/1.0 V	0.20 A	Titanium	Electrode spacing - 19mm. The molten electrolyte had crept way up on the electrodes (due to 48 Si?). Corrosion of top plate (due to TiF4 vap?). Anodic deposit was purple.

omit

B. REDUCTION OF THE MARTIAN ATMOSPHERE

497581
N 93 - 26681
S-25
158354
P-10

Beneficiation of Ilmenite from Lunar Analog

G. Ramadorai¹ and R. Dean²
Department of Mining and Geological Engineering
The University of Arizona

Abstract

The results reported here were obtained on a meteoric eucrite sample called "Millbillillie Sample #173. Optical microscopy studies of the sample showed it to consist of 4 volume percent ilmenite, 2 volume percent troilite, and 94 percent transparent gangue. The transparent gangue consisted of 46 percent feldspar (anorthite), 38 volume percent pyroxenes, 10 volume percent olivines, and 6 percent opaques. Troilite was present in minor quantities. The head sample analyzed 15.5 percent total iron, 11.8 percent ferrous iron, and 0.37 percent titanium. Screen assay analyses of the 30, 100, 200, and 400 US mesh screen fractions showed that minor concentration of titanium occurred in the 200 x 400 and -400 mesh screen fractions.

Scanning electron microscopy (SEM) studies of the bulk sample showed the presence of a variety of ilmenite grains, ranging from 50 micrometers (μm), down to less than 1 μm without any evidence of liberation. Electron Diffraction scans (EDS) confirmed the ratio of Fe to Ti in the ilmenite grains.

Dry magnetic separation in a Frantz Isodynamic Separator was found to be effective only at sizes finer than 150 μm (100 US mesh) and more so at 200 mesh (74 μm). In each case, dedusting of the sample to remove -400 mesh (-0.037 μm) fines was required. Liberation size was determined to be 200 mesh and finer.

The highest grade concentrate assaying 3.45 percent Ti was produced by magnetic separation of the -200 + 400 mesh screen fraction assaying 0.44 Ti (from a -30 mesh sample) at a current setting of 0.35 AMP. This concentrate contained 21.2 percent of the Ti values in the screen fraction with 2.72 weight percent of feed to test.

The results can be projected to a sample stage ground to -200 mesh. Magnetic separation of the -200 + 400 mesh (-0.074 + 0.037 μm) should produce a concentrate accounting for 1.41 weight percent of the feed. This concentrate will analyze 3.45 percent Ti and contain 10.3 percent of the Ti values in the feed. By changing the Frantz Magnetic Separator settings, a lower grade concentrate analyzing 0.98 percent Ti can be produced at an increased recovery of 25.4 percent. The concentrate weight will be 11.7 percent of the feed. It must be emphasized that improved grades and recoveries can be obtained with the -400 mesh fines. However, beneficiation of these extremely fine materials is not possible in a practical process scheme.

¹Adjunct Professor

²Undergraduate Student

Several dry beneficiation processes were tested on -10 mesh and -30 mesh samples. These included the following:

- o Vertical Electrostatic (ES) Free Fall Separator (V-STAT)
- o Electrostatic (ES) Plate Separator
- o Rare Earth Drum Magnet Separator (KHD)
- o High Tension (HT) ES Roll Separator
- o High Intensity Lift Roll Magnet
- o Magstream Gravity Concentrator

The most significant physical upgrading was achieved in a Two-pass High Tension Electrostatic Roll Separator. The feed to the test consisted of the 200 x 400 mesh fraction of the -30 mesh sample. The 200 x 400 mesh fraction constituted 12 percent of the sample assayed 0.42 percent Ti, and contained 13.3 percent of the Ti values. The conductor material from the first pass was retreated in a second stage to produce a concentrate analyzing 2.73 percent Ti, with 39 percent Ti recovery. The two-pass conductor retreat product accounted for 5.44 weight of feed to the test, or 0.67 percent of the original -30 mesh sample. It is most probable that a single pass ES separation was just as effective as the two-pass ES test, since the conductor weight percentages for the single pass and two-pass tests were comparable.

By projecting the above results to a -200 mesh grind, a two-pass ES conductor retreat product accounting for 2.88 weight percent of the total feed should be possible. This product is expected to analyze 2.73 percent Ti, with 18.9 percent recovery of the Ti values in the total feed sample.

The free-fall ES Separator appeared to be effective in removing fines from the coarser sizes in the sample. This technique could be useful in dedusting lunar samples.

Wet Gravimetric-magnetic separation in the Magstream apparatus was successful in upgrading the -200 + 400 mesh fraction (at an apparent specific gravity of 4.25) from 0.42 percent Ti to 1.06 percent Ti, with 52.6 percent recovery in a concentrate representing 20.7 weight percent of feed to the test. This included the paramagnetic product, which was 6 weight percent, and contained 19.3 percent of the Ti values, at an assay of 1.37 percent Ti.

The above results can be projected to a -200 mesh grind sample, containing 51.9 percent as -200 + 400 mesh, and 48 percent of the Ti values. Magstream Separation would produce a heavy concentrate with 10.74 weight percent and 27.3 percent recovery at a grade of 1.06 percent Ti. It would be interesting to determine if ES roll separation of this heavy fraction would improve grade with minimum recovery losses.

Future work along the following lines is recommended on the Eucrite Sample:

- o Wet Magstream, followed by dry ES roll separation of the heavy fraction.
- o Dry Magnetic separation, followed by dry ES roll separation.
- o Test V-Stat separator for efficiency of dedusting.
- o Complete SEM and EDS scans of concentrates produced from tests with the ES two-pass separator, and the Frantz Magnetic Separator.

The additional data to be generated on the eucrite will determine the scope of process, engineering, and scientific studies on the very limited quantities of lunar material (5 to 10 grams) to be made available in 1993.

Introduction

The results summarized in this report are a continuation of beneficiation test work reported previously in *Progress Report Number 1* on Millbillillie Sample #173, characterized as an eucrite in the literature. This report summarizes details of Magnetic, Electrostatic, and Magstream testing completed on the Millbillillie sample.

Sample

The mineralogical makeup of the Millbillillie sample was previously discussed in extensive detail in *Progress Report Number 1*, and will not be repeated here. Sample preparation procedures can also be found in the reference cited earlier.

The screen-size distribution of the -10 mesh, -30 mesh, and -200 mesh samples used in the Electrostatic, Magstream, and Magnetic Separation testing is given in Tables 1 and 2. It is clear that the titanium analysis is quite low at 0.36 percent Ti to 0.39 percent Ti. The analyses for total iron, ferrous iron, and titanium are in the range of 13.73 to 15.08 percent, 12.78 to 13.09 percent, and 0.36 to 0.39 percent, respectively. Previous SEM studies showed the presence of a variety of liberated ilmenite grains ranging from 10 micrometers (10 μm) down to less than 1 μm , as well as 1 μm unliberated and liberated grains. Electron diffraction scans (EDS) confirmed the ratio of Fe to Ti in the ilmenite grains.

TABLE I

Screen Assay Distribution of Samples used in Magstream Separation Tests

US mesh size	Direct Wt. %	Assays (%)			Percent Distribution		
		Tot. Fe	Fe ⁺⁺	Ti	Tot. Fe	Fe ⁺⁺	Ti
-30 + 100	34.4	16.2	13.8	0.34	38.7	37.8	30.8
-100 + 200	20.2	16.6	14.6	0.35	23.3	23.4	17.9
-200 + 400	17.9	14.4	12.4	0.43	17.9	17.6	20.5
-400	<u>27.5</u>	10.5	9.7	0.44	<u>20.1</u>	<u>21.2</u>	<u>30.8</u>
Calc'd Head	100.0	14.4	12.6	0.39	100.0	100.0	100.0

TABLE 2

Head Assays and Screen Size Distribution for Samples
Used in Electrostatic and Magnetic Separation Tests

Millbillillie Sample (-30 Mesh Grind)

Head Assay 14.2% Tot. Fe, 12.9% Fe⁺⁺, 0.36% Ti

U. S. Mesh Size	Direct Wt % Ret.	Assays (%)			Percent Distribution		
		Tot. Fe	Fe ⁺⁺	Ti	Tot. Fe	Fe ⁺⁺	Ti
-30 +200	72.74	14.30	13.50	0.37	75.8	76.8	69.4
200 x 400	11.97	13.31	12.39	0.42	12.6	11.6	13.3
-400	<u>15.29</u>	10.50	9.65	0.44	<u>11.7</u>	<u>11.5</u>	<u>17.3</u>
Calcd Head	100.00	13.73	12.78	0.39	100.0	100.0	100.0

Millbillillie Sample (-200 Mesh Grind)

Assay Head 14.4 % Tot. Fe 12.4% Fe⁺⁺ 0.43% Ti

Head Assay Not Available

-200 + 400	51.85	17.20	15.50	0.34	59.1	61.4	48.4
<u>-400</u>	<u>48.15</u>	12.80	10.50	0.39	<u>40.9</u>	<u>38.6</u>	<u>51.6</u>
Calcd Head	100.0	15.08	13.09	0.36	100.0	100.0	100.0

Millbillillie Sample (10 mesh Head Sample)

(after reducing -10 mesh +200 mesh to -200 mesh and screen)

-200 + 400	33.20	15.50	14.58	0.37	7.2	6.9	32.4
-400	56.70	13.95	12.90	0.37	56.2	56.2	56.8
-400	<u>10.10</u>	10.00	8.95	0.43	<u>36.6</u>	<u>36.9</u>	<u>10.8</u>
Calc'd Head	100.00	14.07	13.02	0.37	100.0	100.0	100.0

Magnetic Separation

Samples

The analyses and screen size distribution for the samples tested were described earlier.

Equipment, Procedures, and Results

Dry Magnetic separation was completed on campus in the Chemical Engineering Department, using the Frantz Isodynamic Separator at a series of current, forward and side slope settings. Ferromagnetic particles were removed by a head magnet before the separation. The data from these tests are summarized in Table 3. The concentrate produced at 0.35 AMP is identified as the final product. The data on the combined 0.35 x 1.25 AMP product is also given for comparison. The head assays for all the screen fractions tested are also noted. Individual test data are compiled in Appendix 2, and the analytical results in Appendix 3.

Discussion of Results

An analysis of the data will lead to the following conclusions:

1. Dry magnetic separation is effective only at sizes finer than 100 mesh (150 μm). In each case, dedusting of the sample to remove -400 mesh (37 μm) fines is essential.
2. The sample has to be ground to -200 (74 μm) mesh for magnetic separation to be effective.
3. The highest grade concentrate assaying 3.45 percent Ti was produced by magnetic separation of the -200 + 400 mesh screen fraction at a current setting of 0.35 AMP. This concentrate contained 21.2 percent of the titanium values in the screen fraction and accounted for 2.72 weight percent of the sample used in the test.

By changing vibrator feed rate, side slope, and forward slope settings, the Ti recovery can be increased to 52.4 percent, but the grade decreases to 0.98 percent Ti. The concentrate weight percent was 22.6 of the sample used in the testing.

The test results described above on the -200 + 400 mesh fraction of -30 mesh sample can be used to project grades and recoveries of the sample stage ground to -200 mesh as discussed below. By stage grinding, a -200 mesh sample can be produced that contains 48.4 percent of the titanium at a grade of 0.34 percent, as shown in Table 2.

Magnetic separation of the -200 + 400 mesh screen fraction of -200 mesh feed sample should

produce a concentrate accounting for 1.41 weight percent of the feed. This concentrate will analyze 3.45 percent Ti, and contain 10.3 percent of the Ti values in the feed.

By changing the magnetic separator settings, a lower grade concentrate assaying 0.98 percent Ti can be projected. The Ti recovery will increase to 25.4 percent. The concentrate weight will be 11.7 weight percent of the feed.

Electrostatic, Magstream, and Magnetic Separator

Samples

The analyses of samples tested and their screen size distribution are summarized in Table 2.

Test Procedures, Equipment, and Results

Two samples of Millbillillie #173 meteoric eucritic material at -10 US mesh and -30 US mesh sizes were tested at the Carpco Laboratories in Florida, with the principal objective of beneficiating the ilmenite. Processes evaluated included the following:

- o Vertical Electrostatic (ES) free-fall separation
- o Electrostatic (ES) plate separation
- o Rare-earth drum magnet separation (KHD)
- o High-tension (HT) ES roll separation
- o High-intensity lift roll magnet separation
- o Magstream gravity concentration

The equipment, flowsheet, and procedures used in the test program is contained in Carpco's report, and will not be discussed here. The Carpco report is attached as Appendix 1. All products were returned to the University of Arizona for detailed analyses by the principal investigator.

A total of twelve tests were completed. The flowsheet details of each of the tests can be found in Carpco's report in Appendix 1. All of the analytical data is compiled in Appendix 3. A summary of the test results is presented in Table 4.

Discussion of Results

Based on visual and binocular optical microscopic examinations during the course of the test program and the test results given in Table 4, the following conclusions are possible:

- o The -30 mesh sample responded poorly to ES free-fall, ES plate, and rare-earth drum magnet separation processes. This was due to the lack of liberation within the sample, and

TABLE 3

Summary of Frantz Magnetic Separation Data on Millbillillie Sample

Test #	Vibrator Setting	Forward Slope (°)	Side Slope (°)	Particle Mesh Size	Wt% of Feed	Wt% of Feed	Final Product*				Calcd Head (%)				
							Analyses (%)		Distribution (%)		Tot. Fe		Ti		Tot. Fe
T-2-1	6-4 AMP	15°	20°	-30 + 100	7.40	21.52	24.4	19.4	0.25	32.8	30.3	16.4	16.0	13.8	0.33
T-2-1-2	10	30°	20°	-30 + 100	7.73	22.46	16.3	13.6	0.37	25.4	24.4	22.0	14.4	12.5	0.38
T-1-1	6	15°	20°	-30 + 100	0.87	2.54	26.1	18.2	0.24	3.2	2.9	2.1	21.1	15.9	0.28
					33.71	97.98**	21.4	16.2	0.30	99.6	99.8	99.3	21.3	15.9	0.28
T-2-2	10	30°	20°	-100 + 200	6.97	34.52	24.2	19.9	0.36	50.8	49.3	38.4	16.4	13.9	0.34
T-1-2	6	15°	20°	-100 + 200	0.65	3.23	26.8	16.2	1.21	4.0	3.2	11.5	21.9	16.5	0.34
					18.89	93.49**	23.3	17.5	0.36	99.5	100.0	99.1	21.9	16.5	0.34
T-2-3	10	30°	20°	-200 + 400	4.05	22.64	25.8	20.2	0.98	36.4	31.7	52.4	16.0	14.4	0.42
T-1-3	6	15°	20°	-200 + 400	0.49	2.72	27.8	21.8	3.45	5.1	5.0	21.2	15.0	11.9	0.44
					13.44	75.07**	18.5	15.1	0.63	92.4	95.8	93.1	15.0	11.9	0.44
From PR Report 1		25°	15°	-30 + 400	44.59	61.50	17.7	15.4	0.36	66.4	68.1	62.9	16.3	13.9	0.35
Head Assay				-30 + 100		34.4	16.2	13.8	0.34	38.7	37.8	30.8			
Head Assay				-100 + 200		20.2	16.6	14.6	0.35	23.3	23.4	17.9			
Head Assay				-200 + 400		17.9	14.4	12.4	0.43	17.9	17.6	20.5			
Head Assay				-400		11.4	10.5	9.7	0.44	20.1	21.2	30.8			

*0.35 AMP Product **0.35 x 1.25 AMP Product

TABLE 4

Summary of Electrostatic and Magnetic Separation Data on Millblindle Sample

Test #	Process	Particle Mesh Size	Final Product				Distribution (%)				Calcd Head (%)				
			Wt%	Tot. Fe	Fe ⁺²	Ti	Tot. Fe	Fe ⁺²	Ti	Tot. Fe	Fe ⁺²	Ti	Tot. Fe	Fe ⁺²	Ti
1	Single Pass, High Tension ES	-30 mesh (100% of feed)	1.05	16.90	10.00	0.65	1.3	0.8	1.9	13.5	13.0	0.36			
2	ES free fall separation	-30 mesh (100 % of feed)	products not assayed												
3	Screen sizing and distribution	only -400 mesh analyzed	products not assayed												
3A	Screen size distribution after grinding	-200 mesh product											15.1	13.1	0.36
4	Single pass ES	-30 mesh -- Products to Test 5													
5	ES -2 pass conductor retreat	-200 + 400 mesh (12% of -30 mesh sample)	5.56	19.05	15.80	2.73	7.6	7.1	39.1	14.0	12.3	0.39			
6	Screen sizing and grinding														
7	ES-2 pass non-conductor retreat + Lift Magnetic Separator	-200 + 400 mesh (33.2% of -200 mesh sample)	5.44	20.10	18.70	0.74	7.1	7.0	10.5	15.5	14.6	0.39			
8	ES-2 Pass non-conductor retreat	-200 + 400 mesh (51.9% of -200 mesh sample)	30.29	18.20	16.60	0.60	32.1	32.3	52.1	17.2	15.6	0.35			
9	Screen for Magstream tests	-30 mesh											13.7	12.8	0.39
10	Magstream spn. --S. G. 4.25	-200 + 400 mesh (12.0% of -30 mesh sample)	14.77	21.5	20.30	0.94	23.5	24.2	33.2	13.3	12.4	0.42			
11	Magstream spn. --S. G. 4.25	-30 + 200 mesh (72.7% of -30 mesh sample)	4.35	21.25	18.40	0.34	6.1	6.2	4.1	15.2	13.0	0.36			
12	ES + Magstream sepn. of conductors from Test 8 at S. G. 4.25	-200 + 400 mesh (conductors were 15.7% of -200 mesh sample)	46.11	22.60	20.20	0.73	57.6	63.9	60.5	18.1	14.6	0.56			

the presence of fines (Tests 1,2,and 3). The free-fall ES separator appeared to be effective in separating the fines from the coarse sizes. It could be useful in dedusting lunar samples.

- o A single pass ES of the -200 + 400 fraction of the -30 mesh sample produced a conductor with 4 weight percent of the feed to the test in Test 4. After visual examination of the products under the microscope, the products were recombined for the two-pass ES test described below.

- o The most significant physical upgrading was achieved in a Two-pass High Tension Electrostatic Roll Separator. The feed to the test consisted of the 200 x 400 mesh fraction of the -30 mesh sample. The 200 x 400 mesh fraction constituted 12 percent of the sample assayed 0.42 percent Ti, and contained 13.3 percent of the Ti values as shown in Table 2. The conductor material from the first pass was retreated in a second stage to produce a concentrate analyzing 2.73 percent Ti, with 39 percent Ti recovery. The two-pass conductor retreat product accounted for 5.44 weight of feed to the test, or 0.67 percent of the original -30 mesh sample, as shown in Test 5 results in Table 4. It is most probable that a single pass ES separation was just as effective as the two-pass ES test, since the conductor weight percentages were comparable on both tests.

- o By projecting the above results to a -200 mesh grind, a two-pass ES conductor retreat product accounting for 2.88 weight percent of the total feed analyzing 0.39 percent Ti should be possible. This product is expected to analyze 2.73 percent Ti, with 18.9 percent recovery of the Ti values in the total feed sample.

- o Attempts to improve ilmenite recovery by scavenging ilmenite values by using a ES two-pass non-conductor retreat method were not effective, as can be seen from the results of Test 8. The increased Ti recovery of 52 percent was gained at the expense of a lower grade of 0.74 percent Ti. Magstream separation of the conductors from Test 8 at an apparent specific gravity (S. G.) of 4.25, upgraded the composite conductor only slightly from 0.60 percent Ti to 0.73 percent in the heavies.

- o Magstream separation did not improve the grade of the ES conductor product in Test 7.

- o Magnetic separation of the ES two-pass conductor retreat product upgraded the Ti only marginally from 0.60 percent Ti to 0.74 percent Ti, with significant Ti recovery losses.

- o Magstream gravimetric separation of -30 + 200 screen fraction at an apparent S. G. of 4.25 was not effective in Test 11 in upgrading the heavy fraction, due to the presence of unliberated ilmenite grains at this particle size. By contrast, the heavy fraction from the -200 + 400 screen fraction (with a significant proportion of liberated ilmenite grains) was upgraded from 0.42 percent Ti to 0.94 percent Ti with 33.2 percent Ti recovery in a concentrate representing 14.8 weight

percent of the feed to the test, contained 19.3 percent of the Ti values, with an assay of 1.37 percent Ti. The combined product would be 20.7 weight percent, with an analysis of 1.06 percent Ti, and 52.6 percent Ti recovery. The metallurgical efficiencies and recoveries of the combined products would be comparable to the previous Magstream test data reported earlier in Reference 1.

- o The above results can be projected to a -200 mesh grind sample, containing 51.9 percent as -200 + 400 mesh, and 48 percent of the Ti values. Magstream separation would thus produce a heavy concentrate with 10.74 weight percent, and 27.3 percent recovery at a grade of 1.06 percent Ti. It would be interesting to determine if ES roll separation of this heavy fraction would improve grade with minimum recovery losses.

Conclusions

- o Dry magnetic separation in a Frantz Isodynamic Separator was effective at 200 mesh and finer sizes. It should be possible to produce a concentrate analyzing between 1 percent Ti and 3.5 percent Ti, corresponding to Ti recoveries between 25.4 percent and 10.3 percent. The concentrate weight will be between 11.7 percent and 1.4 weight percent of the feed. The feed to the test was 0.39 percent Ti.

- o A two-pass dry Electrostatic Roll Separator produced a concentrate analyzing 2.73 percent Ti, with 18.9 percent Ti recovery. The concentrate weight percent was 2.9 percent of the feed.

- o Wet gravimetric-magnetic separation in the Magstream apparatus was successful in producing a concentrate analyzing 1.06 percent Ti with a concentrate weight of 14.8 percent of feed and Ti recovery of 52.6 percent.

- o The vertical V-STAT Electrostatic free-fall separator appeared to hold promise for dedusting samples.

Recommendations

Future work along the following lines is recommended on the Euclite Sample:

- o Wet Magstream, followed by dry ES roll separation of the heavy fraction.
- o Dry Magnetic separation, followed by dry ES roll separation.
- o Test V-Stat separator for efficiency of dedusting.
- o Complete SEM and EDS scans of concentrates produced from tests with the ES two-pass separator, and the Frantz Magnetic Separator.

The additional data to be generated on the euclite will determine the scope of process engineering, and scientific studies on the very limited quantities of lunar material (5 to 10 grams) to be made available in 1993.

References

1. Ramadorai, G. and R. Dean. *Beneficiation of Ilmenite from Lunar Analog: Progress Report Number One* (June 1, 1991 - June 2, 1992). University of Arizona/NASA Space Engineering Research Center, May 29, 1992.

2. Ramadorai, G. and R. Dean. *Beneficiation of Ilmenite from Lunar Analog: Progress Report Number Two* (June 1992 - October 1992). University of Arizona/NASA Space Engineering Research Center, October 16, 1992.

497590
N93-26682

Extraction of Volatiles and Metals from Extraterrestrial Materials

J. S. Lewis

**Lunar and Planetary Laboratory
University of Arizona**

58-25
158355
P-9

Abstract

Recent progress in defining the physical, orbital, and chemical properties of the Earth-crossing asteroid and comet population has been integrated into an elaborate Monte Carlo model of the fluxes of bodies in the inner Solar System. This model is of use in projecting flight opportunities to as-yet undiscovered near-Earth objects and in assessing the impact hazard to life on Earth and the evolutionary consequences of impacts on the other terrestrial planets. We also have made further progress in defining desirable transportation system architectures for the use of non-terrestrial volatiles and metals, including the delivery of propellants to near-Earth space for fuelling of SEI-type expeditions, the construction and resupply of Solar Power Satellite constellations in various Earth orbits (including GEO and Highly Eccentric Earth Orbit (HEEO)), and retrieval of ^3He for use as a clean fusion fuel on Earth. These studies suggest a greater future role for SERC in the exploration of space energy sources to meet Earth's 21st-century energy requirements. Laboratory studies of volatilization and deposition of ferrous metal alloys have demonstrated deposition of strong iron films from carbonyl chemical vapor deposition (CVD), showing the crucial role of additive gases in governing the CVD process, and pointing the way to specific experiments on extraction and deposition of ferrous metals from nonterrestrial materials.

General Research Program

This project includes research into three basic areas: prospects for accelerating the development of non-terrestrial sources of energy for Earth using non-terrestrial propellants and structural materials; transportation system studies on the most efficient return of non-terrestrial materials to near-Earth space for use in large-scale future space activities; and carbonyl processing of nonterrestrial ferrous native metals. In addition, this project includes oversight over SERC science program activities and travel for the purposes of developing research collaborations at other research centers and in industry. These activities are treated separately below.

Energy for Earth from Space

Over the past two years we have carried out preliminary studies of two different schemes for providing energy for Earth from space. These studies suggest that the energy needs of Earth in the 21st century can plausibly be met economically, and with diminished environmental impact, by either building Solar Power Satellites from asteroidal materials in Highly Eccentric Earth Orbit (HEEO) or by returning ^3He from the atmosphere of Uranus for use as a clean fusion fuel in reaction with terrestrial deuterium.

HEEO (in our reference example, 6000 to 400000 km altitude) has several considerable advantages relative to GEO as a site for construction of SPS constellations: 1) It is more accessible than GEO via chemical launch from Earth, the Moon, and near-Earth asteroids. 2) From HEEO there is much easier access to Earth than from GEO (a delta V of under 100 m/s vs. 1461 m/s for return to atmospheric entry), easier access to the Moon than from GEO (2900 vs. 3500 m/s), and easier access to the typical NEA than from GEO (3000 vs. 5400 m/s). 3) The radiation hazard in HEEO is no worse than in GEO, and the cost of providing shielding from any source will always be less in HEEO. 4) The high MPBRs available for return of asteroidal material suggested a careful look at a variety of boot-strapping schemes for return of large masses of asteroidal material to HEEO, using propellants derived from asteroids.

Alternatively, commercial production of electric power from fusion of ^3He with deuterium may be shown to be technically feasible. If so, then: 5) the preferred source for the ^3He is the atmosphere of Uranus, 6) ^3He return from Uranus requires two crucial items of new technology: a nuclear rocket stage using hydrogen as the working fluid and a "hot air balloon" filled with warm hydrogen to suspend the processing package in the uranian atmosphere. 7) Processing of the ambient atmosphere to separate helium from hydrogen and methane and to separate the isotopes of helium

can be done using a small subset of the equipment required to extract ^3He from lunar regolith. Among the features of the lunar scheme that may be omitted entirely are a) the need to mine 10^8 tonnes of dirt per tonne of ^3He , b) the need to beneficiate and size minerals, c) the energy needed to heat 10^8 t of regolith to roughly 1000oC, d) the need for high process temperatures, e) the need to design around a two-week hot day and a two-week cold night, which creates severe temperature-cycling stresses and interrupts continuous processes, and f) the need to handle a wide range of reactive gases along with the ^3He .

Transportation System Architectures

Motivated in large part by the study of possible locations for SPS constellations summarized above, we have looked at a variety of bootstrapping schemes for return of nonterrestrial propellants and metals to near-Earth space. These studies, begun last year, originally involved space stations in highly eccentric Earth orbit as fuel-manufacture sites, near-Earth asteroids as sources of water, and both solar thermal and nuclear thermal "steam rockets" as the means of transport. Single-trip asteroid missions from HEEO were so promising that we were led to consider using the spacecraft for multiple round trips. Constraining the spacecraft specific impulse to 180 to 220 seconds (cool thrust chambers; very long operational lifetimes) and allowing a spacecraft operational life of 10 to 15 years (three round trips to a carbonaceous NEA by each spacecraft) we have demonstrated that real multiple-mission sequences to known near-Earth asteroids of probable C-type composition can provide mass payback ratios of about 100:1. Table 1 presents the model mass-payback ratio calculated for three round trips to a "typical good" NEA (a composite of the dozen best-known NEAs): case A3 in the Table assumes all delta V maneuvers above LEO, including capture into Earth orbit, are carried out using asteroid-derived water as the propellant. Case A4 uses, instead of propulsive capture, an asteroid-derived aerobrake. Table 2 shows that, for the same target asteroid, use of asteroidal propellant returned on the first mission to fuel an "armada" of retrieval vehicles can raise the mass payback to over 100:1. Table 3 documents a series of missions by a single spacecraft to the most accessible known C-type asteroid, 1977 VA. If the "armada" scheme is used from a base in HEEO, MPBRs over 50 can be achieved, as shown in Table 4. Finally, if the initial fueling of the "armada" is carried out in LEO, with all subsequent operations based in HEEO, the MPBR rises to over 80.

These logistic studies, in calling attention to several very attractive features of missions to retrieve materials from near-Earth asteroids, have served to motivate a more careful look at the mass budget, logistic systems design, and processing equipment requirements for realization of schemes

Table 1

Mass Payback Ratios
(three round trips; typical "good" asteroid)

Mission	Return to LEO	Return to GEO	Return to HEEO
E1	1.000	0.334	0.418
A3	3.7	7.8	16.6
A5	24.3***	15.9***	24.9**

* Assuming an aerobrake mass fraction of 0.2 (moderate energy dissipation)

** Assuming an aerobrake mass fraction of 0.3 (high energy dissipation)

Table 2

Mass Payback Ratios
(one trip for fuel; typical "good" asteroid; three-trip "Armada")
(all water returned on first trip used as fuel for new vehicles)

Mission	Return to LEO	Return to GEO	Return to HEEO
E1	1.000	0.334	0.418
A3	6.9	10.8	35.2
A5	92.0***	24.2***	115.0**

* Assuming an aerobrake mass fraction of 0.2 (moderate energy dissipation)

** Assuming an aerobrake mass fraction of 0.3 (high energy dissipation)

Table 3
Mass Payback Ratios
 (four round trips for fuel to 1977 VA)

Earth Launch Date	dV outbound	dV inbound	Earth Arrival	MPBR
Nov 1990	5712	473	Nov 1995	7.0
Nov 1995	2367	316	Nov 2000	14.
Nov 2000	2322	1675	Nov 2005	21.
Nov 2005	2566	776	Nov 2005	28.

This model illustrates real multiple round trips to a single typical good asteroid, using trajectories from Lau and Hulkower (1985).

Original departure is from LEO, and all returns to Earth use an asteroid-derived aerobrake with a mass fraction of 0.2 (moderate E dissipation) to return to HEEO. Outbound propulsion for the first trip is H/O lifted from Earth; on subsequent trips it is H/O made by electrolysis of asteroidal water. Inbound propulsion is by solar thermal steam engine.

Table 4
Mass Payback Ratios
 (one trip for fuel to 1977 VA; three-trip "Armada")
 (all water returned on first trip used as fuel for new vehicles)

Earth Launch	Number of vehicles	dV out m/s	dV in m/s	Earth Arrival	Water Mass in HEEO (t)	MPBR
Nov 1990	1	5712	473	Nov 1995	100	7.0
Nov 1995	52	2367	316	Nov 2000	5200	17.6
Nov 2000	52	2322	1675	Nov 2005	10300	35.0
Nov 2005	51	2566	776	Nov 2010	15400	52.3

This model illustrates real multiple round trips to a single typical good asteroid, using trajectories from Lau and Hulkower (1985). All water returned by the first mission is used to fuel an "Armada" of vehicles delivered to HEEO from Earth. The lifetime of each vehicle is three missions (15 years).

Original departure is from LEO, and all returns to Earth use an asteroid-derived aerobrake with a mass fraction of 0.2 (moderate E dissipation) to return to HEEO. Outbound propulsion for the first trip is H/O lifted from Earth; on subsequent trips it is H/O made by electrolysis of asteroidal water. Inbound propulsion is by solar thermal steam engine.

to use propellants and metals derived from NEAs. In the 1992-1993 budget year we shall be applying the Figure-of-Merit (FoM) software developed at SERC by Ramohalli and his students to the assessment of the overall desirability of retrieval of asteroidal material. This will entail joint support of one engineering graduate student by Ramohalli and Lewis.

Gaseous Carbonyl Process

One of the most important results arising in this project over the past year and a half has been the result of a close and fruitful interaction with a consultant, William C. Jenkin, who is the leading developer of carbonyl chemical vapor deposition (CVD) technology in the world. We have been working with him for over a year on the problem of how best to handle iron carbonyl extracted from non-terrestrial ferrous metal alloys. Iron is the dominant constituent (40 to 93%) of native metals found in meteorites and in asteroidal metal fragments found in the lunar regolith. It is also the dominant metal in the metallic cathode deposits produced by electrolysis of molten lunar silicates, and is formed in large quantities and with a rather high degree of purity (99%) during the reduction of lunar ilmenite. Carbonyl extraction of iron from native Fe-Ni alloy has been demonstrated on a small scale in our own laboratory, but the disposition of the resulting iron pentacarbonyl vapor and liquid is unclear. Iron carbonyl CVD is never used for manufacture of strong metal components because of the tendency to precipitate a very fine-grained powder during thermal decomposition. This iron powder is of exceptional purity and of great metallurgical interest; indeed, it is the source of almost all the analytical-grade iron in the world market. However, the iron powder was something of a disappointment compared to the results of nickel tetracarbonyl CVD, which can quickly fill molds with bright, full-density, very strong nickel. Under similar circumstances, iron carbonyl leaves a mechanically weak, black deposit with a high carbon content. Jenkin, however, brought to our attention some unpublished laboratory experiments in which ammonia is added to the iron carbonyl to suppress carbon codeposition during production of analytical-grade iron powder. He suggested that we examine the effects of addition of ammonia during attempts to plate out tough iron films. Also, based on his own earlier experience, he suggested a similar experiment with water vapor as an additive. (All runs have added hydrogen and carbon dioxide).

The experiments with ammonia last year turned out promising results: two runs at 210 and 230°C with both ammonia and carbon dioxide added both produced bright, tough films, but unfortunately both developed stress cracks and partially peeled off the mandrel surface. But a run with water vapor, carbon dioxide and no ammonia looked even better, without spalling, and remained mirror-bright as long as deposition continued, but closer examination of the surface again shows

Table 5

Mass Payback Ratios
 (one trip for fuel to 1977 VA; three-trip "Armada")
 (all water returned on first trip used as fuel for new vehicles in LEO)

Earth Launch	Number of vehicles	dV out m/s	dV in m/s	Earth Arrival	Water LEO	Mass HEEO	MPBR
Nov 1990	4	5712	473	Nov 1995	400	0	7.0
Nov 1995	44	5712	316	Nov 2000	4	4400	29.1
Nov 2000	44	2322	1675	Nov 2005	4	7964	54.0
Nov 2005	40	2566	776	Nov 2010	4	11888	80.3

This model illustrates real multiple round trips to a single typical good asteroid, using trajectories from Lau and Hulkower (1985). All water returned by the first mission is used to fuel an "Armada" of vehicles delivered to LEO from Earth. The lifetime of each vehicle is three missions (15 years).

Original departure is from LEO and first return is to LEO. All returns to Earth use an asteroid-derived aerobrake with a mass fraction of 0.3 (to LEO) or 0.2 (to HEEO). Outbound propulsion for the first trip is H/O lifted from Earth; on subsequent trips it is H/O made by electrolysis of asteroidal water. Inbound propulsion is by solar thermal steam engine.

extensive cracking. The literature does not report reactions of ammonia with iron carbonyls to displace carbon monoxide (as happens with nickel carbonyl), and it is possible that the participation of ammonia begins with partial decomposition of ammonia and leads to nitriding of the iron surface, and hence to embrittlement.

Analyses of the metal film deposited without ammonia show about 3.9% oxygen and 1.6% carbon, nearly the same proportion as in carbon dioxide. Adsorbed and trapped carbon dioxide gas, not a bizarre alloy, may be responsible for this contamination. Jenkin suggests that deposition at lower pressures may alleviate this problem.

In general, carbon dioxide helps reduce the carbon content of the deposit, but increases the oxygen content. Water, at high concentrations, of course also is an important source of oxygen. Hydrogen suppresses the oxidation of the deposit by carbon dioxide, while helping keep the carbon content

low. The impurity then approaches a C:O molar ratio of 1:2.

It seemed reasonable to try a run with only carbon dioxide as the carrier gas. The resulting deposit was bright, tough, adherent, and had a high deposition rate-- the best yet! Again, the «PG» impurity had the stoichiometry of carbon dioxide, and may be susceptible to removal by exposure to lower pressures or higher temperatures. A similar run with a little added hydrogen produced chemically similar results but had an even higher deposition rate. This year we had hoped to pursue these leads and begin experiments with mixtures of iron and nickel carbonyls, but the Akron fire department shut down Jenkin's laboratory in January 1992. It is reopening within the month, and we hope to resume experiments soon thereafter.

We are making clear progress toward the goal of direct deposition of iron with desirable physical properties. Experiments involving lower pressures, outgassing at higher temperatures, and codeposition of iron and nickel are all planned for Jenkin's laboratory. Here at SERC we are prepared to extend our experiments on carbon monoxide volatilization of ferrous metal alloys of interest in the space resources arena, including native lunar and asteroidal metals and metallic byproducts from schemes for lunar oxygen production. These experiments will require the services of a research staff member with a background in chemical research and experience in carbonyl handling. Fortunately, Dr. Muralidharan, who has played a major role in the development of schemes for platinum-group metal separations under SERC sponsorship, will be available to devote half his time to this project.

Relevant Publications

1. Lewis, J.S. and R.A. Lewis. *Space Resources: Breaking the Bonds of Earth*. New York: Columbia University Press (1987).
2. Lewis, J.S. Extraterrestrial resources. In *Space Manufacturing 6*, AIAA, Washington, D.C. (18) 1987.
3. Lewis, J.S., T.D. Jones, and W.H. Farrand. Carbonyl extraction of lunar and asteroidal metals. In *Engineering, Construction and Operations in Space*, S.W. Johnson and J.P. Wetzel, eds. New York: Amer. Soc. Civil Engineers (1988).
4. Jones, T.D., L.A. Lebofsky, J.S. Lewis, and M.S. Marley, The composition and origin of the C, P and D asteroids: Water as a tracer of thermal evolution in the outer belt. *Icarus* 88 (1990): 172-92.
5. Lewis, J.S. Lunar, Martian and asteroidal resources: Programmatic considerations. In *Proceedings of the 1989 Annual Invitational Symposium on Space Mining and Manufacturing*. UA/NASA Space Engineering Research Center (1990): 1-10.

6. Lewis, J.S. Nonterrestrial resources. In *Space Manufacturing 7* (1990): 5-10.
7. Lewis, J.S. Asteroid resources. In *Proceedings of the La Jolla Workshop on Space Resources*. In press (1990).
8. Lewis, J.S., K. Ramohalli, and T. Triffet. Extraterrestrial resource utilization for economy in space missions. International Astronautical Federation, IAA 90-604 (1990).
9. Lewis, J.S. Extraterrestrial sources of ^3He for fusion power. *Space Power* 10 (1991): 363-72.
10. Lewis, J.S. Construction materials for an SPS constellation in highly eccentric Earth orbit. *Space Power* 10 (1991): 353-62.
11. Lewis, J.S. Non-terrestrial resources of economic importance to Earth. IAF 91 (1991).
12. Lewis, J.S. and M.S. Matthews, eds., *Resources of Near-Earth Space*. Tucson: University of Arizona Press (in press, 1992).
13. Swindle, T.D., J.S. Lewis, and L.A. McFadden. The case for planetary sample return missions, 4: Asteroids. *EOS* 72 (1992): 473-80.
14. Lewis, J.S. and M.L. Hutson. Asteroidal resource opportunities suggested by meteorite data. In *Resources of Near-Earth Space*. J.S. Lewis and M.S. Matthews, eds. Tucson: University of Arizona Press (in press, 1992).
15. Lewis, J.S., D.S. McKay, and B.C. Clark. Using resources from near-Earth space to meet human needs. In *Resources of Near-Earth Space*. J.S. Lewis and M.S. Matthews, eds. Tucson: University of Arizona Press (in press, 1992).
16. Lewis, J.S. Cometary and asteroidal bombardment of Earth: Monte Carlo simulation. In preparation, 1992.
17. Lewis, J.S. Nonterrestrial resources. In *Space Manufacturing 8* (in press 1992).
18. Lewis, J.S. Processing of non-terrestrial materials. *SME* (invited, 1992).
19. Lewis, J.S. Logistical implications of water extraction from near-Earth asteroids. In preparation, 1992.

497591

N 9 3 - 2 6 6 8 3

Oxygen Production on Mars and the Moon

K.R. Sridhar¹, B. Vaniman², S. Miller²

Department of Aerospace and Mechanical Engineering

The University of Arizona

S9-31
158356
p-15

Abstract

Significant progress has been made in the area of in-situ oxygen production in the last year. In order to reduce sealing problems due to thermal expansion mismatch in the disk configuration, several all-Zirconia cells have been constructed and are being tested. Two of these cells have been run successfully for extended periods of time. One was run for over 200 hours and the other for over 800 hours. These extended runs, along with gas sample analysis, have shown that the oxygen being produced is definitely from CO₂ and not from air leaks or from the disk material. A new tube system is being constructed that is more rugged, portable, durable and energy efficient. The important operating parameters of this system will be better controlled compared to previous systems. An electrochemical compressor will also be constructed with a similar configuration. The electrochemical compressor will use less energy since the feedstock is already heated in the separation unit. In addition, it does not have moving parts.

¹Assistant Professor, Department of Aerospace and Mechanical Engineering, University of Arizona

²Graduate Student, Department of Aerospace and Mechanical Engineering, University of Arizona

Introduction

With the forthcoming missions to Mars and the Moon, one way of reducing launch costs is in-situ production of propellant. Since oxygen represents most of the propellant mass, in-situ production of oxygen could provide a dramatic savings in launch mass and therefore launch costs. Thus the motivation for development of a production plant is very strong from an economic point of view. There are many components to consider for such an oxygen production plant, but the main focus of this study is the separation of oxygen from carbon dioxide. The first part of this report will focus on the electrochemical issues of oxygen separation using a disk configuration. The second part will describe the work being conducted in designing a device using tubular cells to separate oxygen and compress it. Basically, the CO_2 is heated to high temperatures where it dissociates into CO and O_2 . The oxygen is then separated from the CO using an electrochemical separation cell. The details of this process are described in [1]. The separation cell, shown in *Figure 1*, consists of a solid Zirconia electrolyte with a precious metal electrode on either side. There are several properties of the electrolyte and the electrode which determine the performance of the cell. One example is that the electrode must be porous enough to allow the oxygen to pass through it but solid enough to be a good electrical conductor. The selection of the optimal electrode and electrolyte materials and understanding the long duration performance of the cell is the objective of the tests conducted on the disk system. This is described in Part A of the report. Tubular electrochemical cells have been used to build proof-of-concept and scale-up testbeds for oxygen production. Details on the design and performance of these systems can be found in [1]. The experience and knowledge gained in operating these systems have been incorporated into developing a new electrochemical cell cluster that has four tubular cells. This new cluster eliminates the problem elements of previous systems. In addition, the design is more robust, easily repairable and more energy efficient. The same cluster can also be used to compress oxygen to higher pressures for liquification and storage. The progress in these areas is described in Part B.

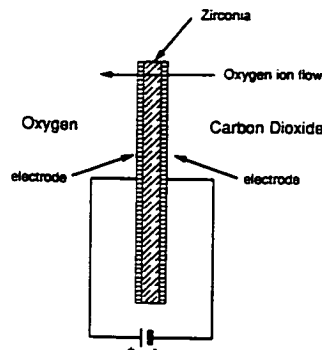


Figure 1 - Electrochemical Separation Cell, Disk Geometry

Part A: Electrochemical Separation of Oxygen From

Carbon Dioxide -- Disk Geometry

Graduate Student: Brian Vaniman

The progress that has been made to date on the disk geometry for the electrochemical cells is discussed here.

Electrolyte and Electrode

The electrolyte used in this study is Ytria stabilized Zirconia (ZrO_2 - Y_2O_3 8% mole). The precious metals Silver and Platinum as well as the perovskite Lanthanum Strontium Manganate (LSM) have been selected as electrode material. The details concerning the choice of these materials are outlined in [1].

Electrolyte Fabrication

There are two techniques being used to fabricate the electrolyte, cold pressing and tape casting. Cold pressing involves mixing the ceramic powder with a dry, powdered binder which is poured into a metal die and uniaxially pressed under 12 to 14 tons of force. The tape casting process is somewhat more complicated. The ceramic powder is mixed with an acrylic binder and ball milled to produce a smooth slurry. This slurry is then poured onto a sheet of glass and a blade is drawn over it to produce a uniform thickness layer of material. After drying, the disk shape can be cut out of the tape. At this point, disks produced by either method must be sintered to evaporate the binder and leave a solid Zirconia disk. The sintering process consists of ramping and holding the temperature at several different levels until the maximum sintering temperature is reached, and then ramping back down. The cold pressed disks are sintered to 1650 °C and the tape cast disks are sintered to 1340 °C. The disks are placed in a Zirconia firing plate and covered with Zirconia powder to keep them from warping during the sintering process. The disks that were cold pressed resulted in flat disks 2.9 cm in diameter and .064 cm thick. The disks from the tape casting could not be fired flat and came out wavy around the edge. These disks were made very thin (~13 mm) and were very brittle. The furnace used to sinter these disks had the capability to ramp at intervals of 1 °C/min. The firing schedule called for a ramp rate of .24 °C/min at some points. Future tape cast disks will be sintered in a furnace with higher resolution ramp rate in an attempt to remove the waviness.

Electrode Application

The electrode material is commercially available in paste form. Hereaus Products Silver and Platinum pastes thinned with ethanol were used. Also used was a LSM paste consisting of LSM in an organic binder thinned with Toluene. The paste is applied to the disk with a swab in a thin layer. Then a connecting wire is dabbed with the paste and laid on the electrode. The disks, with electrode, are then fired to set the paste.

System Testbed

A schematic drawing of the system testbed is shown in *Figure 2*. The CO₂ is supplied by a bottle and is fed into the system through a flowmeter which is used to control the flow rate. The CO + CO₂ exhaust is vented to the air or connected to an oxygen meter to check for air leaks. The O₂ produced flows out through a very sensitive flowmeter and is then either vented to the air or connected to the oxygen meter. There is also a system for collecting the CO + CO₂ exhaust and the O₂ produced in gas sampling bottles which can then be taken to a gas chromatograph or mass spectrometer for analysis. The ZrO₂ cell is raised to temperatures of 800 - 1000 °C using a ceramic clam-shell heater. The heater is controlled by a QuickBasic program running on a PC which reads the temperature of the cell from a thermocouple. The program controls ramping the system up to temperature and holding at temperature. The cell voltage is supplied by an Acopian power supply and two meters measure the voltage across and the current through the disk. The heater and Zirconia cell are surrounded in Kaowool insulation to reduce heat loss.

A schematic drawing of the ZrO₂ cell is shown in *Figure 3*. The disk with electrodes and connecting wires is sandwiched between two Coors Ceramics Zirconia manifolds and cemented together with Aremco's Ceramabond 569 ceramic cement. Prior to this the manifolds have holes drilled in them for the CO₂ feed tube, the CO + CO₂ exhaust tube and the O₂ production tube as well as smaller holes for the connecting wires. The tubes, which are made of alumina (Al₂O₃), and wires are also cemented to the manifolds. The cell is then fired to set the cement. Previously, aluminum silicate had been used for the manifolding material, but there were sealing problems due to thermal expansion differences between the Zirconia disk and the manifold. With the Zirconia manifolds, this aspect of the sealing problem has been eliminated. It should be noted that thermal expansion mismatches still occur due to geometric differences, however this mismatch is not as severe.

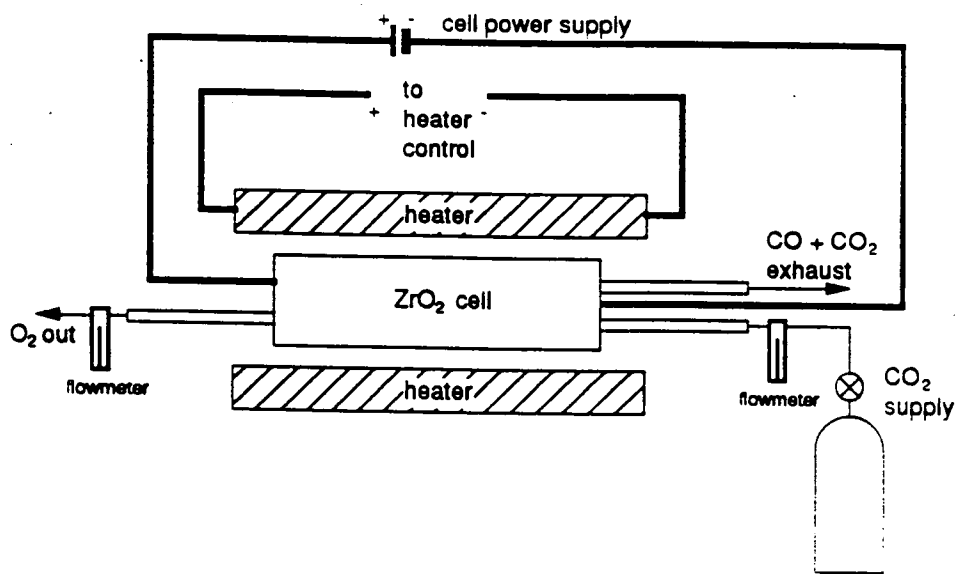


Figure 2 - System Testbed For Disk Geometry

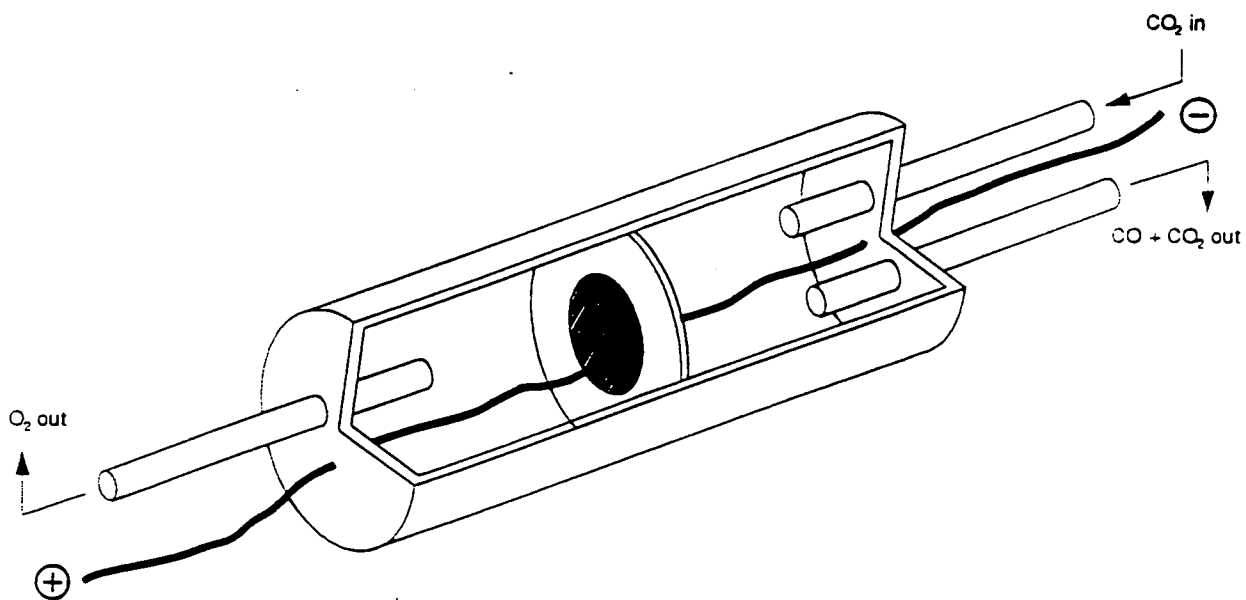


Figure 3 - Cutaway Of ZrO_2 Cell

Results and Discussion

In the last two months, two extended cell runs have been made. The first cell consisted of a cold pressed disk with a Platinum electrode and platinum connecting wires. The potential across the cell was between 1.71 and 1.78 Volts and the cell was at a temperature of 950 °C. This cell was run for over 200 hours and produced oxygen very consistently at approximately .4 cc/min. The oxygen production over time is shown in *Figure 4*. Mass spectrometer analysis of the CO + CO₂ exhaust and the O₂ production gave the gas percentages shown in Table 1.

	Nitrogen	Oxygen	Carbon Monoxide	Carbon Dioxide
CO + CO ₂ exhaust	13.9	0.1	3.6	82.3
O ₂ production	65.0	31.0	not detected	3.0

Table 1 – Gas percentages for first cell

The large amounts of nitrogen on both sides of the cell would indicate an air leak in the cell. When the cell was examined after the run, a crack was found on the CO₂ side of the manifold. This would explain the presence of nitrogen on that side. The nitrogen on the O₂ side could be from diffusion of air into the sample bottle since the flow rate of oxygen is very small (~ .4 cc/min).

The second cell is identical in construction to the first and at the writing of this report is still running. It has been running for over 800 hours and is still producing oxygen consistently at approximately .35 cc/min. The cell potential is between 1.68 and 1.75 Volts. The oxygen production over time for this cell is shown in *Figure 5*. Mass spectrometer analysis of the CO + CO₂ exhaust and the O₂ production gave the gas percentages shown in Table 2.

	Nitrogen	Oxygen	Carbon Monoxide	Carbon Dioxide
CO + CO ₂ exhaust	4.5	0.3	13.7	81.6
O ₂ production	35.3	64.3	not detected	0.4

Table 2 – Gas percentages for second cell

The low amounts of nitrogen and oxygen on the CO₂ side of the cell indicate that there was probably no air leak on that side. Additional proof of this was given by connecting the oxygen meter to the CO + CO₂ exhaust and measuring a value of 0.0% oxygen. This goes to show that the

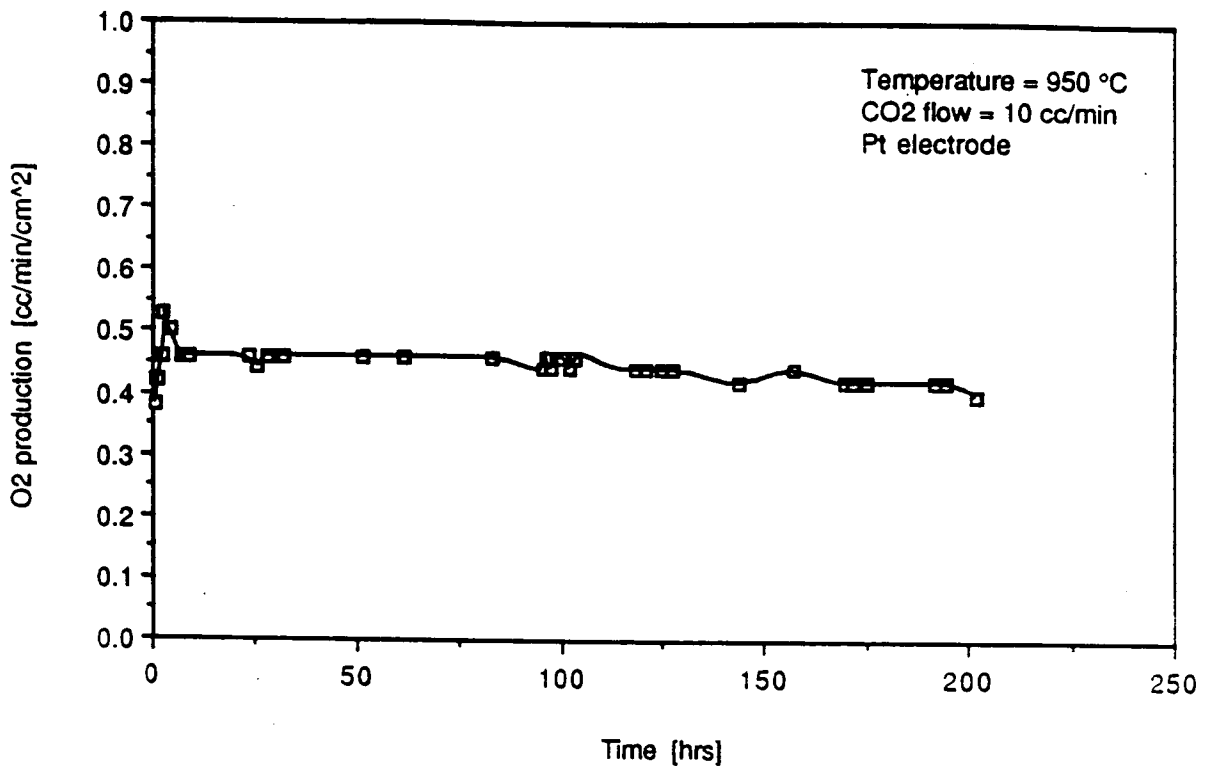


Figure 4 - Cell #1 Performance

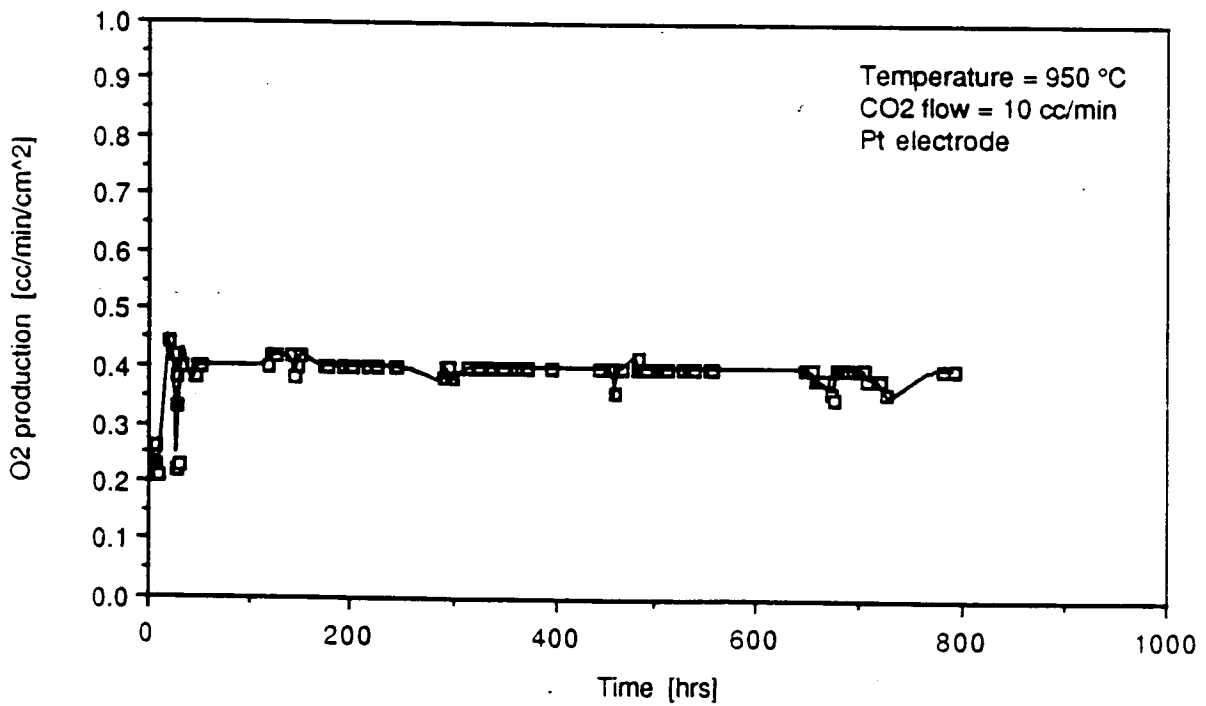


Figure 5 - Cell #2 Performance

oxygen being produced is from the CO₂ and not from air. More proof of this is that .35 cc/min of O₂ produced should show up as .7 cc/min of CO on the exhaust side. Knowing the exhaust flow rate of 10 cc/min, the percentage of CO should be about 7%. Since the percentage measured in the gas analysis is at least this much, it can be said that the oxygen is being produced from CO₂, not air. The nitrogen on the O₂ side could again be from diffusion of air into the sample bottle.

There is also speculation that the oxygen is coming from the disk itself, and not CO₂, since it does contain oxygen. However, a very simple calculation will show that the amount of oxygen in the disk would only last for approximately 24 hours at a flow rate of .4 cc/min. Due to their extended run times, both of these runs show that this is not the source of the oxygen produced.

An additional test was performed on the second cell. This was to see how the CO₂ flow rate effected the O₂ production. The results of this test are shown in *Figure 6*. It can be seen that at a CO₂ flow rate of 3 cc/min and higher, the oxygen production is independent of CO₂ flow rate. Below 3 cc/min, the production of oxygen decreases with decreasing CO₂ flow rate. The utilization of CO₂ is approximately 36% at 2 cc/min of CO₂ flow and approximately 26% at 3 cc/min.

In comparison with the tube system, whose best results gave a .214 cc/min/cm² O₂ production, the non-optimized disk system is approximately 63% more productive at .35 - .4 cc/min/cm². In comparison with an average tube system which gave .132 cc/min/cm² O₂ production, the disk system is approximately 166% more productive. The disk system also has the capacity to be more compact and less massive than the tube system.

Future Plans for the Disk System

Immediate plans call for extensive testing to study the effects of various electrodes, electrode application techniques and disk thicknesses on oxygen production. The next phase of testing for the 2.9 cm diameter disk system is to run it in a vacuum furnace, with the chamber filled with CO₂ at Martian atmospheric pressure. This will show how the system performs at the lower pressure on Mars. The next step is to build cells of larger diameter in order to produce more oxygen. Plans are to build a system based on a 3.5 inch diameter disk. These disks will most likely be made by tape casting, dependant on the acquisition or construction of a tape casting machine.

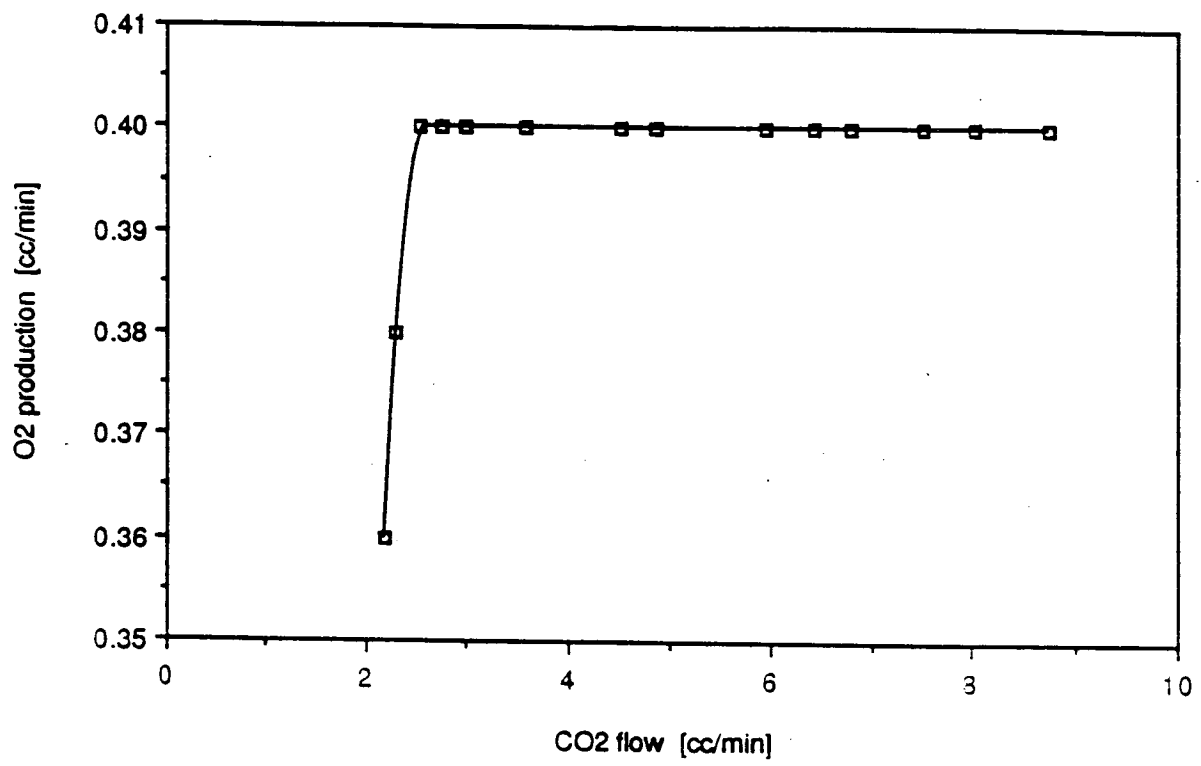


Figure 6 - O₂ Production vs. CO₂ Flow

Part B: Oxygen Production Plant and Compressor

Using Tube Geometry

Graduate Student: Scott Miller

Oxygen Production Plant

The electrochemical cells for the oxygen separation are available in tubular form. This shape offers an alternative to the disk geometry described above and can also function as a compressor for the separated oxygen. The tubes were custom made for UA/NASA SERC by Ceramatec, Inc. of Salt Lake City, Utah. The tubular device and the design motivation will be described here.

The design of the oxygen production plant was made with two main objectives in mind. The development of an operational portable system capable of remote operation, and its use as an oxygen compressor. The motivation behind the design of this device has been to develop a system that is at a higher Technology Readiness Level than the previous devices described in [1]. Some criteria important in the development of a complete system are: ease of use, high efficiency, reliability, repairability, and intelligent control. The compactness and modularity of the process cluster is illustrated in *Figure 7* and *8*. Each subsystem can be removed/replaced without a significant pause in operations. The system can be serviced - replacing of the Zirconia cells for example - by one person with one electric wrench in a matter of seconds. This would be an important consideration on the Moon or Mars. In order to make the device more reliable, all the problems encountered in the development of the 16-cell breadboard were addressed and systematically eliminated in the current design. A few of these issues are discussed below.

Previously, the oxygen plant was fragile because it had alumina feed tubes. This required the complete disassembly of the system and the refitting of the Zirconia tubes with a new alumina feed tube when one broke. The new design employs an Inconel feed tube which does not protrude from the system housing. Another problem in the previous experimental set up was the less than desirable electrical connections to the Zirconia tubes. Improper contacts caused a loss of d.c. potential across the tube, resulting in a lower O₂ production. At elevated temperatures, the sealing of electrical contacts through the system causes gas leaks, compromising the data obtained. This problem was solved in the new system by using Conax type electric feed through fittings for the

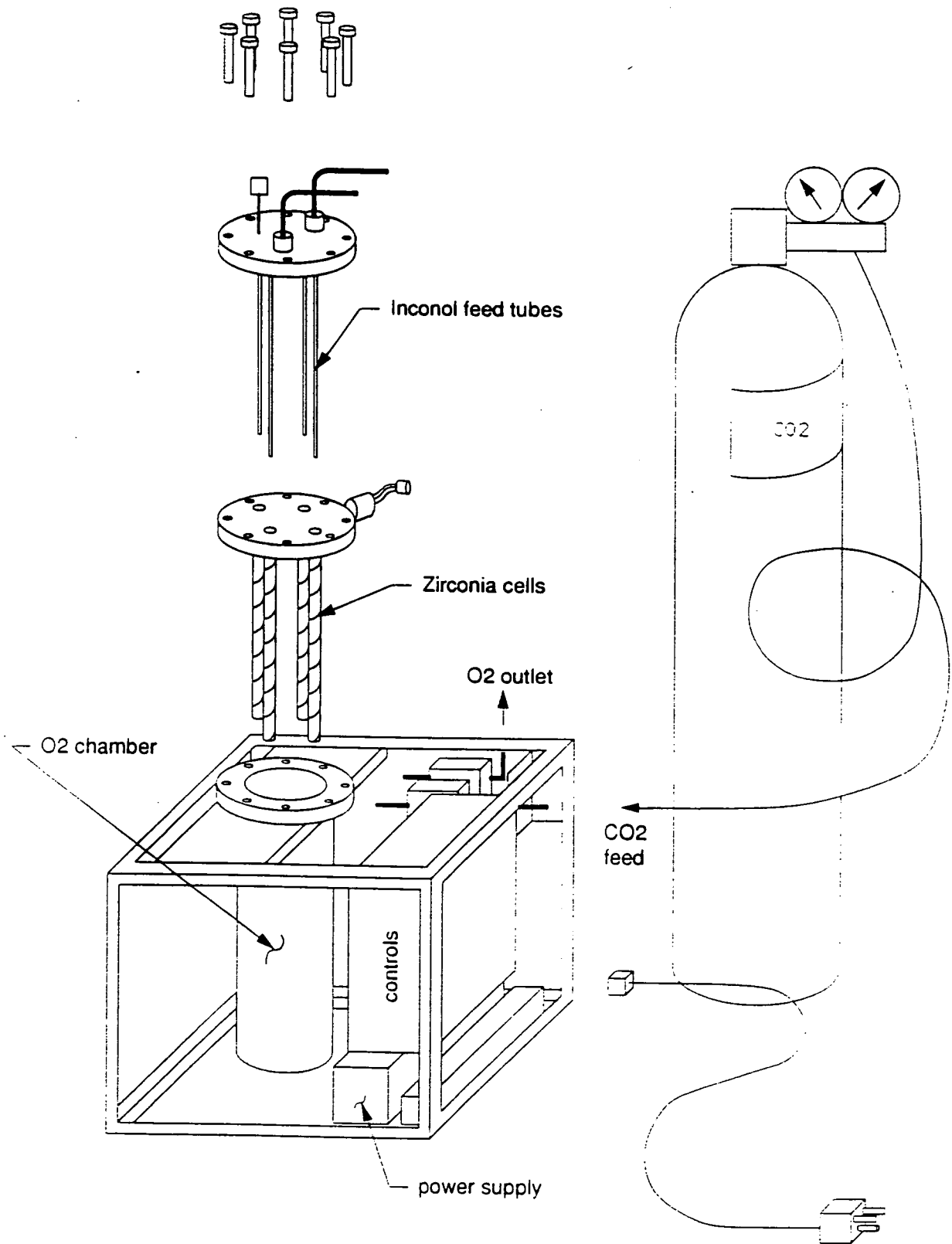


Figure 7 - Design of Oxygen Production Plant and Compressor.

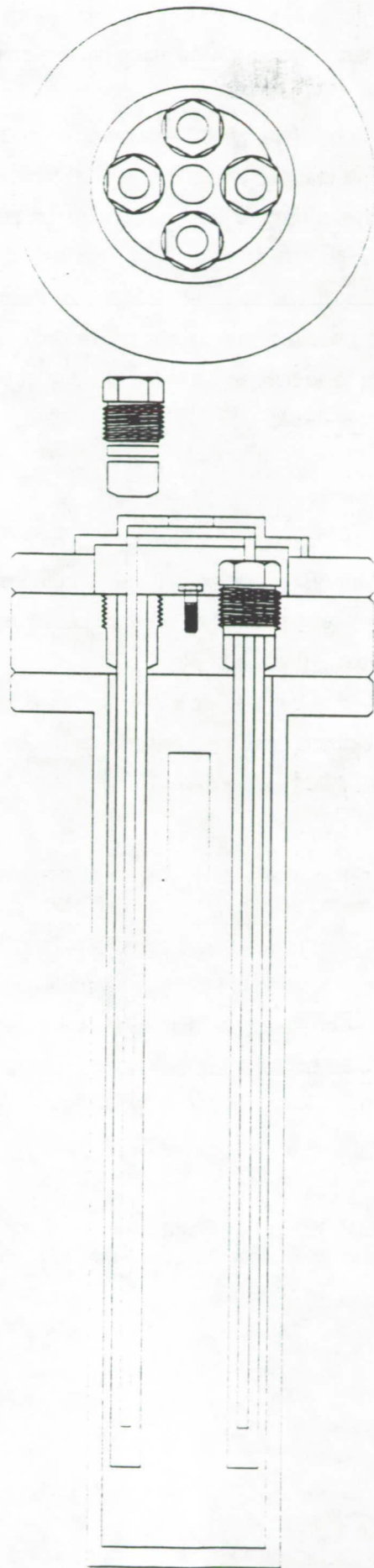


Figure 8 - Cross Section of Oxygen Separation Process Cluster

positive leads and thermocouple. These and other design modifications provide for a robust design.

The 16-cell unit has cold Teflon seals that were water cooled. The new design has Conax type fittings with Lava seals that can withstand the high temperature of operation. With this design, the complete length of the tubular cell can be effectively utilized and the heater power can be drastically reduced. Reliable gas flow monitoring, good electrical contacts, the availability of temperature data at various points in the cluster, and a hot seal provides us with a system in which meaningful control experiments can be run and high confidence level data can be collected. At the time of writing this report, a system has been built and is in the process of being tested. Data on the experiments will be reported in the near future.

Oxygen Compressor

The electrochemical cell can be used as an oxygen compressor. If sufficient d. c. potential is applied to the cell, the partial pressure of oxygen that is pumped can be significantly increased. *Figure 9* is an illustration of a 4-cell unit that has been described in [1]. This unit was used to compress pure oxygen. Oxygen entered the unit at atmospheric pressure and was compressed to 366 psig with this device. The results of this test are shown in *Figure 10*. The cold Teflon seals prevented further pressurization of the chamber. A new design with the hot seals is presently being developed. The results will be reported in the near future.

Acknowledgements

The authors would like to acknowledge Dr. Jerry Sutor and Mr. Bob Losey of the Jet Propulsion Laboratory for the use of their labs and equipment for tape casting. In addition, the authors would like to extend their appreciation to Mr. Peter Kaloupis for his diligent work on the disk configuration which produced most of the results that have been reported here. Also the authors would like to thank Mr. David Lyle for his excellent work in the fabrication of the new tube system. The authors also wish to thank Mr. Otis Gorley for his invaluable assistance in the laboratory.

Reference

1. Sridhar, K.R. and P. Kaloupis, "Electrochemical Separation of Oxygen from Carbon Dioxide", NASA Space Engineering Research Center Annual Progress Report 1991, APR-91/F, University of Arizona, 1991, pp. IB-1 -- IB-22.

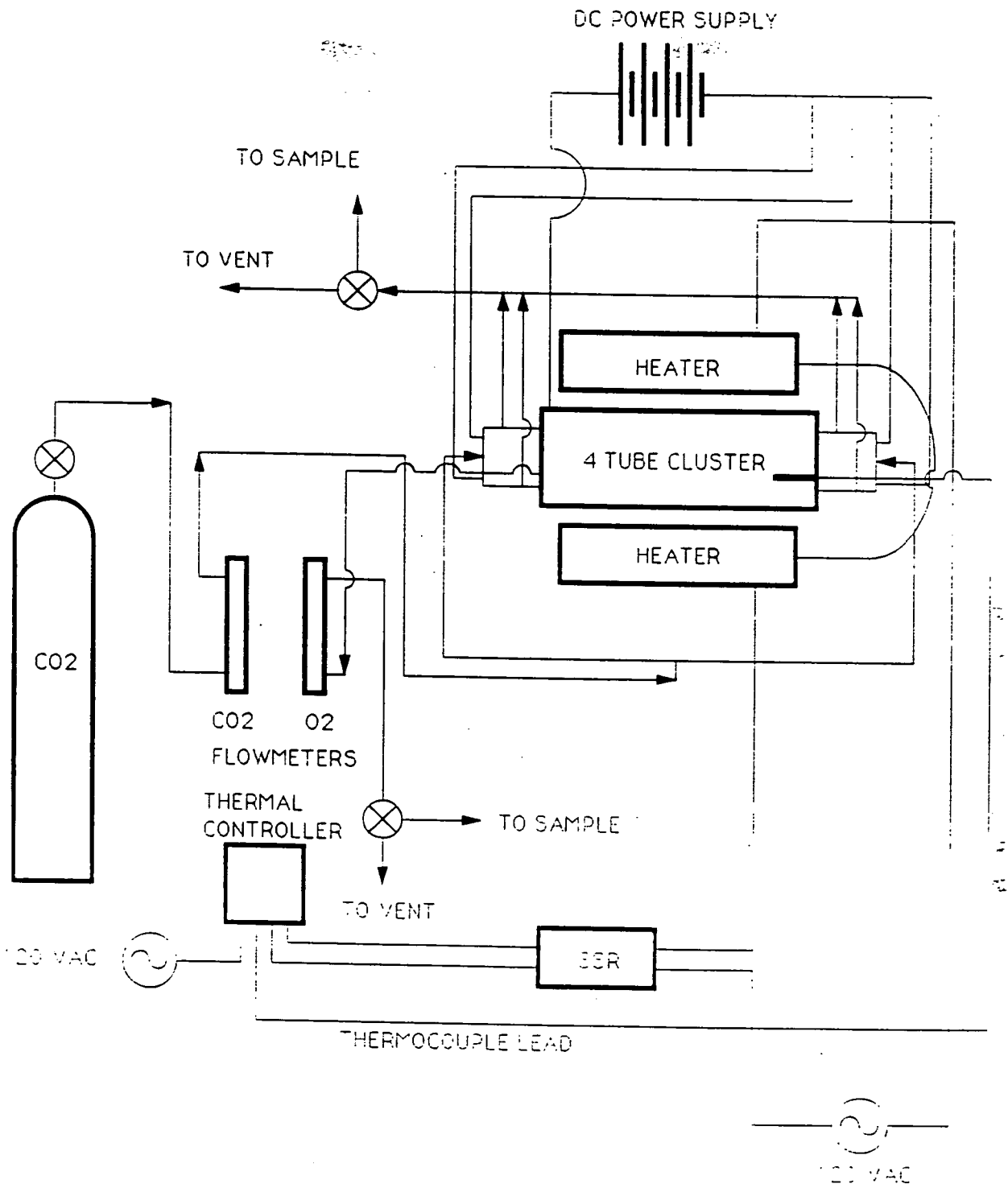


Figure 9 - Block Diagram of Oxygen Production Plant

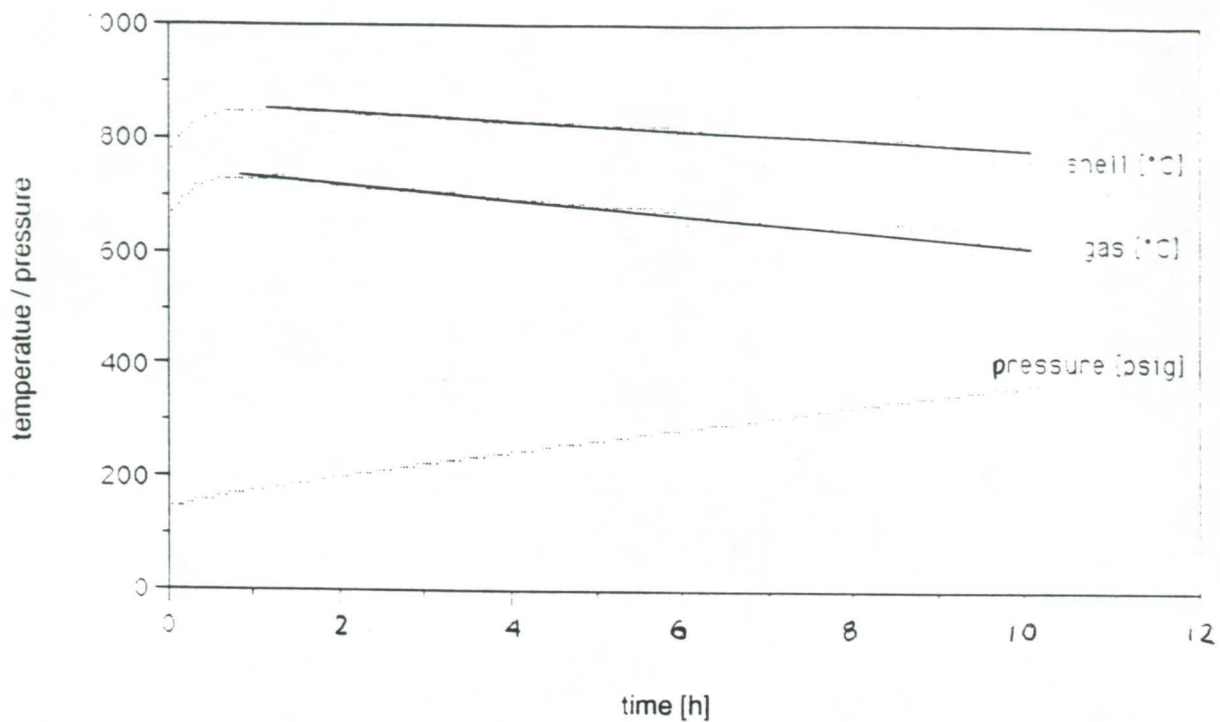


Figure 10 - Temperature / Pressure vs. Time for the Oxygen Compressor

omit

C. REDUCTION OF CARBONACEOUS MATERIALS

497592
N 93 - 26684

**Dehydration Kinetics and Thermochemistry of Selected Hydrous Phases, and Simulated
Gas Release Pattern in Carbonaceous Chondrites**

**Kunal Bose and J. Ganguly
Department of Geosciences
The University of Arizona**

510-25

158357

p. 14

Abstract

As part of our continued program of study on the volatile bearing phases and volatile resource potential of carbonaceous chondrite, we report results of our experimental studies on the dehydration kinetics of talc as a function of temperature and grain size (50 to 0.5 μm), equilibrium dehydration boundary of talc to 40 kbars, calorimetric study of enthalpy of formation of both natural and synthetic talc as a function of grain size, and preliminary results on the dehydration kinetics of epsomite. In addition, we have carried out theoretical calculation on the gas release pattern of Murchison meteorite, which is a C2(CM) carbonaceous chondrite.

The kinetic study of talc leads to a dehydration rate constant for 40-50 μm size fraction of $k = 3.23(10^4)\exp(-Q/RT) \text{ min}^{-1}$ with the activation energy $Q = 376 (\pm 20) \text{ kJ/mole}$. The dehydration rate was found to increase somewhat with decreasing grain size. The enthalpy of formation of talc from elements was measured to be $-5896(10) \text{ kJ/mol}$. There was no measurable effect of grain size on the enthalpy beyond the limits of precision of the calorimetric studies. Also the calorimetric enthalpy of both synthetic and natural talc was found to be essentially the same, within the precision of measurements, although the natural talc had a slightly larger field of stability in our phase equilibrium studies. The high pressure experimental data the dehydration equilibrium of talc ($\text{talc} = \text{enstatite} + \text{coesite} + \text{H}_2\text{O}$) is in strong disagreement with that calculated from the available thermochemical data, which were constrained to fit the low pressure experimental results. The calculated gas release pattern of Murchison meteorite were in reasonable agreement with that determined by stepwise heating in a gas chromatograph by Hashimoto et al. (1979).

Introduction

Carbonaceous chondrites are usually believed to be the primary constituents of near-Earth asteroids and Phobos and Deimos, and are potential resources of fuels that may be exploited for future planetary missions. The most volatile-rich members of this class of meteorite are known as C1 (or CI) and C2 (or CM) classes. Our group has been involved in an integrated study on the thermodynamics and kinetics of reactions of the volatile-bearing phases that are likely to be present in carbonaceous chondrites. The results will provide important constraints on the fundamental aspects concerning nature, abundance, and time scale of formation of volatile-bearing phases in the solar nebula, and the closely related practical problem of the feasibility of extraction of volatiles for fuels from carbonaceous chondrites. Some insight into the latter problem can be gained from the results of step-wise heating experiments of meteorite samples, and analyzing the released gas in an on-line mass spectrometer (e.g. Hashimoto et al., 1979). Our objective is to develop a more general and operationally much simpler approach in which the pattern of volatile release during controlled heating of a meteorite can be depicted into a computer terminal through numerical experiments if one feeds in the data on heating rate, range of temperature of interest and bulk composition of the sample. A preliminary report of this numerical experiment at 1 bar in the temperature range 400 -800°C has been published earlier (Ganguly and Saxena, 1989), in which it is assumed that the equilibrium volatile release is obtained at each heating step. The bulk composition chosen are those corresponding to the average compositions of Orgueil (C1) and Murchison (C2) meteorites. The results of volatile release pattern for Murchison are found to be broadly similar to those of step-wise heating experiments by Hashimoto et al. (1979).

Our on-going project involves determination of thermochemical properties and dehydration kinetics of minerals which are potential components of carbonaceous chondrites, refinement of the numerical experiments by incorporating these data. The latter part of the project has been carried out in collaboration with Professor Surendra Saxena (Brooklyn College, New York and University of Uppsala, Sweden).

The results obtained during the current funding period are reported below.

Dehydration Kinetics of Talc and Epsomite

A) Talc

In our last progress report, we had reported the results of dehydration kinetics of talc in the temperature range 775-985°C. These experiments were carried out at 1 bar pressure, on a 'coarse'

(40-50 μ) grain size of natural talc. However, since reaction kinetics are known to depend on grain size (surface area), we have investigated the dehydration kinetics of fine grain separates (1.0 μ and <0.5 μ) of natural as well as synthetic talc (~1.0 μ). The process of separating small grain size fractions is very tedious, involving repeated cycles of spinning in an ultra-centrifuge with a small (<50 mg) mass yield. The thermogravimetric apparatus built in our laboratory requires at least a gram quantity of sample for dehydration kinetic experiments. Also, a maximum amount of 200 mg of talc can be synthesized at a time in laboratory. Because of these constraints, we have carried out the dehydration kinetic experiments on the synthetic and the fine grain separates of natural talc in a micro-thermogravimetric apparatus (SETARAM) in the laboratory of Professor A. Navrotsky, Princeton University. This instrument is capable of detecting weight changes in the nanogram level. In order to check the reliability and consistency of data obtained at the two laboratories, we repeated the dehydration rate measurement at 900°C on the coarse grain natural talc in TGM apparatus at Princeton. As shown in *Figure 1*, the results are in excellent agreement with those obtained in our laboratory.

Over the temperature range of 775-985 °C, the data on the dehydration kinetics of natural talc can be nicely fitted by a second order rate expression:

$$-d\alpha/dt = k\alpha^2, \quad (1.1)$$

or the equivalent integrated form:

$$1/\alpha = 1/\alpha_0 + kt \quad (1.2)$$

where α is the weight fraction of talc remaining at time t . The results at 950°C are illustrated in *fig.2*. The Arrhenian plot of the rate constant in the range 875-985 °C is shown in *Figure 3*. The least square regression of the data (for 40-50 μ m size fraction) yields

$$k = 3.23(10^4) \exp(-Q/RT) \text{ min}^{-1} \quad (2)$$

where the activation energy $Q = 376 (\pm 20)$ kJ/mol, the error bar representing 1σ uncertainty.

The rate of dehydration for the smaller grain sizes are found to be faster than the coarser fractions (*Figure 4*). However, there is no significant difference in rates between the 1.0 μ and <0.5 μ size fractions of natural talc. This may be the result of clustering of the small grains due to high electrostatic surface charging. It is also possible that the difference between the dehydration rates of talc for the above size fractions is too small to be detectible. It may, however, be noted that in

contrast to these data, Gregg and Razouk (1949) found a maximum around 150- 180 μ size fraction in the rate of dehydration of Brucite as function of grain size.

Figure 5 shows the difference in dehydration rates between the natural and synthetic talcs, indicating a difference in their energetic properties. This is also reflected in our phase equilibrium studies on the dehydration of talc, which showed the natural talc to have a slightly higher field of stability than synthetic talc (see section on Equilibrium Dehydration of Talc).

In order to quantitatively specify the thermochemical property of both natural and synthetic talc along with its dependence on grain size, we undertook a study (in collaboration with Professor A. Navrotsky and Dr. P. Burnley of Princeton University) of the heat of formation of talc by drop solution calorimetry. Unfortunately, the experimental uncertainty was too large to resolve the small difference in the energetic properties of these materials. The heat of solution of three different size fractions, $>1\mu$, 1.0μ and $<0.5\mu$, as well as of the synthetic talc were found to be essentially the same (502 ± 10 KJ/mol). Using previously reported solution enthalpies for quartz, periclase and brucite, we derived a heat of formation from the elements for talc $\Delta H_f = -5896 (\pm 10)$ kJ/mol. This is in close agreement with those obtained by evaluation of phase equilibria data. This work has been submitted as a paper for the Fall Meeting of the American Geophysical Union (AGU), San Francisco, Dec. 7-11, 1992 (See Appendix I).

X-ray powder diffraction studies of the products of dehydration kinetic experiments of talc did not show any x-ray reflection of the products of dehydration, which is likely to be result of their extremely fine grain size. However, in order to formulate the kinetic rate law and mechanism, it is essential to know the products of a reaction. We have, thus, conducted Transmission Electron Microscopy (TEM) studies (in collaboration with Dr. S. Supapan, Material Science Department, University of Arizona) of the starting materials and the dehydration run products. The electron diffraction pattern suggests the breakdown products of talc to be enstatite and quartz. Further work is in progress to characterize these materials unambiguously.

Equilibrium Dehydration of Talc at High Pressure

In order to test the internal consistency of the thermochemical properties of talc and its dehydration products, including water, we have carried out precise experimental determination of the equilibrium boundary of talc (Talc = Enstatite + Quartz(Coesite) + H₂O) upto 40 kbar pressure (this part of the project was only partially supported by the NASA grant). The synthetic talc was found to have a

slightly smaller thermal stability than the natural talc, indicating a higher free energy of the synthetic talc compared to the natural talc. More significantly, the experimentally determined equilibrium is in strong disagreement with that calculated from the available thermodynamic data indicating that the thermodynamic data of one or more phases is in need for significant revision. The results of this study have been submitted as a paper for AGU Fall Meeting, San Francisco, Dec. 7-11, 1992 (see Appendix II).

B) Epsomite

The earlier work of Ganguly & Saxena (1989) on the calculation of modal abundance of minerals in C2 bulk composition has been expanded by incorporating the thermochemical properties of minerals that have been available recently. The major hydrous mineral phases predicted by these calculations are epsomite, talc and brucite. Since the equilibrium dehydration temperature of epsomite at 1 bar is significantly lower ($<160^{\circ}\text{C}$) than that of talc (375°C), the investigation of epsomite as a possible source of easily extractable volatile is needed.

Figure 6 shows α vs time for epsomite dehydration at 160°C . This work was carried out by Rajib Ganguly as part of his undergraduate chemistry honors project at the University of Arizona (Chem 105 H) with the P.I. as his mentor. There are three other known hydrates of magnesium sulfate in addition to brucite ($\text{MgSO}_4 \cdot \text{NH}_2\text{O}$, $n=7$ for brucite, $n=6, 4$ or 1 for hexa-, tetra- and mono hydrate respectively). It is necessary to determine the phase equilibria in this system before one can determine the dehydration kinetics of epsomite. Work is currently under progress to constrain the thermochemical properties of these phases.

Calculation of Volatile Release Pattern of Murchison Meteorite

Using our internally consistent thermochemical database, we have performed, in collaboration with Professor Surendra K. Saxena of the Uppsala University, Sweden, theoretical calculations on the gas release pattern of Murchison meteorite, which is a C2(CM) carbonaceous chondrite. The calculation was performed by the minimization of Gibbs free energy, constrained to the bulk composition of this meteorite. The results are illustrated in *Figure 7*, and compared with those of step-wise heating of a sample of Murchison meteorite and gas chromatographic analysis of the released volatiles by Hashimoto et al. (1979). There is good agreement between the overall pattern, except that in the experimental studies, the gases were released at somewhat higher temperatures than those calculated from the minimization of Gibbs free energy. This may be due to kinetic problem (the extent of overstepping depends on the rate of heating). In contrast to the theoretical calculation, however, the release of water did not begin until 500K in the experimental studies. This is definitely due to the fact that the sample of meteorite was washed in water before heating, which resulted in the loss of epsomite which is a water soluble hydrous phase with very low dehydration temperature.

REFERENCES

Bose, K. and J. Ganguly. High pressure phase equilibria in the system $\text{MgO-SiO}_2\text{-H}_2\text{O}$: quartz-coesite revisited and dehydration of talc. Submitted, Fall 1992 Meeting, American Geophysical Union, Dec. 7-11, 1992.

Burnley, P., K. Bose, and A. Navrotsky. Heat of formation of synthetic and natural talc by drop solution calorimetry: a test of a new technique. Submitted, Fall 1992 Meeting, American Geophysical Union, Dec. 7-11, 1992.

Ganguly, J. and S.K. Saxena. Theoretical predictions of volatile abundances and volatile bearing phases in carbonaceous chondrites. In *Space Manufacturing: Space Resources to Improve Life on Earth* (7). Proceedings of the Ninth Princeton/AIAA/SSI Conference, 1989. American Institute of Aeronautics and Astronautics, Washington D.C.

Gregg, S.J. and R.I. Razouk. The kinetics of thermal decomposition of magnesium hydroxide. *J. Chem. Soc. V* (1949): 536-44.

Hashimoto, A., M. Kumazawa, and N. Onuma. Evaporation of primitive dust material in the early solar nebula. *Earth and Planetary Science Letters* (43): 13-21.

Appendix I

Heat of Formation of Synthetic and Natural Talc by Drop Solution Calorimetry: a Test of a New Technique

P. Burnley (Department of Geological and Geophysical Sciences, Princeton University, Princeton, NJ 08544)

K. Bose (Department of Geosciences, University of Arizona, Tucson, AZ 85721)

A. Navrotsky, (Department of Geological and Geophysical Sciences, Princeton University, Princeton, NJ 08544)

High Temperature solution calorimetry represents one of the few tools we have to directly measure the energetics of synthetic high pressure phases. Due to the instability of many of these compounds at calorimeter temperature, drop solution calorimetry is the preferred technique. Samples are either pressed into pellets or enclosed in platinum or solvent glass capsules and dropped into the calorimeter at room temperature. Synthetic high pressure phases with a Mg:Si ratio > 1 present additional challenges. Pellets with a high Mg content tend not to dissolve rapidly in the solvent, leading to excessive experimental duration and unacceptable levels of uncertainty. Similarly, if the heat effect due to the capsule is much larger than that of the sample the quality of the measurement is degraded. To overcome these problems, we have developed a new ultra light (~ 10 mg) quartz glass capsule. These capsules make only a small contribution to the heat effect measured, dissolving rapidly and exposing the powder within to solvent from all sides. We demonstrate the feasibility of this technique with talc.

We measured the heat of drop solution in molten lead borate of natural samples of talc ($\text{Mg}_{0.99}\text{Fe}_{0.01})_3\text{Si}_4\text{O}_{10}(\text{OH})_2$ using both pellets and ultra light quartz glass capsules. The measured enthalpy of 502 (8) kJ/mol using quartz glass capsules compares well with the value of 495 (5) kJ/mol using pellets; thus demonstrating that this will be a useful technique for size limited samples. We also investigated the effect of particle size using grain size sorted samples of natural talc. Enthalpies for >1 μm , 1 μm and <0.5 μm natural talc samples as well as the synthetic talc were identical to within the limits of the uncertainty (~10 kJ/mol). Using previously reported solution enthalpies for quartz, periclase and brucite, we derive a heat of formation from the elements at 295 K for talc of $\Delta H_f = -5896$ (10) kJ/mol. This value is in close agreement with those obtained by evaluation of phase equilibria data (cf. Hemingway, 1991).

Appendix II

High Pressure Phase Equilibria in the System MgO-SiO₂-H₂O: Quartz-Coesite Revisited and Dehydration of Talc

Kunal Bose and Jibamitra Ganguly (Both at Dept. of Geosciences, University of Arizona, Tucson, AZ 85721)

We have investigated the quartz-coesite transition between 500 - 1100°C and the dehydration equilibrium talc = 3 enstatite + quartz/coesite + H₂O up to 40 kb. The P-T slope of the quartz-coesite equilibrium is ≈ 7 bar/°C, which is in essential agreement with that determined by Bohlen and Boettcher (1982)¹, but disagrees with that of Mirwald and Massonne (1975)². However, the position of the equilibrium is about 1.2 -1.7 kb higher than that determined by Bohlen and Boettcher. All experiments were carried out in Piston-cylinder apparatus with 0.5 or 0.75" inner diameter carbide cores and pressure cells with CsCl outer bushing. The friction characteristic of the pressure medium was determined by continuous (computer) monitoring of the piston-displacement as a function of time at a fixed nominal pressure and analysis of hystereses loops of nominal pressure vs. piston displacement at several run temperatures. Work is in progress to measure melting temperature by in situ DTA to further check the friction behavior of the pressure cell.

The P-T slope of the dehydration equilibrium of talc changes sign ~ 30 kb, which is in sharp contrast to the prediction from the available thermodynamic properties of the phases. The latter leads to a negative dP/dT slope ~ 10 -15 kb. The discrepancy between the measured and predicted equilibrium temperatures at 40 kb is at least 120°C. Work is currently in progress to identify the problem with the thermodynamic data. Our data also extend the field of stability of the 10 Å phase to at least 820°C at 38 kbars.

1) *J. Geophys. Res.*, 87, 7073-7078

2) *J. Geophys. Res.*, 85, 6983-6990

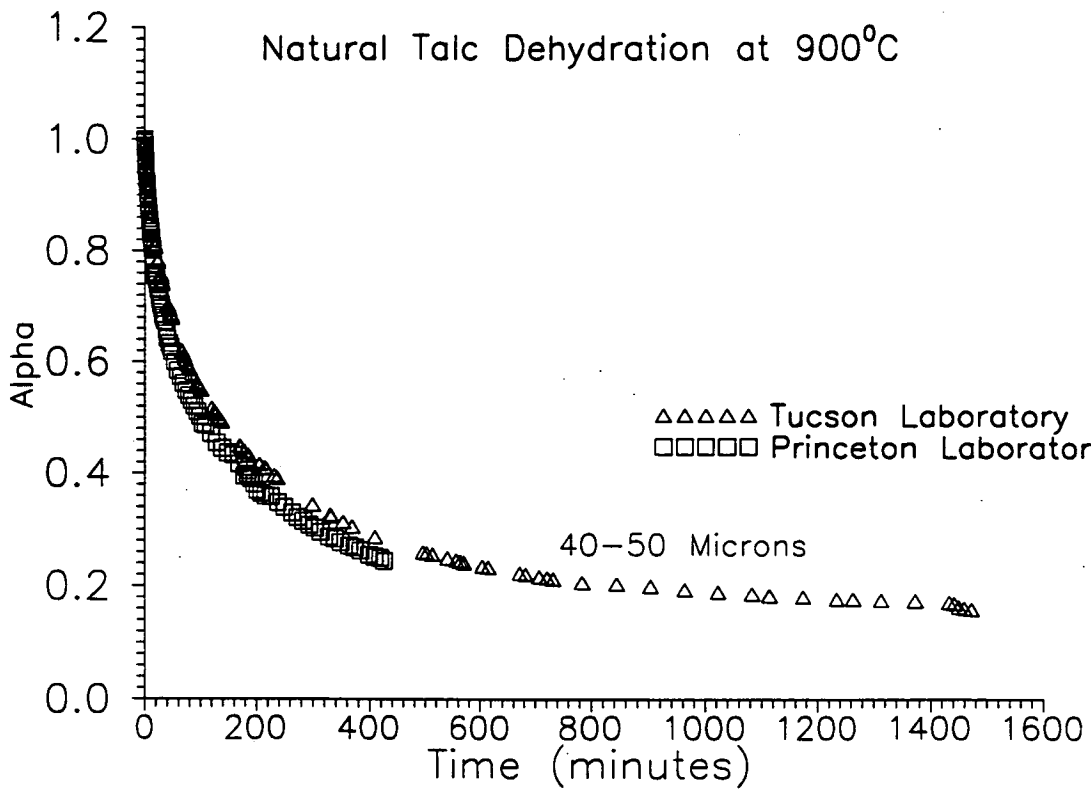


Fig.1: Comparison of dehydration rate measurement of natural talc in our laboratory (Tucson Laboratory) with that measured in the SETARAM micro-thermogravimetric apparatus in Princeton.

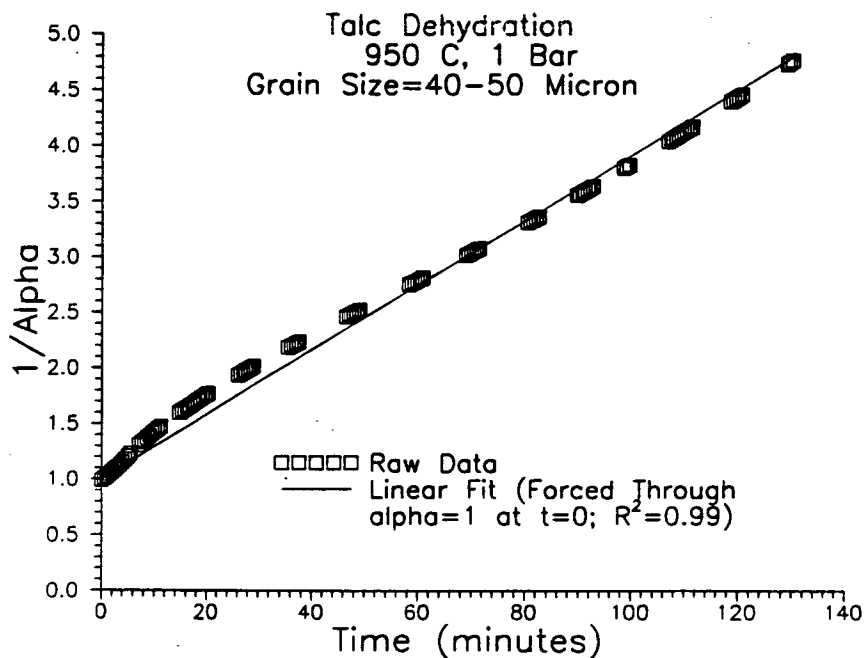
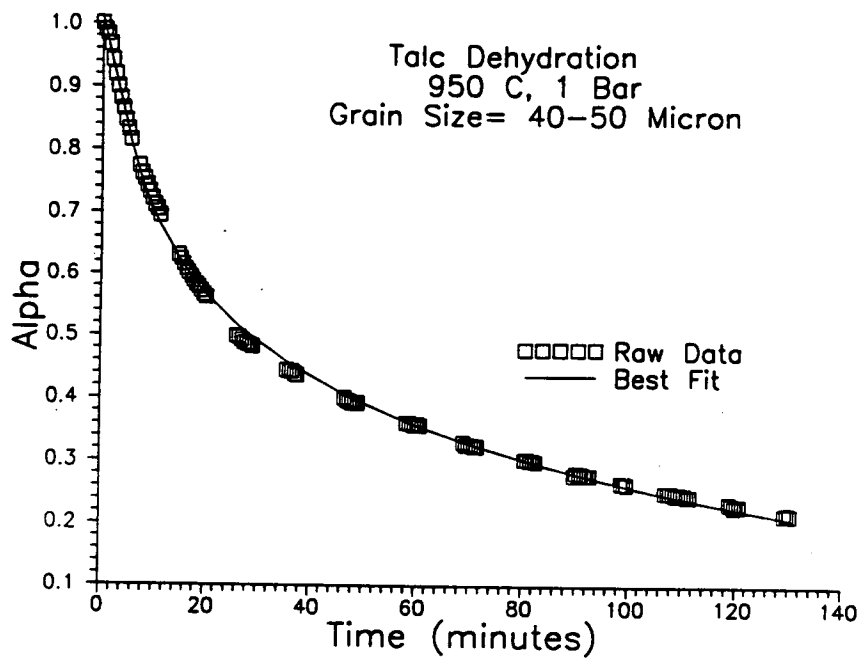


Fig.2: (a) Plot of isothermal dehydration of talc at 950°C, 1 bar. Alpha is the weight fraction of talc remaining at time t. (b) Illustration of the data in terms of $1/\alpha$ vs time. The linear dependence of $1/\alpha$ versus time indicates that the dehydration of talc follows a second order rate law (see text).

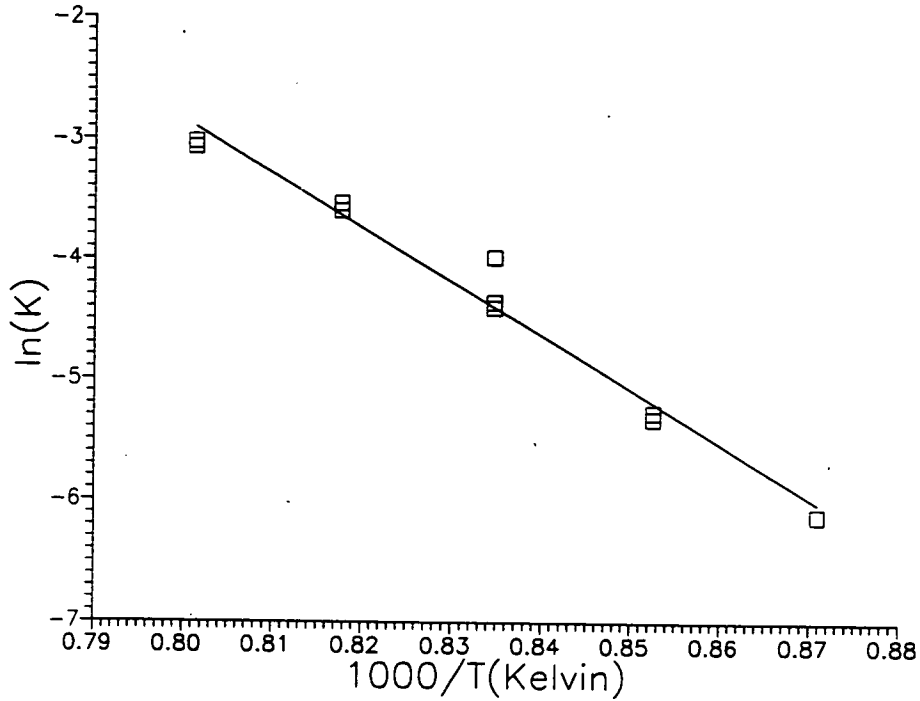


Fig.3: Arrhenius relation of dehydration rate (for 40-50 μm natural talc) constant between 875 and 975°C at 1 bar. The activation energy is 376 kJ/mol.

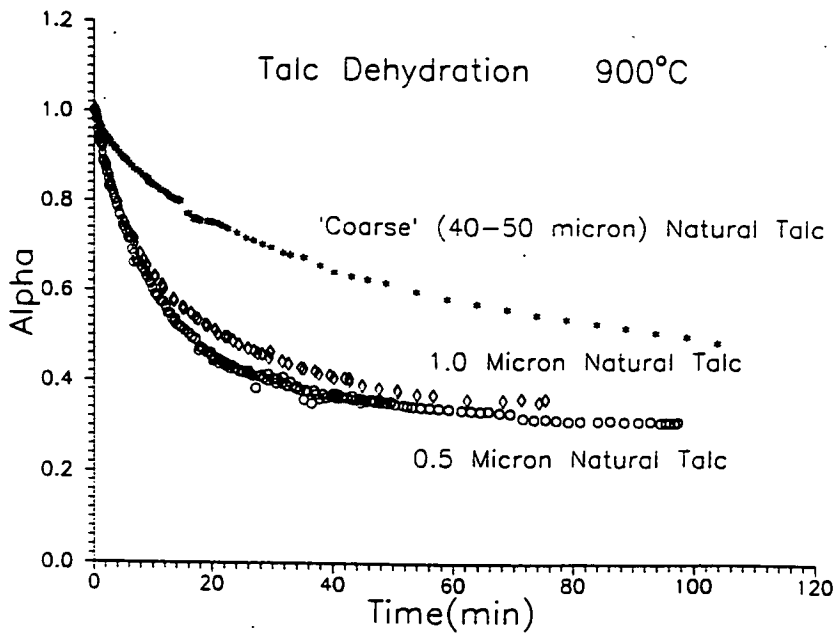


Fig.4: Plot of isothermal dehydration of talc at 900°C as a function of grain size. The smaller grain size fractions show a faster rate of dehydration than the 'coarser' talc. However there is no significant difference in the dehydration rate between the 1.0 μm and <0.5 μm grain sizes.

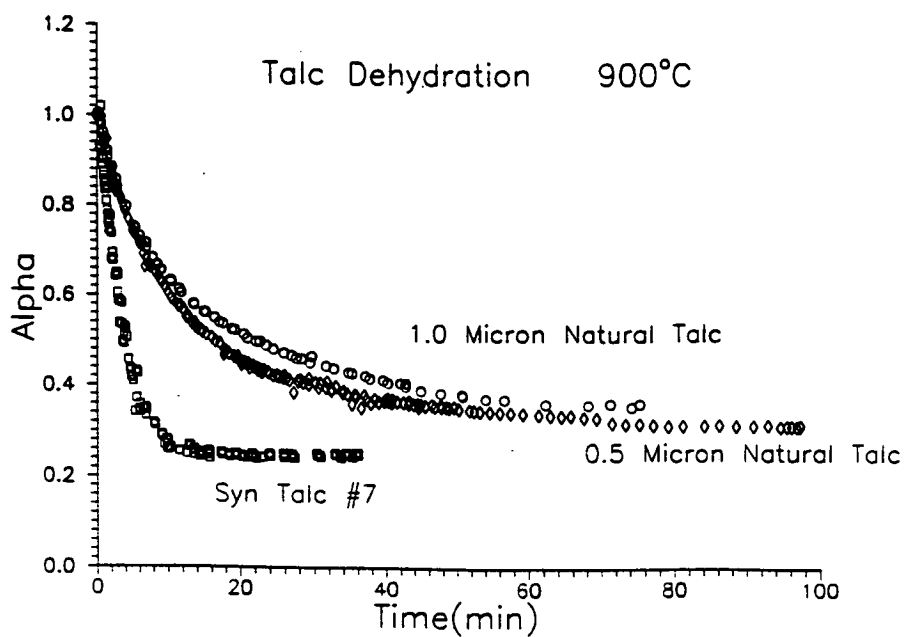


Fig.5: Difference in rate of dehydration of natural versus synthetic talc. The grain size of the synthetic talc was ~1.0 μm .

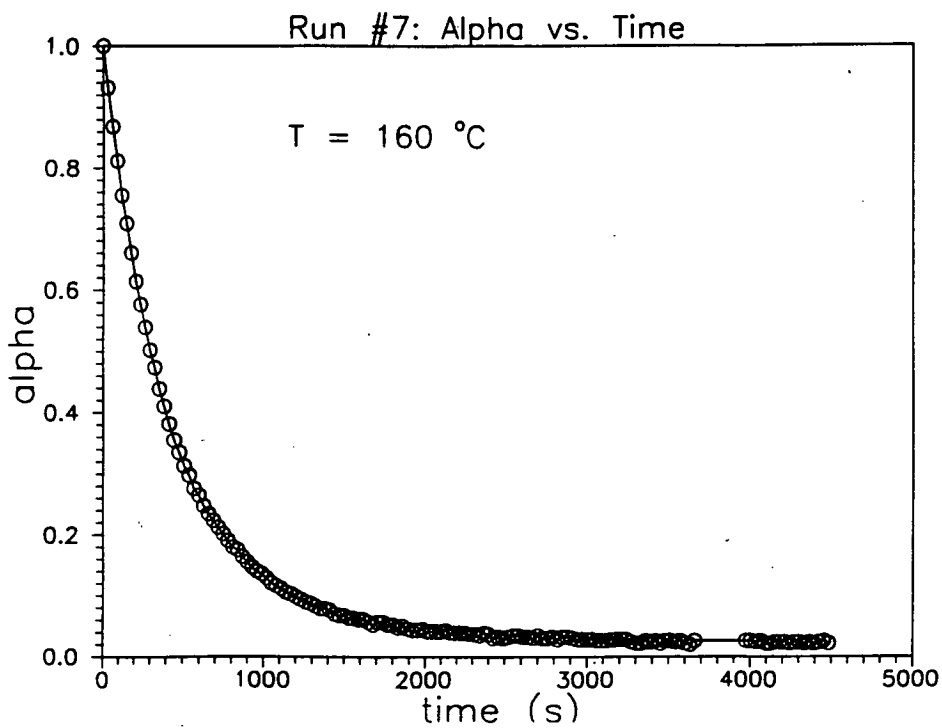


Fig.6: Dehydration of Epsomite at 160°C, 1 bar, as determined by R. Ganguly, as part of an undergraduate Chemistry Honors project.

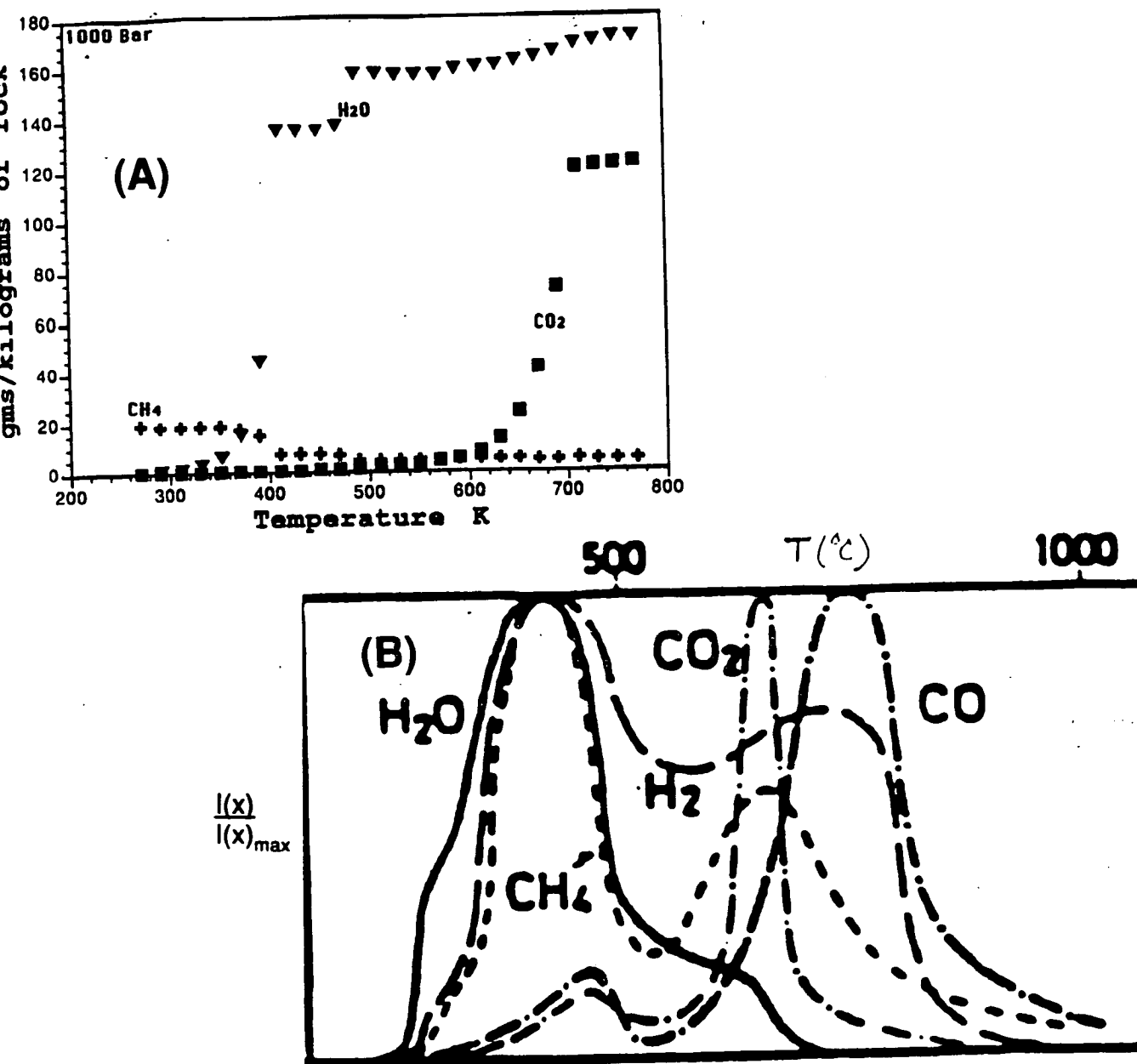


Fig.7: Comparison of calculated (A: this work) and experimental (B: Hashimoto et al, 1979) gas release pattern of Murchison meteorite. $I(x)/I(x)_{max}$ refers to intensity normalized to the maximum observed intensity of the spike for a specific volatile species in a gas chromatograph. Note that the temperature scales for A and B are degree Celcius and degree Kelvin, respectively. The figures were set to match the temperatures (i.e. 773 K in A matches with 500°C in B).

omit

II. PRODUCTION OF STRUCTURAL AND REFRACTORY MATERIALS

497593

N 9 3 5 1 2 5 2 6 7 8 5

158358

P-12

Melt-Processing of Lunar Ceramics

B.D. Fabes, W.H. Poisl, D. Allen, M. Minitti, S. Hawley, and T. Beck

Department of Materials Science and Engineering

University of Arizona

Abstract

The goal of this project is to produce useful ceramics materials from lunar resources using the by-products of lunar oxygen production processes. Emphasis is being placed on both fabrication of a variety of melt-processed ceramics, and on understanding the mechanical properties of these materials. Previously, glass-ceramics were formed by casting large glass monoliths and heating these to grow small crystallites. The strengths of the resulting glass-ceramics were found to vary with the inverse square root of the crystal grain size. The highest strengths (>300 MPa) were obtained with the smallest crystal sizes (<10 μm).

During the past year we continued to examine the kinetics of crystallization in simulated lunar regolith, in an effort to optimize the microstructure and, hence, mechanical properties of glass-ceramics. We also examined the use of solar energy for melt-processing of regolith, and successfully produced strong (> 630 MPa) glass fibers by melt-spinning in a solar furnace. A study of the mechanical properties of simulated lunar glasses was completed during the past year. As on Earth, the presence of moisture was found to weaken simulated lunar glasses, although the effects of surface flaws was shown outweigh the effect of atmospheric moisture on the strength of lunar glasses. The effect of atmospheric moisture on the toughness was also studied. As expected, toughness was found to increase only marginally in an anhydrous atmosphere.

Finally, our efforts to involve undergraduates in the research lab flourished this past year. Four undergraduates worked on various aspects of these projects; and two of them were co-authors on papers which we published.

I. Introduction

While propellant manufacture is one key driving force behind development of indigenous space materials utilization technologies, a variety of solid products - for bricks, pipes, windows, containers, and insulation – will be needed as well. Since the Moon is composed principally of oxide ceramics, this project is concerned with the development of ceramic processing techniques for making simple, useful materials on the Moon, using indigenous resources. And since it is likely that production of oxygen will provide the main impetus for in-situ materials use on the Moon for some time, a further goal of this research is to develop processes which use the by-products of oxygen production schemes as starting materials.

This project is divided into two main components. In our *processing* effort we are concerned with producing, and then optimizing the mechanical properties of glass-ceramic tiles and bricks. In our *scientific* effort, we are working to understand the relationships between structure, and properties of lunar ceramics. Of course, these activities are not independent, as it is the understanding of the interplay between structure, processing, and final properties which will ultimately allow us to produce a variety of high-quality products on the Moon, using indigenous resources. Our current goal, however, is to produce prototypes of simple, useful products, and to lay the groundwork of scientific knowledge, upon which future, advanced development of lunar ceramics can be based.

In the first two years of this program facilities for melting and casting glasses were set up, the effects of common lunar impurities on the rheological properties of glasses were determined qualitatively, glass-ceramics were fabricated, and the effect of grain size on these materials was investigated. During the past year we examined melting of lunar regolith in a solar furnace, and successfully fabricated glass fibers by melt-spinning in a solar furnace. We also conducted a relatively detailed study of the effect of moisture on the strength and toughness of lunar glasses. These accomplishments are discussed in detail in the following pages. Our success in involving undergraduates in these activities is also described, and our plan for future work is presented in the final section.

II. Processing

A. Monolithic glasses and Glass-Ceramics

In previous reports we discussed the production of monolithic glasses and glass-ceramics by melt casting. These activities continued during the past year, using the compositions shown in Table 1. For examining glass-ceramics, we concentrated on two compositions, A14 and A16, representing the average compositions of the regolith at the Apollo 14 and 16 landing sites. Glass fibers were spun using Minnesota Lunar Simulant (MLS), and monolithic glasses were cast using a composition similar to that of lunar rock sample 14049, returned on Apollo 14.

Table 1. Composition of Lunar Simulants used for Glass and Glass-Ceramic Production (in wt%)

Component	Glass-Ceramics		Glasses	
	A14	A16	Monolithic	Fiber*
SiO ₂	48.1	45.1	49	43.9
Al ₂ O ₃	17.4	26.8	17	13.7
MgO	9.4	5.7	11	6.68
FeO	10.4	5.4	10	13.4
CaO	10.7	15.6	8.9	10.1
TiO ₂	1.7	0.6	1.7	6.32
Na ₂ O	0.7	0.43	0.85	2.12
K ₂ O	0.55	0.14	0.53	2.81
Cr ₂ O ₃	0.23	0.11		
MnO	0.14	0.22		
Fe ₂ O ₃				2.6

*MLS Simulant

B. Solar Heating of Regolith.

For materials processing on the Moon solar energy might provide a convenient source of heat, especially if it can be used directly, without conversion to electrical power. While the rate of heating and processing temperature can be difficult to control using direct solar heating, careful control of these parameters is not generally critical for melt processing. Thus, during the past year we began to examine the use of direct solar heating for melt processing of lunar ceramics.

For small samples other researchers have shown that solar heating is a convenient way to melt, and even to volatilize, lunar simulants. For larger samples, necessary for forming useful materials, however, it is difficult to melt an entire charge, since the melt is opaque (as a result of the high concentration of iron in the regolith) and it is, therefore, an effective thermal insulator at the high temperatures necessary for melt processing. As a result, it is not uncommon for the top layer of a glass charge to be completely molten, while the inside of the charge remains relatively unaffected by even an intense solar beam.

To examine this problem we melted samples of MLS in an alumina crucible, using the UA Solar Furnace. We used optical pyrometry to determine the temperature across the surface of a 5 gr charge. The regolith in the center of the crucible, directly under the solar beam, melted readily. As shown in *Figure 1a*, the sample temperature approached 2500 °C in this region. Outside of the direct solar spot, however, the temperature dropped off rapidly, and near the edge of the crucible (only 15 mm from the center) the temperature was well below the solidus temperature of the simulant. By scanning the beam across the sample the entire surface could be melted, but the opaque melt retarded heat transfer into the sample and, as shown in *Figure 1b*, only the top 2 mm was melted.

To melt large samples fully using direct solar heating a crucible with a high thermal conductivity might be used to transport heat to the bottom of the charge. Switching to a graphite crucible, for example, increased the size of the charges which we could melt in the UA Solar Furnace. This approach is likely to provide only minimal improvement for melting extremely large Samples, however, as heat transfer to the center would still be difficult. Alternatively, some kind of mechanical mixing might be used, although the mixer itself would have to be stable under the solar beam. After trying several approaches, we found that spinning the melt using an externally driven motor worked well. This allowed us to use any crucible material, as well as providing a convenient way to produce glass fibers, as described in the next section.

C. Melt-Spun Fibers

Thin, short glass fibers have a number of potential uses on the Moon. They could be fused into bricks, or bonded into mats to make materials for thermal insulation; and if polymers are developed on (or transported to) the Moon, glass fibers could be used for reinforcements in polymer matrix composites. Other researchers have shown that individual fibers can be pulled from melts of lunar glass. For practical applications, however, continuous or large batch processes are more attractive. Thus, we examined melt-spinning for making large batches of short, thin fibers during the past year.

Melt-spinning on Earth is a well established technology, wherein molten glass is fed into a hollow "spinner" with holes on the sidewalls. The spinner rotates rapidly, causing the melt to ride up the walls and out, via centripetal force, through the holes. On Earth, jets of hot air blow the glass streams outside of the spinner into even finer fibers, which are then coated with an organic solution to protect the surface from damage.

To adapt this process to the Moon we drilled holes in a graphite crucible, mounted the crucible in a holder attached to a variable speed motor, and placed the entire assembly in a collection can which was set in the UA solar furnace, as shown schematically in *Figure 2*. The crucible was filled with approximately 3 gr of MLS, exposed to the sun, and spun. Once spinning began the entire charge melted rapidly (without spinning only the central portion, directly under the beam, melted, as discussed in the previous section) and fibers were extruded out of the holes into the collection can. As shown in the optical micrograph in *Figure 3*, fibers up to approximately 10 cm long were formed. The diameters of the fibers varied from less than 30 μm to over 100 μm , as shown in the SEM micrographs in *Figure 4*. This variation was probably due to degradation of the holes in the graphite crucible, which oxidized readily, during heating in air.

We are currently characterizing the mechanical properties of the melt-spun fibers. Preliminary indications are that the fibers are extremely strong. As shown in *Figure 5*, a 16 μm diameter fiber could be bent, 180°, with a radius of curvature of less than 3 mm. This corresponds to a stress of over 600 MPa (tension) within the fiber.

III. Mechanical Properties

A. Glass-Ceramics

As in previous years, the mechanical properties of glass-ceramics were studied by cutting disks, approximately 3 cm in diameter by 2 mm in height from larger cast glass pucks, heat treating the disks using different schedules (shown in Table 2) and breaking the resulting glass-ceramics using a ball-on-ring test jig.

Table 2: Heat treatment schedules for fabricating Glass-Ceramics

Schedule	Nucleation		Crystal Growth	
	Temperature	Time	Temperature	Time
A	720 °C	1 hrs	940 °C	3 hrs
B	750 °C	3 hrs	900 °C	1 hrs
C	800 °C	3 hrs	950 °C	2 hrs
D	800 °C	3 hrs	1050 °C	2 hrs
E	800 °C	3 hrs	1000 °C	2 hrs
F	800 °C	4 hrs	1000 °C	2 hrs

The strengths of samples A14 and A16, heated according to the schedules shown in Table 2, are summarized in *Figure 6*. When nucleated at 800 °C, the strength of sample A14 increased with crystallization temperature (schedules C, D, and E) up to 1000 °C. The highest strength (schedule

E) was 315 MPa. Increasing the nucleating time from 3 to 4 hours (schedules E and F) also resulted in an increase in strength. Increasing the crystallization temperature to 1050 °C, however, resulted in a drastic decrease in strength.

In comparison to these results for sample A14, the strengths of sample A16 were lower. We are currently examining the microstructures (using scanning electron microscopy) and phase compositions (using x-ray diffractometry) of these samples to understand the causes of the dramatic differences in strength. Since the concentrations of FeO and TiO₂ are significantly different in the two samples, we expect that both the kinetics of crystallization, as well as the phases that are formed are different. Howard Poisl has therefore fabricated samples and taken them to Johnson Space Center for Mössbauer analysis to ascertain the oxidation state of the iron, potentially a parameter issue in crystal nucleation and growth.

B. Glasses: Effect of Atmospheric Moisture on Strength

It has been suggested in a variety of symposia, conferences, and conversations throughout the ISMU community that bulk glasses might be strong and tough on the Moon. The lack of water in the atmosphere, and concomitant absence of hydrolytic depolymerization (stress corrosion cracking) is cited as the cause of this hopeful effect. While strong, tough glass would have obvious attractions on the Moon, the strength of glass is controlled, generally, by both surface flaws and stress corrosion cracking. Therefore, the relative importance of both of these strength-reducing mechanisms must be understood before structures are made from lunar glasses. Thus, we undertook a detailed study of the effects of water and surface flaws on the strength and toughness of lunar glasses this past year.

1. Theoretical Background

The strength of a glass is generally controlled by surface flaws, which increase the stress felt by a glass at the tip of the flaw. As given by the Griffith/Orowan/Irwin model, the stress, σ_{tip} , that is felt at the tip of a flaw of length c , is given by

$$\sigma_{tip} = 2s \sqrt{r} F(c,r) \quad (1)$$

where s is the applied tensile stress, and r is the radius of curvature of the flaw. Since glasses are generally quite brittle (i.e., they fracture with little or no plastic deformation) very little blunting of the

crack tip occurs prior to fracture. As a result, r is generally quite small (on the order of atomic dimensions), so that even small flaws cause a dramatic increase in the stress that is transferred to the tip of a flaw. As a result, strength of a glass is reduced markedly by even microscopic imperfections.

Hydrolytic depolymerization - stress corrosion cracking - is a well-documented phenomenon that further decreases the strength of silicate glasses. This weakening is caused by a chemical reaction between the silicon-oxygen bond in the glass and the polar water molecule. It is generally accepted that this reaction occurs through a three-step process. As shown in *Figure 7*, a water molecule first adsorbs to tip of a flaw. The water molecule attaches itself to a bridging Si-O-Si bond, which is strained due to the highly concentrated stress field in the vicinity of the crack tip. Two new bonds are next formed, one between the oxygen atom of the water molecule and the silicon atom and another between a hydrogen atom of the water molecule and the network bridging oxygen atoms. In the third step the original bridging bond is destroyed, leaving two silanol groups at the surface.

This weakening process is practically unavoidable on Earth because of the ubiquitous distribution of water throughout the atmosphere. The lunar environment, however, is anhydrous. Therefore, stress corrosion cracking should not affect silicate glasses when used in engineering applications on the Moon. (An exception to this would be where glass is used within human habitats or other artificial environments that contain moisture on the Moon.)

The effects of water on the strength, s , of a glass in the presence of water can be described by,

$$s = s_0 + \sqrt{\frac{F(2.3RT, V^*)}{B} (\log \frac{F(P_0, P)})} \quad (2)$$

where R is the gas constant, T is temperature, V^* is an "activation volume" (usually determined empirically), and s_0 is the initial strength of the glass under initial partial pressure, P_0 . This equation is based on the thermodynamic increase in the rate of hydrolytic depolymerization (*Fig. 7*) with applied stress. It predicts, correctly, that strength varies inversely with the partial pressure of water. It is important to realize, however, that water is not *necessary* for rupturing the metal-oxygen bonds that make up the glass network. A high applied stress, especially in the presence of surface flaws which intensify the stress at the crack tip, can cause fracture directly. Thus, in the absence of water, the strength does not increase without bound, as implied by Eq. 2.

2. Experimental Procedure

To examine experimentally the effects of water and flaws on the strength of simulated lunar glasses, a chemical composition similar to that of lunar rock sample 14049, returned by Apollo 14, was used (Table 1]. Reagent grade oxides were mixed, melted, quenched, ground, re-melted, and cast into pucks, as described in previous reports. After annealing, the pucks were cut and polished into $3 \pm 0.06 \times 4 \pm 0.06 \times 45 \pm 1.0$ mm bars which were used for 4-point beam-bending. Controlled surface flaws were introduced to one set of bars with a Vickers indenter. The flaw size was controlled by varying the indentation load. By measuring the length of the cracks an average crack length was determined for each indentation load and relative humidity. One set of samples was etched in hydrofluoric acid to eliminate surface flaws. To simulate a glass produced and used on the Moon, some of these samples were then abraded with MLS in a ball mill.

After indentation, the bars were placed in a small oven at approximately 150 °C for 45-60 minutes to eliminate any moisture that may have been present in the fresh flaws. To maintain their dry condition until they could be tested, the samples were immediately placed into a desiccator after heating. Samples that were tested under dry conditions were covered liberally with mineral oil immediately after removal from the oven and before placement into the desiccator. The oil did not exclude all moisture from the crack tips, since there was a some small amount of water dissolved in the oil. Studies in the literature indicate, however, that this of moisture has a negligible effect on the strength.

The bars were tested within one hour using a four-point beam-bending fixture in an Instron material testing system at an extension rate of 1 mm/min at room temperature. The dimensions of each specimen were measured after testing in order to increase the accuracy of the strength calculations. At least six samples were tested at each relative humidity and crack size.

3. Results

The effect of humidity on the strength of lunar glass samples. each having an average crack size of 81 μm , is shown in *Figure 8*. As the humidity decreased, the strength of the lunar glass

increased. The error bars on the graph indicate one standard deviation in strength for each relative humidity. The solid line in *Figure 8* is a least-squares fit of Eq.2, using V^* as the adjustable

parameter. (The best-fit of V_c was $2.78 \times 10^{-4} \text{ m}^3$. The physical basis for this value is not well understood, however, so we do not place any significance on this number.)

While the measured strengths increase as the water content decreases, as predicted by Eq. 2, the key feature in *Figure 8* is the lack of extremely high strengths, as predicted by Eq. 2, as the water content approached 0. The highest strength measured (for samples with 81 μm flaws) was 125 MPa, which occurred under nominally anhydrous conditions. As mentioned previously, this is not surprising, since fracture can occur without stress corrosion cracking, by direct rupture of the network.

The average strength of sample etched in HF is also plotted in *Figure 8*. The etched samples were much stronger than those that had been indented. The strongest sample broke at over 360 MPa, and the average strength was 205 MPa. This is over twice as strong as those samples which had been indented and tested under dry conditions without HF etching. The average strength of samples which were HF etched but then abraded in lunar simulant is also shown in *Figure 8*. Abrasion weakened the samples substantially, with strengths averaging 103 MPa for this treatment, which is similar to what glasses on the Moon will have to withstand.

Comparing the effects of water and flaws, the difference in strength between the HF etched and indented samples tested under the same (dry) conditions is much larger than the strength difference between samples measured at 0 and 100 percent relative humidity with the same flaw size. State differently, surface flaws affect the strength significantly more than stress corrosion cracking. Moreover, surface flaws are likely to be unavoidable in the lunar environment, where one is likely to find dust from human activity and the bombardment of micrometeorites.

Not surprisingly, extremely high strengths were found with melt-spun fibers, as shown in *Figure 5*. Since the largest flaws in a thin fiber can be no larger than the diameter of the fiber, the surface flaws, and, hence, stress intensification, in fibers are necessarily small. In fact, it is noteworthy that the fiber shown in *Figure 5* withstood more than 600 MPa *in air*; where, stress corrosion cracking can take place. (It should be noted, though, that these fibers must also be protected from surface flaws in order to retain their high strength.)

In summary, if lunar-derived glass is fabricated and utilized on the Moon, it will have imperfections, i.e. surface flaws, as on Earth. Regardless of the specific techniques and methods employed in the

production and handling of lunar-derived glass, surface flaws will be present. Even if flawless glasses were produced on the Moon, surface flaws would be unavoidable due to the dusty environment. Therefore, while the anhydrous conditions of the lunar surface will result in a slight increase in strength in comparison to similar glasses on Earth, the strength of lunar-derived glass will still be limited by small surface flaws, which will reduce the strength well below the theoretical value.

C. Glasses: Effect of Atmospheric moisture on Toughness

In addition to high strength, it has been suggested that the lack of water, glass will be tougher (i.e., less brittle) on the Moon because of the lack of water in the atmosphere. We examined this possibility during the past year both from simple theoretical and experimental standpoints.

The fracture toughness, K_{IC} , is defined as

$$K_{IC} = s_f \sqrt{R(\pi c)} = \sqrt{R(2Eg)} \quad (3)$$

where s_f is the fracture strength, c is the flaw size, E is the elastic modulus and g is the surface energy of the glass. Because of the lack of vapor molecules, which adsorb onto and passify the surfaces of freshly fracture glass, it is likely that the surface energy of freshly fractured glass will be higher in an anhydrous environment than in a water-containing environment. While the increase in surface energy may be significant (a factor of two, three, or even ten), the fracture toughness varies with the square root of the surface energy, so that large changes in K_{IC} are unlikely.

To examine this effect quantitatively, we used the Vicker's indenter to produce flaws of three different sizes, and broke the samples under nominally dry, and ambient conditions. The results are shown in *Figure 9*, where the fracture strength is plotted against inverse square root of flaw size. The slope of this plot gives the fracture toughness (Eq. 3). For glass tested in ambient conditions, $K_{IC} \approx 0.7 \text{ MPa}\sqrt{\text{m}}$, which is in the range usually measured for terrestrial glasses. When tested under dry conditions, the fracture toughness increased slightly, to about $1.3 \text{ MPa}\sqrt{\text{m}}$. As demonstrated in *Figure 10*, however, this increase, is insignificant, when compared to the fracture toughness of typical steels, $\approx 50\text{-}90 \text{ MPa}\sqrt{\text{m}}$. In summary, will be brittle in the lunar environment, and tensile stresses will have to be avoided in engineering applications of glass on the Moon.

IV. Undergraduate Involvement

In addition to the science and engineering components, as described above, one important goal of this project to involve undergraduates in the laboratory, and make them part of the research effort. Under the supervision of Brian Fabes (PI) and Howard Poisl (graduate student) four undergraduates (Dan Allen, Michelle Minitti, Steve Hawley, and Tony Beck) worked on this project. Their efforts were an integral part of this work. As a result, both Dan and Michelle's participated as co-authors on papers which we published during the past year.

V. Future Work

In the coming year we plan to continue to examine the kinetics and thermodynamics of crystallization in the multi-component lunar glasses, and to optimize the strength of the resulting glass-ceramics in the A14 and A16 systems. Howard Poisl will spend approximately six weeks at Johnson Space Center, where he will use Mössbauer spectroscopy to determine the coordination state of the iron in the various glasses. Dan Allen and Steve Hawley will continue to assist him in measuring crystallization rates, and to measure strengths in the crystallized glasses.

Bob Crockett, from McDonnell Douglas Corporation recently joined our group as a graduate student. Bob's expertise is in space structures. He has been in contact with Wayne Rogers (U of Co SERC) and is finishing a study of the materials issues in fabrication of structures on the Moon. In his initial investigations Bob has identified joining technologies as a critical issue in building large structures. In the coming year, therefore, Bob plans to investigate the effect of composition and processing on the elastic modulus of lunar glasses. Our ultimate goal here will be to design interface materials that can be used to bind and seal bricks, tiles, and other lunar ceramics together for large-scale structures.

497594
N93-26686
52-26
158359
p 3

Recovery and Separation of Precious Metals From Space

H. Freiser and S. Muralidharan

Strategic Metals Recovery Research Facility

Department of Chemistry

University of Arizona

Abstract

We have developed during the past year a viable procedure centered around centrifugal partition chromatography (CPC), a multistage liquid-liquid partitioning technique for the separation of precious metals (Pt, Pd, Rh, Ir, Os, Ru). We have identified stable and inexpensive ligands that can be readily recycled to achieve the separations of the precious metals. The separation methods developed so far yield three separate fractions: Pt, Pd, and Rh-Ir. The Rh-Ir pair can be separated in a subsequent run. The total amount of precious metals separated in a single experiment varied from 1 to 50 mg. The factors affecting the efficiencies of these separations have been studied. The kinetics of the decomposition of the complex and the ion pair have a major bearing on these efficiencies, with slow kinetics resulting in poor efficiencies. The methods for the improvement of the efficiencies have also been investigated. For example, significant improvement in the efficiencies and separation times for Pt and Pd have been achieved by the use of chloride gradient in the mobile phase.

Two papers were published and talks were presented on our work at the FACSS meeting in Anaheim, October 1991, and at the Pittsburgh Conference in New Orleans, March 1992.

Overall Research Objectives

Our major overall objective in this project is to develop efficient and economical large-scale separation and recovery methods for the metals of the platinum group and other precious metals that are suitable for use in space. Our analysis of the problem has led us to the use of multistage separation processes involving two liquid phases as the optimum direction to pursue. The relatively novel separation technique known as Centrifugal Partition Chromatography (CPC), has been selected as the most promising of the various types of chromatography, particularly from the point of view of scale up, as well as the strong scientific support provided by analogies to solvent extraction, an area of great strength in our group.

Progress to Date

Centrifugal Partition Chromatography (CPC), a recently introduced countercurrent liquid-liquid distribution technique, used mainly for the separation of a broad spectrum of organic compounds, has now been applied to the separations of metal ions. We were the first to demonstrate the efficient separation by CPC of adjacent lanthanides, including the separation of both light and heavy lanthanides in a single run using gradient pH elution.

With NASA support, we were the first to achieve the separation of palladium(II) from the other PGM with CPC using a mixed complex, $\text{Pd}(\text{TOPO})_2\text{Cl}_2$. These studies revealed that, under comparable conditions, CPC efficiencies for metal ions separations were significantly lower, by a factor of 4-5, than those regularly seen for organic compounds. Another anomaly that occurs with metal ion separations is that unlike the behavior of organic compounds, column efficiency depends on the distribution ratio of a given metal species. Although not commented on in the literature, similarly low efficiencies and their dependence on the distribution ratios of the extracted metal species can also be observed in the separation of metals by derivatized solid supports. Generally, in chromatography the column efficiency is constant for a given set of operating conditions, exhibiting no dependence on the distribution ratios of the species being separated. Possibly, because separations of metal ions by CPC involve formation and dissociation of extractable complexes using suitable ligands, chemical factors may be responsible for the differences. During the last project period we undertook systematic investigation to determine whether, and in what manner, chemical factors, in contrast to simple solvation and desolvation as well as mass transfer factors, were responsible for the differences in CPC efficiencies for metals and organic separations. CPC studies coupled with

solution kinetic studies using stopped flow has allowed us to clearly establish the influence of chemical kinetics on CPC column efficiencies and correlate them to the half-lives of the chemical reaction responsible for the lowered chromatographic efficiencies.

In work to date, we have focused our efforts on finding optimal solutions to problems of reagent systems affording great selectivity and sufficiently rapid kinetics to eliminate threats to separation efficiency. First, we developed a CPC procedure which served to separate Pd(II) from the rest of the platinum group metals (PGM). We used our experience here to uncover the chemical factors limiting selectivity and efficiency of separation because we learned that for many metal separation systems, these outweighed the mass transfer factors governing most multistage separations. This study led us to an investigation of the chemical kinetics of extractable complex formation and dissociation reactions and the testing and evaluation of appropriate new systems. During this past project period, we have been successful in separating Pd(II) and Pt(II) from each other and from the remaining PGM.

Nature of Research Proposed

Our current research is directed toward applying the principles we have discovered to the separation and recovery of all of the individual members of PGM and scaling up the best of the systems we find. Finally, we will address the problems of adapting our processes to conditions in space. Before the end of this project period, we expect to apply the separation and recovery schemes to the production of fractions of the individual PGM from the carbon monoxide-treated residue of iron meteorite sample(s) to be made available to us by Dr. John Lewis.

49795
N 93 - 26687

**Development and Mechanical Properties of Construction Materials
From Lunar Simulant**

**Chandra S. Desai
Department of Civil Engineering and Engineering Mechanics
The University of Arizona**

5/3-31
158360
p. 12

Abstract

Development of versatile engineering materials from locally available materials in space is an important step toward the establishment of outposts on the Moon and Mars. Here development of the technologies for manufacture of structural and construction materials on the Moon, utilizing local lunar soil (regolith), without the use of water, is an important element for habitats and explorations in space. It is also vital that the mechanical behavior such as strength and tensile, flexural properties, fracture toughness, ductility and deformation characteristics are defined toward establishment of the ranges of engineering applications of the materials developed.

The objectives here include two areas: (1) thermal "liquefaction" of lunar simulant (at about 1100°C) with different additives (fibers, powders, etc.), and (2) development and use of a new triaxial test device in which lunar simulants are first compacted under cycles of loading, and then tested with different vacuums and initial confining or in situ stress. Details of the development of intermediate ceramic composites (ICC) and testing for their flexural and compression characteristics have been described in various reports and papers.¹⁻² The subject of behavior of compacted simulant under vacuum has been described in previous progress reports and publications³⁻⁴; since the presently available device allows vacuum levels up to only 10^{-4} torr, it is recommended that a vacuum pump that can allow higher levels of vacuum is utilized for further investigation.

Principal Investigator: Chandra S. Desai

Graduate Student: Janos Toth

Undergraduate Student: Bryant Steele

Introduction and Results to Date

The development of new construction materials through liquefaction of lunar simulants with various admixtures (powders and fibers), and determination of mechanical properties using various laboratory testing devices to perform bending and flexure, tension, cylindrical triaxial, and three-dimensional multiaxial tests are the main objectives in this progress report.

The lunar simulant used, called Arizona Lunar Simulant, has been developed locally from a basaltic rock found near Hanford, WA. This material has a mineralogical composition similar to that of the lunar mare soil. The rock is ground so that its grain size distribution falls well within that of the distribution envelopes for the samples of the lunar regolith brought to Earth by Apollo missions, *Figure 1*.

In order to define various engineering properties such as flexure, compressive, tensile and fracture strengths, deformation characteristics, and ductility, the lunar simulant is combined with various powders and fibers. These include steel, stainless steel, aluminum, and fiberglass. The simulant itself, and with various percentages of powders or fibers, is liquefied in a furnace with a temperature capacity of 1700°C. The material is placed and compacted in molds made of graphite and titanium so that appropriately sized specimens for various tests can be obtained as follows:

SHAPE	SIZE	TEST	STATUS
Rectangular	1.0 cm X 2.5 cm X 25 cm	Bending	Completed
Flat	2.5 cm X 10 cm X 15 cm	Tension	Ongoing
Cylindrical	2.5 cm diam. X 5 cm 5.5 cm diam. X 15 cm ht.	Compression Triaxial (compression)	Ongoing Future
Cubical	10 cm X 10 cm X 10cm	Multiaxial (compression)	Future

Diagrams of these samples with loading conditions are shown in *Figure 2*.

In the thermal liquefaction, the simulant melts at about 1100°C and forms a matrix that can be made into various specimen sizes and shapes. The resulting intermediate ceramic, formed solely by the simulant, is relatively brittle. With addition of a powder or fiber, the liquefaction may involve melting of the admixture at a lower or higher temperature than that for the soil simulant. Thus the powder/fiber melts before the heated soil particles or vice versa, resulting in a "ceramic composite."

Such composites can possess a wide range of the aforementioned mechanical properties, and can result into materials with properties similar to mortar, concrete and certain (metal) composites.

An objective of the research is to perform a parametric study in which the ratio of simulant to powder/fiber is varied, together with different levels of temperature and cycles of temperature, the latter is expected to add "prestressing" due to residual expansion of the powder/fiber. It has been noted that such powders and fibers can be manufactured from the lunar regolith.

Specimens of the material combinations thus developed will be tested for bending, tension, fracture, ductility, and stress-strain-strength properties using laboratory testing methods as stated previously. This is a vital step toward potential engineering applications of the materials developed, because based on the parameters and constants determined, the ranges and type of application of the materials developed in space construction can be established.

The previous research so far has included: 1. Acquisition of the furnace, 2. development of a beam bending device as per the ASTM standard, 3. production of a number of beam specimens with varying admixture content, and 4. testing of a number of beam specimens for their load-displacement behavior, described elsewhere.¹⁻² It was found that the addition of fibers contributes greatly to the load-carrying capacity and ductility of the material.

Development of flat, cylindrical and multiaxial specimens will be the subjects of continuing research. The flat specimens will be tested for tensile and fracture characteristics. The multiaxial specimens will be tested in unique three-dimensional devices that allow application of three independent principal stresses, different paths of loading, and static and cyclic loading. Future work will also involve use of the Arizona simulant and the simulant developed at the University of Minnesota to include determination of the effect of agglutinates in this type of research. Agglutinate is a small glass-welded aggregate of rock, mineral, and glass fragments formed during micrometeorite impacts into the regolith. Also considered will be the use of a pump with higher vacuum levels and testing of specimens under higher levels of vacuum, about 10^{-12} torr. This will also be used to continue the study using the new vacuum triaxial device.

Accomplishments During 91-92

A number of special issues related to the development of ICC were investigated. These include the following:

Modified Simulants. The Arizona Lunar Simulant was exhausted. Hence, a new batch was prepared from crushed and ground basalt (Pomona Flow, Hanford, WA). In order to fit better the grain size distribution (GSD) with the Apollo sample, the new batch was ground so that the GSD was as shown by the dashed curve (*Figure 1*); this provided inclusion of particle sizes in the range of 0.6 to 1.2 mm. It was found that the liquefaction temperature of the modified simulant was about the same as that for the previous batch. The chemical composition of both batches remained essentially the same.

Molds. Alternative molds so as to reduce oxidation and lead to high quality specimens.

Additives to Reduce Liquefaction Temperature. Based on a suggestion by Dr. Kumar Ramohalli, and discussion with Dr. Andrew Cutler, NASA-SERC, the publication, "Research on the Use of Space Resources", Jet Propulsion Laboratory, NASA-CR-173213, Carroll, W.F. (Editor), was reviewed. However, this report did not provide information on additives to reduce the liquefaction (melting) temperature. Then, based on discussions with Dr. F. Shadman (Ch. Eng.), lime and sodium hydroxide were considered as additives. Addition of lime (CaOH_2) did not cause significant reduction in the liquefaction temperature. Addition of sodium hydroxide (NaOH) reduced the temperature to about 1000°C , but the resulting material was found to be more brittle than that without the addition. This aspect will need further study. In the meantime, it is proposed to continue liquefaction without such additives.

Tensile Testing

For this purpose a new and special grip system was designed and fabricated for testing flat specimens using the available MTS Test Frame. *Figure 3* shows a flat specimens with grips that are expected to provide a central load and grip with sufficient tensile strength.

A parametric study was performed to identify a glue that can be used in addition to the grips. It was found that Magnolia 6514-65 glue can provide sufficient strength of about 4000 psi which is greater

than the tensile strength of the ICC. This was determined after testing cylindrical specimens of aluminum (6061 T4 Al) and ICC with the glue, *Figures 4a,b*.

As shown in *Figure 3*, it is proposed to monitor ultrasonic characteristics (velocity, attenuation and energy dissipation) so as to identify development of microcracking and fracture within the specimen, in addition to its tensile characteristics.

Specimens

The flat specimens (4 x 6 x 1 inch) are prepared by appropriate grinding of the specimens obtained after liquefaction so as to obtain a smooth surface for mounting the strain gauges and ultrasonic transducers.

Ongoing and Future Work

Tension Testing

A series of flat specimens will be tested with various loading-unloading-reloading cycles for various combinations of additives. The test results will allow determination of the tensile stress-strain-strength properties. A mathematical model will be developed to define damage and fracture characteristics using the disturbed state concept (DSC), in conjunction with the ultrasonic results.

Compression Testing

Cylindrical and cubical specimens will be cast and tested by using the cylindrical triaxial and multiaxial devices under loading, unloading and reloading cycles. The results will provide compressive stress-strain-strength characteristics of specimens with various admixtures.

The final objective of the research is to develop a methodology by which structural materials can be produced on the Moon using locally available and derived (fibers, powders, etc.) materials, formed into useful shapes by thermal solar energy and compaction. In addition to the development of materials, attention must be given to the determination of the mechanical properties necessary for structural design so that the material can be used in a wide range of engineering applications such as roads, foundations, blocks, walls, floors, buildings, support systems, and shields. The research results are expected to represent a significant contribution towards construction of facilities on the Moon.

References

1. Girdner, K. and C.S. Desai. Development of mechanical properties of structural materials from lunar simulants by thermal liquefaction. *Report to NASA-SERC* (1991). Dept. of Civil Engg. and Engg. Mechs., Univ. of Arizona, Tucson.
2. Desai, C.S. and K. Girdner. Structural materials from lunar simulants through thermal liquefaction. *Proc. SPACE 92* (1992). ASCE, Denver, Colorado.
3. Desai, C.S., H. Saadatmanesh, and T. Allen. Effect of vacuum on density and stress-strain-strength behavior of compacted lunar simulants. *Report to NASA-SERC* (1990). Dept. of Civil Engg. and Engg. Mechs., Univ. of Arizona, Tucson.
4. Desai, C.S., H. Saadatmanesh, and T. Allen. Behavior of compacted lunar simulants using new vacuum triaxial device. *J. Aerospace Eng.* (October 1992). ASCE, in press.

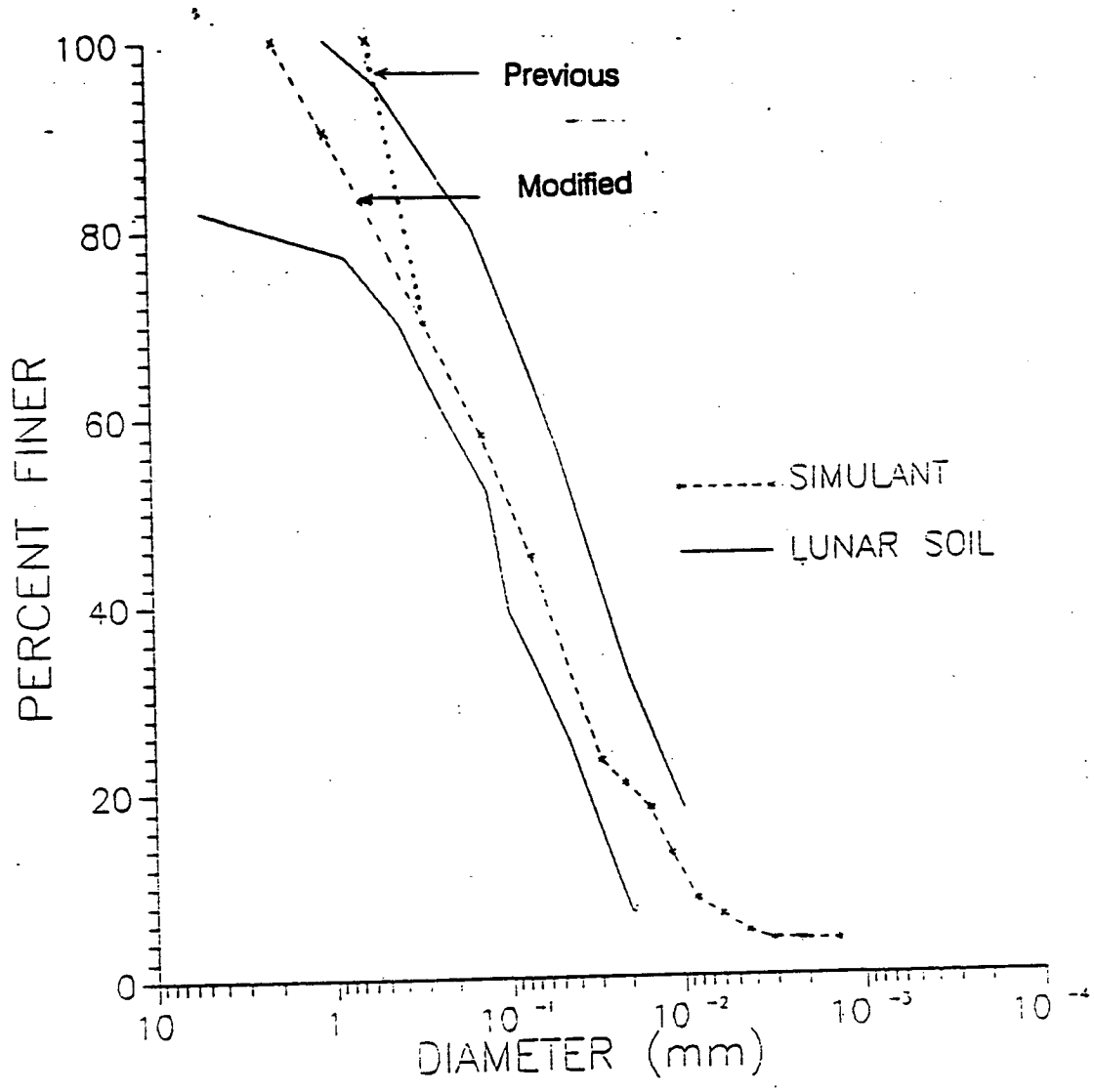
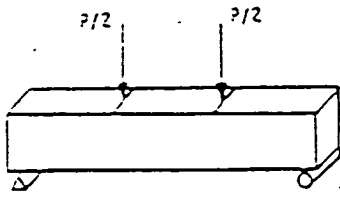
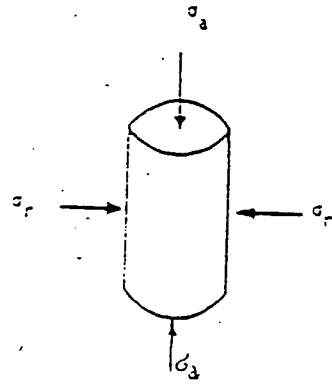


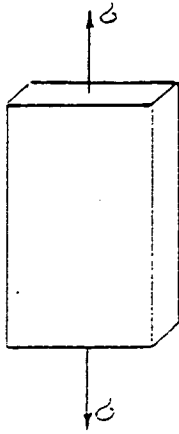
Figure 1. Grain size distribution of actual lunar soil and simulant



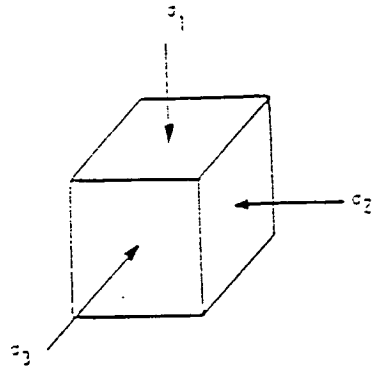
(a) Beam bending



(b) Cylindrical triaxial (compression)

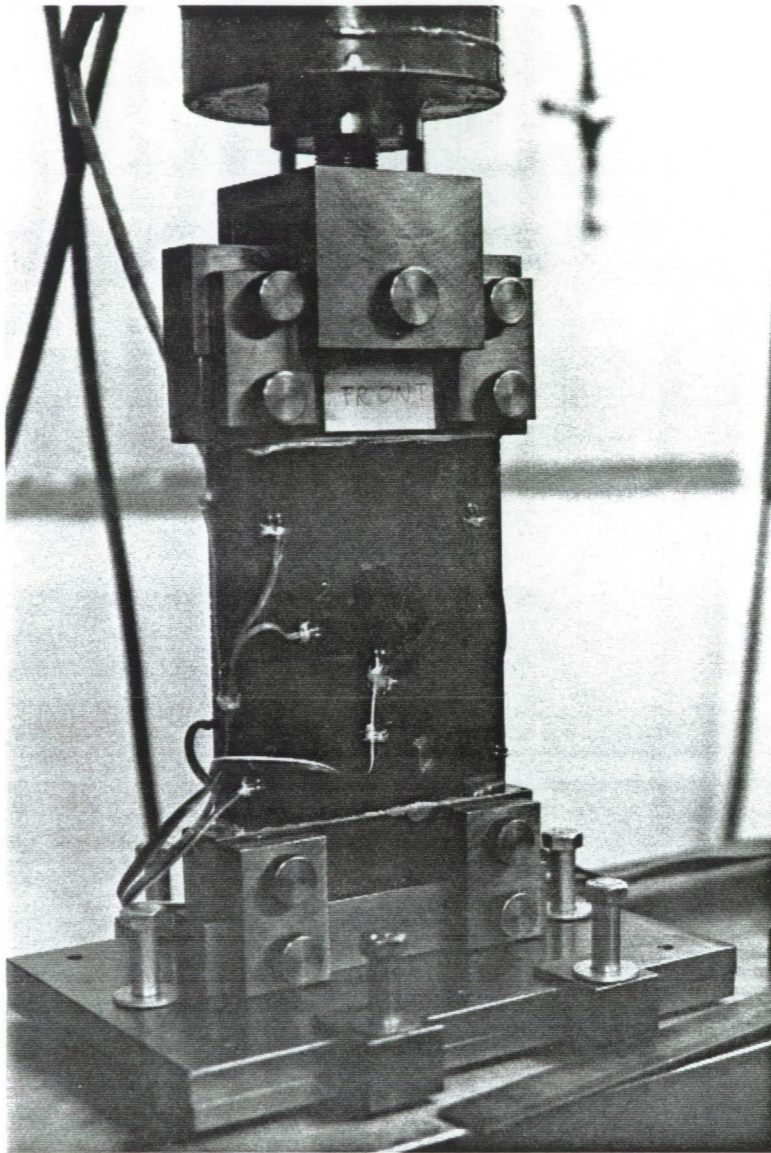


(c) Tensile



(d) Multiaxial (compression)

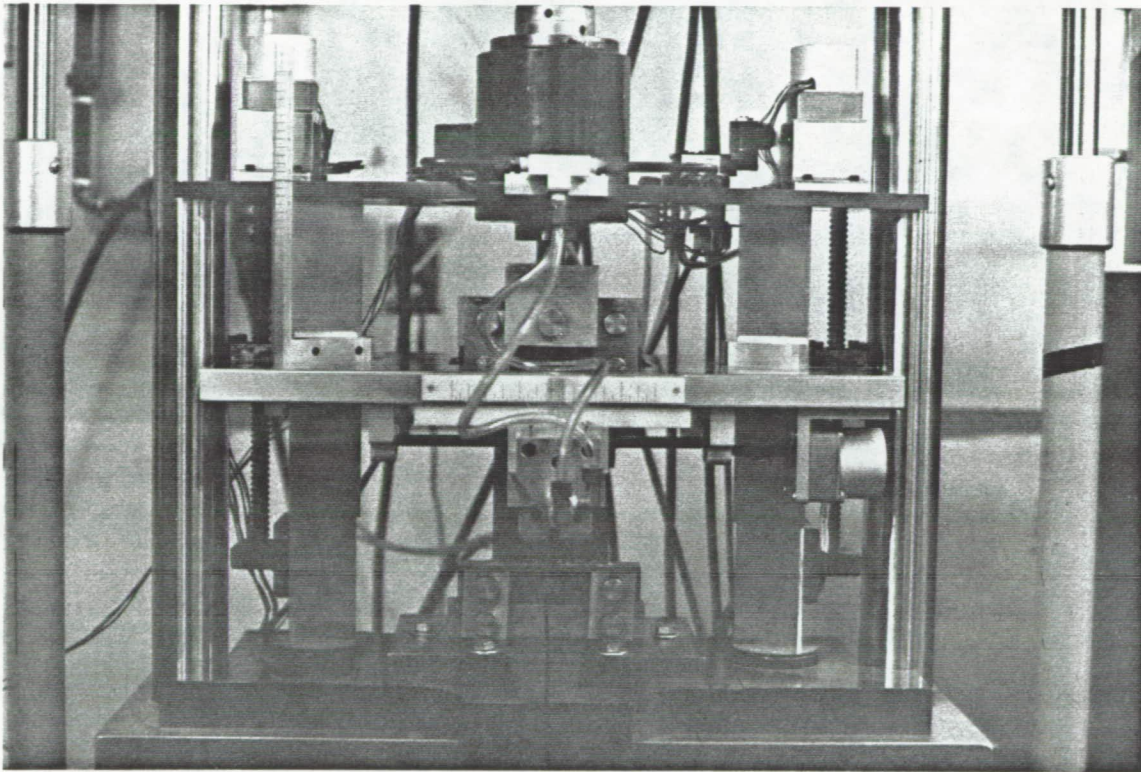
Figure 2. Schematic of Specimens



(a) Flat Specimen with Grips and Strain Gauges

Figure 3. Flat Specimen in MTS Frame

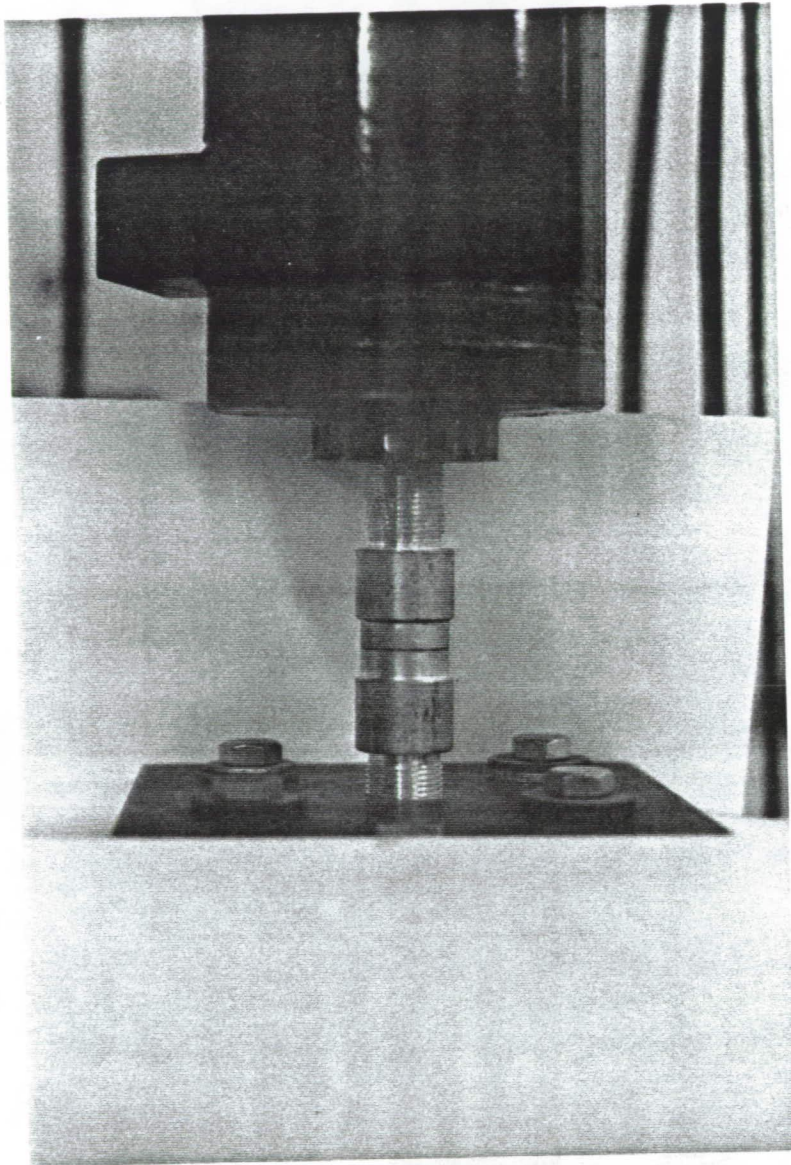
ORIGINAL PAGE
BLACK AND WHITE PHOTOGRAPH



(b) Flat Specimen with Ultrasonic Device

Figure 3 (continued).

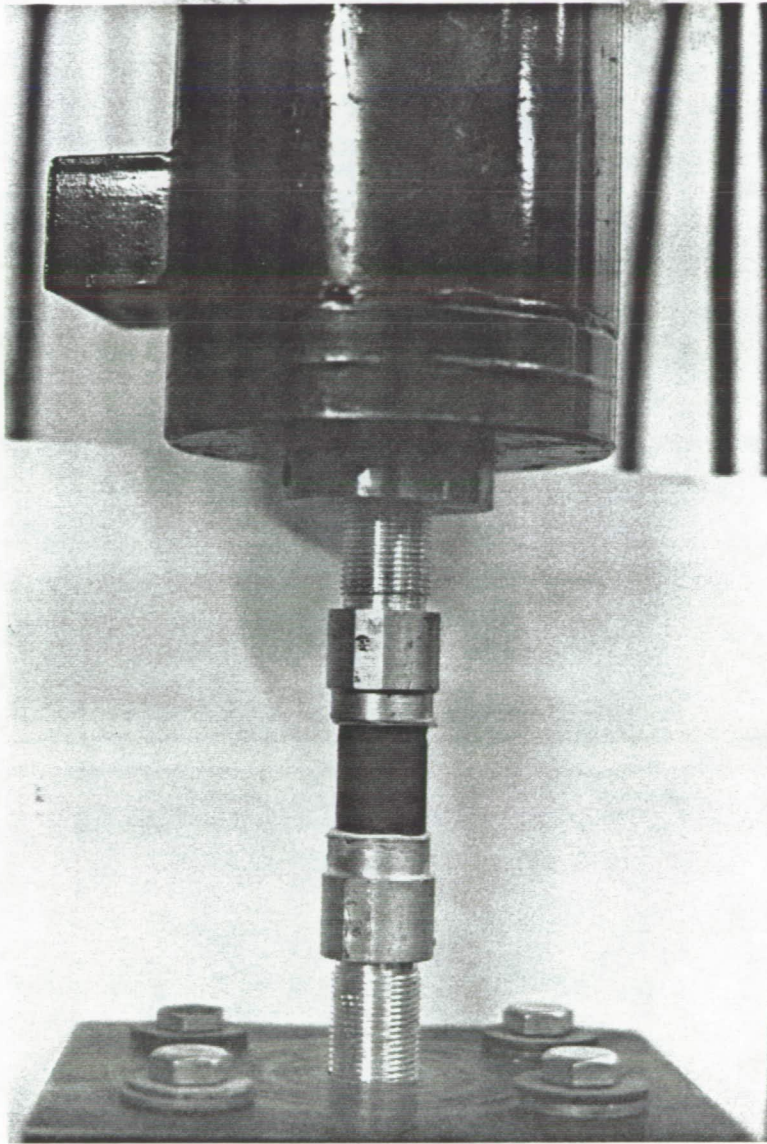
ORIGINAL PAGE
BLACK AND WHITE PHOTOGRAPH



(a) Glue on Aluminum Specimen

Figure 4. Testing for Glue

ORIGINAL PAGE
BLACK AND WHITE PHOTOGRAPH



(b) Glue on ICC Specimen

Figure 4 (continued).

ORIGINAL PAGE
BLACK AND WHITE PHOTOGRAPH

Large Area Solar Cells from Lunar Materials**Read Bryant, Paul Calvert and Jean Corley
Department of Materials Science/Engineering
The University of Arizona**514-44
158361
e-7**Abstract**

The first goal of the project has been to produce polymers from materials available on the Moon. This, apparently simple, aim is made complicated by the fact that there is no carbon on the Moon and there are no polymers (with a couple of irrelevant exceptions) known which do not contain carbon. Because of the abundance of silicon and oxygen in the lunar regolith, we decided to aim to produce siloxane polymers with the (-Si-O-) backbone found in silicones. A univalent side group is also needed but there are no univalent elements available in the regolith which could plausibly make stable structures. Failing this, hydrogen is a good choice for side group since it accounts for a small fraction of the total weight of the polymer. Thus we have a group of target structures such as $(-\text{SiH}_2\text{-O})_n$, $(-\text{Si}(\text{OH})_2\text{-O})_n$.

We have approached this goal via a series of simpler syntheses. During the first year we made polydimethylsiloxane $(-\text{Si}(\text{CH}_3)_2\text{-O})_n$ by controlled hydrolysis of $\text{SiCl}_2(\text{CH}_3)_2$, which is a routine synthesis, and then proceeded to attempt to make polydichlorosiloxane by controlled hydrolysis of SiCl_4 . At the end of the first year we had some infra-red spectra indicating that this product had been obtained.

Polydichlorosiloxane

We now have made gram samples of a yellow-brown rubbery polymer which we believe to be polydichlorosiloxane. This material has remained rubbery for over 6 months, sealed in a glass tube. On exposure to air it slowly converts to a powder, presumably silica. We are working to obtain clearer spectral data on this material. Since it has not been previously reported we have no comparative data to establish the structure.

The decomposition behavior of this material is both pleasing and disappointing. A concern with this polymer is that it might disproportionate, that is convert to silica, SiO_2 , and silicon tetrachloride. Such a reaction could be driven by the very high stability of silica. This apparently does not happen. We also expected the polymer to be very sensitive to hydrolysis, which seems to be the case. We had hoped that it might be self-passivating by forming an impermeable layer of silica which would then prevent further reaction.

Polydihydrosiloxane

We are now in the process of trying to make this polymer by hydrolysis of dichlorosilane SiH_2Cl_2 . This synthesis is rather more tricky since the silane is a gas and is expected to be spontaneously inflammable. A vacuum line has been set up to bubble the silane into tetrahydrofuran containing a small amount of water. After a known amount of gas has been passed into the solution, the solvent is evaporated. So far traces of oily residue have been observed but it is not clear how polymeric this is.

Future directions

The fact that neither the dihydrosiloxane nor the dichlorosiloxane have been prepared previously can be attributed to the expected instability of the materials. As explained above, it may turn out to be self-passivating against oxidation. Disproportionation is also a possibility but there are standard strategies for preventing this in polymers.

The dihydrosiloxane polymer should be the least hindered of any chain molecule so far prepared. This would imply that it should be a very low temperature elastomer. We anticipate using a sol-gel reaction to reinforce the material as necessary to form a series of composites with properties from very flexible up to as stiff as normal reinforced polymers. We envisage this family of materials as fulfilling a range of structural and protective roles in the lunar environment.

PREPARATIVE DETAILS

POLYDICHLOROSILOXANE

Polydichlorosiloxane is formed by the hydrolysis of silicon tetrachloride (SiCl_4) with distilled water. The reaction must be run at a controlled slow rate and the reactants cannot be introduced to each other in the concentrated form. The silicon tetrachloride was diluted by a common solvent, tetrahydrofuran (THF), and the distilled water was diluted by evaporation into a heated nitrogen stream. If these steps to dilute the reactants are not taken and the reactants are mixed at full concentration a violent reaction occurs giving the products HCl gas and silica.

The apparatus for the preparation consisted of a sealed reaction flask, cooled to 0-5 degrees C, that had a continuous flow of dried nitrogen gas. The reaction flask exhaust stream was run through a condenser. The condensed solvents were collected in a second flask sitting in an ice-water bath.

The solvent, 250 ml THF, was placed in the reaction flask and purged with nitrogen gas for about 10 minutes. The first reactant (38 ml SiCl_4) was added to the solvent and stirred continuously throughout the entire reaction by a magnetic stir bar. The second reactant, 5.5 ml distilled water, was introduced by evaporation into the heated nitrogen stream (about 60 degrees C). Stoichiometry dictated that 6 ml of distilled water be used but apparently some of the SiCl_4 was evaporating before the water could be fully introduced. Therefore, we reduced the amount of water by 0.5 ml and the reaction has yielded much more product. The first reaction that was done in this manner had the nitrogen stream at room temperature. This reaction was complete in 47 hours. The nitrogen stream for the second procedure was heated to 40 degrees C, and took 12.5 hours to complete. Total time for complete evaporation for the third and latest procedure was 7.5 hours. The completed reaction was then distilled to remove the remaining solvent. Distillation took an average of 15 hours at 50-55 degrees C. The remaining 10-15 ml of material in the latest procedure was colorless and appeared to have a consistency like that of table jelly at room temperature.

The second reaction produced a product that was a brown color. The reason for this brown color may be that the distillation temperature was too high or that the reagents used were not pure. This is the substance that has been tested to a limited degree. The third reaction product was colorless and tests are about to begin on this sample.

Several attempts have been made to get an accurate FTIR spectrum of the polymer. However, due to the sensitivity of the substance to water in the air the spectra are difficult to obtain. An FTIR spectrum of polydichlorosiloxane in THF overlaid with that of the solvent is attached (*Figure 1*). The peaks of interest are those present in the sample but not in the solvent. A clear peak is seen at around 1100 cm^{-1} which corresponds to the Si-O vibration. In addition there are peaks in the $600\text{-}800\text{ cm}^{-1}$ region which we believe are due to Si-Cl. Silicon tetrachloride has a single peak at 760 cm^{-1} while the polymer has peaks at 614 cm^{-1} and 700 cm^{-1} .

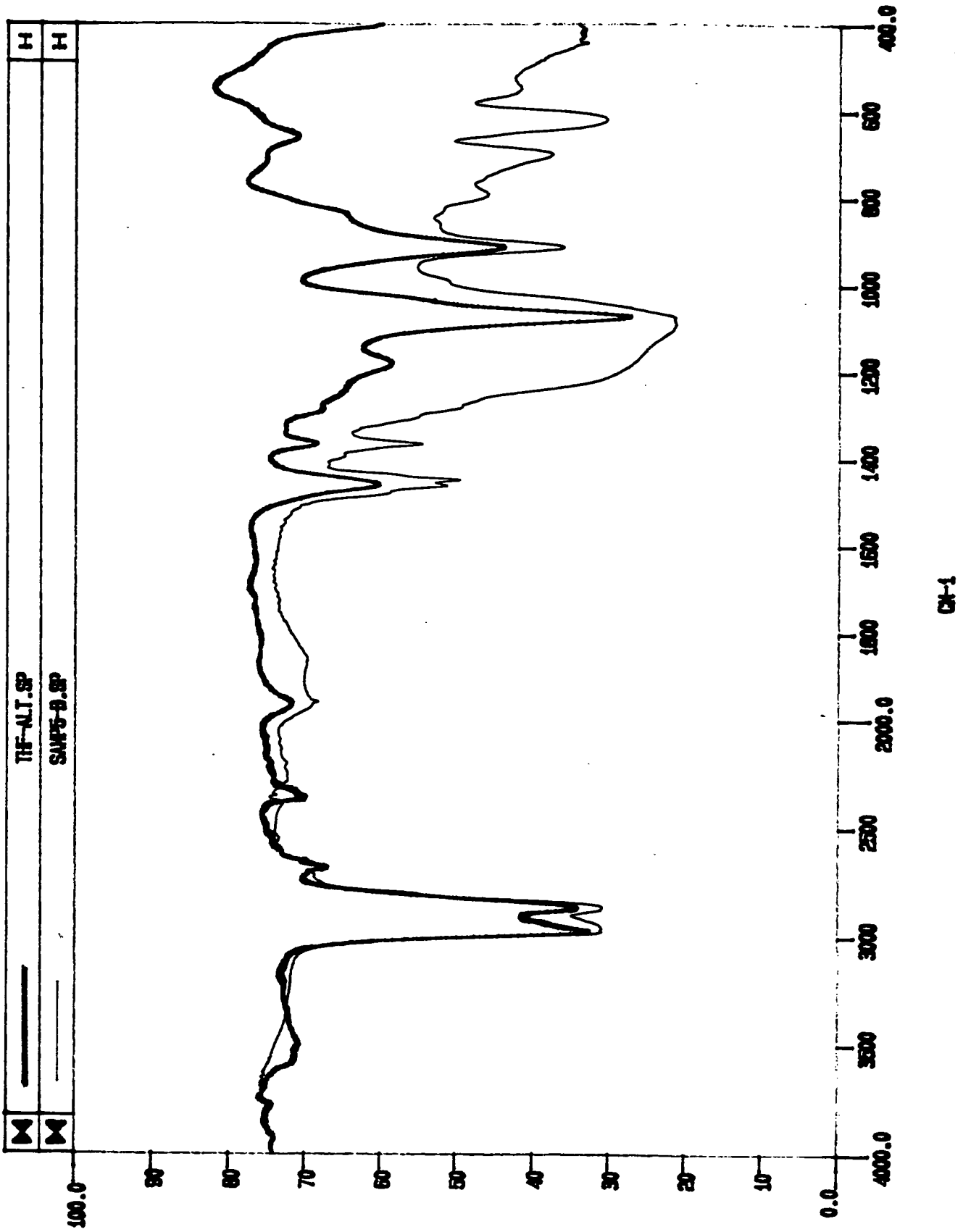
POLYDIHYDROSILOXANE

Polydihydrosiloxane is being synthesized by the hydrolysis of dichlorosilane gas (SiH_2Cl_2). This reaction is being carried out in a vacuum manifold at 1 Torr where the gas is bubbled into a water-THF solution, typically 3 ml water and approximately 140 ml THF. This reaction is being run at room temperature and at reaction times that vary from 30 minutes to 2 hours. After the reaction is determined to be complete, the gas is turned off and the THF is pulled off in the vacuum line and collected in a cold trap. This setup is shown in the attached diagram, *Figure 2*.

The products that have been given off are usually clear light-yellow liquids. If allowed to sit for several days strong fumes are given off and the liquid solidifies without any noticeable visual change. This solid has apparent elastic properties but when prodded with a spatula comes apart like very fine wet sand. This type of product was manufactured several times, but on one occasion a white cloudy substance with a dark brown top layer was noticed. This change happened without explanation.

FTIR spectra from the initial experimental runs show the expected bonds (Si-H and Si-O-Si) although it is difficult to remove all traces of solvent without oxidizing the polymer. The lower spectrum in *Figure 3* shows SiH peaks at 2200 cm^{-1} and SiO peaks at around 1100 cm^{-1} . There is also a substantial amount of residual water which appears as a broad peak at 3400 cm^{-1} and some solvent which is seen as C-H at 3000 cm^{-1} . On exposure to the air to remove the final amount of solvent, it can be seen from the upper curve that there is also some oxidation of the polymer with loss of the SiH and a change in the SiO peak as silica is formed. What we cannot be sure of as yet is how far the polymerization has continued and to what extent we have low molecular weight hydroxysilanes.

FIGURE 1



SI

REACTION APPARATUS FOR POLYDIHYDROSILOXANE

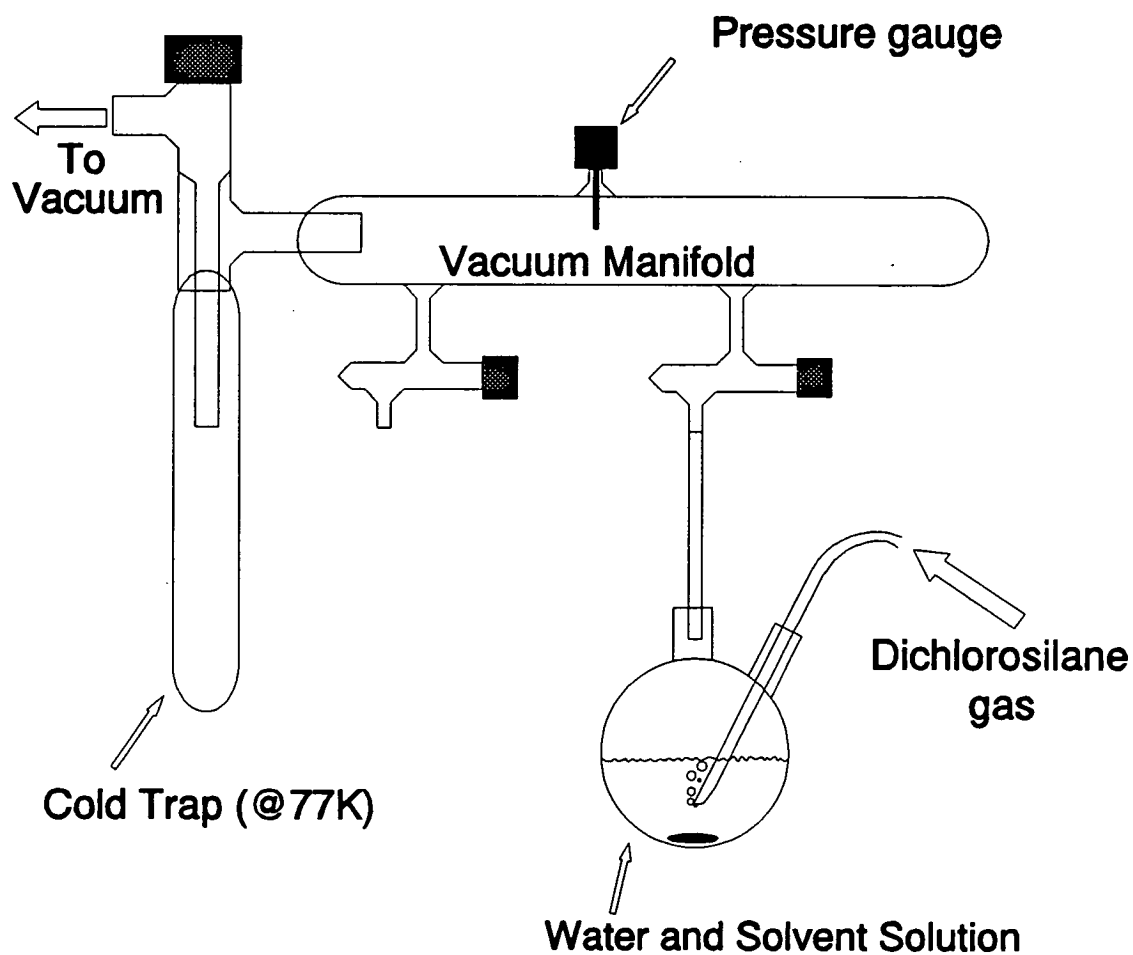
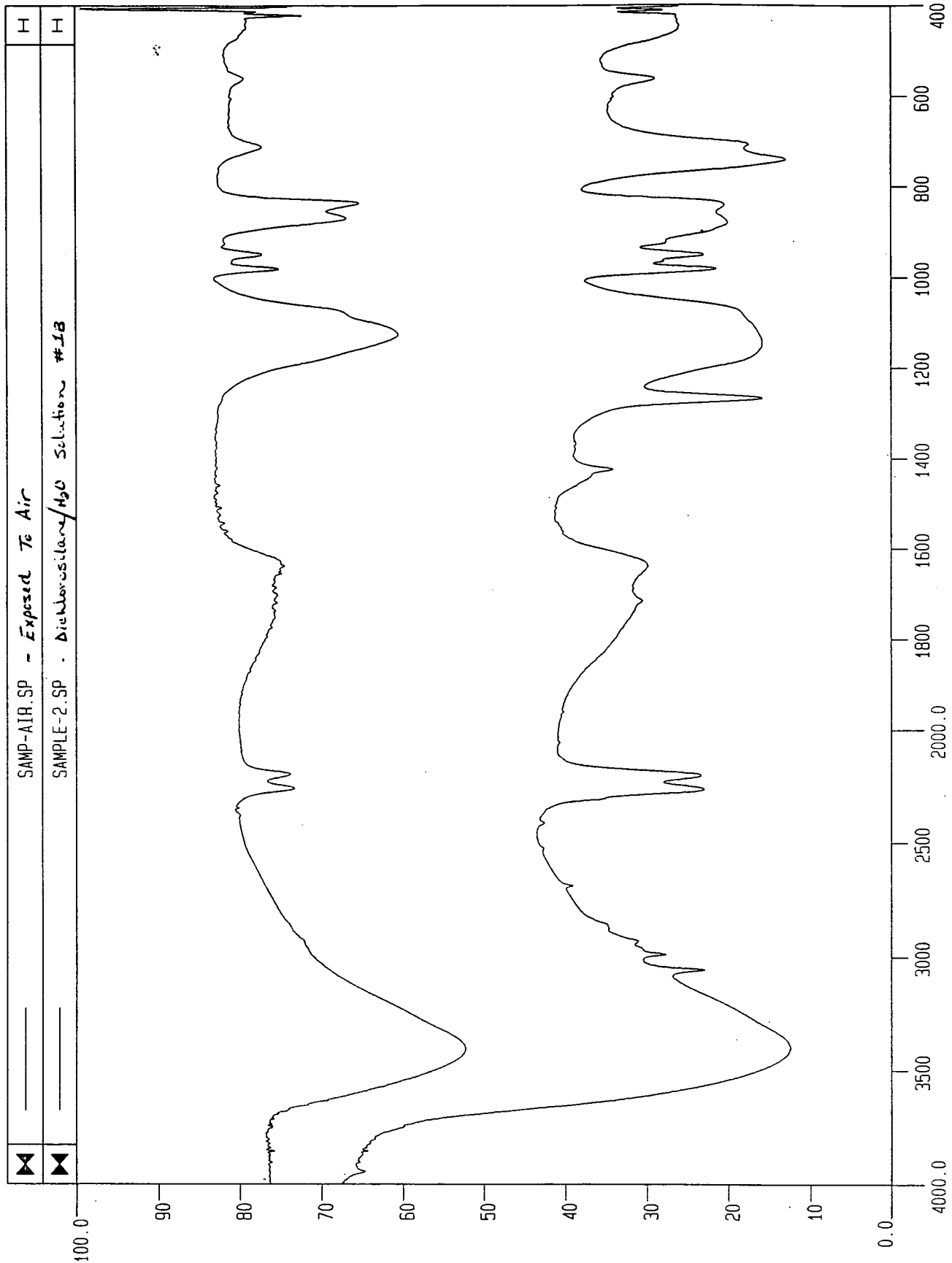


FIGURE 2

Exp: 11



—	SAMP-AIR.SP - Exposed To Air	I
- - -	SAMPLE-2.SP - Dichlorosilane/H ₂ O Solution #18	I

%T

II-34

CM-1

omit

III. RESOURCE DISCOVERY AND CHARACTERIZATION

497597

N 9 3 - 2 6 6 8 9

Determination of Lunar Ilmenite Abundance from Remotely Sensed Data

S.M. Larson, D.E. Melendrez, J.R. Johnson and R.B. Singer

Planetary Image Research Laboratory (PIRL)

Department of Geosciences/Lunar and Planetary Laboratory

The University of Arizona

315-91

158362

P. 6

**ORIGINAL DOCUMENT
COLOR REPRODUCTIONS**

Abstract

Of fundamental importance in the utilization of indigenous resources for a future permanently manned lunar base is the identification and mapping of the abundance distribution of the mineral ilmenite, which is currently considered the most readily identifiable and most easily accessible source of oxygen needed for human consumables and spacecraft propellant. Solid state detector array technology now permits the use of groundbased multispectral remote sensing techniques to produce maps with better than one kilometer spatial resolution and uncertainties of about two weight-percent TiO_2 abundance. We have used an empirical relationship between the weight-percent abundance of titanium dioxide and the 400/560 nm spectral ratio measured in returned lunar samples. Because this abundance correlation is valid only for mature lunar mare regolith, we have also qualitatively mapped the distribution of immature mafic minerals which we have found to be correlated primarily with steep slopes exposing bedrock. The first mapping phase focussed on the entire lunar nearside at 5.3 km per pixel (Johnson et al, 1991a), and on experiments with more sensitive spectral ratios. Relative spectrophotometry was employed to aid in identifying wavelengths that provide greater spectral contrast. We found that the 400/730 nm ratio improved the abundance sensitivity by 37% (Johnson et al, 1991b), while the 950/730 nm ratio improved mafic mineral contrast about 100% (Larson et al, 1991). The second mapping phase utilized a large experimental CCD at 280m per pixel to map the high titanium regions identified in the phase one mapping. The high resolution maps provide data on the small scale (500m) variations in abundance and their relationship to morphological units (Melendrez et al, submitted to *JGR*).

Recent Results

Efforts over the past year have been aimed at defining the peak abundance levels of high TiO₂ deposits on the highest spatial scales achievable from the ground (~500 m), and investigating possible phase function effects on the image ratios used to generate our maps. Photometrically calibrated multispectral imaging data were obtained over four months at the Tumamoc Hill Observatory to obtain a full lunation of phase angles of five areas containing high and low abundance TiO₂ regions, representative highland material, pyroclastic deposits and the standard reference MS-2. A spin-off of this major observing effort was the acquisition of several excellent image sets with essentially pixel-limited (440m) resolution. Although previous data with a 2048 x 2048 pixel CCD on two nights at the Catalina 1.5m telescope had 280m pixels, the atmospheric seeing limited the resolution to 0.5-1.0 km. Our new data provides important new confirmation of the complex small scale morphology of the high TiO₂ bearing deposits in the lunar regolith, and more precise abundance maps because of improved photometric controls. The higher resolution maps show TiO₂ abundances of 14 weight-percent (or more) in regions as large as 20 square km. in Mare Tranquillitatis (see *Figure 1*). The complex spatial distribution of the highest TiO₂ units appear to be a result of specific flow episodes which have overlaid, and later been partly covered by low TiO₂ basalt flows in a complex manner dictated by local topography and vent location.

The lunar phase function had been previously determined for the integrated disc and for some small areas, but in very limited spectral bandpasses. We used our standard 340, 400, 560, 730 and 950 nm filters in this phase function study to quantify effects on various spectral ratios used to define the TiO₂ abundance and soil maturity. Although past mapping efforts were concentrated near full moon (phase angle < 10 degrees), this range contains the major effects of the lunar opposition "surge". With the help of Jim Collins, a student using the complex data reduction process as a class project in Singer's remote sensing class, we measured the brightness of 36 points in the five bandpasses at 13 phase angles. The sampled 1 km square points covered a broad range of TiO₂ abundances, and we now know that in spite of the appreciable phase angle wavelength dependence, it has minimal effect on the relative abundance values. The greatest phase effect is in the 950nm band which contains the major absorption band of crystalline pyroxene and is used as a qualitative indicator of agglutinate content. The results of this work, which is currently being prepared for publication, are highly applicable to the design of orbital and surface optical remote sensing experiments.

Future Work

We anticipate expanding this work into near-infrared wavelengths (0.7-2.6 μ m) to facilitate mapping abundances of Fe, Ca and Mg in the lunar regolith. We are also interested in better characterizing optical effects of the pyroclastic deposits which do not follow the empirical TiO₂ calibration we use, but may still contain very high amounts of ilmenite. This work will require the use of a new near-IR CCD array sensitive to the 0.7 - 2.6 micron region. As before, telescopic data will be obtained at kilometer resolution to determine the surface abundance distribution. Deriving abundances of other potential resources will require supporting laboratory spectral measurement of returned lunar samples and terrestrial laboratory analogs to provide calibration of appropriate spectral bands. We anticipate establishing a spectrogoniometer facility to provide the optical characterization and calibration needed for quantitative remote sensing in this mineralogically diagnostic spectral region.

References

- Johnson, J.R., S.M. Larson, and R.B. Singer. (1991a) Remote sensing of potential lunar resources 1. Near-side compositional properties. *J. Geophys. Res.* 96 (18): 861.
- Johnson, J.R., S.M. Larson, and R.B. Singer. (1991b) A reevaluation of spectral ratios for lunar mare TiO₂ mapping. *Geophys. Res. Lett.* 18 (No. 11): 2153.
- Larson, S.M., J.R. Johnson, and R.B. Singer. (1991) Evaluation of the sensitivity of reflectance ratios to mafic minerals in the lunar regolith. *Geophys. Res. Lett.* 18 (No. 11): 2149.
- Larson, S.M., J. Collins, D.E. Melendrez, J.R. Johnson, and R.B. Singer. (1992) Remote sensing of potential lunar resources 3. Lunar phase function effects and spectroscopy. Submitted to *J. Geophys. Res.*
- Melendrez, D.E., S.M. Larson, J.R. Johnson, and R.B. Singer. (1992) Remote sensing of potential lunar resources 2. High spatial resolution mapping of near-side mare TiO₂ abundances. Submitted to *J. Geophys. Res.*

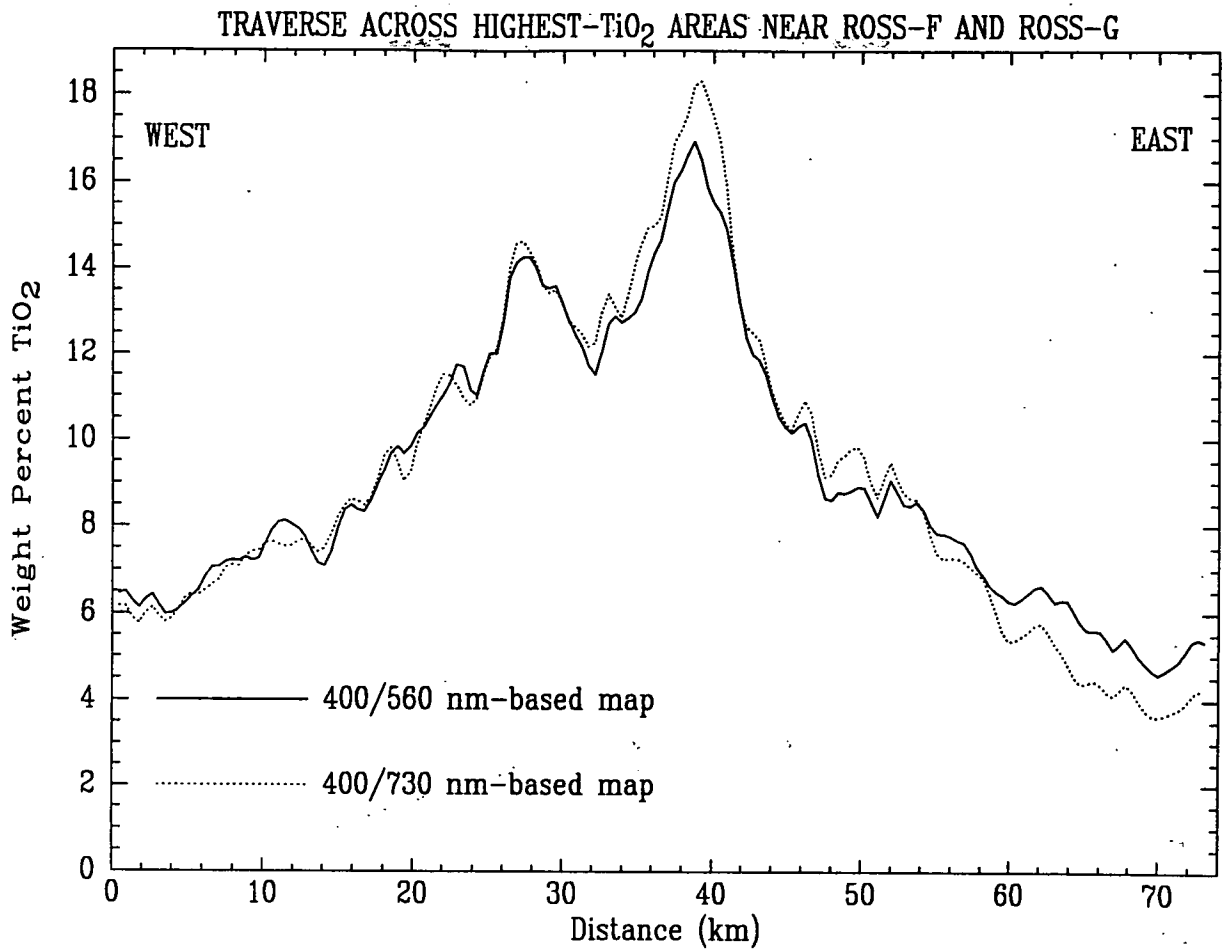
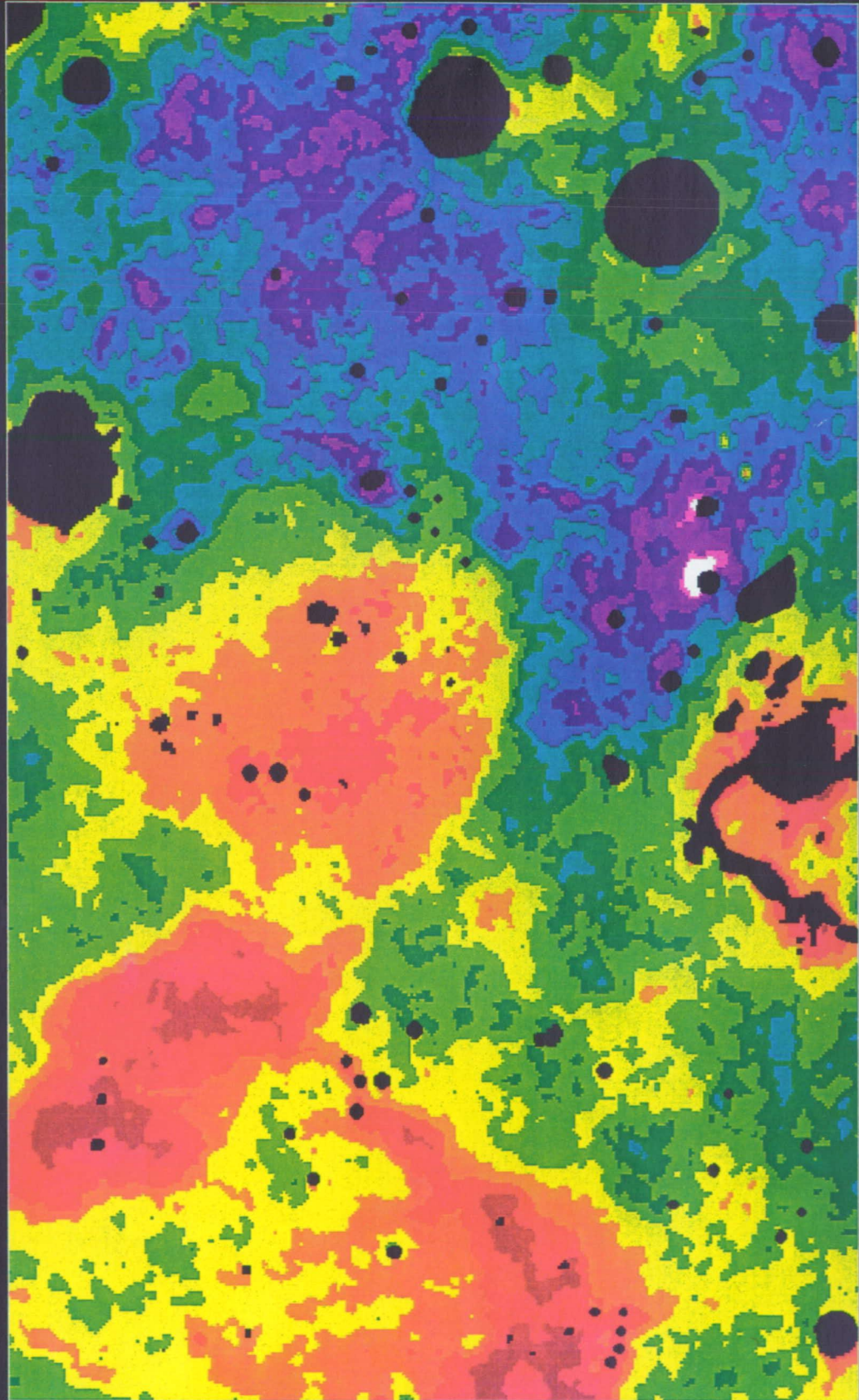
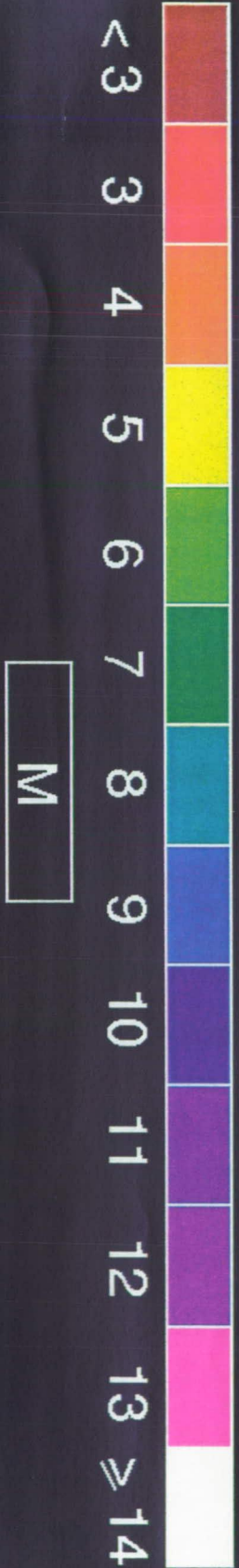


Fig.1 Traces of the weight-percent of TiO₂ across the high abundance region in central Mare Tranquillitatis showing the generally good correspondence between the traditionally calibrated 400/560 nm ratio, and the 400/730 nm ratio. At a scale of 440 meters per pixel, this trace shows the localized nature of the high TiO₂ bearing regolith.

Fig.2 (next page) High resolution TiO₂ abundance map for central mare Tranquillitatis. The frame height is about 140 km. Areas not applicable to the TiO₂ calibration have been blacked out.



497598
2
N 93 • 26690
158363
p-6

Composition of Near-Earth Asteroids

Larry A. Lebofsky

Lunar and Planetary Laboratory

The University of Arizona

Abstract

The continuing goal of this study is to determine whether any of the near-Earth asteroids or the satellites of Mars contain hydrated phyllosilicate (clay) minerals. If these minerals are present, they would provide a ready source of water for propellant generation and use in life support systems. Many of the dark mainbelt asteroids have been shown to contain hydrated phyllosilicate minerals. Some of the near-Earth asteroids are also dark, but telescopic detection of water on these near-Earth asteroids is complicated because of the faintness of these small asteroids and because thermal emission masks the diagnostic spectral features beyond 3μ due to water of hydration for objects within 2 AU of the Sun. New techniques for asteroid classification based on spectral reflectance *and* mineralogy will be necessary to determine whether the water absorption features are present on any of the near-Earth asteroids. This past year, we have begun looking for better ways to classify "wet" vs. "dry" asteroids in the main belt. This new classification may allow us to determine the presence of water of hydration in the surface minerals of near-Earth asteroids even when we can only observe them at wavelengths that are not affected by thermal emission.

Introduction

The CI1 and CM2 carbonaceous chondrite meteorites are known to contain hydrated phyllosilicate (clay) minerals. However, the fine grain size has made it difficult to determine the specific minerals present. Some of the CI1 meteorites contain evaporite minerals which are believed to have been deposited when a heating event allowed liquid water to migrate through the parent body, eventually depositing the evaporates. Asteroidal-sized bodies with these compositions would prove to be rich sources of water and oxygen, and the resources might be easier to extract from phyllosilicates than from other oxides.

Reflectance spectra of the hydrated carbonaceous chondrites meteorites are similar to telescopic spectra of some of the dark C-class asteroids in the main asteroid belt, implying similar mineralogy. Unfortunately, it is difficult to obtain accurate telescopic spectra of dark asteroids, and the dark components in their surface mask the diagnostic, near-infrared absorption features of the silicate minerals presumed to be present. The major water-of-hydration absorption feature at approximately 3μ is sufficiently strong that it is not masked by the dark components of the surface, which makes it possible to determine whether hydrated phases are present, even if it is not possible to determine the exact mineral species. Detection of water on Ceres by Lebofsky confirmed both the presence of water in the asteroid belt, and the feasibility of detecting it telescopically. It also led to the general idea that all dark asteroids were primitive and volatile rich.

Telescopic surveys by Lebofsky and coworkers have shown that many of the dark asteroids do contain hydrated minerals, but not all (*Figure 1*), which has forced a re-evaluation of the simple idea that dark necessarily means volatile rich. They have proposed that the dark asteroids in the main asteroid belt accreted from water ice and anhydrous silicates, and heating events later melted the water in some of them, producing hydrated silicates. If this explanation is correct, then at least the dark asteroids in the outer asteroid belt probably do contain volatiles, even if they are no longer present at the surface. An additional complication for the inner asteroid belt has been proposed by Dan Britt who has shown that black chondrites, which are shock darkened ordinary chondrites (which are totally anhydrous) are spectrally indistinguishable from some of the dark asteroids in the visible and near-infrared. Both ideas together explain many problems in interpreting the history of the asteroid belt, but they complicate the determination of the composition of individual asteroids tremendously.

The near-Earth asteroids are dynamically much easier to reach than the mainbelt asteroids, which

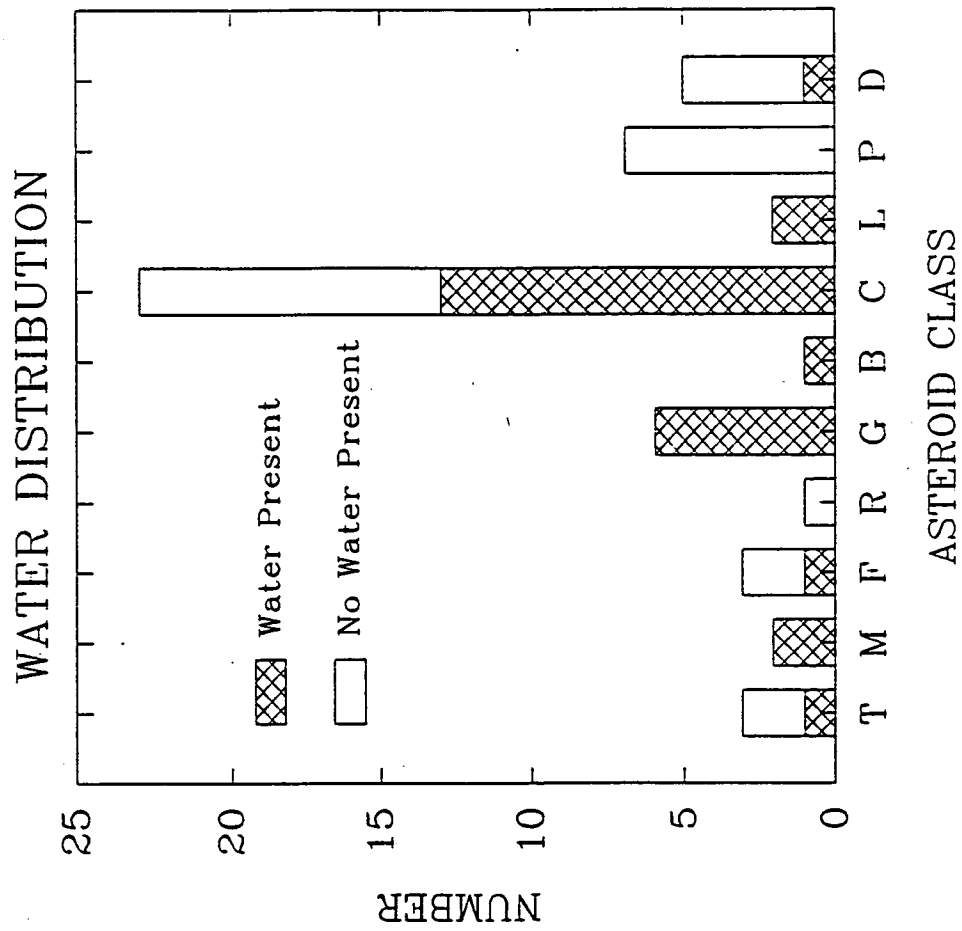


FIGURE 1

would make them more feasible resource targets. Most of the taxonomic C-class asteroids known in the main asteroid belt have been found in the near-Earth asteroid population, as well as one which has not yet been detected in the main belt. Unfortunately, as the previous paragraph mentioned, asteroids which are the same taxonomic type may well be compositionally different because the taxonomy was originally defined using only visible and extremely-near-infrared wavelengths, which do not include the wavelengths which are sensitive to hydrated minerals. This makes it impossible to predict which dark near-Earth asteroids will contain water without more extensive telescopic spectra. In addition, the near-Earth asteroids are nearer to the Sun than the main belt, which makes them warmer, which in turn moves the peak of their thermal emission to shorter wavelengths. This is particularly true of the dark asteroids. For the dark near-Earth asteroids, the thermal emission is large enough to mask the absorption feature caused by hydrated minerals. Simple thermal models can be used for the mainbelt asteroids because they are much cooler, but these models are insufficient to correct the near-Earth asteroids for thermal emission.

Over the past few years, we have been attempting to model, simultaneously, the reflected light and thermal emission from near-Earth asteroids. However, we have found this to be a less than productive task. It appears that we may never be able to accurately remove the thermal component from spectra in order to be able to see the $3\text{-}\mu$ feature when the thermal emission dominates this spectral region. Therefore, it has become necessary to try to find other ways of identifying asteroids that may have hydrated silicates in their surface materials.

Results for this Year and Proposed Work

We finished a review paper on asteroid composition for the *Resources of Near-Earth Space* book, in conjunction with Dan Britt. The paper will update the existing review papers on asteroid compositions, and provide comprehensive spectral figures of all the asteroid and meteorite types in one place for the first time. Several abstracts have been written and papers presented relating to our ongoing asteroid studies. We have also submitted a paper on asteroid taxonomies using neural networks which we discuss below.

Funds for this project have gone, in part, to support the work of graduate student Ellen Howell. She has been studying the relationship between comets and asteroids and has been involved the observations of the mainbelt and near-Earth asteroids and in the development of the new taxonomic system using neural networks. Because near-Earth asteroids are faint, and thus difficult to observe, we have been able to get only limited visual and near-IR observations of about 10 near-Earth

asteroids over the past 2 years. However, we have been much more successful in our overall study of the low-albedo asteroids. To date, we have observed and studied about 75 low-albedo asteroids and small satellites out to at least 3μ . Our goal for the next year is to study, in detail, the spectra of these mainbelt asteroids and make new observations, if necessary. By using neural networks, we are now attempting to categorize these asteroid spectra as a first attempt to classifying them based on spectrum *and* mineralogy. By looking at the spectra in this way we have been able to determine the validity of the taxonomic classification of asteroids as a determinant of asteroid mineralogy (*Figure 2*).

The next step is to see if the neural network technique can correctly classify asteroids that have limited signal to noise and spectral range (only out to 2.5μ) as is the case for most near-Earth asteroids. It is our hope that we will be able to distinguish between "wet" and "dry" (the presence or absence of water of hydration) asteroids even when we do not have data in the 3μ region.

497599

N 9 3, ~~26691~~

158364

R 7

Spacewatch Discovery of Near-Earth Asteroids

Tom Gehrels

**Lunar and Planetary Laboratory
The University of Arizona**

Abstract

Our overall scientific goal is to survey the solar system to completion -- that is, to find the various populations and to study their statistics, interrelations, and origins. The practical benefit to SERC is that we are finding Earth-approaching asteroids that are accessible for mining. Our system can detect Earth-approachers in the 1-km size range even when they are far away, and can detect smaller objects when they are moving rapidly past Earth. Until Spacewatch, the size range of 6 - 300 meters in diameter for the near-Earth asteroids was unexplored. This important region represents the transition between the meteorites and the larger observed near-Earth asteroids (Rabinowitz 1992).

One of our Spacewatch discoveries, 1991 VG, may be representative of a new orbital class of object. If it is really a natural object, and not man-made, its orbital parameters are closer to those of the Earth than we have seen before; its delta V is the lowest of all objects known thus far (J. S. Lewis, personal communication 1992).

We may expect new discoveries as we continue our surveying, with fine-tuning of the techniques.

Introduction

The data accumulated in the following tables are the result of continuing observation conducted as a part of the Spacewatch program. T. Gehrels is the Principal Investigator and also one of the three observers, with J.V. Scotti and D.L. Rabinowitz, each observing six nights per month. R.S. McMillan has been Co-Principal Investigator of our CCD-scanning since its inception; he coordinates optical, mechanical, and electronic upgrades. He is also the PI for the radial-velocity search for planets of other stars, which uses the remainder of the time, centered on full Moon, on the Spacewatch Telescope. M.L. Perry works with McMillan on various electronic and mechanical design problems, and he is responsible for electronic and mechanical maintenance of the Spacewatch Telescope. Scotti is responsible for the astrometry, working closely with B.G. Marsden, E.L.G. Bowell, and other colleagues for the follow-up of our discoveries and sometimes of others' discoveries as well. Rabinowitz makes improvements in the Solbourne/Sun Station system, and is our leading investigator of the statistics for near-Earth asteroids.

Proposed Work

We propose to continue using the Spacewatch Telescope during 18 nights per month, to find more candidates for mining. With the new CCD we have acquired we should nearly double our discovery rate.

Preliminary results we have already reported, namely that there is an excess by as much as a factor of 100 over the power-law extrapolation from our findings of the larger ones. The explanation of the excess is in terms of origin and evolution of the orbits.

Magnitude-frequency analysis may be made also for other populations such as for the mainbelt asteroids; we may do some of this depending on available time and/or funding, perhaps for a dissertation. There is an enormous database because Spacewatch finds nearly 2,000 mainbelt asteroids per month. All the data are preserved, and we propose, in fact, to make these generally available via e-mail to whoever wants them; a beginning of this has been made, with e-mail to the Minor Planet Center.

Spacewatch Discoveries, Until Summer 1991

Identification	Perihelion distance (AU)	Aphelion distance (AU)	Inclination (deg)	Diameter	Date of Discovery (km)	Remarks
1989 UP	0.98	2.7	3.9	0.3	27 Oct. 1989	elongated; perihelion at Earth
1990 SS	0.89	2.5	19.4	0.9	25 Sep. 1990	
1990 TGI	0.77	4.2	9.1	4.6	14 Oct. 1990	discovered at 2.9 AU from Sun
1990 UN	0.81	2.6	3.7	0.09	22 Oct. 1990	H=23.5
1990 UO	0.30	2.2	29.3	0.4	22 Oct. 1990	perihelion at Mercury orbit
1990 UP	1.10	1.5	28.1	0.4	24 Oct. 1990	Amor; slow rotation
1990 VA	0.71	1.3	14.2	0.6	9 Nov. 1990	Aten; perihelion at Venus orbit
1991 AM	0.51	2.8	29.7	2.3	14 Jan. 1991	crosses Venus orbit
1991 BA	0.71	3.8	2.0	0.009	18 Jan. 1991	smallest object found so far
1991 BN	0.87	2.0	3.4	0.5	19 Jan. 1991	
1991 CB1	0.64	2.7	15.8	1.3	15 Feb. 1991	
1991 EE	0.84	3.6	9.8	1.5	13 Mar. 1991	
1991 FA	1.08	3.0	3.2	1.5	17 Mar. 1991	Amor
1991 FE	1.07	3.5	4.5	5.8	18 Mar. 1991	Amor
1991 JR	1.04	1.8	10.1	0.14	8 May 1991	Amor; associated with the δ -Boötids meteor stream
1991 LH	0.37	2.3	51.1	1.0	14 June 1991	

In addition to the discoveries, Spacewatch "rediscovered" (1865) Cerberus, P/Kopff, P/Taylor, P/Helin-Roman-Alu 1, and P/Hartley 1. Also, five objects were followed because of their apparent fast motion, but the eventual orbit indicated they were on the inside of the asteroid belt, and another two were in geocentric orbit.

Spacewatch Discoveries, to date

Identification	Perihelion distance (AU)	Aphelion distance (AU)	Inclination (deg)	Diameter (km)	Date of Discovery	Remarks
P/Spacewatch	1.54	4.8	10.0	--	8 Sep. 1991	1991x
1991 RJ2	1.26	3.2	9.0	0.7	2 Oct. 1991	Amor
1991 TT	1.00	1.4	14.8	0.03	6 Oct. 1991	
1991 TU	0.94	1.9	7.7	0.009	7 Oct. 1991	
1991 VA	0.93	1.9	6.5	0.02	1 Nov. 1991	
1991 VG	0.97	1.1	0.2	0.01	6 Nov. 1991	*
1991 XA	0.98	3.6	5.3	0.09	3 Dec. 1991	
1992 AD	8.7	32.3	24.7	>40	9 Jan. 1992	(5145) Pholus
1992 AE	1.13	2.2	5.8	2.9	10 Jan. 1992	Amor
1992 BA	1.25	1.4	10.5	0.4	27 Jan. 1992	peculiar orbit
1992 DU	0.96	1.4	25.1	0.05	26 Feb. 1992	
1992 HF	0.61	2.2	13.2	0.6	24 Apr. 1992	
Spacewatch	3.2	--	125.2	--	1 May 1992	1992h
1992 JG	1.30	3.9	5.6	1.5	2 May 1992	deep Mars crosser
1992 JD	1.00	1.1	13.6	0.05	3 May 1992	

*This may be an upper stage of an Apollo spacecraft, or, if natural, a new type of asteroid with orbit nearly the same as that of the Earth. In addition to the discoveries, Spacewatch rediscovered 3288 (an Apollo), 3122 (an Amor), P/Shoemaker-Levy 5, P/Gunn and (2060) Chiron (!) and made the first ground-based observation of a cometary dust trail (for P/Faye). 1991 RJ2 had been discovered by Helin in September, but it was then lost. We also obtained preliminary orbits for objects that looked promising, namely 1 Trojan, 1 Hilda, 1 Flora, 5 Mars-Crossers, and 3 Hungarias.

Pertinent Publications (Chronological)

van Houten, C.J., I. van Houten-Groeneveld, P. Herget, and T. Gehrels. The Palomar-Leiden survey of minor planets. *Astron. & Astrophys. Suppl.* 2 (1970): 339-448.

Gehrels, T. Some interrelations of asteroids, Trojans and satellites. In *Comets, Asteroids, and Meteorites*, A. H. Delsemme, ed. Univ. of Toledo Press, 1977: 323-25.

Gehrels, T. Faint comet searching. *Icarus* 47 (1981): 518-22.

Gehrels, T. Asteroids and comets near the Earth. *Science Today*. XV (7) 1981: 23-29; transl. in *l'Astronomia* 13: 3-9 (in Italian) and *Ziran Zazhi* 5 (1982): 115-20 (in Chinese).

Gehrels, T., and R.S. McMillan: CCD scanning for asteroids and comets. In *Sun and Planetary System*, W. Fricke and G. Teleski, eds. (Dordrecht: D. Reidel Publ. Co., 1982): 279-84.

Frecker, J.E., T. Gehrels, R.S. McMillan, W.J. Merline, M.L. Perry, J.V. Scotti, and P.H. Smith. A CCD system for photometry of direct and spectroscopic images. In *Proc. of the NASA/SDSU Workshop on Improvements in Photometry*, W. J. Borucki and A. Young, eds. NASA CP-2350 (1984): 137-51.

Gehrels, T. Comparison of a 1.8-m CCD scannerscope with a 1.2-m Schmidt camera. In *Proc. of the 2nd Asian-Pacific Reg. Mtg. on Astron.*, B. Hidajat and M. W. Feast, eds. (Jakarta: Tira Pustaka, 1984): 335-40.

Gehrels, T.: Fundamental studies of asteroids. *Bull. Astron. Soc. of India* 12 (1984): 16-39; also in *l'Astronomie* 98 (1984): 115-32 and 159-70 (in French); also in *Astrum* 54 (1984): 5-13 (in Spanish).

Gehrels, N., T. Gehrels, J.V. Scotti, J.E. Frecker, and R.S. McMillan. Optical monitoring of gamma-ray burst source fields. In *Proc. 19th Int. Cosmic Ray Conf.* Vol. 1 (NASA CP-2376) 1985: 19-22.

Gehrels, T. Asteroids and comets. *Physics Today* 38 (1985): 32-41.

Gehrels, T., and F. Vilas. CCD search for geosynchronous debris. *Icarus* 68 (1986): 412-17.

Gehrels, T. On the feasibility of observing small asteroids with the Galileo, Venera, and Comet-Rendezvous-Asteroid-Flyby Missions. *Icarus* 66 (1986): 288-96; also in *Astron. Vestnik*, 20 (4): 306-18 (in Russian).

Gehrels, T., B.G. Marsden, R.S. McMillan, and J.V. Scotti. The Spacewatch camera: A progress report. *Proc. Lunar Planet. Sci. Conf.* 17 (1986): 257.

Gehrels, T., B.G. Marsden, R.S. McMillan, and J.V. Scotti. Astrometry with a scanning CCD. *Astron. J.* 91 (1986): 1242-43.

McMillan, R.S., T. Gehrels, J.V. Scotti, and J. E. Frecker. Use of a scanning CCD to discriminate asteroid images moving against a background of stars. In *Proc. S.P.I.E.* (627) D. L. Crawford, ed., "Instrumentation in Astronomy-VI" (1986): 141-54.

Gehrels, T., J.D. Drummond, and N.A. Levenson. The absence of satellites of asteroids. *Icarus*, 70 (1987): 257-63.

Gehrels, T. Asteroid impacts and planet formation. In *On the Glassy Sea, an Astronomer's Journey* (New York: Amer. Inst. of Physics, 1988): 183-202.

van Houten-Groeneveld, I., C.J. van Houten, M. Wisse-Schouten, C. Bardwell, C., and T. Gehrels. The 1977 Palomar-Leiden Survey. *Astron. Astrophys* 224 (1989): 299-302.

Gehrels, T., R.S. McMillan, J.V. Scotti, and M.L. Perry. Drift scanning with a TK 2048 CCD. *Astron. Soc. of Pac. Conf. Ser.* (8) "CCD's in Astronomy," G. H. Jacoby, ed. (Provo: Brigham Young University Press, 1990): 51-52.

Rabinowitz, D.L., J.V. Scotti, M.L. Perry, T. Gehrels, and R.S. McMillan. Near real-time detection of Earth-approaching asteroids. *B.A.A.S.* 22 (1990): 117.

Rabinowitz, D.L.: Detection of Earth-approaching asteroids in near real-time. *Astron. J.* 101 (1991): 1518-59.

Gehrels, T. Scanning with charge-coupled devices. *Space Science Reviews* 58 (1991): 347-75.

Gehrels, T., R.S. McMillan, M.L. Perry, D.L. Rabinowitz, and J.V. Scotti. Spacewatch CCD-scanning and numerical discovery of asteroids and comets. In *Proceedings of Conf. on Near-Earth Asteroids*, Oct. 10-11, 1991, St. Petersburg, Russia (in English).

van Houten, C.J., I. van Houten-Groeneveld, M. Wisse-Schouten, C. Bardwell, D.W.E. Green, and T. Gehrels. The second Palomar-Leiden Trojan Survey. *Icarus* 91 (1991): 326-33.

Scotti, J.V., D.L. Rabinowitz, and B.G. Marsden. Near-miss of the Earth by a small asteroid. *Nature* 354 (1991): 287-89.

Gehrels, T., T. Nagatani, and T. Sato. Spacewatch project: Its past, present and future. *The Heavens* 72 (1991): 134-39 (in Japanese).

Gehrels, T., and R.S. McMillan, eds., *Spacewatch Report No. 5* (1991).

Gehrels, T., M. Guerrieri, M.S. Matthews, R.S. McMillan, M.L. Perry, D.L. Rabinowitz, and J.V. Scotti. Spacewatch and Spaceguard. *AIAA Space Programs and Technologies Conf.* AIAA 92-1498, March 24-27, 1992, Huntsville, AL.

Gehrels, T., R.S. McMillan, D.L. Rabinowitz, M.L. Perry, and J.V. Scotti. Spacewatch discoveries of near-Earth asteroids. Presented at SCLERA Symposium. "Selected Topics in Science and Technology." Nov. 19-22, 1991, Tucson, AZ. To be published in conference proceedings by World Scientific Publ. Co. (Singapore).

Rabinowitz, D.L. 1992: The flux of small asteroids near the Earth. In *Asteroids, Comets, and Meteors IV*, eds. A. Harris and E. Bowell (Houston: Lunar and Planetary Inst.). In press.

Scotti, J.V., T. Gehrels, and D.L. Rabinowitz. 1992: Automated detection of asteroids in real-time with the Spacewatch telescope. In *Asteroids, Comets, and Meteors IV*, eds. A. Harris and E. Bowell (Houston: Lunar and Planetary Inst.). In press.

Drummond, J., D. Rabinowitz, and M. Hoffmann, M. 1993: On the search for near-Earth asteroids. *Resources of Near-Earth Space*, eds. J. S. Lewis and M. S. Matthews (Tucson: University of Arizona)

Press). In press.

Rabinowitz, D.L. 1993: The size distribution of the Earth-approaching asteroids. Submitted to the *Astrophysical Journal*, 1992.

Scotti, J.V., 1992: Asteroids colliding with Earth. *Newton* 12 (No. 10): 40-47 (in Japanese).

Bailey, M.E., J.E. Chambers, G. Hahn, J.V. Scotti, and G. Tancredi. 1992: Transfer probabilities between Jupiter and Saturn family orbits: Application to 1992 AD = 5145. In *Proc. 30th Liège Coll. Observations and Physical Properties of Small Solar System Bodies*. In press.

Scotti, J.V., D.L. Rabinowitz. 1993: An automated system for astrometric reduction of scanned CCD images. In preparation.

Bailey, M.E., J.E. Chambers, G. Hahn, J.V. Scotti, and G. Tancredi. 1993: Chaotic evolution and dynamical transfer of Saturn family comets. In preparation.

Anderson, J.D., and T. Gehrels. 1993: A search for the tenth planet. *Icarus*. In preparation.

The Spacewatch discoveries and astrometry are published in *Minor Planet Circulars*, *Spacewatch Reports*, *Spacewatch Announcements* (e-mail), and special ones also in *IAU Circulars*.

497600

N93-26692

Abundance of ^3He and Other Solar-Wind-Derived Volatiles in Lunar Soil

Timothy D. Swindle

**Lunar and Planetary Laboratory
University of Arizona**

SIB-91

158365

P-8

Abstract

Volatiles implanted into the lunar regolith by the solar wind are potentially important lunar resources. Wittenberg et al. (1986) have proposed that lunar ^3He could be used as a fuel for terrestrial nuclear fusion reactors. They argue that a fusion scheme involving D and ^3He would be cleaner and more efficient than currently-proposed schemes involving D and T. However, since the terrestrial inventory of ^3He is so small, they suggest that the lunar regolith, with concentrations of the order of parts per billion (by mass) would be an economical source of ^3He . Solar-wind implantation is also the primary source of H, C and N in lunar soil. These elements could also be important, particularly for life support and for propellant production.

In a SERC study of the feasibility of obtaining the necessary amount of ^3He , Swindle et al. (1990) concluded that the available amount is sufficient for early reactors, at least, but that the mining problems, while not necessarily insurmountable, are prodigious. The volatiles H, C, and N, on the other hand, come in parts per million level abundances (Fegley and Swindle, 1992). The differences in abundances mean that a) a comparable amount of H, C and/or N could be extracted with orders of magnitude smaller operations than required for ^3He and b) if ^3He extraction ever becomes important, huge quantities of H, C, and N will be produced as by-products.

Introduction

Previous work on identifying promising sites for ^3He mining has focused on ilmenite (and hence Ti) content (e.g., Cameron, 1991), since ilmenite retains a higher fraction of the implanted He than do other common lunar minerals. Discussions of the abundances of H, C, and N, which are less dependent on mineral chemistry, generally assume that these volatiles are rather uniformly distributed in the lunar regolith, with only local variations as a result of local impact cratering history (Haskin 1989; see also Taylor 1991).

However, there are geometric factors affecting the abundance of all solar-wind-derived volatiles that have not been previously considered in discussions of resource utilization. In particular, since the Earth's magnetosphere shields the Moon from the solar wind during the portion of each month in which the subsolar point is at the central nearside, that region has been exposed to considerably less solar wind than has the central farside. In addition, equatorial regions should receive more solar wind than polar regions because the direction of the flow of the solar wind is close to the plane of the Moon's equator. Whether this translates into a difference in volatile content depends on how important saturation effects are: if the surfaces of samples from the central near side (such as the well-studied Apollo samples) are saturated with solar-wind derived volatiles, additional exposure will not lead to higher volatile contents.

In a previous nine-month grant, calculations were made of the expected size of variations in the solar wind fluence. Under the current grant, we have combined these calculations with estimates of lunar chemistry based on both telescopic and Apollo observations to identify sites that are promising either as resources, or as areas to test for the effects of saturation. We have acquired some crucial lunar samples and have performed some of the analyses to test for saturation, although these experiments have not yet been completed.

Variations in solar wind fluence

As a first step, we calculated how the integrated solar wind fluence varies with latitude and longitude on the Moon. The latitude effect is simply proportional to the cosine of the latitude. The longitude effect is more complicated, since it depends on the details of the Earth's magnetotail and magnetosheath. Rather than modeling the magnetosheath in detail, we assumed that the Moon is completely shielded for 25% of the lunar cycle. Under those conditions, the central near side receives less than 30% of the fluence that the central far side receives, and only about 35% of the fluence received by the limbs. A map of the relative fluence is given in *Figure 1*. Changing the

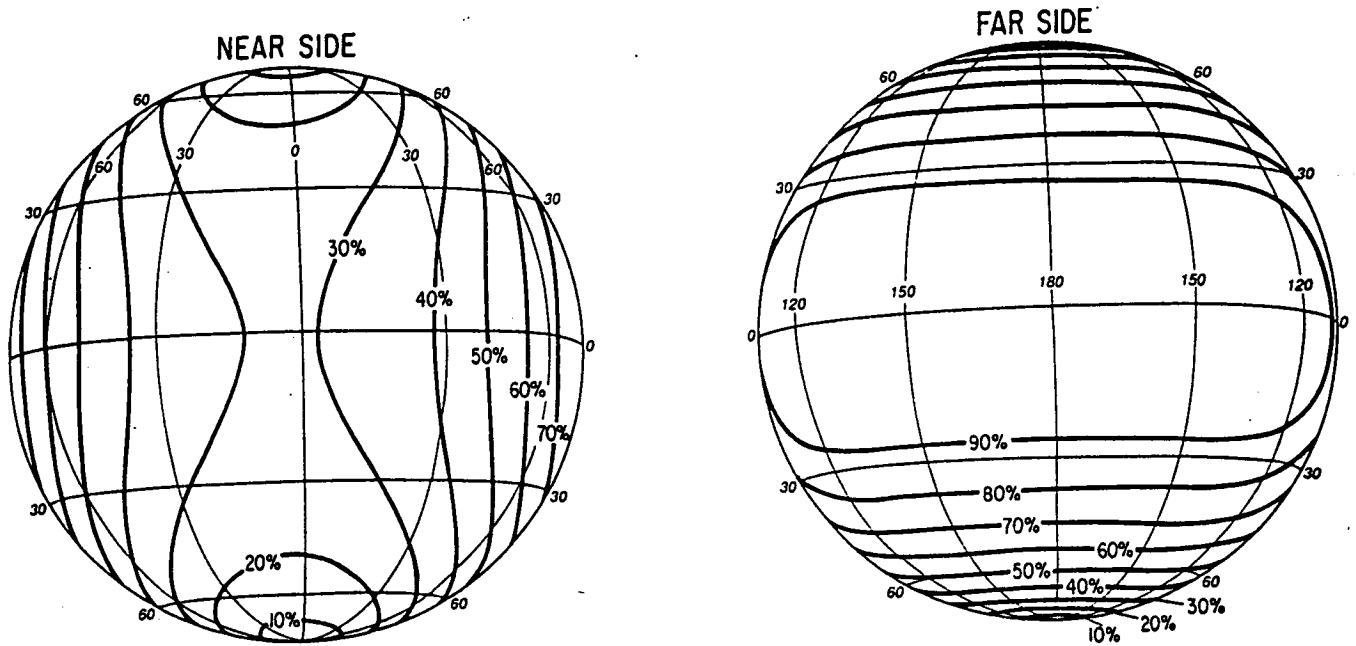


Figure 1: Relative fluence of solar wind incident on various lunar locations. The maximum fluence (defined as 100%) is received at the equator on the far side.

details of the shielding (i.e., changing the amount of time shielded, or including partial shielding for the whole duration of the magnetosheath passage, rather than total shielding for part of the duration) will change the details of the map, but not the overall pattern. For elements for which soil chemistry is not important (probably all the elements of interest except He), a global abundance map should be look nearly the same (except for local variations in impact history), unless saturation effects are important. If saturation is important, the volatile abundances of high-solar-wind-fluence sites would still be expected to be higher than low-solar-wind-fluence sites, although there might be a saturation abundance which would be approached.

For ^3He , we must include soil chemistry to estimate abundances. Jordan (1989) has shown that the abundance of ^3He in Apollo (central nearside) samples is proportional to the product of a parameter called I_s/FeO (which measures duration of surface exposure, and will be discussed in more detail below) and Ti content. This is reasonable, since the first factor should be proportional to the amount of solar wind received, and the second is proportional to the fraction retained (since ilmenite retains far more than other minerals). Generalizing to consider fluence variations, we would expect the abundance to be proportional to the product of the fluence and the Ti content. We have generated a map of estimated ^3He abundance based on that assumption, using the fluence variations calculated as described above, and maps of estimated Ti abundance based on spectrophotometry of the Moon (Johnson et al. 1991) and on the Apollo gamma-ray spectrometer Ti results (Davis 1980). These maps are shown in *Figure 2*.

Since the highest Ti abundances are concentrated in the central near side, where the solar wind fluence is lowest, the two effects tend to cancel each other. Mare Tranquillitatis, with its very high Ti content, but low longitude, is still one of the best places to look for ^3He , but some other areas with moderate Ti content but higher longitudes (e.g., western Oceanus Procellarum, Mare Fecunditatis, Mare Smythii) are potentially as promising. With a few exceptions (most notably in and around Mare Smythii on the eastern limb), there are few promising sites on the far side, despite the higher solar wind fluence.

Testing the importance of saturation effects

We have noted that we can convert solar wind fluence to estimated volatile abundance only if saturation effects are not important. In the lunar sample literature, the question of whether or not some grain surfaces are saturated is not settled. The best solar-wind simulation studies were performed recently by Futugami et al. (1990), who bombarded pure mineral samples with He ions.

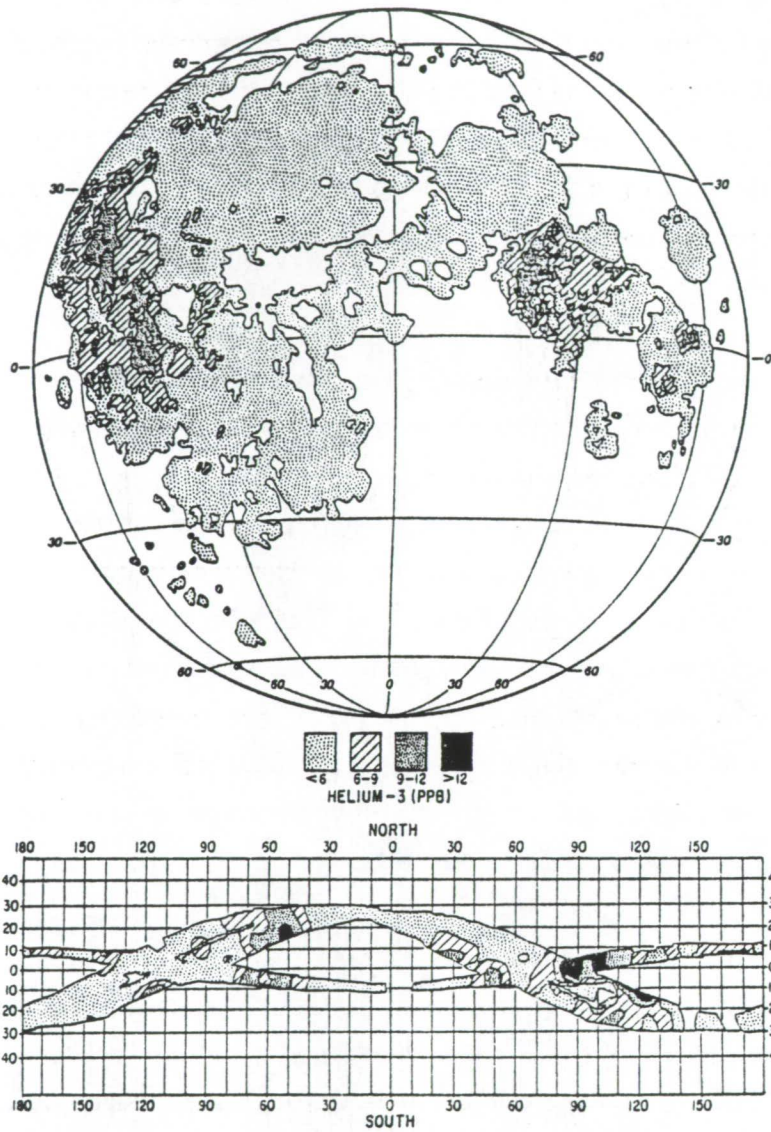


Figure 2: ^3He abundance at various lunar locations, based on the correlation of Jordan (1989), the relative fluence shown in Fig. 1, and estimates of Ti content. Top map uses estimates from visible and near-infrared spectroscopy (Johnson et al., 1991), bottom map uses estimates from Apollo gamma-ray spectrometry (Davis, 1980). Note that these assume that saturation does not occur.

They concluded that saturation of a free grain in space could occur in about 10 years of completely unshielded exposure (corresponding to a few decades of exposure on the Moon). Under these conditions, saturation of He, at least, would be expected to be important. In a study of actual lunar samples, Wieler et al. (1980) concluded that He saturation of grain surfaces occurs for "a considerable fraction" of the grains they analyzed. However, they also concluded that saturation of Ar occurs for few samples. Since Ar abundances correlate well with abundances of C and N (and, with poorer data, H), even at high abundances, it seems likely that these species are not saturated either.

To test for saturation effects, we should compare volatile abundances in samples from locations which we would predict to have a range of solar wind fluences. The Apollo samples all come from a limited geographic range on the central near side. The location with the highest estimated fluence (Apollo 17) would have only 50% more than the location with the lowest fluence (Apollo 15), and only 15% more than the mean of the Apollo samples. The ideal samples would be ones from documented locations on the central farside, but such samples are, of course, not available. The best samples, then, are the Russian Luna samples, which come from closer to the eastern limb of the nearside, and hence would be expected to have about twice the solar wind fluence as the average Apollo sample, and more than 60% more than even Apollo 17.

We acquired samples of two soils each from Luna 16 and Luna 20 ferromagnetic resonance (FMR) and noble gas analyses. The FMR analyses, which were performed by R. V. Morris of NASA Johnson Space Center, are essential to determining the ratio of reduced to oxidized iron (I_s/FeO), a widely-used, probably impact-driven, measure of "maturity" or exposure history (Morris 1976). These measurements, the first I_s/FeO measurements on Luna 16 or Luna 20 samples, suggest that both are quite mature. The few previous noble gas analyses on Luna samples scatter by more than would be expected from heterogeneity (i.e., some of the calibrations were probably incorrect), so we are in the process of measuring the noble gas abundances in these four Luna soils. The He analyses are obviously relevant to the question of 3He abundances, while the analyses of the heavier noble gases (Ar, Kr and Xe), whose abundances are not affected by the chemistry of the soil, provide a good analog for volatiles such as C and N. At the time of submission of the progress report, instrument calibration for these measurements is underway, and the measurements should be completed during the final weeks of the grant.

Well-calibrated measurements are essential to answering the question of saturation. The previous He measurements of Luna 16 and Luna 20 soils, when combined with Ti abundances and the new I_s/FeO results, scatter enough to overlap predictions based on either no saturation or complete saturation, although the mean is more consistent with complete saturation. For Xe, the scatter in abundances measurements is even larger, although the mean is considerably higher than predicted based on I_s/FeO . Although it would not be surprising if saturation effects were stronger for the more abundant gas, He, our conclusions will have to await our own analyses.

Bibliography

Cameron E. N. Mining for helium – site selection and evaluation. In *Lunar Helium-3 and Fusion Power* (NASA Conference Pub. 10018) 1988: 35-63.

Cameron E. N. (1991) Helium resources of Mare Tranquillitatis. In *Resources of Near-Earth Space* (Abstracts). UA/NASA Space Engineering Research Center AIS/A-90 (1991): 16.

Davis P. A. Jr. Iron and titanium distribution on the Moon from orbital gamma ray spectrometry with implications for crustal evolutionary models. *J. Geophys. Res.* 85 (1980): 3209-3224.

Fegley B. Jr., and T.D. Swindle. 3He and other lunar volatiles. *Resources of Near-Earth Space* (J. S. Lewis and M. S. Matthews, eds.). Tucson: University of Arizona Press. In press.

Futugami T., M. Ozima, and Y. Nakamura. Helium ion implantation into minerals. *Earth Planet. Sci. Lett.* 101 (1990): 63-67.

Haskin L. A. The Moon as a practical source of hydrogen and other volatile elements (abstract). *Lunar Planet. Sci.* XX (1989): 387-88.

Johnson J. R., S.M. Larson, and R.B. Singer. Remote sensing of potential lunar resources: I. Near-side compositional properties. *J. Geophys. Res.* 96 (1991): 18,861-18,862.

Jordan J. L. Predictions of the He distribution at the lunar surface. In *Space Mining and Manufacturing* (abstracts of papers submitted to the 1989 Annual Invitational Symposium of the UA/NASA SERC, Tucson).

Morris R. V. Surface exposure indices of lunar soils: A comparative FMR study. *Proc. Lunar Sci. Conf.* 7th (1976): 315-35.

Swindle T. D., C.E. Glass, and M.M. Poulton. Mining lunar soils for 3He . UA/NASA Space Engineering Research Center TM 90/1 (1990).

Taylor L. A. Helium abundances on the Moon: Assumptions and estimates. In *Resources of Near-Earth Space* (Abstracts) UA/NASA Space Engineering Research Center AIS/A-90 (1991): 40.

Wieler R., Ph. Etique, P. Signer, and G. Poupeau. Record of the solar corpuscular radiation in minerals from lunar soils: A comparative study of noble gases and tracks. *Proc. Lunar Planet. Sci. Conf.* 11th (1980): 1369-1393.

Wittenberg L. J., J.F. Santarius, and G.L. Kulcinski. Lunar source of ^3He for commercial fusion power. *Fusion Technology* 10 (1986): 167-78.

Publications supported by the current grant (November 1 -- September 15)

Boynton W., W. Feldman, and T. Swindle. A lunar penetrator to determine solar wind-implanted resources at depth in the lunar regolith. In *Joint Workshop on New Technologies for Lunar Resource Assessment*, Santa Fe, NM (1982): 6-7.

Fegley B. H. Jr. and T.D. Swindle. ^3He and other lunar volatiles. *Resources of Near-Earth Space* (J. S. Lewis and M. S. Matthews, eds.). Tucson: University of Arizona Press. In press.

Johnson J. R., T.D. Swindle, S.M. Larson, and R.B. Singer. Systematic variations in solar wind fluence with lunar location: Implications for resource utilization. *Bulletin American Astron. Soc.* 23 (1991): 1201.

Swindle T. D., M.K. Burkland, J.R. Johnson, S.M. Larson, R.V. Morris, B. Rizk, and R.B. Singer. Systematic variations in solar wind fluence with lunar location: Implications for abundances of solar-wind-implanted volatiles. *Lunar Planet. Sci. XXIII* (1992): 1395-1396.

omit

IV. SYSTEM AUTOMATION AND OPTIMIZATION

N 9 3 - 2 6 6 9 3

Modeling, Simulation, and High-Autonomy Control of a Martian Oxygen Production Plant

497601

L.C. Schooley, F.E. Cellier, F.-Y. Wang, B.P. Zeigler

Department of Electrical and Computer Engineering
and
Department of Systems and Industrial Engineering
The University of Arizona

59-31

158366

l-20

Abstract

This report documents progress on a project for the development of a high-autonomy intelligent command and control architecture for process plants used to produce oxygen from local planetary resources. A distributed command and control architecture is being developed and implemented so that an oxygen production plant, or other equipment, can be reliably commanded and controlled over an extended time period in a high-autonomy mode with high-level task-oriented teleoperation from one or several remote locations. During this reporting period, progress has been made at all levels of the architecture. At the remote site, several remote observers can now participate in monitoring the plant. At the local site, a command and control center has been introduced for increased flexibility, reliability and robustness. The local control architecture has been enhanced to control multiple tubes in parallel, and has been refined for increased robustness. The simulation model has been enhanced to full dynamics descriptions.

Introduction

A distributed command and control architecture is being developed that ultimately will provide the capability to teleoperate one or several process plants located on Mars, Luna, the asteroids, and/or other objects in space in a supervisory control mode from one or several locations on planet Earth.

The architecture must be able to guarantee reliable and robust control over an extended time period in a high-autonomy mode with high-level task-oriented teleoperation. The architecture must be resilient to temporary breakdowns in communication links, and must be able to accommodate a varying number of remote participants and local plants to be controlled. New remote observers should be able to join the operation at any time, while others may sign off. New plants can be added to the control umbrella at any point in time, while others can be removed after they have accomplished their respective goals.

These demands can be satisfied by a systematic and consistent application of the object-oriented programming paradigm. Each module within the overall command and control architecture acts as an independent intelligent agent. No bilateral links are established that will endanger the overall architecture by spreading a "disease" of one agent across the network to other agents. Each agent must be able to function autonomously, though not necessarily in an optimal manner. Agents can request information from their environment for improved operation, but they have no knowledge of the current network configuration or of who might be out there to fill their request. If the request is filled, the operation of the agent will improve, if not, it must be able to function with the resources that are at its disposal at the time. Each agent carries a model of itself that allows it to estimate its current performance level.

These are the ultimate goals of the project, not a reflection of the current state-of-the-art. However, the reporting period has brought us a good deal closer to realizing these goals in comparison with the state of affairs one year ago (Schooley et al., 1991).

In this report, we shall first explain the overall command and control architecture, then look at the individual parts of this architecture starting at the site of the remote commander and successively progressing towards the plant site.

The Overall Command and Control Architecture

Figure 1 shows the overall command and control architecture. Each site is equipped with a Command Communication Center (CCC). This is the gateway to the longhaul communication network and manages the resources available at the site. The reliability of the CCCs themselves can be guaranteed by standard technology such as resource duplication. Each participating plant or operator communicates with its own CCC only through a plant (operator) interface computer.

On Earth, the "remote" site in this document, each operator communicates to the CCC through a workstation running the Oasis software. The operator workstations are called Remote Commanding Computer (RCC) and Remote Observing Computer (ROC) respectively. There is no fundamental difference between the two types of workstations. They run the same software. They differ only in the privileges given to the operator of the workstation. The privileges are a resource that is maintained by the CCC. Additional privileges can be requested from the CCC at any point in time. The CCC will grant these privileges if the operator of the workstation has a sufficiently high clearance, and if granting these privileges is not in conflict with other demands. For example, no plant should be commanded by several remote commanders simultaneously in an intrusive fashion since it can be expected that, due to a lack of communication between the remote commanders, such an operation would lead to confusing situations.

In the current implementation, only one CCC (located at the "local" site, i.e., planet Mars) manages both the resources of the plant as well as those of the remote operators (Doser, 1992). This is somewhat awkward since the different remote operators need to communicate with each other via the longhaul network (through planet Mars), but we didn't have an extra computer available to be dedicated as a second CCC. Conceptually, this problem is easy to fix. The operator privileges are symbolized in our current implementation by a privilege "key," that is maintained by the CCC. This key can be requested by remote operators to establish them as temporary remote commanders. If the key has been requested, but is currently in use by another operator, the CCC will inform the current key holder of the request. It is then the responsibility of the key holder to relinquish the key when it is no longer needed.

On Mars, the "local" site in this document, the oxygen production plant communicates with its CCC through the so-called Local Controlling Computer (LCC). As shown on *Figure 2*, even the LCC

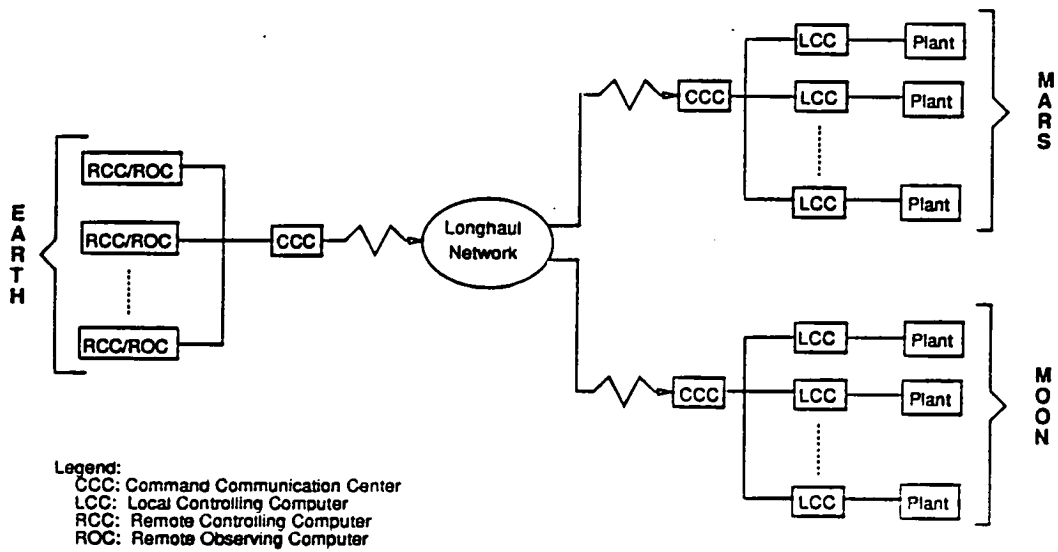


Figure 1. Global Remote Command and Control Architecture

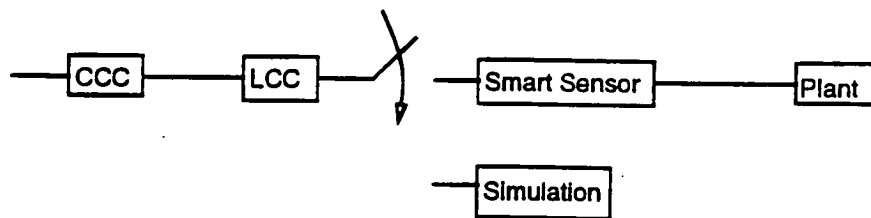


Figure 2. Local Control Architecture

comprises a distributed control architecture (Farrenkopf and Doser, 1992).

The plant itself is interfaced with a hardware controller (the so-called functional interface) that monitors and controls the current and voltage levels of each tube, and time-multiplexes the monitored signals for consumption by the next higher-level controller, the so-called smart sensor (Taglianetti, 1992). The duties of the functional interface could be performed by the smart sensor itself, but individual control of each tube by the smart sensor would have meant buying more interface cards for the smart sensor, a solution that was deemed undesirable due to its high cost and due to the amount of space that would have been consumed by the interface. The hardware solution is much cheaper and much more compact, albeit less flexible. The smart sensor is responsible for implementing low-level control strategies. The LCC itself translates high-level task-oriented commands received from the CCC into sequences of low-level commands, downloads the corresponding low-level control programs into the smart sensor, and initiates the control action by enabling the smart sensor control. Notice that, on *Figure 1*, the term LCC denotes the overall local control architecture, whereas, on *Figure 2*, LCC is only a part of the local control architecture.

A full-dynamics simulator has been added as an additional component to the local control architecture (Farrenkopf, 1992). It can be used for three different purposes:

1. To design and test new control strategies without risking the destruction of any tubes;
2. As a "second plant" without incurring the cost of actually building a second plant, allowing to demonstrate the capability of the control architecture to deal with multiple plants; and
3. As a model for the intelligent control to estimate its own level of performance.

Since the full-dynamics model was completed only recently, it has not yet been used for purposes other than #1 above.

The Remote Site

In the reporting period, the remote site has been enhanced to accommodate several ROCs beside from the RCC. A key passing mechanism has been introduced that allows ROCs and RCC to exchange their roles (Doser, 1992). Previous reliability issues have been resolved. It is now possible to switch any ROC on and off arbitrarily during an experiment without jeopardizing the overall

mission. If the RCC goes down, the CCC immediately retrieves the privilege key and informs the LCC that it is currently on its own. When the key is requested by another remote workstation, that workstation becomes the new RCC, and the LCC is instructed to again operate under remote control.

The Command and Communication Center

The CCC is a new element in the overall Command and Control Architecture (Doser, 1992). It serves three purposes:

1. **Software-decoupling the individual computers from each other.**

Each interface computer (be it an LCC or an RCC) needs to know only the language of its client (the plant or the operator) and the language of the CCC. Different interface computers need not know anything of each others characteristics and physical location, how many such computers are in the system, and how they operate. Each LCC can talk a different language to its client, and in principle, the same holds true for each RCC (although different RCC interfaces may not be desirable for other reasons).

2. **Managing the resource umbrella of its clients.**

Each CCC is responsible for managing the limited resources of its clients (the RCCs and the LCCs). A restricted resource of the RCCs is their privilege level, implemented through the privilege key in the current prototype. Restricted resources of the LCCs may be the amount of energy to be used at any one time or the useable communication bandwidth between the LCC and its CCC.

3. **Managing the communication with the other CCCs.**

Together, the CCCs manage the longhaul communication network.

Since there is up to now only one CCC in the prototype, the third function is not currently implemented. Consequently, it is still the duty of each RCC/ROC to worry about whether its commands have been received by the CCC (located at the other end of the longhaul network) or need to be resubmitted. In the future, the time delays between the RCC/ROCs and their closest CCC will be short, and a simple message acknowledging protocol can be enabled so that the RCC/ROC need not keep track any longer of multiple commands that have been submitted but not

yet acknowledged. It will then be the duty of the CCCs to ensure proper transmission of commands and telemetry packets across the inherently less reliable longhaul network.

The Local Control Architecture

The Local Controller

The LCC is the heart of the autonomous control system designed for the Oxygen Production Plant four-tube unit. The control system, which is placed at the site of the plant (planet Mars), includes the LCC (Local Controlling Computer) and the Smart Sensor (Intelligent Controller). The LCC communicates with its CCC (Command Communication Center) to receive control parameters and sends telemetry data back to the RCC (Remote Commanding Computer) on Earth. Users' commands include commands to set control parameters, telemetry data requests, system start-up commands, and system shut-down commands.

The Communication Protocol

In the current reporting period, the LCC has been enhanced to communicate with other computers/controllers simultaneously with executing the local control procedures. Thus the communication process is included as part of the control program. *Figure 3* shows the overall protocol for the communication between the LCC and CCC.

The LCC, physically a PC-386, first sets up communication links to the Smart Sensor in order to initialize the sensors and actuators of the plant. Then it tests the communication link to the CCC. Upon receipt of the control parameters and the start-up command from the CCC, the LCC begins to control the plant.

The Intelligent Control Strategy

To implement autonomous control of the plant, we have developed a real-time expert system that has rule bases to govern normal control operation as well as fault detection, diagnosis and recovery. *Figure 4* shows the decision process for control of start-up and steady-state operations.

In order to operate in real-time, the inference engine of the expert system has a clock to check time constraints on control rules. When the real-time expert system receives tasks from the RCC, it schedules the appropriate control actions to execute them. During the execution, it continually monitors the state of the plant.

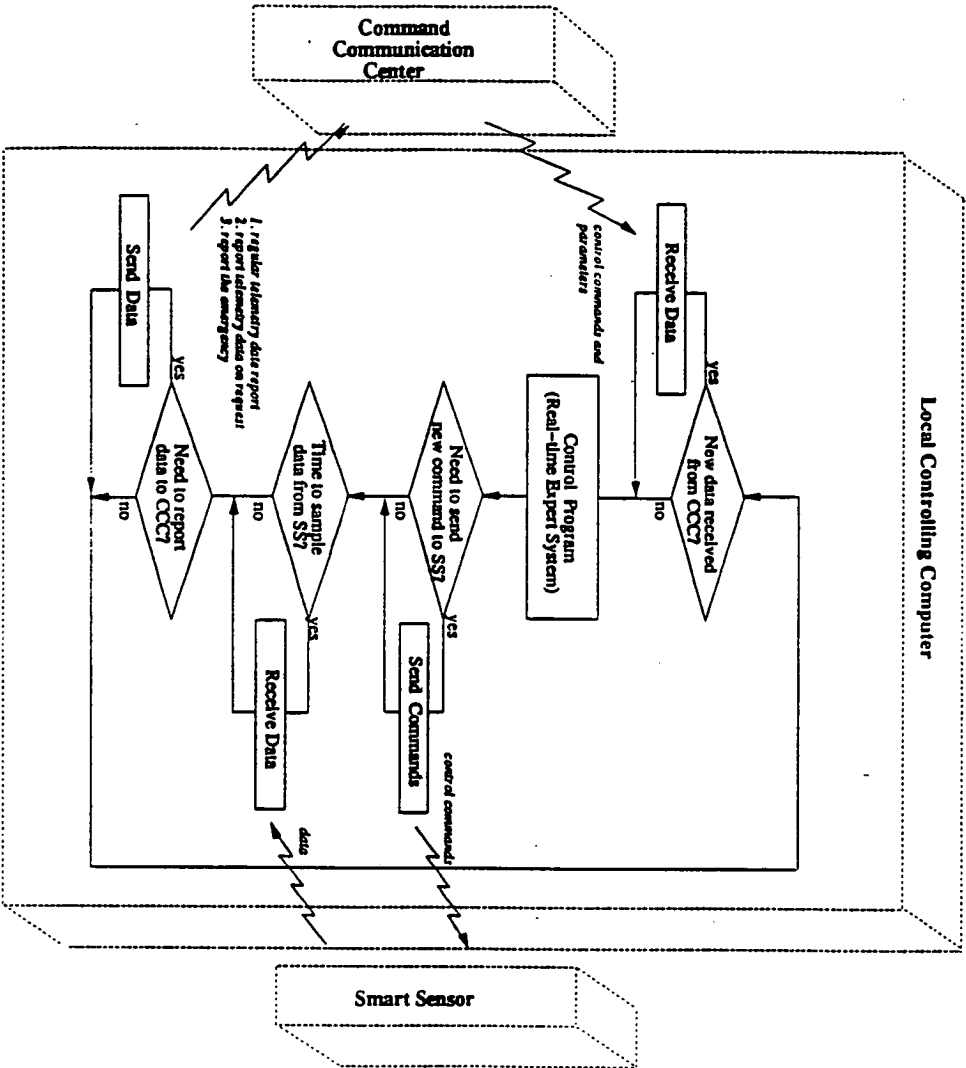


Figure 3. Protocol in the LCC for Communicating with the CCC and the Smart Sensor

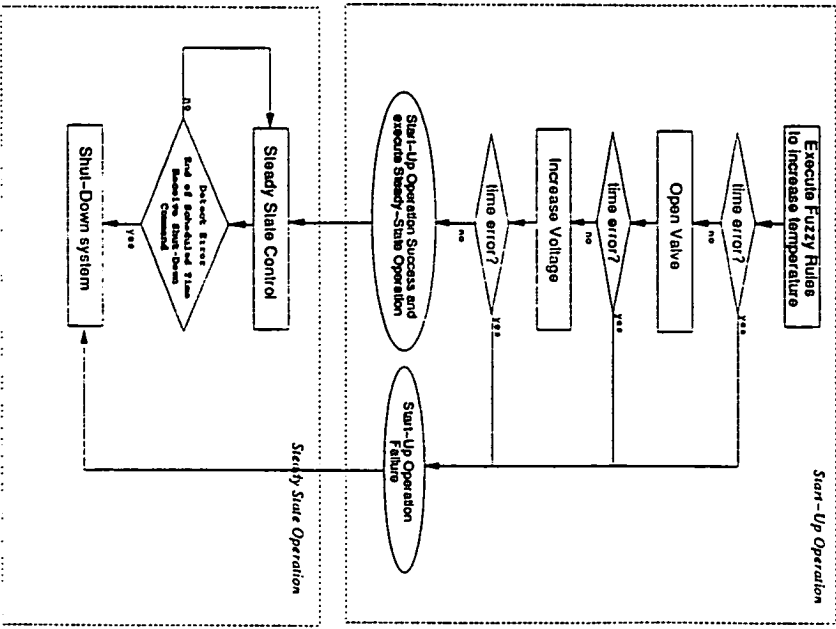


Figure 4. Flow Diagram of Start-Up and Steady-State Control Scheme

The LCC needs to control three kinds of state variable of the plant, viz, temperatures of the ZrO₂ tubes, flow rate of the CO₂ gas and voltages across the ZrO₂ tubes. Since the unit must operate at high temperature, a control algorithm is used to increase the temperature as fast as possible while still preventing the seal between metal pipe and ZrO₂ input tubes from breaking. An increase of 10 C deg/min was set as the goal rate for the control algorithm.

We have integrated fuzzy logic (Cellier and Mugica; Lee, 1990) with event-based control (Zeigler, 1989; Zeigler and Kim) to design the temperature controller. When the LCC receives a goal temperature from the RCC, the expert system sets a number of check point temperatures between the initial temperature and goal temperature intended to assure that the desired rate of temperature increase is maintained. A pair of successive check points can be considered as a small segment that must be successfully controlled to reach the final goal temperature. Event-based control is employed for each segment, i.e., after reaching one check point and issuing a control output to reach the next, the latter should be reached within a pre-estimated time window. If the next check point temperature is reached too early or too late, this represents a fault situation that the system needs to diagnose. At each check point, the fuzzy logic controller computes an appropriate control command, which is realized as a pair of on/off heater durations (for example <2,3> might mean heater on for two seconds, then off for three seconds.) High thermal mass in the plant necessitates this kind of operating regime (that is, the ZrO₂ temperature tends to lag and overshoot the nominal value). A fuzzy logic approach to this problem is useful in view of the difficulty of developing exact models for the thermal behavior. Although, a full-dynamics simulation model has been recently developed, it has not yet been fully validated against the real plant. The integration of event-based and fuzzy logic control paradigms provides a powerful new approach to ensuring and testing for "hard" real-time control subgoals, (offered by event-based control) while providing for flexible behavior-based "soft" control responses (offered by fuzzy control).

To design the fuzzy control algorithm, we have employed fuzzy membership functions (e.g. Negative Small, Negative Zero, Positive Zero, Positive Small) for the state variable, rate of ZrO₂ temperature increase. Calibration of the fuzzy logic membership parameters, as shown in *Figure 5*, was obtained from experiments with a mock-up of the real system (representing the proper thermal mass of the system).

Figure 6 shows a typical temperature control experiment using the integrated fuzzy

NS : Negative Small
 ZB : Zero
 PS : Positive Small

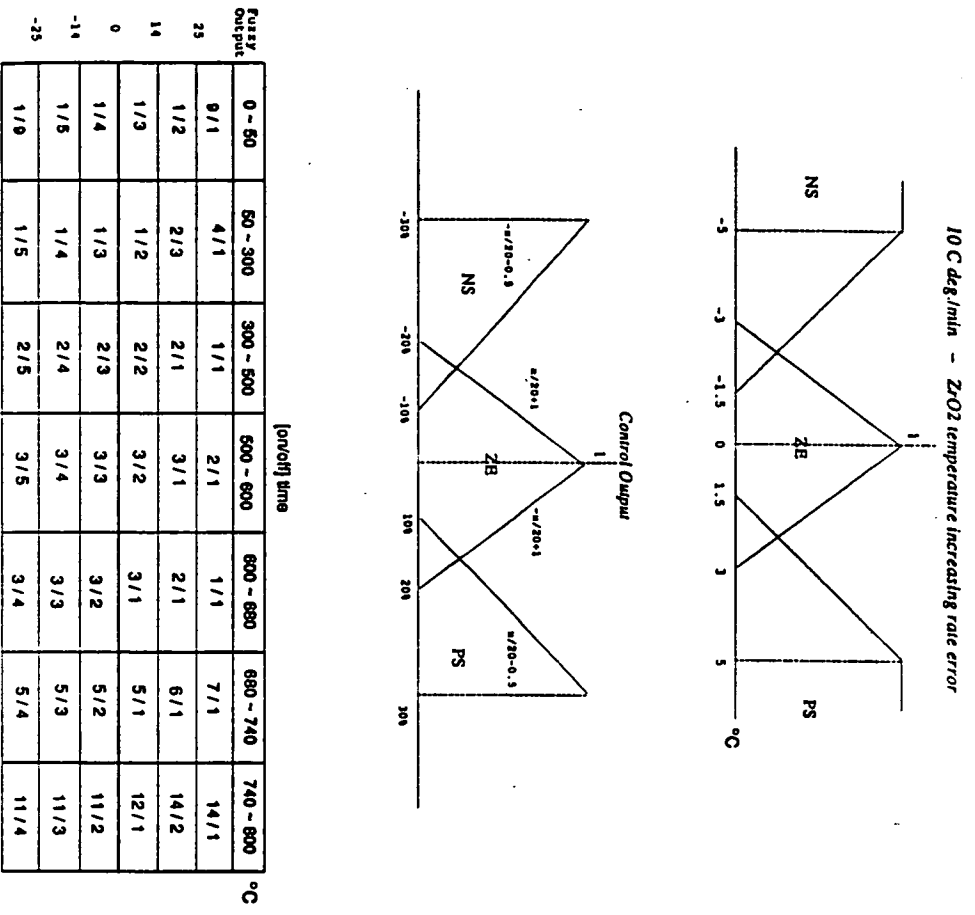


Figure 5. Fuzzy Membership Function and Defuzzified Control Output

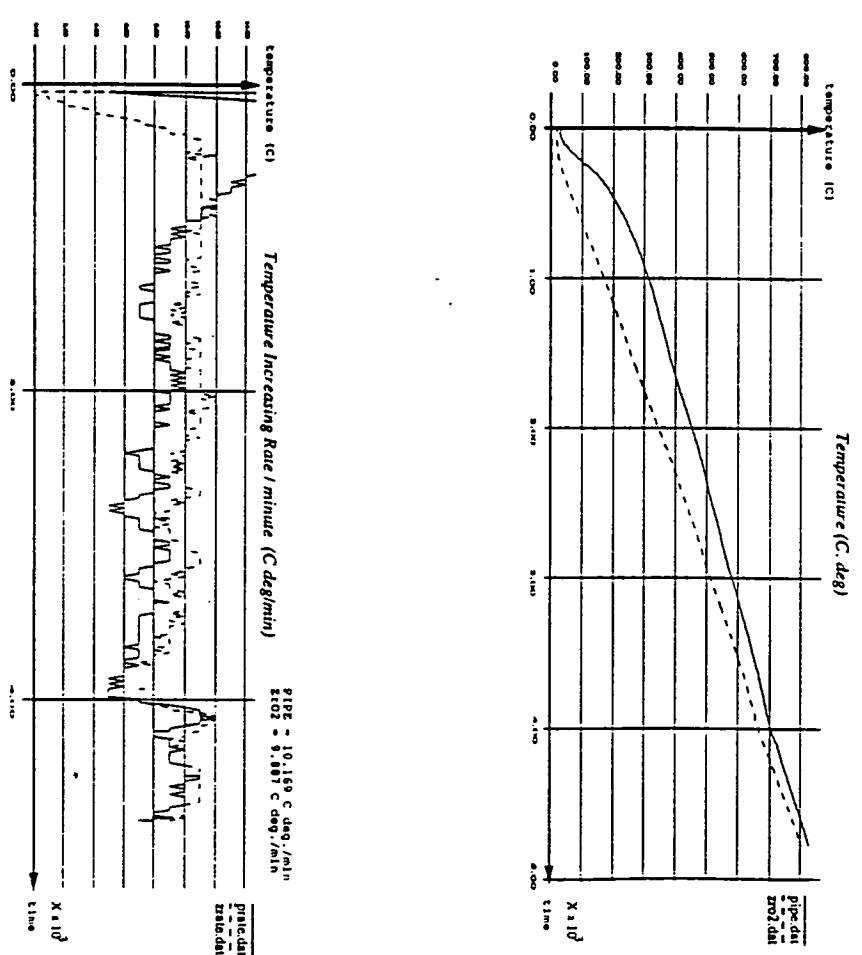


Figure 6. Temperature Control Experiment Using

logic/event-based controller.

As indicated before, the option of replacing a real plant with a dynamic simulation also allows us to perform calibration experiments in an off-line manner.

When steady-state operation has been reached, the behavior of each state variable is controlled by a dedicated watchdog monitor (Cellier et al, 1992). Each watchdog monitor has upper/lower limits for its state variable. Violation of these limits causes the watchdog monitor to activate diagnosis rules to execute appropriate recovery actions. If recovery is not possible, the expert system automatically executes a benign shut-down procedure to protect the plant from further damage. The LCC and SS (Smart Sensor) together form a two level hierarchical control architecture. The reasoning and high-level logic just described are realized in the LCC in an expert system shell written in C. On the other hand, the Smart Sensor contains simple control programs in memory and executes low-level control tasks in accordance with the parameters received from the LCC. This bi-level partition of functionality enables fast local control under the guidance of slower, more global, intelligent control.

Fault Management

As shown in *Figure 7*, interspersed with the control tasks just described, the LCC reads sensory data from the SS and reports telemetry data to the CCC to update the RCC's data base.

If the LCC detects a faulty situation, it reports the fault detection to the RCC and starts its diagnosis inferencer. During the diagnosis process, the LCC sends data more frequently to the RCC, which represent the error state transition behavior of the plant. This alerts the user at the RCC to the deviant behavior of the plant. On such an occasion, or indeed, at any time, the RCC can route new commands or parameter values through the CCC to the LCC to re-schedule control tasks and/or to establish new control set points. Also, the RCC can send shut-down commands to interrupt the system. This can happen even while the system is in start-up mode.

Sensor Fusion and Process Fault Diagnosis Using Neural Networks

The nature of extraterrestrial environments makes the automatic process fault diagnosis an essential prerequisite for the further development of supervisory control system of the Martian Oxygen Production Plant. This fault diagnoser must be very reliable. Since it is impossible to foresee all faults that might occur, it is desirable to build some redundancy into the fault monitoring and

diagnosis procedures. For this reason, a second process fault diagnosis system using multiple sensors for data acquisition and neural networks for information processing has been developed (Wang; Wang and Wu, 1992). The execution of this system has been divided into three stages:

1. **Fault Detection:**

At this stage a possible process fault is detected by checking if particular measurable or estimable variables are within a certain tolerance of the normal values. For example, the measured temperature of the Zirconia tube should be above 790K but below 815K under normal situation. If this check is not passed, it leads to a fault message that activates the next stage of fault diagnosis.

2. **Fault Diagnosis:**

The fault is located and the cause of it is established at this stage using a multilayer back-propagation neural network that fuses the data from several sensors. For example, output O₂ flow rate is too low because the input CO₂ valve is only partially opened. Eight representative fault situations have been selected in a simulation study.

3. **Fault Evaluation:**

An assessment is made of how the fault identified in the second stage will affect the production process. The faults have been classified into different hazard classes according to a simple fault tree analysis. After the effect of the fault is determined, a decision on the actions to be taken will be made. If the fault is found to be tolerable, the production process may continue. If it is conditionally tolerable, a change of operation has to be performed by either modifying the local control algorithm or sending a request to the higher level of control for guidance. However, if the fault is intolerable, the process will be shut down immediately and an emergent request will be made to the higher level to eliminate the fault. For example, if a malfunction in the heater has been determined to be the cause of high temperature, the operation will be stopped immediately and a request for changing the heater will be made.

A simulation study has been performed based on a computer model of the Martian Oxygen Production Unit. Ten sensor readings were used for sensor fusion in a neural network. One thermocouple transducer is located inside the Zirconia tube. On each of the CO₂, O₂, and CO₂/CO pipes, one thermocouple, one pressure, and one flow rate transducers are located. All readings are

scaled to a range from -1.0 to +1.0. The scaling makes the sensor fusion easier to perform because the original measurement data contains both small and large values. Eight representative fault situations have been chosen in the simulation:

1. CO₂ valve partially opened;
2. O₂ valve partially opened;
3. CO₂/CO valve partially opened;
4. Thermocouple transducers broken;
5. Leak flow in tube;
6. Malfunction in heater;
7. CO₂ flow rate too high; and
8. CO₂ flow rate too low.

A multilayer feedforward neural network with one hidden layer has been used. The input layer has ten nodes representing the ten sensor readings, and the output layer has eight nodes - one for each of the selected fault situations. The hidden layer has six nodes. The standard sigmoid has been used as the activation function for the output neurons, while the hyperbolic tangent has been used for hidden neurons in order to speed up the learning process. The training data consist of 450 measurement patterns (each pattern contains 10 sensor readings), 50 patterns for the normal production operation and for each of the fault situations. For the normal operation, the network should produce a value near zero (< 0.1) at all the output nodes, whereas for the situation of fault number one, the network should produce a value near one (> 0.9) at the first output node and a value near zero (< 0.1) at the rest of the output nodes, and so on. The learning is conducted using the conjugate back-propagation algorithm.

The simulation programs used are PlanNet and Matlab. The network has been trained 10,000 times to learn the specified fault situations correctly. For 100 additional measurement patterns that are not in the training data, 83 patterns have been classified correctly. *Figure 8* illustrates an example of diagnosis of the fault situation number 5.

It is planned to integrate this fault diagnoser with the actual plant, but this has not been done yet.

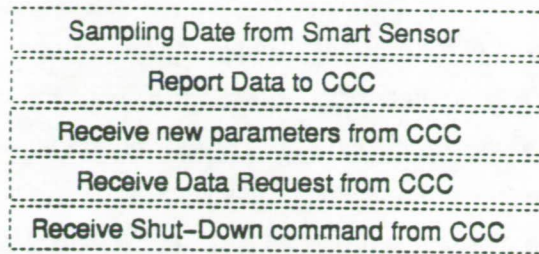


Figure 7. Demon Processes for the Control System

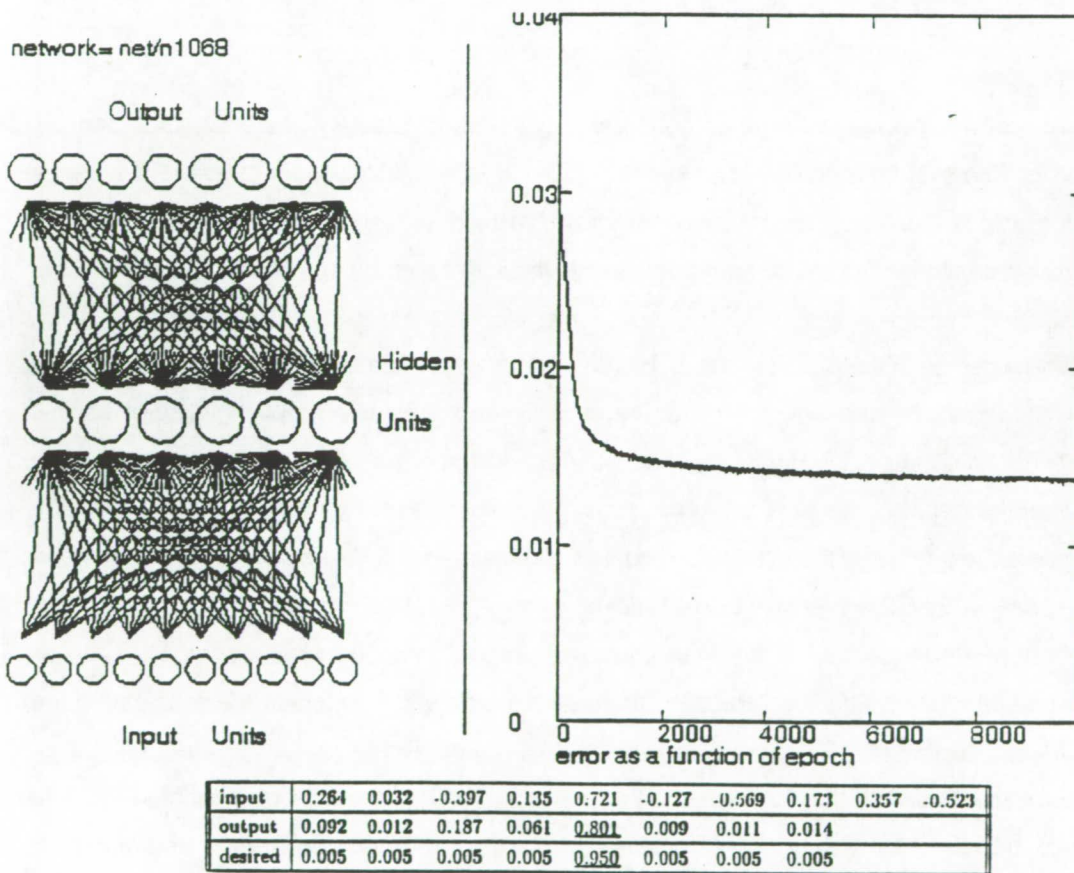


Figure 8. Network Architecture, RMS Output Error During 10,000 Training Epoches, and Example of Diagnosis of Fault #5

Full-Dynamics Model of the Martian Oxygen Production Plant

Modeling Methodology

A full-dynamic simulation model of the four-tube oxygen production system has been completed. This model is based on a modeling and design methodology involving the use of Bond Graphs (Cellier, 1991). This method is advantageous because the power that moves through the system is topologically as well as mathematically represented in the model. In addition, the power flow in the thermal dissociation of carbon dioxide into oxygen and carbon monoxide can also be modelled using Bond Graphs, and this model can be conveniently connected to the thermal model of the overall system to obtain a full-dynamic system model that can be used to simulate both steady-state operation (flow equilibrium) as well as start-up and shut-down phases correctly.

System Description

The actual system topology consists of concentric cylinders of different materials that perform different tasks. The system topology is shown on *Figure 9*. A cylindrical ceramic heater surrounds a metal pipe, but is itself surrounded by a cylinder of insulation. Carbon dioxide gas enters the system through an alumina pipe and then passes over the surface of the surrounding Zirconia tube.

These cylinders can be described in terms of thermal resistance and capacitance elements. Thermal resistance elements are dependent on the shape, size, direction of entropy flow, and thermal conductivity of the material comprising the cylinder, and thermal capacitance elements are dependent on the density, specific heat, temperature, and volume of the cylinder (Hollman, 1986). Since the power flow through the system is modeled, the resistance to entropy flow is used instead of the resistance to heat flow because the product of entropy flow and temperature is of type power. The temperature dependence of the resistance and capacity values are accounted for. The temperature dependent relations for the specific heat of the different materials are available in the literature (Perry and Green, 1991) and were used in this model. Some of the cylinders consist of gas, which means heat flow due to convection as well as conduction must be accounted for. The radiation heat transfer from the pipe in contact with the heater to the Zirconia tubes is also modeled.

A lumped-heat-capacity type model has thus been constructed where the temperature of the individual elements is assumed to be uniform. If a temperature distribution at several points along any of the cylinders is of interest, then the cylinder can be divided into several subsections, each with its own resistance and capacitance properties. Our system is fairly symmetric so the

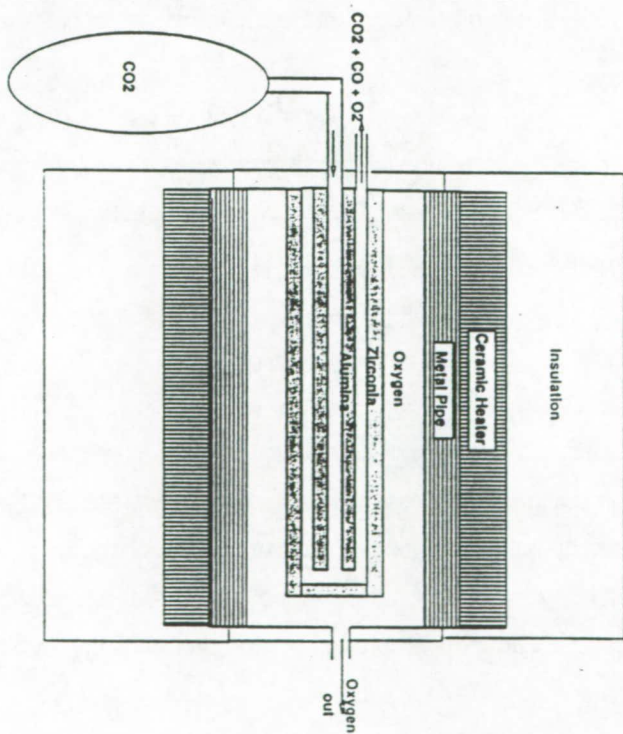
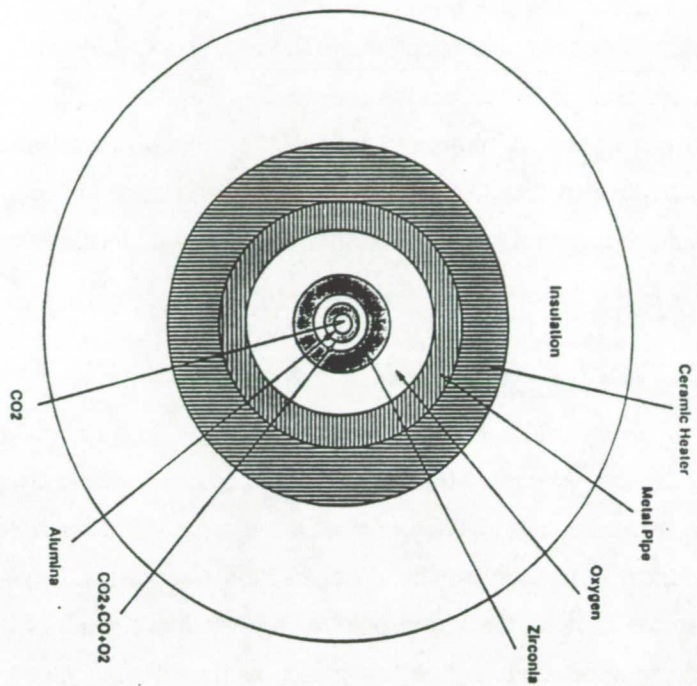


Figure 9. Topology of Zirconia Tube

temperature distribution along the cylinders is expected to be approximately uniform; the cylinders were thus divided into at most two sections. This allows for a smaller, less complex model with better simulation response, yet with acceptable accuracy. The Bond Graph thermal model of the system is shown on *Figure 10*.

Rather than include four identical tube descriptions in the model, the thermal characteristics of a one-tube description were changed to reflect the presence of four tubes. For a four-tube system, there is four times as much tube component mass, so the thermal capacitance values for the one-tube system are multiplied by four (remember, thermal capacitance is linearly proportional to volume). Similarly, a four-tube system will provide four times the load, so the resistance to entropy flow for the tube system components was divided by four.

Chemical Reaction Model and Oxygen Production

The process of the thermal dissociation of carbon dioxide into carbon monoxide and oxygen is essentially a chemical reaction, which can be easily modeled using the Bond Graph methodology. Chemical, thermic, and hydraulic/pneumatic forms of power are considered here. The number of moles of the reactant and the volume in which the reaction occurs are known. This model is modularly connected to the tube model at the point where the input gas has been heated. The molar flow rate of oxygen produced is then multiplied by the efficiency of the Zirconia tube separation process, which is a temperature and applied tube voltage dependent quantity. The system's oxygen production rate is thus predicted. The Bond Graph model of the chemical reaction system is shown on *Figure 11*.

The model has been calibrated for the one-tube system. In this case, the dynamical behavior of the model and the real system are very similar indeed. The four-tube model has not yet been calibrated since no measurements for the four-tube system are available yet.

Future Work

The future work on remote supervisory control of high autonomy ISMU process plants will build on the strong base established in the past. It is essential to next address the problems of increasing autonomy by introducing carefully balanced concepts of redundancy, autonomous diagnosis and repair capabilities, and graceful degradation of performance with reduced resource availability. The focus will be on further extension and development of core technology applicable to diverse

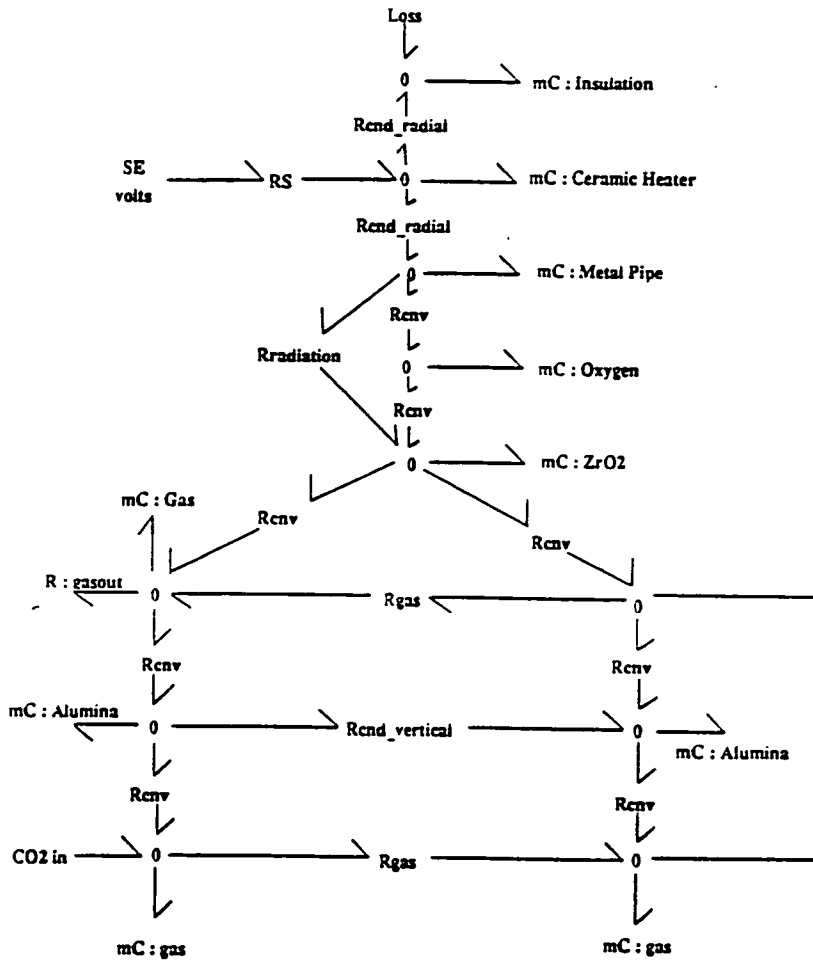


Figure 10. Thermal Bond Graph Model of Zirconia Tube

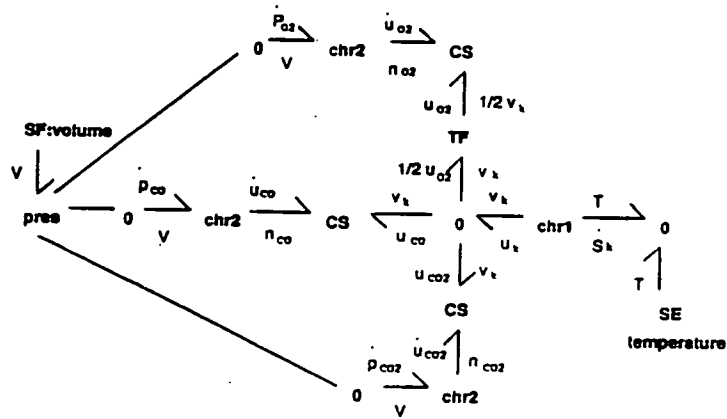


Figure 11. Chemical Reaction Bond Graph of Zirconia Tube

processes and plant designs. This will include:

1. Software engineering of common modules that are easily adaptable to different applications.
2. Implementation of advanced concepts in the higher levels of hierarchical planning, sensing, control, and exception handling, emphasizing additional knowledge-based, neural network, and fuzzy artificial intelligence concepts for increased autonomy and graceful degradation of performance with reduced resource availability due to resource sharing and/or resource failure.
3. More robust interaction with remote commanders under conditions of realistic time delays in the communication system. Real-time communication system performance will be analyzed by means of timed petri nets.
4. Integration of computer vision and other advanced sensory capabilities (including sensor fusion) for world state assessment as well as fault detection, diagnosis, and recovery.
5. Incorporation of light weight, low power, flight/space qualified hardware in the computer/communication systems.
6. Further development of software design tools for optimum process design and mass/power reduction.

References

Cellier, F.E. *Continuous System Modeling* (1991). Springer-Verlag, New York.

Cellier, F.E., and F. Mugica Alvarez. Systematic design of fuzzy controllers using inductive reasoning techniques. Submitted to *IEEE Transactions on Control System Technology*.

Cellier, F.E., L.C. Schooley, M.K. Sundareshan, and B.P. Zeigler. Computer-aided design of intelligent controllers: Challenge of the nineties (1992) in: *Recent Advances in Computer Aided Control Systems Engineering* (M. Jamshidi and C.J. Herget, eds.). Amsterdam: Elsevier Science Publishers.

Doser, A. Multiple user communications for telescience (1992). M.S. Thesis: Department of Electrical and Computer Engineering, University of Arizona (available also as: *Technical Report TSL-028/92*, Telescience Laboratory, Electrical and Computer Engineering Department, University of Arizona, Tucson, Arizona.

Farrenkopf, G. Full-dynamics simulator of the Martian oxygen production prototype (1992). Technical Report, Telescience Laboratory, Electrical and Computer Engineering Department, University of Arizona. In preparation.

Farrenkopf, G. and A. Dosser. Remote command and simulation of an oxygen production plant. *SERC Newsletter*. 3 (1992) 1: pp. 5-6.

Hollman, J.P. *Heat Transfer*. New York: McGraw-Hill, 1986.

Lee, C.C. Fuzzy logic in control systems: Fuzzy logic controller – part I. *IEEE Transactions on Systems, Man, and Cybernetics*. 20 (1990) 2.

Perry, R.H., and D.W. Green, eds. *Perry's Chemical Engineer's Handbook*. New York: McGraw-Hill, 1991.

Schooley, L.C., F.E. Celler, B.P. Zeigler, A. Doser, G. Farrenkopf, J. Kim, Y. Pan, and B. Williams. Automation and control of an oxygen extraction plant. *Annual Report (1991) NASA/SERC*.

Taglianetti, F. The functional interface of the distributed intelligent controller to the Martian oxygen production plant prototype. Senior Project (1992), Department of Electrical and Computer Engineering, University of Arizona.

Wang, F.-Y. Building knowledge structure in neural nets using fuzzy logic. Submitted to *Journal of Fuzzy and Intelligent Systems*.

Wang, F.-Y., and F. Wu. Sensor fusion and process fault diagnosis for Martian oxygen production plant using neural nets. *Technical Report #42 (1992)*, Robotics and Automation Laboratory, Department of Systems and Industrial Engineering, University of Arizona.

Zeigler, B.P. The DEVS formalism: Event-based control for intelligent systems. *Proceedings of IEEE* 77 (1989) No. 1: 27-80.

Zeigler, B.P., and J. Kim. Extending the DEVS-scheme knowledge-based simulation environment for real-time event-based control. Submitted to *IEEE Transactions on Robotics and Automation*.

497602

N 93-26694
20-37

158367

P-9

**Development of a Material
Processing Plant for Lunar Soil**

Ulix Goettsch and Karl Ousterhout

**Department of Aerospace and Mechanical Engineering
The University of Arizona**

Abstract

Currently there is considerable interest in developing in-situ materials processing plants for both the Moon and Mars. Two of the most important aspects of developing such a materials processing plant is the overall system design and the integration of the different technologies into a reliable, lightweight, and cost-effective unit. This paper develops the concept of an autonomous materials processing plant that is capable of producing useful substances from lunar regolith.

In order for such a materials processing plant to be considered as a viable option, it must be totally self-contained, able to operate autonomously, cost effective, light weight, and fault tolerant. In order to assess the impact of different technologies on the overall systems design and integration, a one-half scale model has been constructed that is capable of scooping up (or digging) lunar soil, transferring the soil to a solar furnace, heating the soil in the furnace to liberate the gasses, and transferring the spent soil to a "tile" processing center. All aspects of the control system are handled by a 386 class PC via D/A, A/D, and DSP (Digital Signal Processor) control cards.

I. Introduction

The Artemis program, initiated by NASA, is geared toward the development of a Common Lunar Lander (CLL) that will serve as a platform for a wide variety of robotic exploration missions to the lunar surface. The CLL is envisioned as a small lander which is capable of being launched from an existing launch vehicle and that will carry an autonomous payload for performing a variety of experiments. Currently, planned payloads include in situ materials utilization (ISMU) experiments and astronomical observatories. NASA is conducting work in two separate but interrelated areas: the development of the Artemis Lander and the Artemis Lander's payloads. This paper discusses preliminary research underway at The University of Arizona's Space Engineering Research Center to design and build a one-half scale autonomous oxygen production facility for inclusion in the Artemis program.

II. Mission and Task Requirements

The mission requirements for the autonomous oxygen production facility are straight forward: the plant must be capable of autonomous oxygen production for a period of 35 to 365 days, the payload may have a maximum mass of 65 Kg (143 lbf), the payload must fit within the envelope illustrated in *Figure 1*, and the payload must operate from a platform as illustrated in *Figure 2*.

Additionally, the four main tasks for the autonomous oxygen production facility can be decomposed as shown below in Table 1:

-
- 1) Soil sample acquisition:
 - Move primary arm and gather soil.
 - Sift soil to remove large impurities.
 - Transfer sifted soil to crucibles.
 - Transfer crucible from rack to reactor with secondary arm.
 - 2) Reactor operation:
 - Mix solid carbon powder with soil.
 - Insert crucible at the focal point.
 - Control heating temperature.
 - Measure and identify gasses.
 - Remove residue and reprocess to make tiles.
 - 3) Data Management
 - Obtain measurements and store data.
 - 4) Telemetry
 - Adjust antenna and either transmit to Earth or receive data from Earth.

Table 1. Mission requirements for the autonomous oxygen production facility.

The autonomous oxygen production facility combines two related experiments into one payload. The first experiment, lunar oxygen production, will serve to demonstrate the feasibility of using solar energy to reduce lunar soil and release the oxygen which is bound within the ilmenite (chemically known as iron titanate, FeTiO_3). The second experiment, lunar brick production, will demonstrate the feasibility of making "lunar bricks" from the previously processed lunar soil. At the completion of the "lunar brick" production process, the lunar soil will be in a hardened brick-like form suitable for building lunar structures.

III. Payload Design, Layout, and Operation

In order for the autonomous oxygen production facility to fit the mission requirements, the current design allows for the four main components - the primary mirror, the secondary mirror, the primary arm, and the secondary arm - to be stowed in the configuration shown in *Figure 3* for space flight.

Once the CLL has landed on the Moon, the primary mirror, the secondary mirror, and the primary arm will deploy and operate as illustrated in *Figures 4 and 5*. The individual components of the autonomous oxygen production facility are illustrated in *Figure 6*.

The turntable and pallet contain the mounting interface to the lander itself. The turntable is the foundation upon which all of the other components of the payload (except the pallet) are mounted. Additionally, the turntable allows for 360 degree rotation of the payload for soil collection, solar tracking, and telemetry. The pallet, which is fixed to the lander and does not rotate with the turntable, is used for storage of the crucibles which will be filled with collected soil for processing. It accommodates both small crucibles (10 g capacity) for oxygen production and large crucibles (50 g capacity) for glass production.

The primary arm is used to collect soil and deposit it into a sieve mechanism which returns large soil particles (rocks) to the lunar surface and fills the crucibles with the fine soil. The arm is a four degree-of-freedom (waist, shoulder, elbow, and wrist) robot with a scoop for soil collection. Besides the waist joint (the turntable), all of the motors are contained in a drive assembly located at the shoulder joint. Torque is transmitted through gear/chain and pulley/cable combinations and position feedback is obtained through the use of optical encoders located at each of the joints. Since the payload must be autonomous, the arm is instrumented with strain gauges to provide force feedback along three orthogonal axis. This will inform the controller in the event that the arm contacts immovable obstacles such as large surface or subsurface rocks.

Once the lunar soil is placed in the hopper by the scoop attached to the primary arm, it is then processed through a sieve consisting of a series of screens with decreasing mesh size. Particles that are too large for production purposes are allowed to exit the sifter at each stage where they are allowed to return to the lunar surface. The fine soil that passes through the sieve is collected in a hopper where it can then be poured into a crucible. This last step is accomplished by rotating the turntable until one of the empty crucibles is positioned directly below the spout of the hopper. After one of the crucibles has been loaded with lunar soil, the turntable is rotated to a position where the secondary arm can pick up the crucible and transfer it to the furnace for either oxygen or glass production.

When producing oxygen, the secondary arm positions the crucible under the transparent furnace lens and against a seal which traps the evolved gas. Solar energy collected by the mirrors focuses

on the soil sample and heats it to the proper temperature for oxygen generation. Once the oxygen production process is completed, the secondary arm returns the crucible along with the spent sample to the pallet. When producing lunar bricks, the large crucible is positioned just above the furnace, where the nearly focused beam hits the soil sample. Gases evolving during the melting process are allowed to escape to the lunar atmosphere. Once the soil sample is molten, the secondary arm positions the crucible over one of molds and pours the molten soil into it. Once the glass sample has cooled, the secondary arm moves it to the materials testing unit where it is ejected from the mold and its mechanical properties are determined.

The solar energy needed to process the lunar soil is collected and focused onto the furnace via a primary and secondary mirror system. The two meter diameter parabolic primary mirror is mounted on a cart which rides a circular arc to follow the sun vertically above the horizon and the turntable rotates to follow the sun horizontally across the horizon. The convex secondary mirror is located at the center of the circular arc to maintain a constant focal length. The secondary mirror directs the collected solar energy downward into the furnace, elongating the beam so that the focal point is inside the furnace. A tracking system, consisting of a two by two solar panel array, is used to track the sun throughout the lunar day. All of the power to operate the robotics, analytical equipment, computers, and telemetry is provided by solar panels which deploy from the rear of the primary mirror. This mounting configuration insures that the solar panels are always optimally positioned with respect to the sun. The only time that the solar panels are not tracking the sun is when either the primary arm is collecting soil or the secondary arm is selecting a crucible from the pallet. When these operations are taking place, power is supplied by batteries.

IV. Controls and Electronics

As mentioned previously, all aspects of the control system are handled by a 386 class PC via D/A, A/D, and DSP (Digital Signal Processor) control cards. This hierarchical control system allows for the 386 class PC to act in supervisory mode while the individual motions of each of the axis of movement are controlled via the DSP control cards. Thus, the PC is able to process data taken during experiments or run diagnostics while the manufacturing process is underway.

Although the PC is capable of transmitting data to a mother craft or Earth during the lunar day, a rechargeable battery will be included within the system so that data reduction and communications

can be conducted during the lunar night. During the lunar day, the photovoltaic cells mounted to the rear of the primary mirror will recharge the battery. The electrical power requirements and the masses of the individual components are shown below in Table 2.

	Power (w)	Mass (kg)		
Communications	10/120	3.5		
Computer	16	4.25		
Sensors/Actuators				
Servo motors (8)	480.0	6.4		
Flow meters (2)	7.5	0.8		
Pressure sensors sensors (2)	0.2	0.1		
Force/torque sensors (2)	*	1.0		
Proximity sensors; strain gauges			*	*
Flow control valves	2.4	1.2		
Thermocouples (2)	*	*		
CCD Camera (1)	3.0	0.2		
Mass Spectrometer (1)	2.0	0.5		
Total	495.1	10.2		

*Negligible

Table 2. Power and mass breakdown.

Conclusion

The technologies developed over the last four years at The University of Arizona NASA Space Engineering Research Center are being integrated into the design of the Common Lunar Lander. At this time, a one-half scale model has been constructed and testing is currently underway. Although the current design of the autonomous materials production facility is highly automated, the main focus of this research is to integrate the necessary technologies in such a manner that the completed design is highly reliable and fault tolerant.

References

Taylor, I. Common lunar lander. Artemis Workshop, February 3-5, 1992.

Ramohalli, K., K. Ousterhout, K.R. Sridhar, and J.M. DiFrancesco. A robotic common lunar lander concept in support of the space exploration initiative. Accepted for presentation at the ASME winter Annual Meeting, Anaheim, California, 1992.

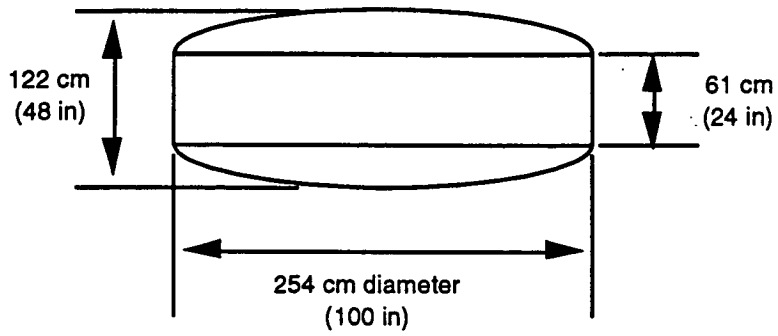


Figure 1. Approximate CLL Payload Dimensions.

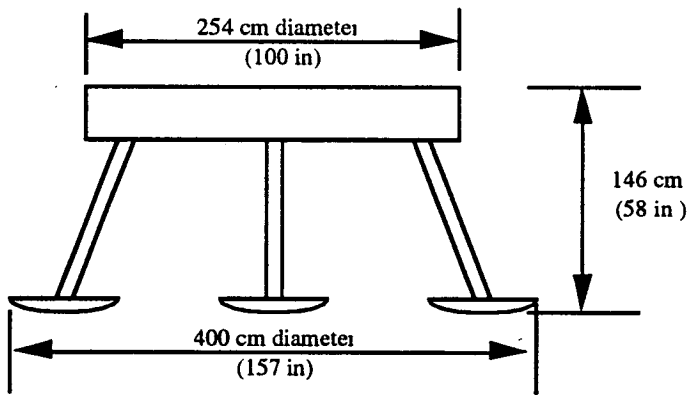


Figure 2. Approximate CLL Dimensions.

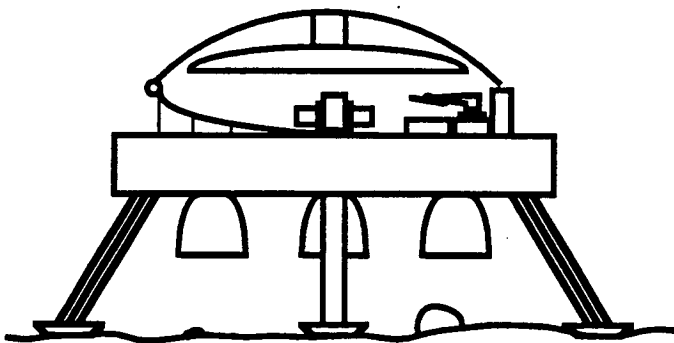


Figure 3. The CLL As Landed - In An Undeployed State.

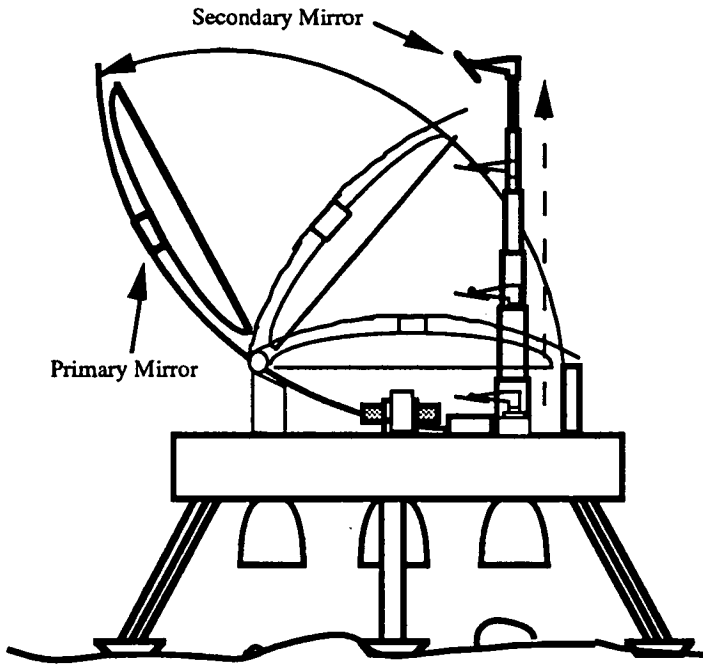


Figure 4. Primary and Secondary Mirrors Deploying.

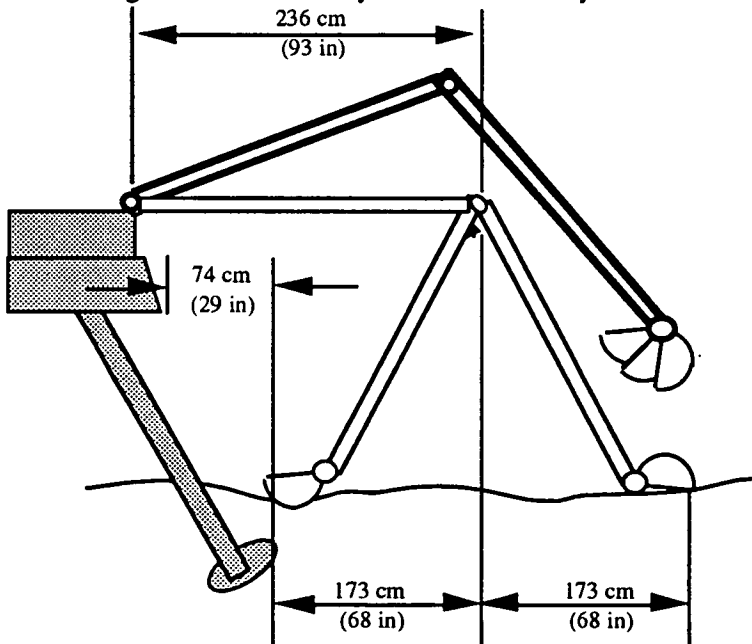


Figure 5. Primary Arm Operating Range.

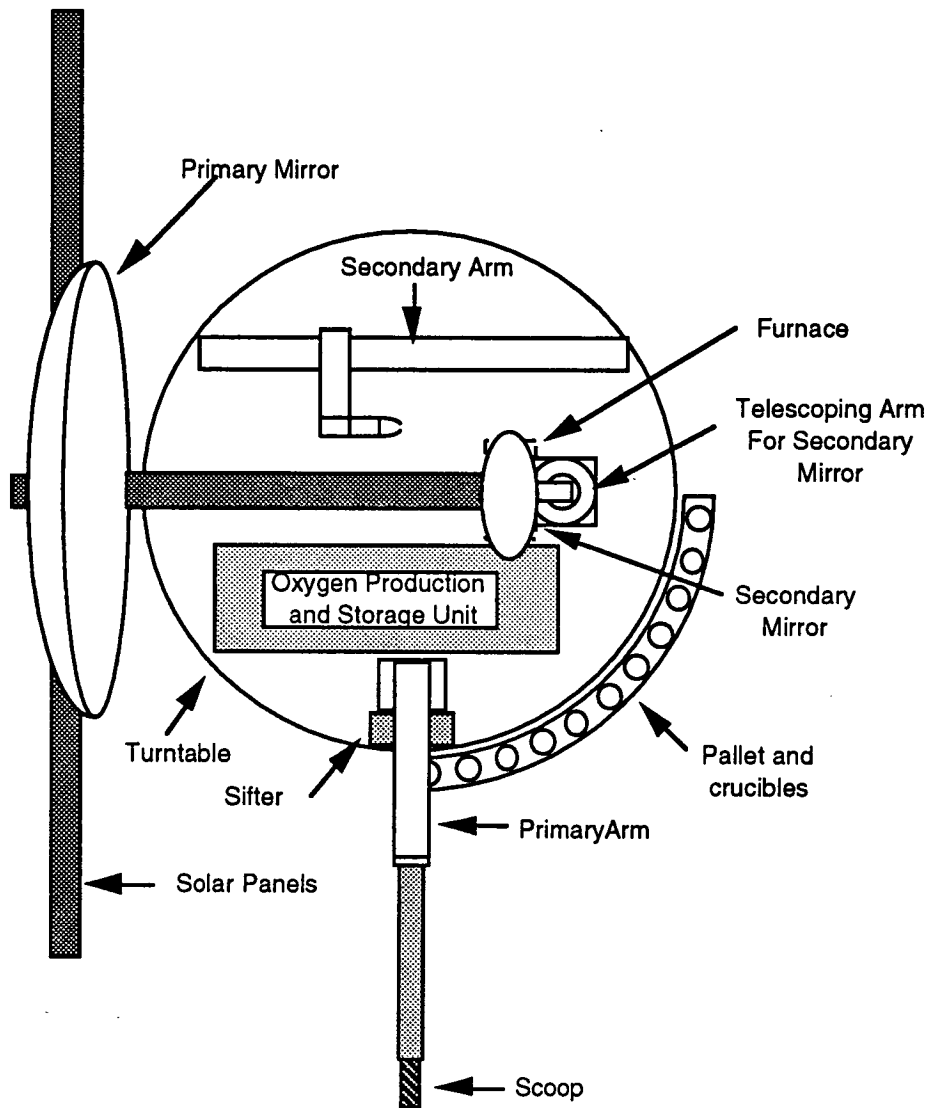


Figure 6. Top View of The Robotic Oxygen Production Facility.

497603

N98-26695

**In-Situ Materials Processing Systems and Bioregenerative Life Support Systems
Interrelationships**

**George V. Mignon and Robert J. Frye
Environmental Research Laboratory**

S21-24

158368

p-3

Abstract

This project was to investigate the synergy and linkages between bioregenerative life support systems and the materials produced by in-situ materials processing systems. Such systems produce a broad spectrum of byproducts such as oxygen, hydrogen, processed soil material, ceramics, refractory, and other materials. Some of these materials may be utilized by bioregenerative systems either directly or with minor modifications. The main focus of this project was to investigate how these materials can be utilized to assist a bioregenerative life support system. Clearly the need to provide a sustainable bioregenerative life support system for long term human habitation of space is significant.

Approach

In order to narrow our investigation we chose a lunar mission scenario in which a fully functional bioregenerative life support system would be fully implemented at base maturity.

There are four basic functions that any life support system must achieve:

Atmospheric Regeneration

The atmosphere of any life support system needs to have contaminate gases such as CO₂, CO, HC, etc... removed and replenished with O₂. This is accomplished in a bioregenerative system by the interaction of micro-organisms and higher plants. A bioregenerative system will enable the complete recycling of these gases by utilization of CO₂ and production of O₂ by photosynthesis and the removal of contaminant gases by soil microorganisms residing in the substrate used for plant growth.

Water Purification

Water purification can be easily achieved by physicochemical means, however water recycling is not so easy. Within a bioregenerative system water is recycled and purified by the mechanism of plant evapo-transpiration and condensation on cooling coils. The only losses in this cycle would be due to leakage and export of water.

Waste Processing

The major waste to be processed is human waste. These wastes are really basic nutrients for growing plants and with proper treatment (composting, etc...) can be readily incorporated into a soil based bioregenerative system. Waste would be stored during base establishment and processed (for pathogen removal) via non-destructive methods. The waste material would then be latter utilized with lunar regolith to develop a living soil system. As organic matter is a limiting component of bioregenerative systems in space, all potentially usable forms of organic matter must be conserved for later re-use. The organic matter used to construct a soil from lunar regolith will provide the necessary cation exchange capacity and nutrient retention characteristics necessary to provide optimal microbial communities and thus higher plant growth. Re-use of human and other forms of organic material is a necessary component in closing the cycles of bioregenerative life support systems. The major thrust of our efforts has been to quantify the available nutrients which may be efficiently recycled.

Food Production and Processing

The fundamental function of a bioregenerative system is to facilitate the production of food through the support of higher plant growth and development. In the absence of energy and technology

intensive hydroponic culturing, soil microorganisms provide the nutrient regulation mechanism for food production. Under the proper conditions higher plants and soil microorganisms constitute an integrated system of high reliability and stability.

The basic elements required by a bioregenerative system are carbon, hydrogen, oxygen, nitrogen, and phosphorus. The first four are relatively abundant in organic matter and through correctly designed recycling systems can be conserved and continuously recycled. The other macro-nutrients required, potassium, magnesium, calcium, and sulfur are available in lunar regolith and would not be limiting. Micronutrients such as iron, manganese, zinc, copper, boron, molybdenum and chlorine can be supplied initially through terrestrial sources. A mature bioregenerative life support system will maintain these nutrients in adequate quantities and in useable forms.

The Moon, as far as we know, does not contain adequate quantities of water or nitrogen in any useable form. These two items may be the limiting factors in the productivity of a bioregenerative life support system. If local sources of water cannot be found or produced then all water must ultimately originate from terrestrial sources. Food production could provide one part of a water reuse system through transpiration and condensation. Nitrogen may ultimately be harvested from the atmosphere using nitrogen fixing microorganisms that form symbiotic relationships with higher plants.

The lunar regolith contains much of the essential materials necessary for a good agricultural soil. The availability of these nutrients will not be known until living soil systems can be constructed from reprocessed human waste, other transported organic matter and lunar regolith.

Conclusion

It is very apparent that some form of bioregenerative life support system will be required for long duration space missions such as a lunar base. The extent of closure will be determined by design trade off between cost of resupply and the first cost of establishment of the bioregenerative system. For a lunar base scenario it is also evident that there are really only two basic in situ materials of great benefit to a bioregenerative system; lunar oxygen and lunar soil. A detailed literature study has been conducted and citations compiled. The report, tabulates and summarize the requirements for a bioregenerative life support system on a per person day basis and what materials can be provided by the proposed in situ processing schemes.

**Full System Engineering Design and Operation of an
Oxygen Plant**

James Colvin, Paul Schallhorn, and Kumar Ramohalli

University of Arizona/NASA Space Engineering Research Center

497604
N93-26696

S22-31

158369

P-17

Abstract

This paper describes one area of a project whose general aim is to produce oxygen from the indigenous resources on Mars. After discussing briefly the project's background and the experimental system design, specific experimental results of the electrolytic cell are presented. At the heart of the oxygen production system is a tubular solid zirconia electrolyte cell that will electrochemically separate oxygen from a high-temperature stream of Coleman grade carbon dioxide. Experimental results are discussed and certain system efficiencies are defined. The parameters varied include 1) the cell operating temperature; 2) the carbon dioxide flow rate; and 3) the voltage applied across the cell. The results confirm our theoretical expectations.

Introduction

Background

A primary concern for any mission to Mars must be how much energy will be necessary to complete the mission. An important consideration has to be: Should we continue to bring all propellants with us from Earth, or should we take advantage of the many known resources that are available to us on Mars? With this idea in mind and wishing to expand on the success of the Martian Viking program, Ash, Dowler, and Varsi¹ in the late seventies envisioned an in-situ propellant plant which would make use of the Martian atmosphere to produce an oxygen and methane propellant.

The heart of this system would be an array of yttria stabilized zirconia solid electrolyte cells. These cells have the ability to selectively conduct oxygen ions, thus allowing the production of pure oxygen. The oxygen plant has undergone many changes since it was first envisioned by Ash¹ et al. Frisbee and Lawton have done extensive work on improving the overall system by reducing the total system mass and increasing the total system reliability.²⁻⁴

Their improved system would have the Martian atmosphere drawn in through an electrostatic dust filter, which is necessary as there are numerous long-term dust storms on the Martian surface. The atmosphere, which consists of approximately 95% carbon dioxide, will be drawn into the system by a CO₂ adsorption compressor. Present plans³ require the atmosphere to be compressed from the ambient pressure of 6.8 mb to a pressure of 1 bar for delivery to the cathode of the electrolyte. Before entering the zirconia array, the flow will pass through a heat exchanger which will raise the temperature from the CO₂ compressor's exit temperature of 600 K to approximately 1000 K. The source of the heat for the heat exchanger is the exhaust flow from the array. Once the flow has entered the array, it will be further heated to a temperature of 1273 K.

This temperature is sufficient to partially dissociate the carbon dioxide into carbon monoxide and diatomic oxygen. The O₂ will be increased to 4 bar. The cell's exhaust will consist of mostly CO₂ with some CO resulting from the removal of O₂. The O₂ produced at the anode will pass through a radiator where it will be cooled from 1270 to 250 K with a pressure of 3.8 bar. The O₂ will next pass through an O₂ adsorption compressor where its pressure will be increased to 28 bar and its temperature to 400 K. After passing through a radiator, the flow will be cooled to 230 K. The O₂ will be finally cooled to 100 K by a molecular adsorption cryo-cooler refrigerator and stored for its final use. The use could initially be the oxidizer for the propellant necessary to return a Martian sample

to earth, and then eventually, life support for a manned Martian mission.

Yttria-Stabilized Zirconia Solid Electrolyte

In Lawton's work,³ he lists development risk factors for components. In his option III, the oxygen cell is the only component still listed as risk factor 4, meaning "there are still serious problems that must be addressed as well as some intensive development required." This is an area of current research. Further details were worked out in Reference 5. Since the Martian atmosphere is predominantly CO₂, the remainder of this report will refer to the atmosphere as CO₂. The CO₂, when it enters the cell array, will be heated to 1273 K. At this temperature, the CO₂ will begin to partially dissociate into CO and O₂. The zirconia electrolyte is sandwiched between two porous platinum electrodes. The dissociation will occur at the cathode with the O₂ entering the electrode and moving towards the electrode-electrolyte interface. The driving force for this movement is the partial pressure gradient developed by the electrolyte removing oxygen from the interface area. Once the O₂ reaches the interface, it is further reduced to monatomic oxygen. The oxygen received two electrons from the negative electrode and becomes an oxygen ion and begins to migrate through the zirconia electrolyte towards the anode. Upon reaching the anode, the ion will release its two electrons to the positive electrode and then recombine with another oxygen atom to reform the O₂ molecule. Qualitatively, this describes the oxygen separation process. *Figure 1*⁴ shows this process schematically.

Richter performed the initial intensive testing of this electrochemical process with the aim of quantifying this physical procedure.⁶ His work was performed using a tubular zirconia cell. He developed the basic thermodynamic and electrochemical models for the reduction of CO₂ and the subsequent production of O₂. A few years later, Suito continued the investigation.⁷ In his experiment, he used the disk geometry for his cells. Additionally, he investigated the use of different electrode materials. Although his supply gas was air, many of his results can also be applied when CO₂ is the supply gas.

In this study, zirconia cells with the tubular geometry were used. The aim was to develop various cell efficiencies by varying several system control parameters. These parameters were: the potential applied across the electrolyte, the electrolyte operating temperature, and the incoming CO₂ flow rate. We would like to know how the CO₂ production rate varies as a function of these parameters. The various efficiencies include the cell's Nernst efficiency (a measure of the theoretical energy required against the actual energy put into the system). The definitions of these efficiencies will be

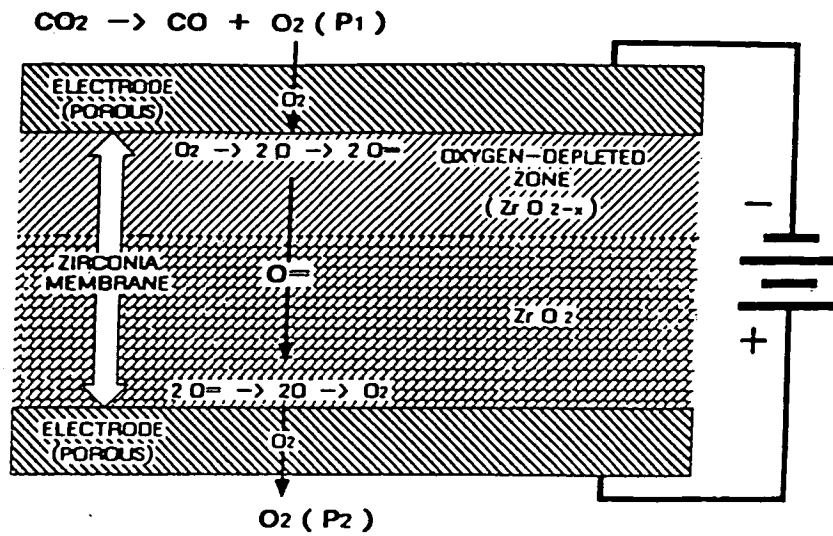


Fig. 1 Oxygen migration through the ZrO_2 cell.

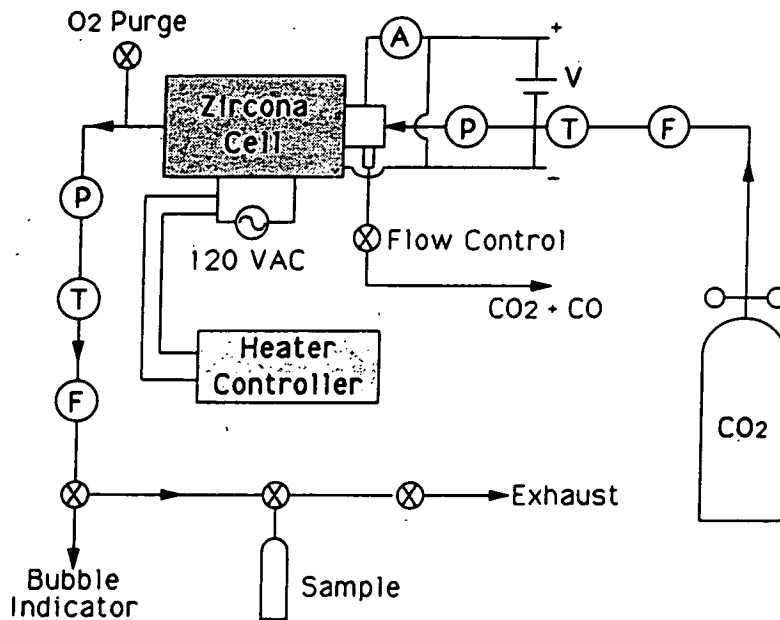


Fig. 2 Single cell test bed (schematic).

developed later in this report. The single zirconia cell test bed currently being studied is shown schematically in *Figure 2*. The test bed consists of the following: 1) one tubular zirconia cell; 2) one voltage DC power supply; 3) two digital multimeters; 4) two ceramic clam shell heaters; 5) one Watlow heater controller; 6) Kaowool type ceramic insulation; 7) one O₂ pressure transducer (0-500 psia); 8) one CO₂ pressure transducer (0-500 psia); 9) one O₂ flow meter (0-50 sccm); 10) one CO₂ flow meter (0-5000 sccm); 11) three ktype thermocouples; (12) Coleman grade CO₂ for supply gas; 13) one PC/386 processor for data acquisition; and 14) Varian model 3700 gas chromatograph.

To simulate the Martian atmosphere, which contains approximately 95% CO₂ and only 0.13% O₂, Coleman grade CO₂ was used to supply the test bed. This grade contains less than 20 ppm O₂. The flow was maintained at slightly above local atmospheric pressure (13.7 psia) at a temperature of 75°F. The flow rates were varied between 38 and 1475 sccm. Flow would enter the zirconia tube through a 1/8 in. alumina tube and then pass to the far end of the zirconia chamber (see *Figure 3*). The clam shell heaters are centered about the middle 7 in. of the zirconia device. This means heating of the flow will begin in the alumina tube. Exiting the alumina tube, the flow reverses direction while continuing to be heated and flows across the cathode of the electrolyte. The CO₂, now heated, begins dissociation and is drawn to the cathode. The free stream is now a mixture of CO₂, CO, and O₂. O₂ is dissociated to monatomic oxygen at the electrode-electrolyte interface and electrochemically conducted through the zirconia to the anode while the CO₂ and CO exhaust pass out through the exit of the tube. The supply CO₂ flow rate is controlled by a metering valve in the exhaust flow. The O₂ produced (at approximately 13.7 psia) flows through the mass flow meter and then can be directed to a water bubbling device, a sample cylinder, or directed to the gas chromatograph for analyzing. The zirconia electrolyte and its platinum electrode have an upper temperature limit of 1150°C where a phase change in the zirconia will take place. A critical voltage limit of 2.23 VDC was assumed in accordance with the work of Frisbee.⁴ Keeping below this potential will prevent the oxygen from being driven from the zirconia lattice structure causing permanent damage to the cell. With these material limits in mind, a self-imposed limit of 1100°C, and 2.0 VDC was used during all testing.

Single-Cell Test Results

Fundamental Results

A series of tests were conducted to attempt to characterize the effects of temperature, cell potential, and carbon dioxide flow rate on the production rate of oxygen. During testing, the temperature was varied from 800 to 1100°C in increments of 25°. Cell potential varied from approximately 0.6 to 2.0 VDC in increments of 0.1 volts. The CO₂ flow rate varied from 38 to 1475

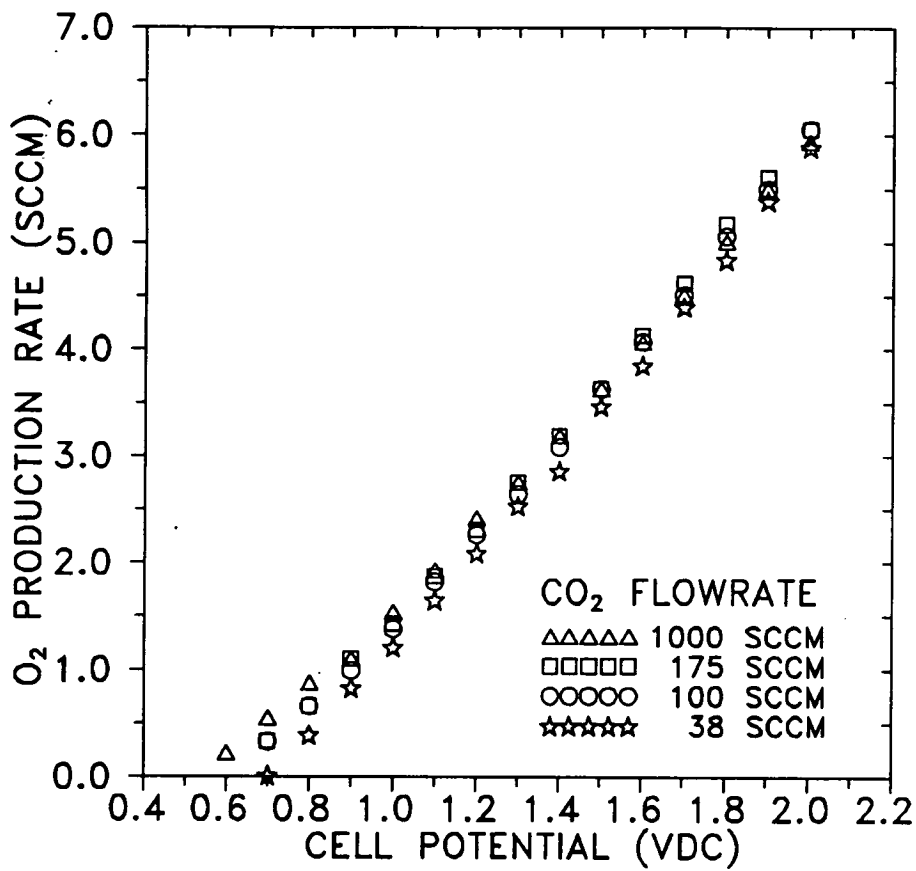


FIGURE 4

SINGLE ZIRCONIA CELL SCHEMATIC

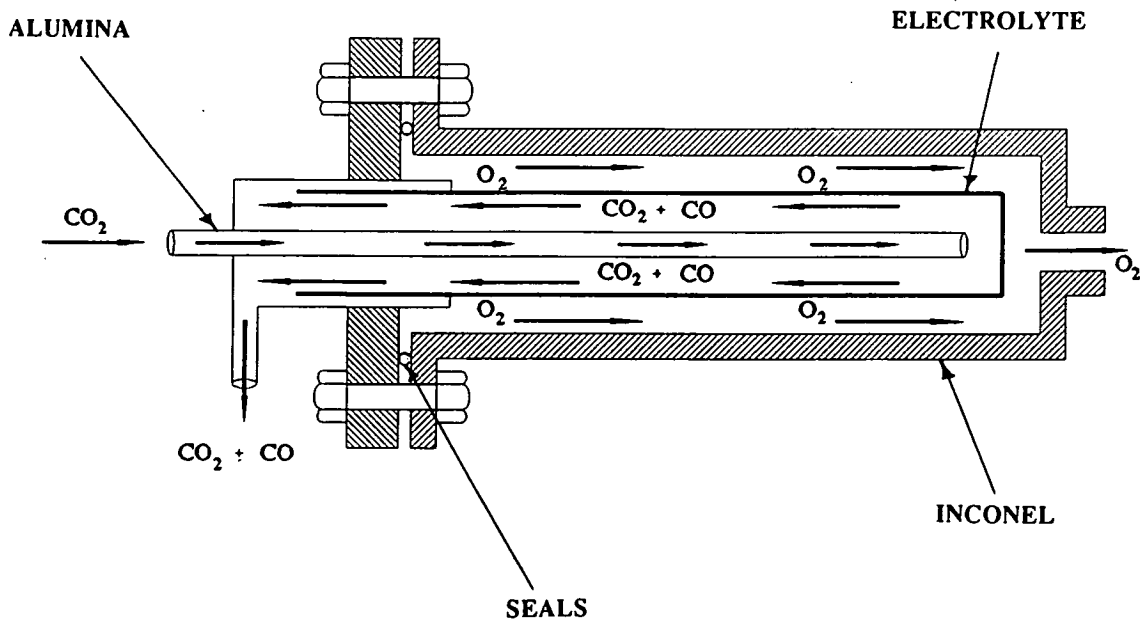


FIGURE 3

sccm. The following figures show the results of this testing. *Figure 4* shows the dependence of the production rate of O₂ on the applied cell potential for a variety of CO₂ flow rates at a temperature of 1000°C, while *Figure 5* displays the production at four different temperatures at a CO₂ flow rate of 138 sccm. Note, on both Figs. 4 and 5, the second-order dependence of oxygen production on the applied cell potential.

Figure 6 demonstrates the dependence the oxygen production has on the temperature of the cell with an applied cell potential of 2.0 VDC. Notice the weak dependence the oxygen production has on the carbon dioxide flow rate. *Figure 7* presents the oxygen production vs cell temperature at a carbon dioxide flow rate of 138 sccm. *Figure 7* also clearly depicts the dependence on voltage of the oxygen production rate.

Figure 8 indicates the O₂ production rate dependence on the CO₂ supply flow rate for an applied cell potential of 2.0 VDC. This is the most graphic illustration of the lack of dependence on the carbon dioxide flow rate for the oxygen production rate, especially for CO₂ flow rates greater than about 200 sccm. *Figure 8*, like the previous figures, shows the dependence on the temperature for the O₂ production rate.

Interpretation of the Results

The results of the extensive system analysis can be discussed in five areas: 1) flow rate effects, 2) mass flow ratio, 3) oxygen conversion efficiency, 4) Nernst efficiency, and 5) the system efficiency. Each of these areas will be addressed in order.

The flow rate effects were the easiest to interpret. The basic schematic is shown in *Figure 2*. It was initially found that the oxygen yield rate (production rate) increased as the CO₂ flow rate increased, but only up to a certain point, after which increased flow rate actually resulted in the decrease of the yield of oxygen. This was observed while other parameters such as cell voltage and cell temperature were held constant. It was suspected that the carbon dioxide may not have had sufficient residence time within the heated cell to achieve the required temperature at the high flow rates. To verify this hypothesis, a simple thermal diffusivity analysis was performed, after confirming that the flow within the tube is indeed laminar via simple Reynolds number calculation. The residence time is given by l/u , where l is the tube length and u is the mass averaged velocity. The characteristic time for heat transfer within the tube is given by $(d/2)^2/\alpha$, where d is the cell inside diameter and α is the thermal diffusivity ($k/\rho c_p$) of the carbon dioxide at high temperatures. As can

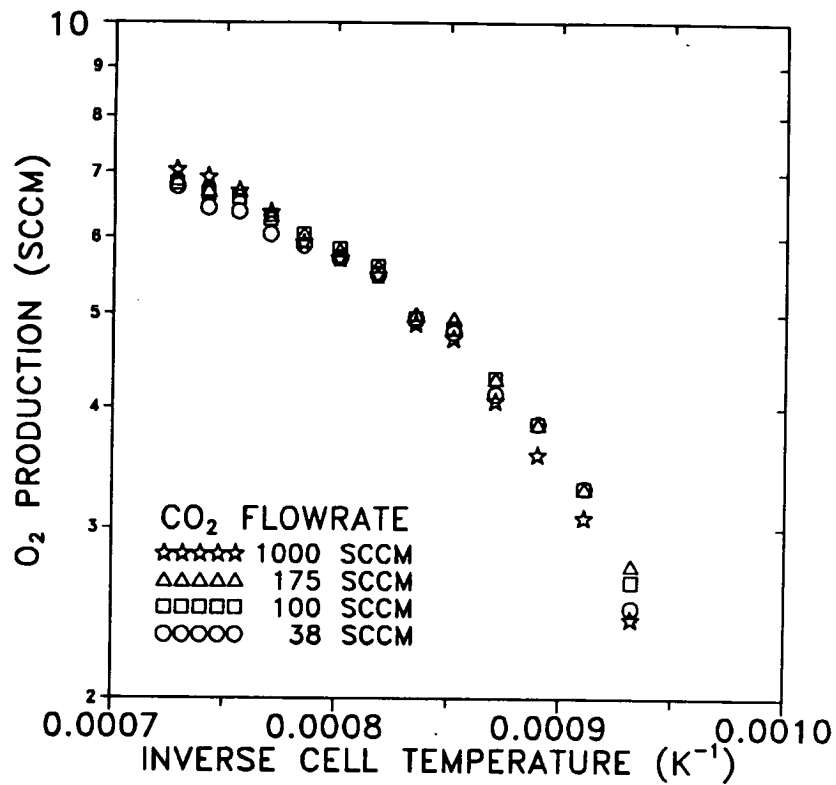


FIGURE 6

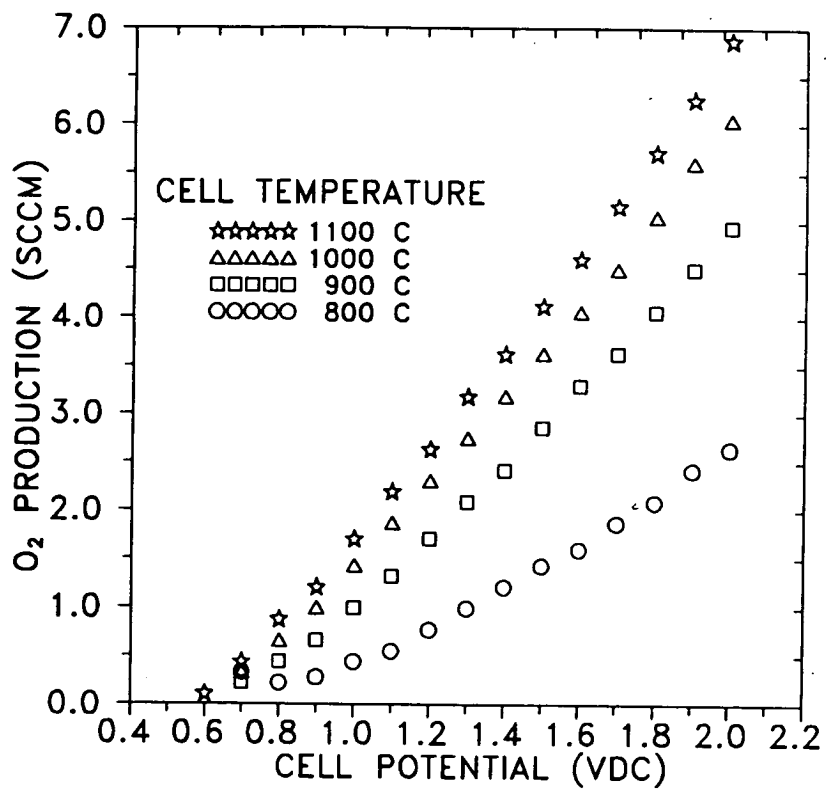


FIGURE 5

be seen in *Figure 9*, the peak occurs almost precisely where the two times become equal. It is thus clear that up to the point where the residence time is sufficient to bring the carbon dioxide to the requisite temperature, the production rate of the oxygen increases with the flow rate, but beyond this point the production rate falls off. It would be instructive to measure the actual gas temperature, and not merely the cell wall temperature as is done in the experiments reported here.

The mass flow ratio (the mass production rate of O₂ divided by the CO₂ supply mass flow rate) is of much interest. This is due to sizing constraints within scaled-up systems such as the primary carbon dioxide compressor, the heat exchanger, and the radiators. For these reasons, Figs. 10 and 11 plot the mass flow ratio vs CO₂ flow rate and temperature, respectively.

In previous studies of the propellant production plant, the emphasis was placed on sizing of the total production system.²⁻⁴ For these studies, oxygen conversion efficiencies of 25-30% were used when considering the estimated surface area needed to produce a required amount of oxygen per day. The use of these efficiencies was necessary to minimize oxygen plant mass. However, when considering the operation of the zirconia cell alone, *Figure 12* shows the complete range of oxygen conversion efficiencies.

As the concern of this report is the complete characterization of the zirconia electrolytic cell, all conversion efficiencies must be investigated. Richter, in his early work⁶ on the reduction of CO₂ began with the basic Nernst relation:

$$E_N = \frac{RT}{zF} \ln \left[\frac{P_2}{X_{O_2} P_1} \right]$$

Here, E_N is the Nernst voltage, T is the temperature (K), z is charge/mole ($z = 4$), R is the universal gas constant, and F is the Faraday constant. Additionally, P_2 is the pressure at the anode while $X_{O_2} P_1$ is the partial pressure of the oxygen in the supply CO₂ flow stream at the cathode. Richter then continued with his model and developed an instantaneous Nernst potential

$$E_{Ni} = \frac{RT}{zF} \ln \left[\frac{P_2}{\left(\frac{K(1-\eta)}{\eta} \right)^2} \right]$$

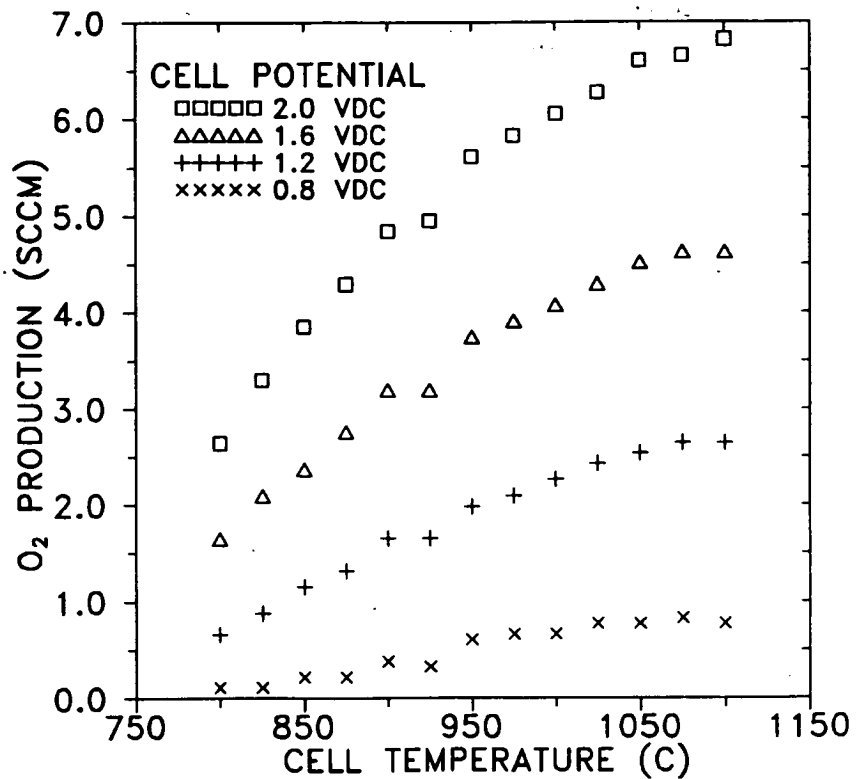


FIGURE 7

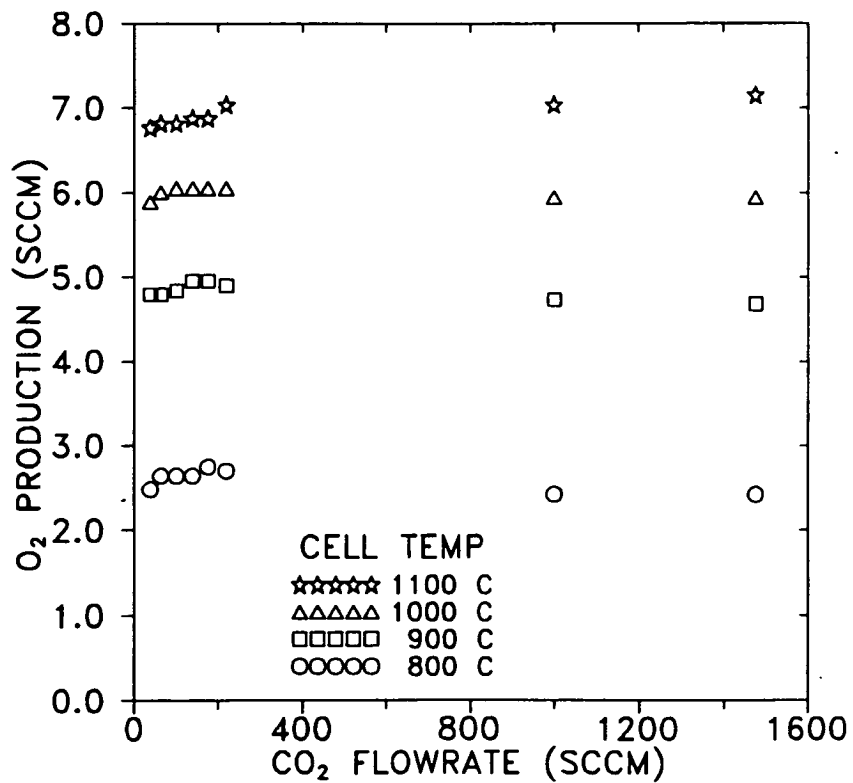
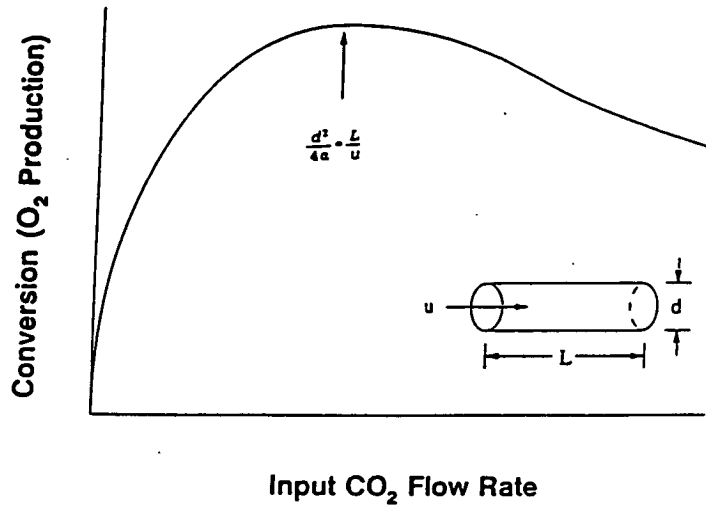


FIGURE 8

EXPLANATION OF FLOW-RATE EFFECT



[α is the thermal diffusivity of CO₂ at 1000°C]

Fig. 9 Thermal diffusivity vs residence time.

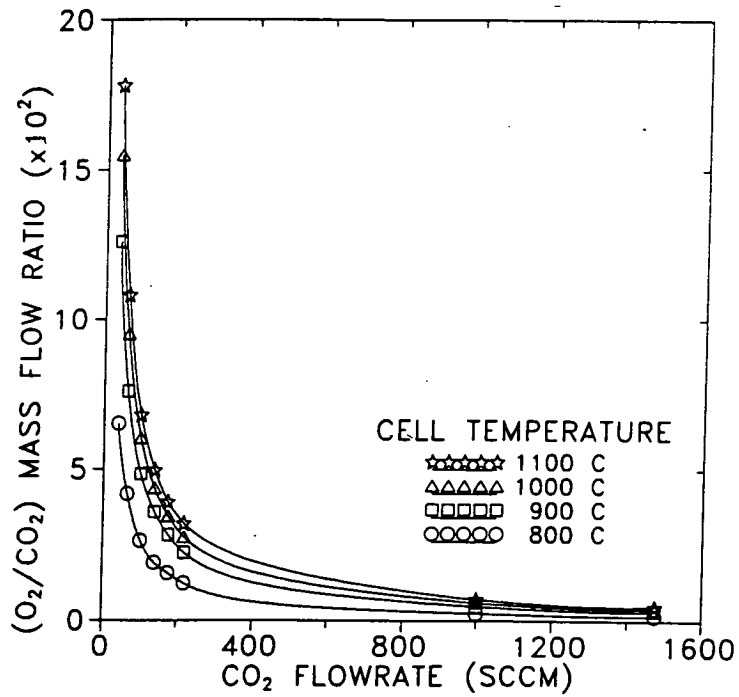


Fig. 10 O₂/CO₂ mass flow ratio vs CO₂ flow rate, cell potential = 2.0 VDC.

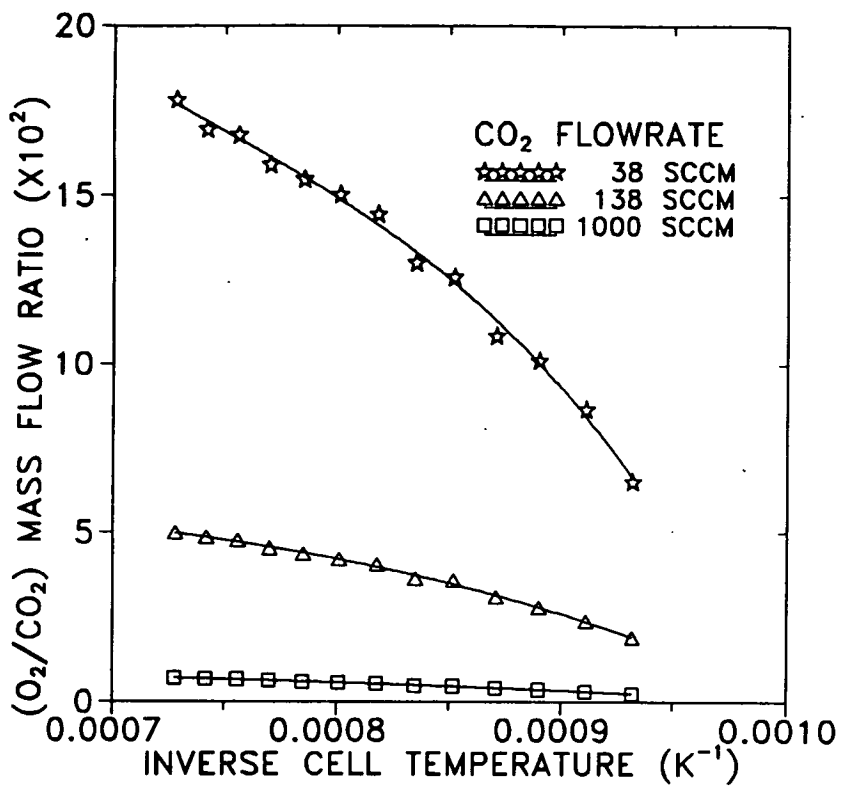


FIGURE 11

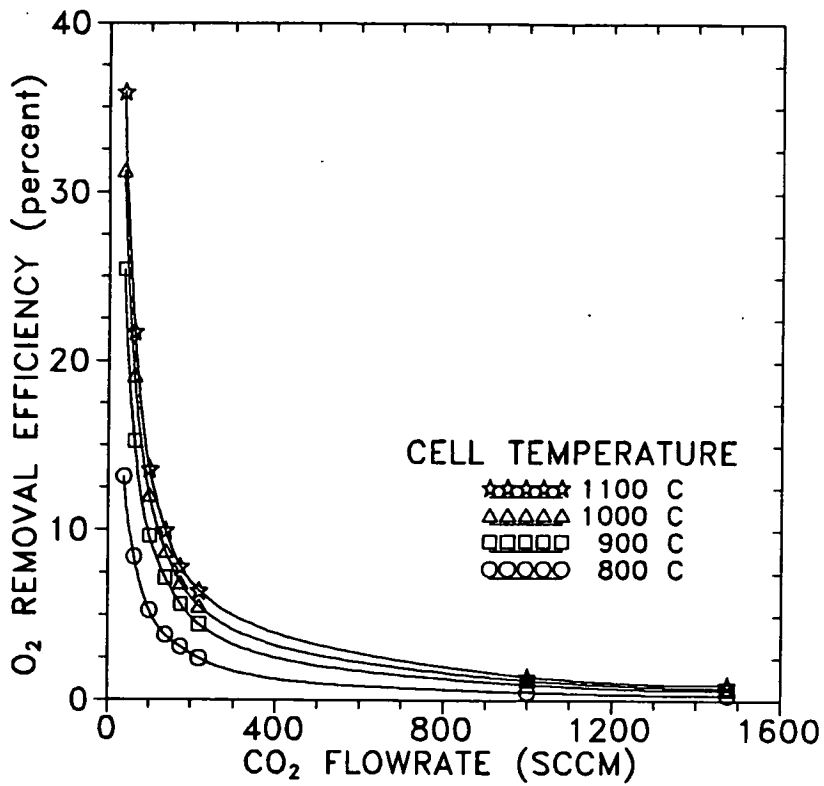


FIGURE 12

In this equation, K is the normal equilibrium constant and n is the mole fraction of CO_2 reduced to CO . The value n can be calculated from this equation:

$$n = C \left(\frac{I}{\dot{V}_{\text{CO}_2}} \right)$$

The value C is a constant from Richter's work ($C = 6.969$), I is the measured current produced across the cell, and \dot{V}_{CO_2} is the volumetric flow rate of the supply CO_2 stream. The current (A) was measured experimentally, as well as the volumetric flow rate of the CO_2 (sccm). The cell temperature (K) was measured by a k -type thermocouple positioned at the outside wall of the cell, and the pressure of the O_2 collection side of the cell was assumed to be one atmosphere. Using the proper values for the equilibrium constant K ,⁸ there was enough information available to calculate the instantaneous Nernst voltage. Richter cautions the use of this equation by stating that it is valid only if the critical voltage over the cell is not reached. The critical voltage can be defined as the potential which will be just sufficient to begin removing oxygen from the lattice of the zirconia. This process would be apparent from an "elbow" being observed in the current vs. potential plot in the higher potential range (> 2 VDC). *Figure 4* shows this potential has not been reached due to the lack of an elbow. According to Richter then, the potential can be expressed as a function of the operating temperature and the actual amount of O_2 removed and not the partial pressure of the O_2 at the cathode. The instantaneous Nernst potential was used in defining the Nernst efficiency:

$$\eta_N = \frac{E_{Ni}}{E_{act}}$$

This equation shows the Nernst efficiency is the ratio of the theoretical potential divided by the actual potential (E_{act}). What this indicates is the instantaneous amount of cell overpotential. *Figure 13* shows the results of this analysis.

It is apparent from this figure that the amount of cell overpotential rises as the applied cell potential rises. One source of this overpotential could be the pressure drop through the porous electrode. It is important to remember that from *Figure 4*, the rise in O_2 production is almost directly proportional to the potential applied to the cell. Ash⁹ et al. point out that experiments have shown that as the O_2 production rate rises, there is an increase in the pressure drop across the negative

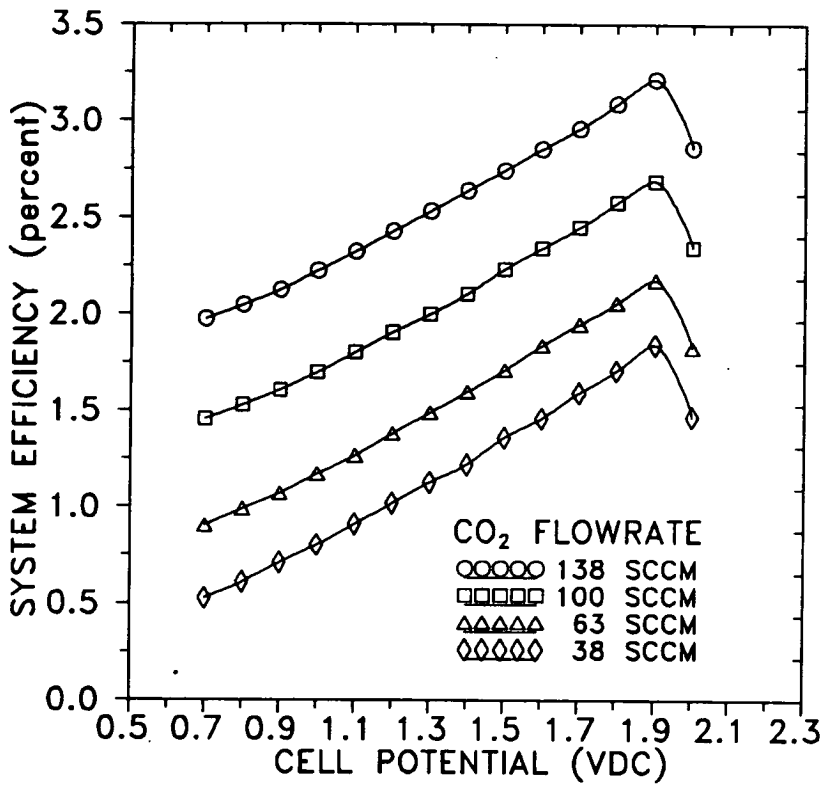


FIGURE 14

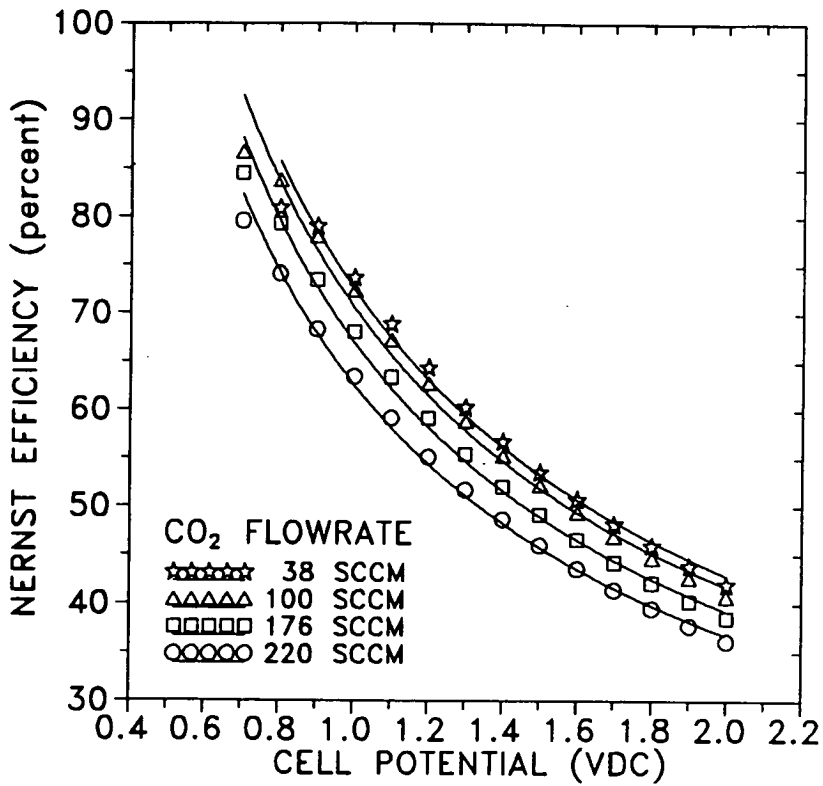


FIGURE 13

electrode which can approach the partial pressure of the oxygen in the CO₂ stream resulting in an ever increasing pumping power requirement. Another possible source of the overpotential is slow diffusion, adsorption, or dissociation processes near the electrode-electrolyte interface of the cell resulting in concentration overpotential.¹⁰ This report also states the possibility of a transition overpotential due to slow electrochemical reaction. The sources of overpotential cannot be experimentally determined with this system as currently constructed, but any future characterization of the zirconia electrolyte should definitely seek to identify the source of these overpotentials.

With the Nernst efficiency established, it was next desired to arrive at a system efficiency. The control volume is taken around the entire cell system. The useful work inside the control volume is divided into two parts. The first being the rate of thermodynamic energy being used to dissociate the CO₂. The second being the work required to electrochemically conduct the oxygen ions through the zirconia. The power passing into the control volume is also divided into two components. The first being the power delivered to the ceramic heaters, and the second being the power delivered to the electrolyte. The energy required to thermally dissociate the CO₂ is given by the equation:

$$\dot{Q}_{TH} = \sum_P N_i (\Delta h_f^\circ + h_T - h_{298})_i - \sum_R N_j (\Delta h_f^\circ + h_T - h_{298})_j$$

Here, Q_{TH} is the thermodynamic power input with the calculation showing the normal enthalpy of reaction equation with the enthalpy of formation and sensible enthalpies. The subscripts *i* and *j* represent the products and reactants respectively. The coefficient *N* represents the molar flow rate of each respective constituent. This value and the other power values give the following definition for the system efficiency:

$$\eta_{sys} = \frac{E_N I_{cell} + \dot{Q}_{TH}}{E_{cell} I_{cell} + E_{heat} I_{heat}}$$

In this equation, the subscript heat refers to observed values of the ceramic heater, and the subscript cell refers to observed values with the electrolyte, *E* being the potential (V) and *I* being the current (A). *Figure 14* displays the results of this analysis.

Summary

This paper has presented results from the first phase of a well-planned multiphase research program aimed at significantly reducing costs of future space missions; terrestrial applications are always

kept in mind. This proof of concept study has used full system hardware, realistic solid electrolytic cell material, realistic operating temperatures, full cell voltages, and full scale flow rates. These features distinguish our experiments from the usually understood test-tube demonstrations, where the conditions are substantially different from the real life counterpart. The only feature that is not duplicated here is the scale of oxygen production.

Important efficiencies are defined and measured. The basic electrolytic efficiency refers to the efficiency of using electrical input in producing oxygen, while the overall system efficiency refers to the enthalpy difference achieved between the product stream and the reactant stream divided by the overall energy input. The carbon dioxide flow rate, cell voltage, and cell temperature are all varied parametrically. A simple heat transfer theory explains the flow rate effects. The voltage effects are in good agreement with the manufacturer's specifications.

These thorough characterizations of the component performance parameters naturally lead us to the next step of scale-up and full system demonstration with active controls. Creative solutions to these engineering designs indicate that future space missions could realize substantial cost savings through the use of local (in-space) resources.

Acknowledgments

Research was supported by NASA Code R, through the University of Arizona Grant NAGW-1332. The authors are grateful to Murray Hirschbein and Gordon Johnston for funding and helpful comments.

References

- ¹Ash, R., Dowler, W., and Varsi, G., "Feasibility of Rocket Propellant Production on Mars," *Acta Astronautica*, Vol. 5, 1978, pp. 705-724.
- ²Lawton, A.L., and Frisbee, R.H., "A New Look at Oxygen Production on Mars ISPP," Jet Propulsion Lab. Paper D-2661, Sept. 1986.
- ³Lawton, A.L., "Risk Factors in the Development of Zirconia Cell Technology for the Production of Oxygen from the Martian Atmosphere," Jet Propulsion Lab. Paper D-3546, Aug. 1986.
- ⁴Frisbee, R.H., "Mass and Power Estimates for Martian In-Situ Propellant Production Systems," Jet Propulsion Lab. Paper D-3648, Oct. 1986.
- ⁵Ramohalli, K., Lawton, E., and Ash, R., "Recent Concepts in Mission to Mars: Extraterrestrial Processes," *Journal of Propulsion and Power*, Vol. 5, No. 2, 1989, pp. 181-187.

⁶Richter, R., "Basic Investigation into the Production of Oxygen in a Solid Electrolyte," AIAA Paper 81-1175, June 1981.

⁷Suitor, J.W., Berdahl, C.M., Ferrall, J.F., Marner, W., Schroder, J.E., and Shichta, P.J., "Development of an Alternate Oxygen Production Source Using A Zirconia Solid Electrolyte Membrane," Jet Propulsion Lab. Paper D-4320, May 1987.

⁸Wark, K., *Thermodynamics*, 3rd ed., McGraw-Hill, New York, 1977, p. 840.

⁹Ash, R., Richter, R., Dowler, J.A., Hanson, and Uphoff, C.W., "Autonomous Oxygen for a Mars Return Vehicle," International Astronautical Federation Paper 82-210, 1982.

¹⁰Etsell, T.H., and Flengas, S.N., "Overpotential Behavior of Stabilized Zirconia Fuel Cells, *Journal of the Electrochemical Society*, Vol. 118, No. 12, 1971, pp. 1890-1900.

omit

V. DATABASE DEVELOPMENT

497605
N93-26697

An Integrated Database With System Optimization and Design Features

A. Arabyan, P. E. Nikraves, and T. L. Vincent
Department of Aerospace and Mechanical Engineering
University of Arizona

S23-82
158370
P-8

Abstract

A customized, mission-specific relational database package has been developed to allow researchers working on the Mars oxygen manufacturing plant to enter physical description, engineering, and connectivity data through a uniform, graphical interface and to store the data in formats compatible with other software also developed as part of this project. These latter components include an optimization program to maximize or minimize various criteria as the system evolves into its final design; programs to simulate the behavior of various parts of the plant in Martian conditions; an animation program which, in different modes, provides visual feedback to designers and researchers about the location of and temperature distribution among components as well as heat, mass, and data flow through the plant as it operates in different scenarios; and a control program to investigate the stability and response of the system under different disturbance conditions. All components of the system are interconnected so that changes entered through one component are reflected in the others.

Introduction

This specific project was initiated with the aim of providing data storage, classification, system design, optimization and simulation and control system design capabilities for the oxygen manufacturing plant that the Space Engineering Research Center at the University of Arizona has undertaken to build on Mars. Because of the multidisciplinary nature of the plant's design process, this integrated software project was designed to provide uniform access to all the different groups working on the design and testing of the plant. This project consists of the following principal components (see *Figure 1*):

- i) A relational database of component and model libraries with system integration capabilities;
- ii) An optimization system to maximize specified performance criteria while meeting weight, thermal, cost and other constraints.
- iii) A visualization system for animation of the plant's dynamics;
- iv) A control design system associated with data collection equipment connected to an experimental setup.

This report focuses on the technical features and current status of the first two of these principal components.

Current Project Status

Relational Database

The design and implementation of the database entry, organization and storage program has been completed. A brief description of the program and its objectives and design philosophy were provided in earlier progress reports^[1,2]. In essence, components of the plant are abstracted into simple functional databases which are then connected in a compatible manner to produce necessary connectivity data to other programs. The program, implemented in the FoxPro 1.02 environment on a 80386-based personal computer, features libraries of component types (e.g. pump, heat exchanger, compressor, etc) as well as libraries of specific manufactured models of each component type. The first set of libraries sets up fields for the general characteristics of a component type (e.g. the flow capacity of a pump or heat exchanger), in effect creating blank templates for actual data entry. The second set of libraries contains the actual data supplied by the manufacturers of specific models of components or data generated in house for equipment

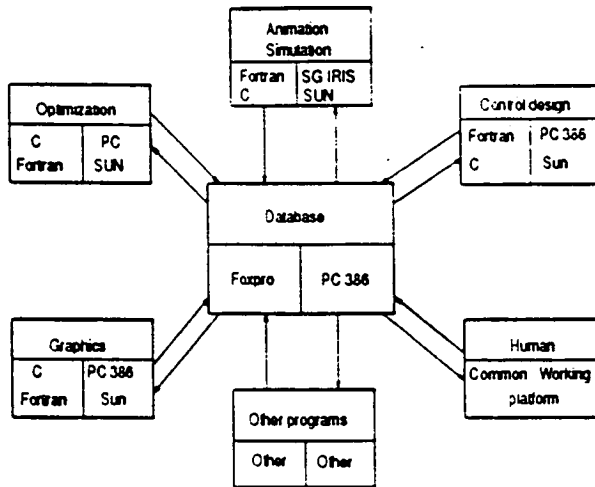


Figure 1. Overview of integrated database system

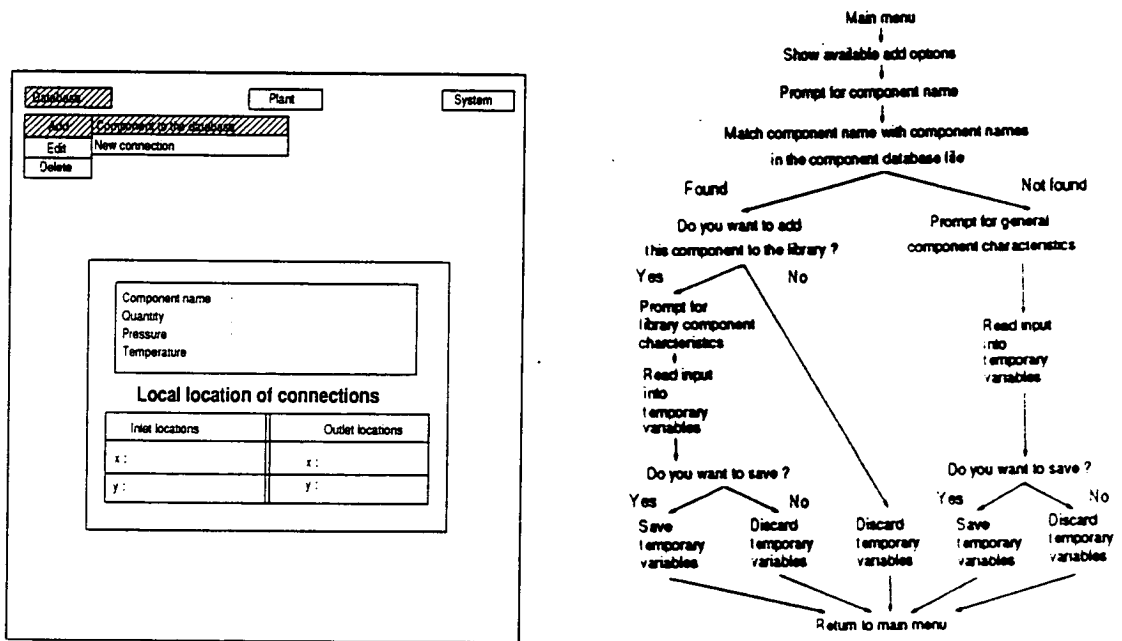


Figure 2. Entry of general component characteristics and associated flowchart

designed in university laboratories. Similarly, libraries of connection types and specific models of connections are maintained for pipes, cables and couplings. Each of these libraries can be accessed from a graphical user interface using a pointing device. In addition, the user can enter new component types of his own, edit the existing database or delete components from the database using simple point-and-click commands. A sample new component addition menu set and its associated flow chart are illustrated in *Figure 2*.

Once libraries of components and connections are built, the user can pick any number of different models of components and connections, and install them in a model of the plant of arbitrary design. This is also accomplished by simple point-and-click commands with the program guiding the user through the different steps. A graphical display system to enable the user to view the current status of the layout of the plant is also incorporated in the program and can be called from a drop-down menu using a pointing device. *Figure 3* illustrates some of the menu items that are available at this stage. When the user is finished installing components and connections in the plant, the program links the installed components by the proper connections and checks for any physical interference between any two components or between a component and the frame of the plant. In the event a physical interference is found, the program attempts to relocate the components so that the interference is eliminated. If no positions can be found to eliminate the interference the user is prompted to enter a new component model.

A complete report about the design and use of the database program has been written and is available at the Computer-Aided Engineering Laboratory^[3,4].

Optimization Software

A new customized software system has been developed to optimize the packaging of the oxygen manufacturing plant. The principal purpose of this system is to ensure that the components of the plant are located relative to each other in such a way that user-defined cost functions are minimized. The system, which can be called from a drop-down menu using a pointing device, reads all the information it needs about the properties and connections of the components in the plant from the relational database and then relocates the components iteratively until the cost or objective function that has been defined is minimized. At the present time, two different objective functions are used. The first objective function, O_1 , consists of a weighted sum of all heat and pressure losses that occur within the plant through radiation between components and from connecting pipes, convection through fluid flow, conduction along pipes and fluid friction within pipes. Because of the

different types of losses included in the function, system parameters (e.g. temperatures at desired points or surfaces or pressures at certain inlet or outlet positions) occur in nonlinear form in the function. The second objective function, O_2 , is made up of a weighted sum of component and connection weights and costs. The optimization program searches the space of possible locations for components in the plant plus all possible component and connection models that can be substituted for each component and connection model to reduce the value of both objective functions to a minimum.

The optimization process is complicated by the fact that some of the variables that change the values of the two objective functions are continuous while others are discrete. For example, the locations of the components in the plant, specified by their coordinates in a reference frame, are continuous variables whereas their sizes, costs and weights are discrete because they change abruptly from one model to another. As a result, the optimizing program proceeds in four different stages. In Stage 1, the program divides up the frame of the plant into n equal regions where n is the number of components in the plant. It then places the initial (user-specified) set components in each of the regions making sure that there is no physical interference anywhere in the plant. In doing that each component is represented by the smallest rectangle that completely encloses the component (see *Figure 4*). In Stage 2, the program relocates each component in all possible regions computing the value of O_1 in each case. The configuration that results in minimum O_1 is retained. In Stage 3, the program substitutes each component in each region and each connection among them with all possible models from their respective libraries. In this stage the minima of both O_1 and O_2 are sought. In Stage 4, the set of components and connections resulting in minimum O_1 and O_2 are subjected to fine-tuning adjustments within their own regions to reduce O_1 further. Stage 1 is accomplished using a novel approach that employs modulo arithmetic. Stage 2 uses a modified brute-search method, Stage 3 uses a brute-force search method, and Stage 4 uses the steepest-descent method. *Figure 5* shows the different stages of optimization by a flow chart.

The program's output can be viewed interactively as it searches for the optimal configuration or graphically whereby the program displays the initial (nonoptimal) and final (optimal) configuration of the plant, together with figures for total heat and pressure losses. *Figure 6* shows different configurations tried by the program for a nine-component design. The system is currently being enhanced to export data about the optimal configuration it finds to the relational database program so that it can update its appropriate databases and export them to other programs that make up the integrated system.

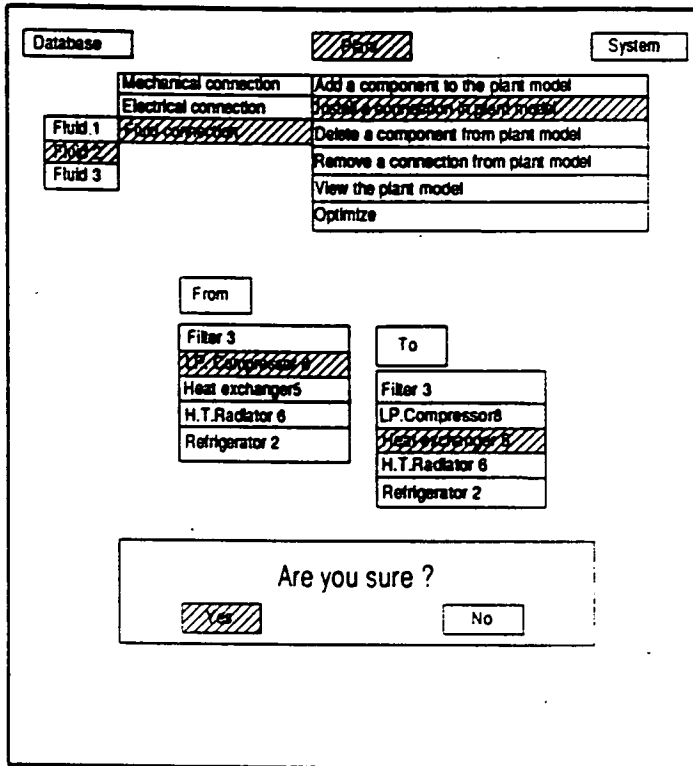


Figure 3. Installing components and connections in plant model

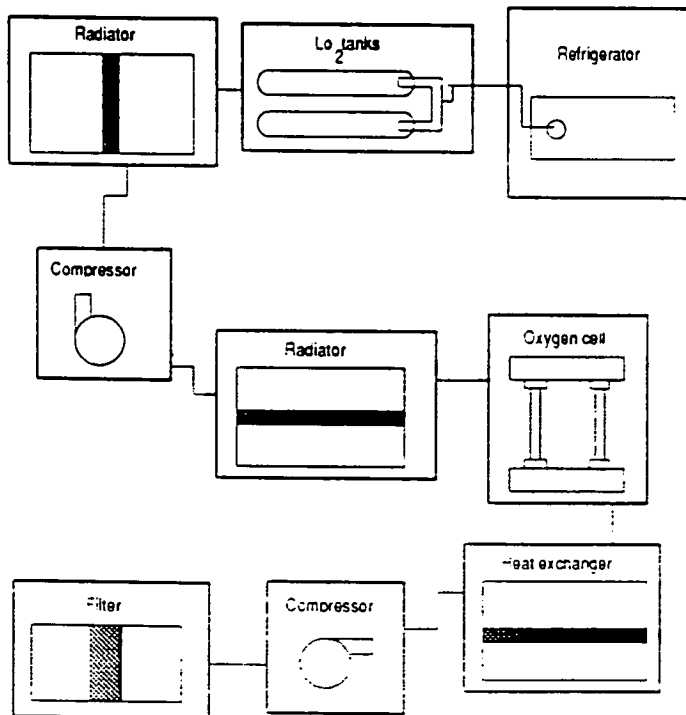


Figure 4. Components enclosed in rectangles

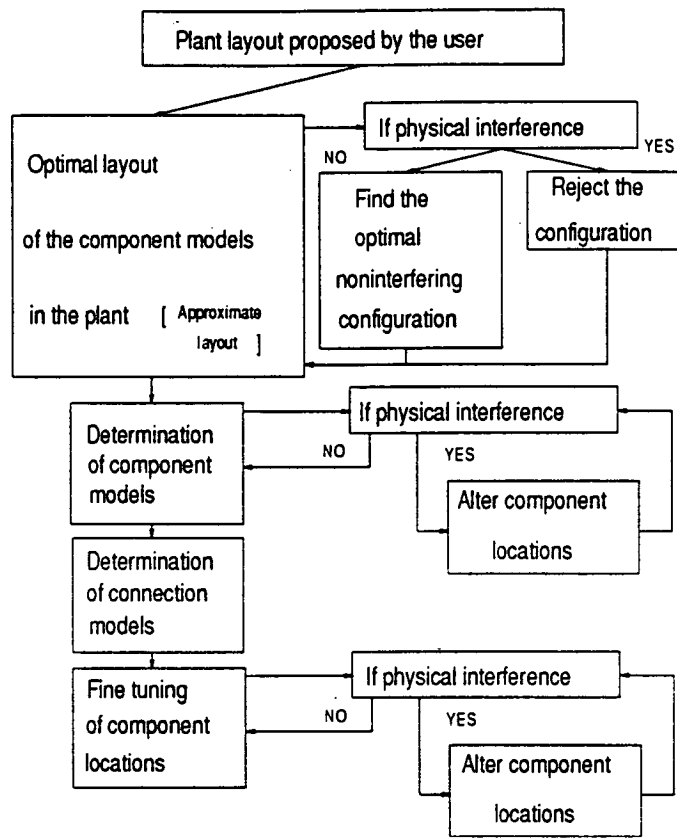


Figure 5. Stages in optimization process

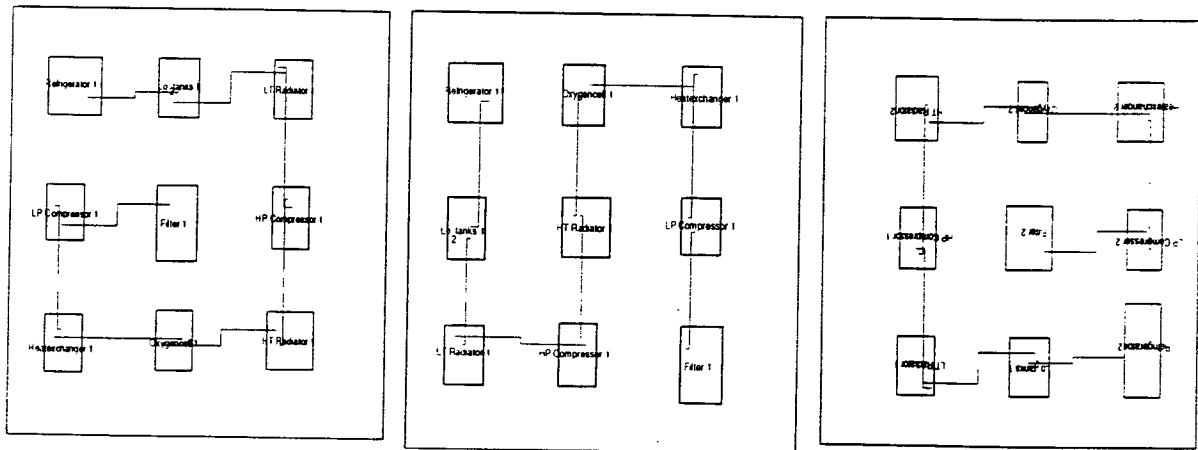


Figure 6. Successive configurations in optimization process

A complete report about the design, operation and current status of the optimization program has been written and is available at the Computer-Aided Engineering Laboratory⁴.

References

¹Arabyan, A., P.E. Nikraves, T.L. Vincent. Quantitative simulation of extraterrestrial engineering devices. *NASA/SERC Annual Progress Report 1990-91, APR-91: IV-7-12.*

²Arabyan, A., P.E. Nikraves, and T.L. Vincent. Quantitative simulation of extraterrestrial engineering devices. *NASA/SERC Annual Progress Report 1991, APR-91/F: IV-31-34.*

³Krishnasamy, A., A. Arabyan, and P.E. Nikraves. An integrated design database for the Mars oxygen manufacturing plant. CAEL-91-6 (Computer-Aided Engineering Laboratory, Tucson, Az.) July 1991.

⁴Santhanam, V. Optimization of the packaging of the Mars oxygen manufacturing plant. M. Sc. thesis, University of Arizona (July 1992).

497606
N93-26698

The Steward Observatory Asteroid Relational Database

Mark V. Sykes and Elizabeth M. Alvarez del Castillo

**Steward Observatory
The University of Arizona**

524-82

158371

P-5

Abstract

The Steward Observatory Asteroid Relational Database (SOARD) has been created as a flexible tool for undertaking studies of asteroid populations and sub-populations, to probe the biases intrinsic to asteroid databases, to ascertain the completeness of data pertaining to specific problems, to aid in the development of observational programs, and to develop pedagogical materials. To date SOARD has compiled an extensive list of data available on asteroids and made it accessible through a single menu-driven database program.

Users may obtain tailored lists of asteroid properties for any subset of asteroids or output files which are suitable for plotting spectral data on individual asteroids. A browse capability allows the user to explore the contents of any data file. SOARD offers, also, an asteroid bibliography containing about 13,000 references. The program has online help as well as user and programmer documentation manuals. SOARD continues to provide data to fulfill requests by members of the astronomical community and will continue to grow as data is added to the database and new features are added to the program.

Introduction

Asteroids are characterized by their diversity. We study them using a wide variety of remote sensing techniques in an attempt to determine their composition and physical properties, and relate this information to processes effecting asteroids and other solar system bodies over the age of the solar system. Observations are obtained through groundbased telescopes and radar, and spacecraft such as the Infrared Astronomical Satellite (IRAS). These observations are dedicated surveys or focussed on individual objects of particular interest. SOARD incorporates the data obtained from these various observations into a single database.

In order to evaluate and exert some quality control over the data, it is critical to be able to trace each datum to its origin. In addressing scientific issues it is important also to have a knowledge of and access to the existing literature on the subject. SOARD contains an asteroid bibliography containing about 12,000 references, from the 19th century into the year 1992.

In addition to being objects of scientific investigation, asteroids are potential resources to be utilized in support of the expansion of humans into the solar system. The most accessible of these are the Near Earth Asteroids (NEA's) whose motions around the Sun bring them within reach of low-energy transfer orbits from the Earth. Until recently, the information available on the NEA's has been relatively limited, but with increased rates of discovery and greater numbers of observational programs focussing on these objects, this information is expected to grow rapidly. Since NEA's derive from the main asteroid belt (though some may be extinct comets), knowledge of their source populations provides additional insight into the nature and physical properties of NEA's.

SOARD's goal is to incorporate ALL published asteroid data into one generally accessible database for use in research and in expanding our general and specific understanding of asteroid populations.

SOARD is a menu-driven asteroid database management system which utilizes dBase IV software in a fashion transparent to the user. It allows four basic system outputs at this time: (1) files of designations of asteroids satisfying range criteria for parameters or functions of parameters, (2) subsets of database parameters for subsets of asteroids, (3) files of multiband photometry or spectroscopy for individual asteroids (for plotting), and (4) files of bibliographic references satisfying users' search criteria. Any data file may be examined using a SOARD browse capability.

Table 1. SOARD Data Sets

Asteroids II

- Proper Orbital Elements
- Taxonomic Classifications
- Family Designations
- Pole Orientations
- Magnitudes, UBV Colors, Albedos, and Diameters

IRAS

- Radiometric Diameters and Albedos
- Individual IRAS Observations
- Polarimetry file
- Lightcurve file
- UBV Observations
- 8-Color Spectroscopy
- 24 Color Spectroscopy

Miscellaneous

- 52-Color Spectroscopy (J. Bell)
 - Osculating Orbital Elements (E. Bowell)
 - Preliminary Designations and Discovery Circumstances (MPC)
 - Photometric Parameters (MPC)
 - Proper Elements (Milani and Knezevic)
 - Radar Observations (S. Ostro et. al.)
- Asteroid Bibliography (C. Cunningham)

Table 2. Existing Data Sets for Future Addition

- CCD Spectroscopy (L. McFadden, F. Vilas)
- Near-IR Spectra (Lebofsky, Bus, et. al.)

SOARD Data

Table 1 lists the individual data sets which are currently online and accessible through SOARD. It combines ground based observations which were published in ASTEROIDS II, radiometric data collected by IRAS, ancillary IRAS data sets of groundbased polarimetry, lightcurve, and spectroscopic observations, Jeff Bell's 52-color near-IR survey, osculating orbital elements for 19,945 asteroids, discovery information and photometric parameters published through the Minor Planet Circulars (MPC), ground based radar observations, and 12,742 literature references. As data is incorporated into SOARD, it receives a reference to its source in the literature which is listed in the bibliography file. This provides online information on the origin of the data and allows maximum understanding of data quality. Data evaluation is critical to its use in an engineering context.

SOARD Reference Capability

SOARD has acquired and incorporated Clifford Cunningham's asteroid bibliographic reference file. Cooperation led to suggestions for expansion of his original file. Fields which were added include a keyword field and a field which lists the asteroids to which the reference pertains. This expansion which has been implemented already for the major journals and for recent publications is currently a part of SOARD. Full implementation for all citations would require further man hours. Cliff Cunningham was very helpful in agreeing to alter his file format to make it more compatible with SOARD requirements. Although he is marketing his database as a salable product, he has generously given permission to distribute it as part of SOARD to the test sites. In its implementation in SOARD, a user can search the reference file by author, title, date, publication, keyword, asteroid numbered designation, some subset of authors or words in a title, or any combination of these parameters. We regard this utility as a powerful addition to SOARD. SERC will need to contract with Clifford Cunningham and develop a licensing agreement if they wish to continue to distribute his product.

Updating the Database

Ongoing observations and research promise a continually growing body of data which should be added to SOARD. Current monthly updates to SOARD include data available through literature searches, data sent by individual observers, and data obtained from the Minor Planet Circulars (MPC). Maintenance of this ongoing update program of the data sets already incorporated into SOARD is the most efficient way of preserving the work which has brought the database to its current level of usefulness. SOARD should eventually expand to include the data sets listed in Table 2. Some of the data, such as CCD spectroscopy of certain asteroids, has been published. Some data is collected and needs to be reduced and published. Data addition procedures have been fully

documented in the SOARD programmer's manual so they can be undertaken at any point by a person with basic computer knowledge.

Expanding SOARD

Additional programming will expand the features available through SOARD. A fourth main menu item will allow the user to concatenate functions of asteroid parameters. If a file contains orbital elements such as semi-major axis and eccentricity, the user may calculate the perihelion distance as an output parameter of specific interest. This feature will minimize data which must be distributed with the system while allowing the user maximum choice for customized output of asteroid parameters.

All SOARD programs have been fully documented and logged in the programmer's manual so as to facilitate future expansion of the SOARD interface.

User Interface and Testbed Activities

User's and programmer's manuals have been completed and offer more comprehensive guidance than is desirable with the on line help capability previously built into SOARD. SOARD testbed activities include the following sites: the California Space Institute in La Jolla, California (Dr. Lucy-Ann MacFadden); the Institute for Astronomy in Honolulu, Hawaii (Dr. David Tholen); the Lunar and Planetary Laboratory at the University of Arizona in Tucson, Arizona (Dr. Larry Lebofsky and Ellen Howell), and the Park School in Brookline, Massachusetts (Dr. Linda French). A transportable execution version of the relational database has been distributed to these sites to test without the assistance of prior tutoring but with the help of online documentation only. Already they have provided substantial input into the overall user friendliness of the system and made suggestions for improving the SOARD environment. With the addition of a test site at the Park School the educational applications of SOARD at the pre- collegiate level are being explored. Input from test sites has been and will continue to be incorporated into the SOARD planning and programming process.

Community Support

We respond to all moderate requests from the community and have provided data in support of observing, research, and teaching programs. For instance, for the last few years SOARD has been asked for assistance and has supplied pedagogical materials for the University of Arizona's Steward Observatory run Adult, Beginning, and Advanced Teen Space Camps.

497607 2

Near-Earth Asteroids:

N 9 3 - 2 6 6 9 9

Observer Alert Network and Physical Observations

**Donald R. Davis and Clark R. Chapman
Planetary Science Institute**

S25-82

158372 ✓

Abstract

P-7

This project strives to obtain physical observations on newly discovered Near-Earth Objects (NEOs) in order to provide fundamental data needed to assess the resources available in the population. We have the goal of acquiring data on all objects brighter than magnitude $V=17.0$. To accomplish this, we have established an electronic mail alert and observer information service that informs observers around the world as to the status of physical observations on currently observable NEOs. We also acquire such data ourselves through a cooperative program with European colleagues that uses telescopes on La Palma to obtain spectra of NEOs and through observations made from a local telescope on Tumamoc Hill. This latter telescope has the advantage that large amounts of observing time are available, so that whenever a new NEO is discovered, we can be assured of getting time to observe it.

Near-Earth Objects: Observer Alert Network and Physical Observations

Progress Report and Proposed Research:

Near-Earth objects (NEOs) are being discovered at an increasing rate; however, usually only a preliminary orbit and an estimate of the brightness of the asteroid is obtained during the discovery apparition. This is due to the brief interval (typically days to weeks) that the asteroid is bright enough to be observed by workers at 1-2 meter class telescopes. Unfortunately, it is usually several or many years before a newly discovered NEO makes another close approach to Earth; thus little is known about the physical properties of NEOs until long after their discovery and no physical data at all exists for most NEOs. However, as NASA is becoming increasingly interested in NEOs as potential mission targets and as a source of resources for expanded space activities, it is essential to learn more about these bodies as early as possible in order to meet the needs of the space program.

The importance of timely observations during the discovery apparition was recently emphasized by Wisniewski of the Lunar and Planetary Laboratory, who found that over the next few years, roughly twice as many newly discovered NEOs will be bright enough for physical observation as there will be "old" NEOs this bright. In order to stimulate awareness of the need for NEO observations, the Planetary Science Institute established an Observer Alert Network in October, 1990. We have twenty observers on our active list that we communicate with whenever an appropriate NEO is discovered. We also assist in alerting observers of the need to obtain positions of high priority newly discovered fast moving objects, both prior to and following the release of an IAU circular.

In the past year, we have expanded this Network to include an Observer Information File that provides current information about physical observations, both accomplished and planned, for NEOs that are currently observable. The contents of the current file are given in Appendix A. This file is updated every working day and is available over Internet to the global community of NEO observers. Use of this information will enable the observer community to plan observations so as not to duplicate those already acquired by others and to fill in "holes" in the data before the NEO fades to unobservability.

We propose to continue our information and alert service to the community as a way of maximizing the value of physical observations of NEOs. As can be seen from Appendix A, the community has been doing a fairly good job in recent months in acquiring physical observations and through our service we plan to keep emphasis focussed on these important objects.

We have also progressed on our program to acquire physical observation of NEOs both from Tumamoc Hill and in association with Dr. Alan Fitzsimmons (University of Dublin) from La Palma Observatory. Our program to acquire spectra using service observers on the 4.2m and 2.4m telescope resulted in successful observations of four NEOs. *Figure 1* gives the spectra for three of these, while the fourth one, 1992KD, has not yet been reduced. We are proposing to continue this program, one of only two programs in the world that is able to get spectra in the range from 0.4-1.0 microns on a fairly regular basis. We anticipate that we will be able to get 3-4 service nights per year and would expect to observe between 4-6 asteroids per year under this program. If newly discovered NEOs are not available when service nights are offered, then we will apply to obtain spectra of previously discovered NEOs for which no compositional information now exists.

We also propose to continue our observing program using the Tumamoc Hill Observatory a potentially usable site for obtaining physical observations for many NEOs. This 20" telescope has been used only sporadically in the past due to the lack of instrumentation, the poor state of the tracking and acquisition system, and the bright sky at the observatory which is located at the western edge of the city of Tucson. However, many of the difficulties have been corrected in the past year: 1) Photometric Corporation, Ltd., has loaned a CCD camera and controller to the Observatory and this instrument is now permanently mounted on the telescope. 2) The University of Arizona (S. Larson) provided a computer for data acquisition and storage. 3) Encoders are being added to the drive to aid in pointing the telescope and in acquiring faint objects. 4) The Planetary Science Institute provided a rack and pinion dome drive. All of these improvements are either in place or will be in place in the next few weeks. Tests by S. Larson have already established that a 19th magnitude (V) star can be detected with this CCD/telescope using a two-minute integration time.

In the past several months, we have continued to develop this observatory for carrying out physical observations. A problem occurred when the pointing system on the telescope was tested earlier this summer and it was discovered that the drive stepper-motors produced excessive vibration and caused drift in the tracking system. This required that a new set of stepper motors be installed, which has been done. Currently, R. Tucker is reprogramming the pointing system to give us basic pointing capability. As soon as this is completed, currently expected to be by the end of September, then we can start to use the observatory for physical observations. Other problems have been successfully addressed in the past several months. Software has been acquired at PSI so that we can read the data images generated by the Macintosh system at the telescope, thus we can use

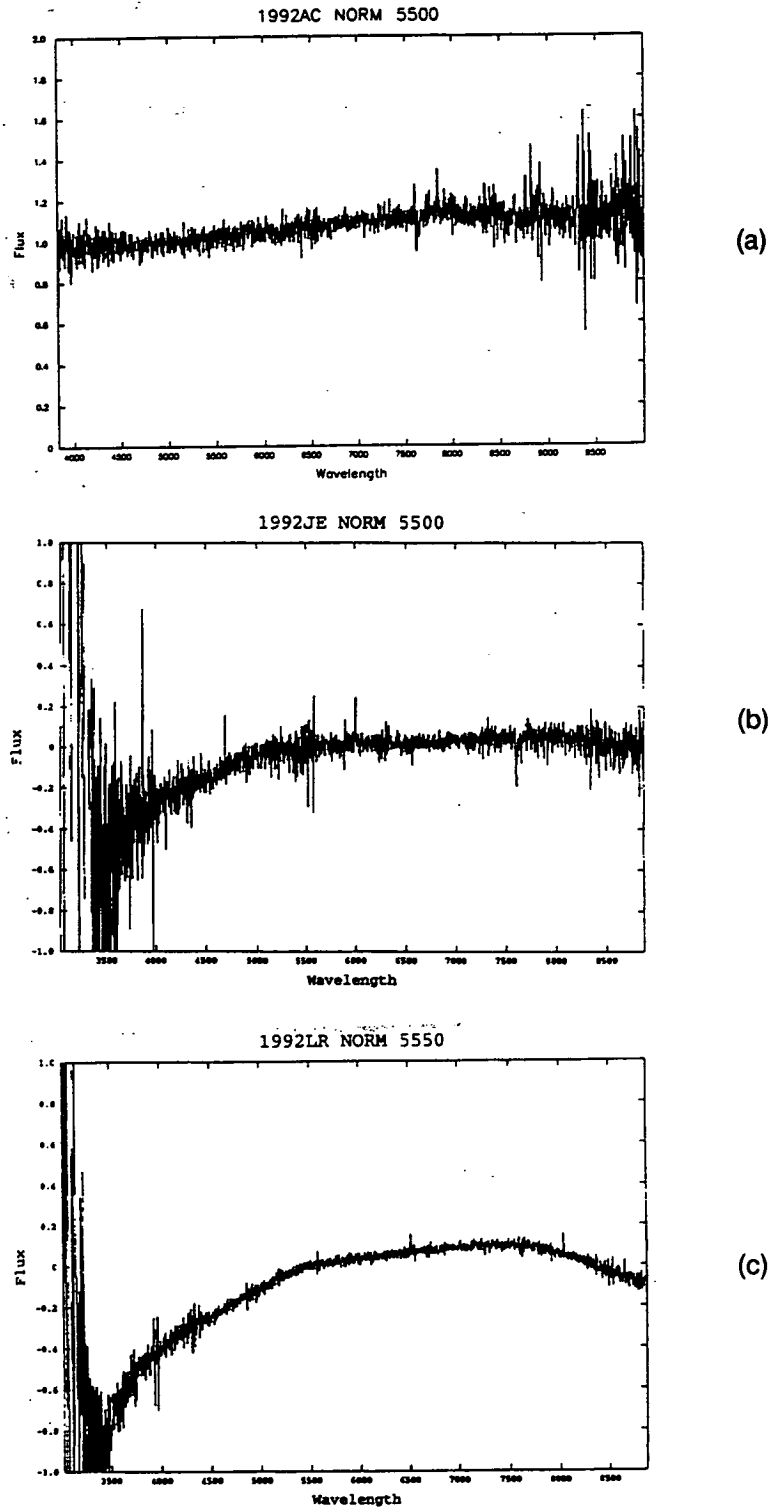


Figure 1. Spectra of 3 NEOs obtained using the 4.2m Herschel telescope on La Palma. As seen in part (a), 1992AC shows the characteristically flat spectra for an EMP type, while 1992JE, part (b), has the slightly more curved signature of the C-type asteroid. 1992LR, part (c), shows the flattening toward the red end of the spectrum characteristic of an S-type asteroid.

IRAF on our in-house Sun SPARC for data reduction. Also, we now have in-house software to produce ephemerides using the J2000.0 coordinate system, which is the system that B. Marsden uses to report newly discovered NEOs. In addition, we have hired a part-time observing assistant, Dr. Carol Neese, who will be responsible for acquiring most of the data once procedures and techniques have been established. We, as part of a consortium of scientists that is developing the Tumamoc Observatory – the Tumamoc Hill Users Group, otherwise known by the acronym THUG – have written a successful proposal for a small grant from the American Astronomical Society to purchase a Digital Audio Tape system, which will enable us to transfer and archive images that are taken at Tumamoc. Currently, images have to be written to a floppy disk which only holds at most 2-3 images, so if 100-200 images are acquired in a night, it takes a lot of disks as well as a lot of time to transfer them to the home institution. With this new system, a single tape will hold several hundred images.

We propose to use the Tumamoc Observatory on a regular basis to acquire physical observations of brighter NEOs. The exact limiting magnitude remains to be determined but it will be in the range of 15-17 (V), depending on how fast the object is moving and where it is located in the sky. But having access to an available telescope is essential to a program to observe newly discovered NEOs and to the goal of this program of acquiring physical observation of all such objects brighter than $V = 18.0$.

APPENDIX A

Example of the
NEO Observer Information File

Welcome to the Near-Earth Asteroid Observer Information Network. Here follows information concerning physical observations, both accomplished and planned, for all newly discovered NEO's brighter than V=18.5. All observers are strongly encouraged to report to the network their observing plans and the outcome of those plans so that they can be added to the list. Please send information to Don Davis or Elaine Owens at 5470::PSIKEY, fax 602/881-0335, or telephone 602/881-0332.

This file was last updated on 09/11/92.

92QN discovered on IAUC 5602 on 09/03/92.
V magnitudes from Circular:

08/26/92 15.7
09/15/92 16.7
10/05/92 17.8

Observer	Data Type	Telescope	Dates	Results
----------	-----------	-----------	-------	---------

92NA discovered on IAUC 5556 on 07/05/92.
Updated on IAUC 5582.
Improved orbital elements from MPC 20647.
V magnitudes from Circular:

08/20/92 13.5
08/30/92 13.1
09/15/92 14.1

Observer	Data Type	Telescope	Dates	Results
W. Wiesniewski	lightcurve, colors	60" UA/Mt. Lemm.	08/26-30/92	u,b,v,w,x filters C type V=12.90
R. Binzel	spectra	McGhill/Kitt Pk. MDM 2.4	09/05-12/92	C type 0.4-1 um spectra 1992Sep9 UT

92LR discovered on IAUC 5548 on 06/22/92.
Updated on IAUC 5560 and 5581.
Improved orbital elements from MPC 20646.
V magnitudes from Circular:

08/20/92 14.2
08/30/29 14.8
09/11/92 15.5

Observer	Data Type	Telescope	Dates	Results
S. Larson	colors	61" Catal. Sta.	06/26-27/92	B,V,R filters
A. Fitzsimmons	spectra	4.2m La Palma	07/21/92	spectra (.35-.9) probable S type
W. Wiesniewski	lightcurve, colors	60" UA/Mt. Lemm.	08/26-30/92	P=7h17m A=0.45m(V) Max V=14.67 u,b,v,w,x filters S type

92JE discovered on IAUC 5515 on 05/07/92.

Updated on IAUC 5542.

Improved orbital elements from MPC 20644.

Updated on V magnitudes from Circular:

08/16/92 16.7
07/26/92 16.8
09/15/92 16.9

Observer	Data Type	Telescope	Dates	Results
S. Larson	colors	61" Catal. Sta.	06/26-27/92	B,V,R filters
W. Wisniewski	lightcurve, colors	90" UA Kitt Pk.	06/??/92	
A. Fitzsimmons	spectra	4m. La Palma	07/21/92	spectra (.4-.9) probable C type
W. Wiesniewski	lightcurve	60" UA/Mt. Lemm.	06/26-30/92	

92HE reported on IAUC 5559 on 07/08/92.

Improved orbital elements from MPC 20644.

V magnitudes from Circular:

08/16/92 15.9
08/26/92 15.9
09/05/92 15.7

Observer	Data Type	Telescope	Dates	Results
S. Larson	colors	61" Catal. Sta.	06/26-27/92	B,V,R colors
W. Wiesniewski	lightcurve	60" UA/Mt. Lemm.	06/26-30/92	
R. Binzel	spectra	McGhill/Kitt Pk.	09/05-12/92	

You may ftp this file to your location if you wish. Simply ftp and use the "put" command. The file name is neo.txt.